

# **Morphology control of polystyrene foams with supramolecular additives**

DISSERTATION

zur Erlangung des akademischen Grades  
eines Doktors der Naturwissenschaften (Dr. rer. nat.)  
in der Bayreuther Graduiertenschule für Mathematik und  
Naturwissenschaften (BayNAT)  
der Universität Bayreuth

vorgelegt von

**Bastian Klose**

geboren in Amberg

Bayreuth, 2021



Die vorliegende Arbeit wurde in der Zeit von Juli 2016 bis September 2020 in Bayreuth am Lehrstuhl für Makromolekulare Chemie I unter Betreuung von Herrn Professor Dr. Hans-Werner Schmidt angefertigt.

Vollständiger Abdruck der von der Bayreuther Graduiertenschule für Mathematik und Naturwissenschaften (BayNAT) der Universität Bayreuth genehmigten Dissertation zur Erlangung des akademischen Grades eines Doktors der Naturwissenschaften (Dr. rer. nat.).

Dissertation eingereicht am: 30.08.2021

Zulassung durch das Leitungsgremium 21.09.2021

Wissenschaftliches Kolloquium 14.01.2022

Amtierender Direktor: Prof. Dr. Hans Kepler

Prüfungsausschuss:

Prof. Dr. Hans-Werner Schmidt (Gutachter)

Prof. Dr. Holger Ruckdäschel (Gutachter)

Prof. Dr. Markus Retsch (Vorsitz)

Prof. Dr. Jürgen Senker



Die vorliegende Arbeit ist als Monographie verfasst.

Teile der Arbeit sind bereits in den folgenden Publikationen erschienen:

*Morphology control of extruded polystyrene foams with benzene-trisamide-based nucleating agents*

M. Aksit<sup>1</sup>, **B. Klose**<sup>1</sup>, C. Zhao, K. Kreger, H.-W. Schmidt, V. Altstädt, *J. Cell. Plast.*, **2019**, 55, 249–261  
(<sup>1</sup> contributed equally to this work)

**DOI:** 10.1177/0021955X19837508

Diese Publikation ist in der vorliegenden Arbeit mit der Literaturstelle [67] zitiert.

*Extruded polystyrene foams with enhanced insulation and mechanical properties by a benzene-trisamide-based additive*

M. Aksit<sup>1</sup>, C. Zhao<sup>1</sup>, **B. Klose**, K. Kreger, H.-W. Schmidt, V. Altstädt, *Polymers* **2019**, 11.  
(<sup>1</sup> contributed equally to this work)

**DOI:** 10.3390/polym11020268

Diese Publikation ist in der vorliegenden Arbeit mit der Literaturstelle [68] zitiert.

*Kinked Bisamides as Efficient Supramolecular Foam Cell Nucleating Agents for Low-Density Polystyrene Foams With Homogeneous Microcellular Morphology*

**B. Klose**, D. Kremer, M. Aksit, K. P. van der Zwan, K. Kreger, J. Senker, V. Altstädt, H.-W. Schmidt, *Polymers*, **2021**, 13(7), 1094.

**DOI:** 10.3390/polym13071094

Diese Publikation ist in der vorliegenden Arbeit mit der Literaturstelle [191] zitiert.



## Abbreviations

<b><math>^1\text{H}</math> NMR</b>	Proton nuclear magnetic resonance
<b>ATR</b>	Attenuated total reflection
<b>BA</b>	Blowing agent
<b>BTA</b>	Benzene trisamide
<b>CAGR</b>	Compound Annual Growth Rate
<b><math>\text{CDCl}_3</math></b>	Deuterated chloroform
<b><math>\text{CF}_3\text{COOD}</math></b>	Deuterated trifluoroacetic acid
<b>CFC</b>	Chlorofluorocarbons
<b>d</b>	Doublet (NMR)
<b>DMF</b>	Dimethylformamide
<b>DMSO</b>	Dimethyl sulfoxide
<b>DSC</b>	Differential scanning calorimetry
<b>EI</b>	Electron ionization
<b>EPS</b>	Expanded polystyrene
<b><math>\text{Et}_3\text{N}</math></b>	Triethylamine
<b>EtOH</b>	Ethanol
<b>H-Bond</b>	Hydrogen bond
<b>HC</b>	Hydrocarbons
<b>HCFC</b>	Hydrochlorofluorocarbons
<b>HFC</b>	Hydrofluorocarbons
<b>IR</b>	Infrared
<b>IUPAC</b>	International Union of Pure and Applied Chemistry
<b>L/D</b>	Effective screw length/screw diameter
<b>LiCl</b>	Lithium chloride
<b>m</b>	medium (IR)
<b>MeOH</b>	Methanol
<b>MS</b>	Mass spectra
<b>Mtoe</b>	Million metric tons of oil equivalent
<b>NMP</b>	N-Methyl-2-pyrrolidone
<b>PBT</b>	Poly(butylene terephthalate)

<b>PE</b>	Polyethylene
<b>PET</b>	Polyethylene terephthalate
<b>PLA</b>	Polylactic acid
<b>PO</b>	Polyolefin
<b>PolMic</b>	Polarization microscope
<b>PP</b>	Polypropylene
<b>PS</b>	Polystyrene
<b>PU</b>	Polyurethane
<b>PVC</b>	Polyvinyl chloride
<b>PVDF</b>	Poly(vinylidene fluoride)
<b>PVF</b>	Polyvinyl formal
<b>q</b>	Quartet (NMR)
<b>qi</b>	Quintet (NMR)
<b>s</b>	strong (IR)
<b>s</b>	Singulett (NMR)
<b>SE2</b>	Secondary electrons
<b>SEC</b>	Size exclusion chromatography
<b>SEM</b>	Scanning electron microscopy
<b>sx</b>	Sextet (NMR)
<b>t</b>	Triplet (NMR)
<b>TGA</b>	Thermogravimetric analysis
<b>THF</b>	Tetrahydrofuran
<b>TiO<sub>2</sub></b>	Titanium dioxide
<b>TRGO</b>	Thermally reduced graphite oxide
<b>USD</b>	United States dollar
<b>VER</b>	Volume expansion ratio
<b>w</b>	weak (IR)
<b>XPS</b>	Extruded polystyrene

## Symbols

$\tilde{\nu}$	[cm <sup>-1</sup> ]	Wavenumber
$\mu$	[A m <sup>-2</sup> ]	Supramolecular macrodipole
$A_{\text{cell}}$	[ $\mu\text{m}^2$ ]	Area of an individual cell
$A_{\text{mic}}$	[ $\mu\text{m}^2$ ]	Area of the micrograph
$C$	[mol l <sup>-1</sup> ]	Concentration
$c_0$	[mol l <sup>-1</sup> ]	Concentration of gas in the uninfluenced volume
$D$	[m <sup>2</sup> s <sup>-1</sup> ]	Diffusion coefficient
$D_0$	[m <sup>2</sup> s <sup>-1</sup> ]	Temperature-independent diffusivity factor
$F$	-	Shape factor for heterogeneous nucleation
$f_s$	-	Fraction of struts
$K_n$	-	Knudsen number
$K_R$	[cm <sup>-1</sup> ]	Roseland mean extinction coefficient
$K_{\text{solid}}$	[cm <sup>-1</sup> ]	Extinction coefficient of the solid polymer
$K_{\text{struts}}$	[cm <sup>-1</sup> ]	Extinction coefficient of struts
$K_{\text{walls}}$	[cm <sup>-1</sup> ]	Extinction coefficient of cell walls
$L$	[mm]	Thickness
$l_{\text{mean}}$	[nm]	Mean free path
$M$	[g mol <sup>-1</sup> ]	Molar mass
$m/z$	[%]	Mass-to-charge ratio
$M^+$	-	Molecular ion peak
$M_0$	[wt.%]	Saturation concentration
$m_{\text{air}}$	[g]	Mass of the foam in air
$M_{\text{mic}}$	-	Magnification
$M_t$	[wt.%]	Quantity of gas absorbed
$m_{\text{water}}$	[g]	Buoyancy of the foam in water
$n$	-	Number of cells
$n_{\text{ref}}$	-	Effective index of refraction
$N_v$	[cm <sup>-3</sup> ]	Cell density
$P$	[Pa]	Pressure
$p_0$	[Pa]	Partial pressure in a cell

<b><math>p_{BA}</math></b>	<b>[Pa]</b>	Vapor pressure of the blowing agent
<b><math>p_{water}</math></b>	<b>[Pa]</b>	Water pressure at the underwater granulation
<b><math>Q</math></b>	<b>[W]</b>	Thermal energy
<b><math>R</math></b>	<b>[J K<sup>-1</sup> mol<sup>-1</sup>]</b>	Gas constant
<b><math>r</math></b>	<b>[<math>\mu\text{m}</math>]</b>	Radius
<b><math>R(t)</math></b>	<b>[<math>\mu\text{m}</math>]</b>	Radius of the bubble
<b><math>r^*</math></b>	<b>[<math>\mu\text{m}</math>]</b>	Critical radius of the bubble
<b><math>S</math></b>	<b>[mol J<sup>-1</sup>]</b>	Solubility coefficient
<b><math>K(t)</math></b>	<b>[m]</b>	Radius of the influence volume
<b><math>S_0</math></b>	<b>[mol J<sup>-1</sup>]</b>	Temperature-independent solubility factor
<b><math>T</math></b>	<b>[K]</b>	Absolute temperature
<b><math>T_{-5wt. \%}</math></b>	<b>[°C]</b>	Temperature at which 5 % mass is lost
<b><math>T_c</math></b>	<b>[°C]</b>	Temperature of the crystallization peak (minimum)
<b><math>T_{die}</math></b>	<b>[°C]</b>	Temperature of extrusion die
<b><math>T_g</math></b>	<b>[°C]</b>	Temperature of the glass transition
<b><math>T_m</math></b>	<b>[°C]</b>	Temperature of the melting peak (maximum)
<b><math>T_{melt}</math></b>	<b>[°C]</b>	Temperature of the polymer melt
<b><math>V</math></b>	<b>[<math>\mu\text{m}^3</math>]</b>	Volume
<b><math>V_{struts}</math></b>	-	Volumetric fraction of struts
<b><math>V_{walls}</math></b>	-	Volumetric fraction of cell walls
<b><math>W_{ini}</math></b>	<b>[g]</b>	Initial weight of the sample
<b><math>W_t</math></b>	<b>[g]</b>	Weight of the sample at time t
<b><math>\beta</math></b>	<b>[°]</b>	Conical angle between the additive and the bubble
<b><math>\gamma_0</math></b>	<b>[J m<sup>-2</sup>]</b>	Surface tension
<b><math>\gamma_{\alpha\beta}</math></b>	<b>[N m<sup>-1</sup>]</b>	Interfacial energy
<b><math>\delta</math></b>	<b>[ppm]</b>	Chemical shift
<b><math>\Delta E_D</math></b>	<b>[J mol<sup>-1</sup>]</b>	Activation energy for diffusion
<b><math>\Delta G</math></b>	<b>[J]</b>	Change in Gibb's free energy
<b><math>\Delta G^*_{Het}</math></b>	<b>[J]</b>	Gibb's free energy barrier for heterogeneous cell nucleation
<b><math>\Delta G^*_{Hom}</math></b>	<b>[J]</b>	Gibb's free energy barrier for homogeneous cell nucleation
<b><math>\Delta H_s</math></b>	<b>[J mol<sup>-1</sup>]</b>	Heat of solution
<b><math>\Delta P</math></b>	<b>[Pa]</b>	Pressure difference

$\Delta V_{\text{free vol}}$	-	Free volume due to the presence of heterogeneous particles
$\theta$	[°]	Contact angle between bubble surface and additive
$\lambda_{\text{bulk}}$	[W m <sup>-1</sup> K <sup>-1</sup> ]	Thermal conductivity of the solid material
$\lambda_c$	[W m <sup>-1</sup> K <sup>-1</sup> ]	Heat convection through the cells
$\lambda_g$	[W m <sup>-1</sup> K <sup>-1</sup> ]	Heat conduction through the gas
$\lambda_{g0}$	[W m <sup>-1</sup> K <sup>-1</sup> ]	Thermal conductivity of the gas in the cells
$\lambda_r$	[W m <sup>-1</sup> K <sup>-1</sup> ]	Radiation across voids and through cell walls
$\lambda_s$	[W m <sup>-1</sup> K <sup>-1</sup> ]	Heat conduction through the solid polymer
$\lambda_t$	[W m <sup>-1</sup> K <sup>-1</sup> ]	Total thermal conductivity
$\rho_{\text{bulk}}$	[kg m <sup>-3</sup> ]	Density of the bulk polymer
$\rho_{\text{foam}}$	[kg m <sup>-3</sup> ]	Density of the foam
$\rho_{\text{rel}}$	-	Relative density
$\rho_{\text{water}}$	[kg m <sup>-3</sup> ]	Density of water
$\sigma$	[W m <sup>-2</sup> K <sup>-4</sup> ]	Stefan-Boltzmann constant
$\tau$	-	Efficiency of the energy transfer between gas molecules
$\varphi$	[μm]	Cell size
$\varphi_m$	[μm]	Mean cell size



# Table of Contents

<b>Summary .....</b>	<b>1</b>
<b>Zusammenfassung .....</b>	<b>3</b>
<b>1 Introduction.....</b>	<b>5</b>
1.1 Polymer foams.....	5
1.2 The foaming process .....	7
1.2.1 Blowing agents .....	8
1.2.2 Cell nucleation .....	14
1.2.3 Bubble growth and stabilization.....	17
1.3 Different foaming techniques .....	20
1.3.1 Batch foaming.....	20
1.3.2 Extrusion foaming.....	22
1.3.3 Bead foaming.....	25
1.3.4 Foam injection molding.....	27
1.4 Classification and properties of polymer foams.....	30
1.4.1 Classification of polymer foams .....	30
1.4.2 Foam structure and morphology characterization .....	33
1.4.3 Thermal conductivity.....	36
1.5 Self-assembly and supramolecular additives .....	42
1.5.1 The self-assembly process.....	43
1.5.2 Supramolecular polymer additives.....	45
1.5.3 Supramolecular additives as foam nucleating agents.....	46
<b>2 Aim of the thesis .....</b>	<b>49</b>
<b>3 Foaming polystyrene with benzene trisamides .....</b>	<b>53</b>
3.1 Synthesis and properties of the selected benzene trisamides.....	54

3.1.1	Synthesis and characterization.....	54
3.1.2	Self-assembly behavior.....	55
3.1.3	Solubility in polystyrene .....	57
3.2	Batch Foaming.....	58
3.2.1	Foam sample preparation .....	58
3.2.2	Production of neat references .....	64
3.2.3	Foaming with benzene trisamides .....	66
3.3	Foam extrusion.....	71
3.3.1	Foam sample preparation .....	71
3.3.2	Foaming with the selected benzene trisamide .....	72
3.4	Conclusion .....	85
<b>4</b>	<b>Foaming polystyrene with bisamides.....</b>	<b>87</b>
4.1	Synthesis and properties of the selected bisamides.....	88
4.1.1	Synthesis and characterization.....	89
4.1.2	Self-assembly behavior.....	91
4.1.3	Solubility in polystyrene .....	95
4.2	Batch foaming.....	97
4.2.1	Foaming with the reference bisamides.....	97
4.2.2	Foaming with the kinked bisamides without a substitution at the central unit .....	100
4.2.3	Foaming with the kinked bisamides with the methyl substitution at the central unit .....	105
4.2.4	Foaming with the kinked bisamides with the ethyl substitution at the central unit .....	109
4.3	Foam extrusion.....	113
4.3.1	Foaming with the selected bisamide.....	113
4.3.2	Comparison of the trisamide and the bisamide as foam nucleating agents.....	121
4.4	Foam injection molding.....	124
4.4.1	Foam sample preparation .....	124

4.4.2	Foaming with the selected bisamide.....	125
4.5	Conclusion .....	131
<b>5</b>	<b>Experimental part .....</b>	<b>135</b>
5.1	Polymer and chemicals.....	135
5.2	Analytical methods.....	137
5.3	Experimental procedures .....	140
5.3.1	Self-assembly and solubility of the additives .....	140
5.3.2	Batch foaming.....	141
5.3.3	Extrusion foaming.....	143
5.3.4	Foam injection molding.....	144
5.4	Synthesis of the additives.....	145
5.4.1	Synthesis of the benzene trisamides.....	145
5.4.2	Synthesis of the bisamides .....	149
<b>6</b>	<b>Appendix .....</b>	<b>201</b>
6.1	SEM micrographs of the polystyrene batch foams .....	201
<b>7</b>	<b>References.....</b>	<b>219</b>
<b>8</b>	<b>Acknowledgement .....</b>	<b>233</b>
	<b>(Eidesstattliche) Versicherungen und Erklärungen .....</b>	<b>235</b>



## Summary

In view of the climate change and CO<sub>2</sub> reduction, polymer foams are an important material class for insulating and lightweight products. A significant proportion of the world's energy consumption is attributed to heating and cooling of houses and buildings. Therefore, polystyrene foams are widely used for insulation purposes. Heat transfer depends primarily on the density and morphology of the foams. At very low-densities, heat transfer via the solid phase is significantly reduced however the mechanical properties often suffer. Controlling the morphology towards homogeneous, smaller cell sizes, further reduces the heat transfer via the gas phase, as well as via thermal radiation. For this reason, this thesis addresses the *morphology control of polystyrene foams using supramolecular foam nucleating agents*.

The unique feature of supramolecular additives is the ability to self-assemble in polymer melts to supramolecular nanostructures through intermolecular non-covalent interactions. Supramolecular additives must be tailored with respect to the selected polymer in terms of solubility, self-assembly behavior, optimum concentration and applied processing procedure including different processing parameters. Supramolecular additives are used for example as nucleating and clarifying agents for semi-crystalline polymers and recently as foam nucleating agents. So far supramolecular foam nucleating agents have been mainly investigated and developed for polypropylene foams. In this thesis the concept of supramolecular nucleating agents is transferred to *tailor the morphology of amorphous polystyrene foams*.

The first part of this thesis deals with C<sub>3</sub>-symmetric *benzenetrisamide (BTA) additives as foam nucleating agents*. In addition to a commercially available *BTA* used as reference additive and benchmark, a second *BTA* more compatible to the polystyrene matrix was used. The first additive is a 1,3,5-triaminobenzene-based core with three *t*-butyl side groups. The second additive consists of 1,3,5-benzenetricarboxylic acid with three *i*-pentyl side groups, resulting in a higher solubility in the polystyrene melt. Self-assembly experiments revealed that both additives can form supramolecular nanofibers in polystyrene melts, whereby those of the second *BTA* have a significantly smaller diameter. Both *BTAs* were used in a concentration range of 0.01 - 1.0 wt.% in a *temperature-induced batch foaming process*. In screening experiments the optimal CO<sub>2</sub> concentration, the foaming temperature and the foaming time for the batch process were established. With these conditions, both foams with and without additives were produced and analyzed. The foam morphology of samples with the additive showed that both *BTAs* were able to nucleate the formation of the foam cells and significantly reduce the cell sizes in contrast to the neat

## Summary

---

reference foam. By improving the solubility from the first to the second BTA, it was possible to reduce the average cell size with 1.0 wt.% of the BTA by a factor of 4.5 compared to neat polystyrene foams.

To verify the concept of the morphology control by supramolecular additives on a *larger scale*, *foam extrusion* was employed. Extruded polystyrene foams with the BTA revealed an average cell size of 18  $\mu\text{m}$  corresponding to a reduction by a factor of more than 20 compared to the neat reference foam. The thermal conductivity was reduced about 15 %. Despite this substantial improvement, the limited solubility of the BTA in the polystyrene melt is a drawback.

Therefore, the second part of this thesis, deals with a novel class of *kinked bisamides as supramolecular foam nucleating agents*. Here, the central unit consists of two benzene rings connected by a methylene linker, which increases the solubility in polystyrene. In addition, by varying the substituents on the central unit and the peripheral substituent, the solubility and self-assembly behavior can be tailored. A total of twelve kinked bisamide additives were investigated. Extensive self-assembly studies in xylene as a model solvent for polystyrene showed that, depending on the structure, different supramolecular objects are formed in the form of fibers, ribbons or platelets.

A comprehensive investigation of these kinked bisamides in the *batch foam process* identified two candidates capable of forming foams with a homogenous morphology and an average cell size below 4  $\mu\text{m}$ . This equals a cell size reduction of 80 % compared to the neat reference foam.

To reveal the industrial potential including the ability to control the foam morphology for this class of additives, *foam extrusion* was carried out with one selected kinked bisamide consisting of an ethyl substituted central unit and cyclohexane groups in the periphery. Such extruded foams featured a homogeneous morphology with an average cell size of 10  $\mu\text{m}$  and a foam density of 71  $\text{kg m}^{-3}$  by using only 0.5 wt.% of the additive. These low-density polystyrene foams exhibit a reduction of the thermal conductivity by 26 % compared to the neat polystyrene reference foam. In addition, the effect of the *kinked bisamide* was also investigated in *foam injection molding process*. Here, it was also possible to reduce the average cell size and improve the homogeneity of the resulting polystyrene foams.

## Zusammenfassung

In Anbetracht des Klimawandels und der CO<sub>2</sub> Einsparung sind Polymerschäume eine wichtige Werkstoffklasse für Dämm- und Leichtbauprodukte. Ein erheblicher Teil des weltweiten Energieverbrauchs wird für das Heizen und Kühlen von Häusern und Gebäuden aufgewendet. Dementsprechend werden Polystyrolschäume in großem Umfang für Dämmzwecke verwendet. Die Wärmeübertragung hängt in erster Linie von der Dichte und der Morphologie der Schäume ab. Bei sehr niedrigen Dichten ist der Wärmetransport über die feste Phase deutlich reduziert, allerdings leiden die mechanischen Eigenschaften oft darunter. Die Steuerung der Morphologie in Richtung homogener, kleinerer Zellgrößen reduziert zudem den Wärmetransport über die Gasphase sowie über die Wärmestrahlung. Aus diesem Grund befasst sich diese Arbeit mit der Morphologiekontrolle von Polystyrolschäumen unter Verwendung supramolekularer Schaumnukleierungsmittel.

Die besondere Eigenschaft von supramolekularen Additiven ist die Fähigkeit, sich in Polymerschmelzen durch intermolekulare, nicht-kovalente Wechselwirkungen zu supramolekularen Nanostrukturen zu ordnen. Sie müssen in Bezug auf Löslichkeit, Selbstorganisationsverhalten, optimale Konzentration und angewandtes Verarbeitungsverfahren einschließlich der Verarbeitungsparameter auf das ausgewählte Polymer maßgeschneidert werden. Supramolekulare Additive werden beispielsweise als Nukleierungs- und Klärmittel für teilkristalline Polymere und neuerdings auch als Schaumnukleierungsmittel eingesetzt. Bisher wurden supramolekulare Schaumnukleierungsmittel hauptsächlich für Polypropylenschäume untersucht und entwickelt. In dieser Arbeit wird das Konzept der supramolekularen Nukleierungsmittel auf die Kontrolle der Morphologie von amorphen Polystyrolschäumen übertragen.

Der erste Teil dieser Arbeit befasst sich mit C<sub>3</sub>-symmetrischen Benzotrisamiden (BTA) als Additive zur Schaumnukleierung. Neben einem kommerziell erhältlichen BTA, das als Referenzadditiv und Benchmark fungiert, wurde ein zweites BTA verwendet, das auf die Polystyrolmatrix besser angepasst ist. Das erste Additiv basiert auf einem 1,3,5-Triaminobenzol-Kern mit drei *t*-Butyl-Seitengruppen. Das zweite Additiv besteht aus 1,3,5-Benzotricarbonsäure mit drei *i*-Pentyl-Seitengruppen, was zu einer höheren Löslichkeit in der Polystyrolschmelze führt. Experimente zur Selbstorganisation zeigten, dass beide Additive in Polystyrolschmelzen supramolekulare Nanofasern bilden können, wobei die des zweiten BTA einen deutlich geringeren Durchmesser aufweisen. Beide BTAs wurden in einem Konzentrationsbereich von 0,01 - 1,0 Gew.-% in einem temperaturinduzierten Batch-Schäumprozess eingesetzt. In Screening-Experimenten wurden die optimale CO<sub>2</sub>-Konzentration sowie die Schäumtemperatur und die Schäumzeit für den Batch-Prozess ermittelt. Unter diesen Bedingungen wurden sowohl Schäume mit als auch ohne

Additive hergestellt und analysiert. Die Schaummorphologien der Proben mit Additiv zeigte, dass beide BTAs in der Lage waren, die Bildung der Schaumzellen zu nukleieren und die Zellgrößen im Gegensatz zum reinen Referenzschaum deutlich zu reduzieren. Durch die Erhöhung der Löslichkeit vom ersten zum zweiten BTA konnte die durchschnittliche Zellgröße mit 1,0 Gew.-% des BTA um den Faktor 4,5 im Vergleich zu reinen Polystyrolschäumen verringert werden.

Um das Konzept der Morphologiekontrolle durch supramolekulare Additive auch in Großtechnischen Verfahren zu verifizieren, wurde Schäume mittels Schaumextrusion angefertigt. Hierbei wiesen die extrudierten Polystyrolschäume mit BTA eine durchschnittliche Zellgröße von 18  $\mu\text{m}$  auf, was einer Verringerung um einen Faktor von mehr als 20 im Vergleich zum reinen Referenzschaum entspricht. Zudem wurde die Wärmeleitfähigkeit um etwa 15 % verringert. Trotz dieser erheblichen Verbesserung ist die begrenzte Löslichkeit des BTAs in der Polystyrolschmelze ein Nachteil.

Daher befasst sich der zweite Teil dieser Arbeit mit einer neuartigen Klasse von gewinkelten Bisamiden als supramolekulare Schaumkeimbildner. Hier besteht die zentrale Einheit aus zwei Benzolringen, die durch einen Methylenlinker verbunden sind, wodurch die Löslichkeit in Polystyrol erhöht wird. Durch Variation der Substituenten an der zentralen Einheit und in der Peripherie lassen sich zudem die Löslichkeit und das Selbstorganisationsverhalten anpassen. Insgesamt wurden zwölf gewinkelte Bisamide untersucht. Umfangreiche Selbstorganisationsstudien in Xylol als Modelllösungsmittel für Polystyrol zeigten, dass sich je nach Struktur unterschiedliche supramolekulare Objekte in Form von Fasern, Bändern oder Plättchen bilden.

Bei einer intensiven Untersuchung der gewinkelten Bisamide im Batch-Schaumverfahren wurden zwei Kandidaten identifiziert, die in der Lage sind, Schäume mit einer homogenen Morphologie und einer durchschnittlichen Zellgröße von unter 4  $\mu\text{m}$  zu bilden. Dies entspricht einer Verringerung der Zellgröße um 80 % im Vergleich zum reinen Referenzschaum.

Um das Potenzial zur Morphologiekontrolle für industrielle Anwendungen aufzuzeigen, wurde das gewinkelte Bisamid welches eine ethylsubstituierte zentrale Einheit und eine Cyclohexangruppe in der Peripherie trägt für eine Schaumextrusion ausgewählt. Die extrudierten Schäume besitzen eine homogene Morphologie mit einer durchschnittlichen Zellgröße von 10  $\mu\text{m}$  und einer Schaumdichte von 71  $\text{kg m}^{-3}$  bei der Verwendung von nur 0,5 Gew.-% des Additivs. Diese Polystyrolschäume besitzen eine um 26 % geringere Wärmeleitfähigkeit als der reine Polystyrol-Referenzschaum. Schließlich wurde die Wirkung des gewinkelten Bisamides auch im Schaum-Spritzguss verfahren untersucht. Hier war es ebenfalls möglich die durchschnittliche Zellgröße zu verringern und die Homogenität der Polystyrolschäume zu verbessern.

# 1 Introduction

Due to the constantly increasing worldwide energy demand paired with the increasingly scarce fossil energy sources, it must be a concern of modern society to reduce the overall energy usage. An efficient way to achieve this is to reduce the huge energy consumption of buildings, which accounts for about 40 % of the total consumption of the European Union.<sup>[1]</sup> More than 60 % of this is wasted through heat loss from building elements such as floors, roofs, windows and walls. Expressed in numbers, this means that of the 1688 million metric tons of oil equivalent (Mtoe) consumed by the European union in 2018, about 675 Mtoe have been consumed by buildings, of which approximately 400 Mtoe are lost through heat loss.<sup>[2-4]</sup> To counteract this, good thermal insulation materials are of the utmost importance. The most commonly used materials are glass or mineral wool and polymer foams.

## 1.1 Polymer foams

The highest growth rate is predicted for polymer foams due to their better insulating properties.<sup>[5]</sup> In 2018 the global polymer foam market size was valued at 109 billion United States dollar (USD). It is predicted that the market will continue to grow with a Compound Annual Growth Rate (CAGR) of 4 % and reaches a size of approximately USD 144 billion in 2025. The two biggest driving forces are the growing demand in the automotive industry and the building and construction sector. The latter made the largest contribution in 2018, accounting for 37 % of the total volume. Looking at the foam market in terms of the matrix material used polystyrene (PS) foams account for the largest share of global sales with a percentage of 32 %. Due to its easy foamability, low price, excellent thermal insulation and mechanical properties, polystyrene foams are widely used in floor panels and in basement outer walls of buildings.<sup>[6,7]</sup> The second largest segment are polyurethane (PU) foams, followed by polyolefin (PO), phenolic and polyvinyl chloride (PVC) foams.<sup>[8]</sup> Since this work only deals with Polystyrene foams, this polymer should be discussed in more detail.

Polystyrene is one of the longest known plastics of all. The first records date back to 1839 as the pharmacist Eduard Simon, extracted styrene out of the sweetgum tree and observed a thickening to a gel-like substance after a few days.<sup>[9]</sup> His false assumption that this was an oxidation was refuted in 1866 by Marcellin Berthelot, who first recognized the polymerization process.<sup>[10]</sup> 64 years later in 1930, the first production of polystyrene began by IG Farbenindustrie AG in Ludwigshafen, Germany.<sup>[11]</sup> In 2018, global demand already reached a level of around 11.2 million tons.<sup>[12]</sup>

## Introduction

---

Polystyrene is a thermoplastic polymer which is in his casual form an amorphous, atactic transparent solid. The most common production method is a free radical polymerization in suspension using peroxide as initiators. Due to its good polymerization properties, an anionic, cationic or Ziegler-Natta catalyzed polymerization is possible, too.<sup>[13]</sup> Depending on the polymerization, the end product has a density of 1040 - 1060 kg m<sup>-3</sup> and a glass transition ( $T_g$ ) at 90 - 102 °C. Polystyrene is furthermore characterized by its hardness and stiffness, as well as its low water absorption. Besides it is distinguished by its low thermal conductivity of 0.170 W m<sup>-1</sup> K<sup>-1</sup>.<sup>[14]</sup> Due to its amorphous nature and its good melt strength, PS is the perfect matrix material to produce polymer foams.

There are two different types of polystyrene foams based on their production process which are used at an industrial scale. First, there is extruded polystyrene (XPS), which, is produced by foam extrusion. The polystyrene is loaded with the blowing agent (mostly CO<sub>2</sub> or N<sub>2</sub>) in the extruder and starts to foam when the pressure drops at the die. In this process, foam sheets of any size with good mechanical properties can be produced.<sup>[7]</sup> The second type are the so-called particle foams, which can be distinguished between two types: Expanded and expandable polystyrenes (EPS). In both cases, the material is usually loaded with the blowing agent directly during polymerization. If the resulting particles are foamed right after, this is referred to expanded beads. If, on the other hand, foaming is suppressed, for example by underwater granulation, expandable beads are produced. In both cases, the resulting particles can be firmly welded in a mold and thus be brought into many different shapes.<sup>[15,16]</sup> The best-known EPS is Styropor®, manufactured by BASF.

By foaming the polymer, the material gets several advantages over the unfoamed polymer, such as lightweight and thus a high strength to weight ratio<sup>[17]</sup>, excellent thermal insulation properties<sup>[17]</sup>, high impact strength and toughness<sup>[18]</sup>, good electrical insulation<sup>[19]</sup> and high fatigue life<sup>[20]</sup>. For all these benefits, the cell morphology and its uniformity as well as the density is of crucial importance.<sup>[21-23]</sup> These two parameters are decisive for the final properties of the material.<sup>[15,24-28]</sup> For this reason, it is the concern of many research groups to precisely control these two parameters. One possible way to accomplish these aims is by tuning the process parameters in terms of temperature<sup>[29-38]</sup>, pressure<sup>[33,35,37-43]</sup>, die geometry<sup>[44]</sup> and blowing agent (BA).<sup>[27,30,45-48]</sup> Another very frequently utilized method is the use of additives. A lot of different substances such as inorganic materials like talc<sup>[49-51]</sup> and nanoparticles<sup>[32,52-57]</sup> could be used. These act as nuclei for the nucleation of the foam bubbles, whereby a reduction of the cell size can be achieved. Another widely used class of additives are carbon materials<sup>[58-66]</sup> like activated carbon or carbon nanofibers/tubes. These have the advantage that, in addition to their cell nucleating effect, they also exhibit very good IR absorption, which can further reduce thermal conductivity. A common problem

regarding these additives however is their insolubility, which can ultimately lead to an inhomogeneous dispersion in the polymer matrix.

In this work, supramolecular additives are used.<sup>[67,68]</sup> These can be completely solved in the polymer matrix and can form supramolecular objects upon cooling. These homogeneously distributed objects can act as nuclei for the foam bubble formation. By a targeted adaptation of the additives to the polymer matrix, it is possible to control the morphology and thus improve the thermal conductivity of the resulting foams. Previous studies have already shown that supramolecular additives are able to control the morphology of polypropylene (PP) foams.<sup>[69,70]</sup> This concept is now to be transferred to amorphous polymers such as polystyrene.

## 1.2 The foaming process

The foaming process can basically be divided into three steps. These are shown schematically in **Figure 1.1**.

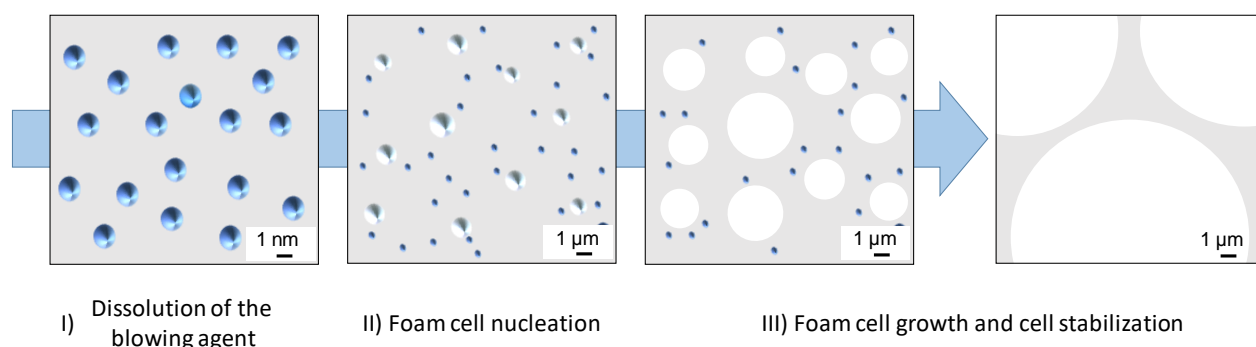


**Figure 1.1:** Schematic representation of the general steps in the foaming process of polymer materials (blue: blowing agent; grey: polymer phase; white: foam cells). Source: University of Bayreuth; Macromolecular Chemistry I and Polymer Engineering.

In step **I**, a blowing agent must be introduced into the matrix material and homogenized with the polymer to form a single-phase system. In the next step **II**, the solubility of this blowing agent is strongly reduced by a change in the thermodynamic equilibrium, which leads to nucleation of the foam cells and thus to foaming of the material. During step **III**, these nucleated cells continue to grow by diffusion of further blowing agent into the bubbles until the material is solidified by cooling, which stops the growth and stabilizes the foam into its final structure.

The different steps are explained detailed in the following chapters.

### 1.2.1 Blowing agents

Blowing agents are defined as substances which create a cellular structure in a polymer mass. Such substances include gases which expand when the pressure is reduced, liquids which are converted to a gaseous state, and chemical substances which react or decompose to release one or more gases. The first two are referred to as physical and the latter as chemical blowing agents. It should be noted that the gases emitted after the decomposition of the chemical substances act in the same way as a physical blowing agent. Each blowing agent must be directly adapted to the production process in order to reach its full potential and achieve the desired properties of the resulting foams. In the following, the two different types of blowing agents will be explained more precisely.

#### Physical blowing agents

As already mentioned, physical blowing agents are either gases, which are introduced into the polymer melt under very high pressures and subsequently expand the material by a drop in pressure, or liquids, which evaporate at the corresponding temperatures and thus ensure the expansion of the polymer as a gas.

In the past, almost exclusively halogenated hydrocarbons were used as blowing agents because of their outstanding properties. These include their low boiling point, non-toxicity, low thermal conductivity, low molecular weight and non-flammability. Chlorofluorocarbons (CFCs) were the most commonly used, until 1974, when Rowland and Molina published their thesis that CFCs reach the stratosphere, decompose to chlorine and catalytically destroy the ozone layer.<sup>[71]</sup> This led to the development of the International Montreal Protocol, which severely restricts the production and use of substances that damage the ozone layer.<sup>[72]</sup> The acceptance of this agreement in 1987 led to the search for alternative propellants. One possibility was the substitution of halogen by hydrogen since hydrochlorofluorocarbons (HCFCs) are chemically more unstable and therefore decompose into hydrogen halides and formyl fluorides before they reach the stratosphere. In 1992, the Copenhagen Amendment was added to the Montreal Protocol, which limits the production and use of HCFCs and bans them completely until 2040.<sup>[72]</sup> If no chlorine is used at all, the resulting hydrofluorocarbons (HFCs) have no ozone depletion potential. Due to their high costs and their negative effect on global warming, however, they are only used occasionally as physical blowing agents. As an alternative, there are some low-boiling short-chain hydrocarbons (HC) like propane, butanes and pentanes, which have properties which allow them to be used as blowing agents. They are inexpensive, halogen-free, have a high specific volume, no ozone-damaging effect, contribute little to global warming and are compatible with most conventional polymers. However, HCs also have a decisive

disadvantage as they are extremely flammable. For this reason, a great deal of effort must be invested in handling these substances in order to be able to use them safely as blowing agents.<sup>[16]</sup> Today, the most commonly used physical blowing agents are inert gases such as carbon dioxide and nitrogen. Both are cheap, abundant and very environmentally friendly. Of these two gases, CO<sub>2</sub> is the most commonly used in the production of polymer foams. Although CO<sub>2</sub> is considered a greenhouse gas, it can still be considered greenhouse neutral if it is produced as a by-product or extracted from natural sources. Another benefit is the low critical temperature of 31 °C and a moderate critical pressure of 73.8 bar of this gas. When the gas is in a super critical state, its solubility in the polymer increases enormously which benefits the homogenization and the overall uptake of the polymer melt.<sup>[16]</sup>

In addition to the use of individual gases as just described has been demonstrated in recent years that a blend of different blowing agents can be used to further tailor the properties of the resulting foams. In addition, it often leads to a better process controllability. For example, one blowing agent can be used for its inflation role and combined with another agent that ensures better stabilization of the process. Also, the total amount of blowing agent can be increased by blending if the solubility limits of the individual blowing agents are too low. A well-known example is the mixture of CO<sub>2</sub> and ethanol (EtOH) in the foam extrusion of PS. Here it was shown that the use of ethanol as a second blowing agent greatly improves overall plasticization and process stability and thus foams with extremely low-densities could be realized.<sup>[48,66]</sup>

To sum things up, the most important properties which distinguish a gas or liquid for the use as a physical blowing agent are listed again: Adequate vapor pressure, sufficient solubility in molten and low solubility in solid resin, low diffusivity, chemical inertness, safety, reasonable cost and environmentally-friendly. However, it is important to note that the blowing agent must be adapted for each polymer and process. An example is the foam extrusion with *n*-pentane as blowing agent. It has a boiling point of 36 °C and can generate negative pressure in the cells as it cools. If polystyrene is used as the matrix material, the rigid foam can withstand this pressure. If low-density polyethylene is used, however, cell collapse occurs during cooling.<sup>[7]</sup>

### Chemical blowing agents

Chemical blowing agents are low-molecular inorganic or organic compounds which can undergo a chemical reaction or decompose at a certain temperature. They lead to a release of gases like carbon dioxide, carbon monoxide, nitrogen or ammoniac, which then act like a physical blowing agent. They are normally added to the polymer in the form of granules or powder before the melting starts which leads to an easy dosing. For this reason, this type of blowing agents can be used with very little effort even on existing extrusion lines. Furthermore, an easy storage is possible and no special equipment for handling is necessary.

A further subdivision of chemical blowing agents can be made by the type of reaction that takes place leading to a distinction between endo- and exothermic reactants. The best known endothermic chemical blowing agent is sodium bicarbonate.<sup>[73]</sup> The decomposition reaction to carbon dioxide, water and sodium carbonate in this endothermic equilibrium is strongly favored by the elevated temperatures that have to be applied when melting the polymer. Other endothermic chemical blowing agents are for example ammonium bicarbonate, zinc carbonate, calcium azide or citric acid derivatives.<sup>[16]</sup> The most used exothermic chemical blowing agent is azodicarbonamide.<sup>[74]</sup> Its decomposition reaction releases very large amounts of nitrogen at temperatures around 200 °C. Carbon monoxide and ammoniac are also formed to a lesser extent but still contribute to the expansion process. The polymerization products of the isocyanic acid, which is also generated, remain in the foam.<sup>[75]</sup> Due to its very high gas yield of 220 ml g<sup>-1</sup>, azodicarbonamide is considered very economical.<sup>[76]</sup> Other exothermic chemical blowing agents include hydrazo carbonamide, benzenesulfonyl hydrazide, dinitrosopentamethylene tetramine, toluene sulfonyl hydrazide, azobisisobutyronitrile, and barium azodicarboxylate.<sup>[77]</sup>

No matter if endo or exothermic, the various chemical blowing agents react or decompose at different temperatures and must therefore be adapted to the prevailing process conditions and the polymer used. The most important factor is to ensure that the gas release temperature corresponds quite precisely to the process temperature. If this temperature is too high, there will be a limited gas release during processing due to incomplete decomposition, resulting in poor foaming of the material. However, if the temperature is too low, this has a negative effect on the cell structure and surface quality. In addition, the gas release should take place as fast as possible but still in a controlled manner within a small temperature range. Another aspect to be considered is the production of other substances beneath the desired gas, which can have a negative effect on the matrix material and thus on the long-term performance of the foam. Because chemical blowing agents are relatively expensive and the decomposition products remain

in the material, they are most likely used to produce foams with a high or medium-density 400 – 800 kg m<sup>-3</sup> where not as much blowing agents content is needed.

In the succeeding section, the solubility and diffusivity of the blowing agent in the polymer matrix will be discussed in more detail, as these two factors have a major impact on the resulting foam morphology and density of the foams produced.

### Solubility and Diffusivity

For the foaming process a single-phase polymer-gas mixture must be present before the actual foaming takes place to ensure the production of homogeneous cell structures and high cell densities. For this reason, it is necessary that the gas which is directly injected into the polymer melt or released by a chemical reaction is completely soluble. If the blowing agent is not completely dissolved and there are still gas voids in the polymer melt, gas molecules will diffuse into them leading to a further growth.<sup>[78]</sup> Since the generated large gas spaces have a lower pressure than the smaller cells, a diffusion-driven coalescence of the nearby nucleated cells into this large gas cavities takes places resulting in an inhomogeneous cell morphology and a low cell density.<sup>[79,80]</sup> For this reason it is mandatory to adjust the blowing agent concentration to the polymer and the prevailing process parameters.

In theory, the solubility of a blowing agent at equilibrium and with an ideal sorption is described by Henry's law (1):<sup>[81]</sup>

$$S = \frac{C}{p} \quad (1)$$

Here S describes the solubility coefficient, C the concentration of gas absorbed per unit mass of polymer and p the gas pressure. However, in nearly all cases this is not a linear relationship, as sorption is not ideal in most polymer gas systems. This is also the case, for example, with the sorption behavior of nitrogen and carbon dioxide in polystyrene, since both gases swell the polymer.<sup>[82]</sup> However, the solubility coefficient is not only dependent on pressure but also on temperature. Using Henry's law, the Arrhenius equation and the van't Hoff relationship, the dependence of the solubility from temperature can be expressed as (2):<sup>[28,83,84]</sup>

$$S = S_0 \cdot e^{\frac{-\Delta H_s}{R \cdot T}} \quad (2)$$

## Introduction

---

$S_0$  represents the temperature-independent solubility factor,  $\Delta H_s$  the heat of solution,  $R$  the general gas constant and  $T$  the absolute temperature. In the following figure the courses of the two equations (1) and (2) are shown schematically.

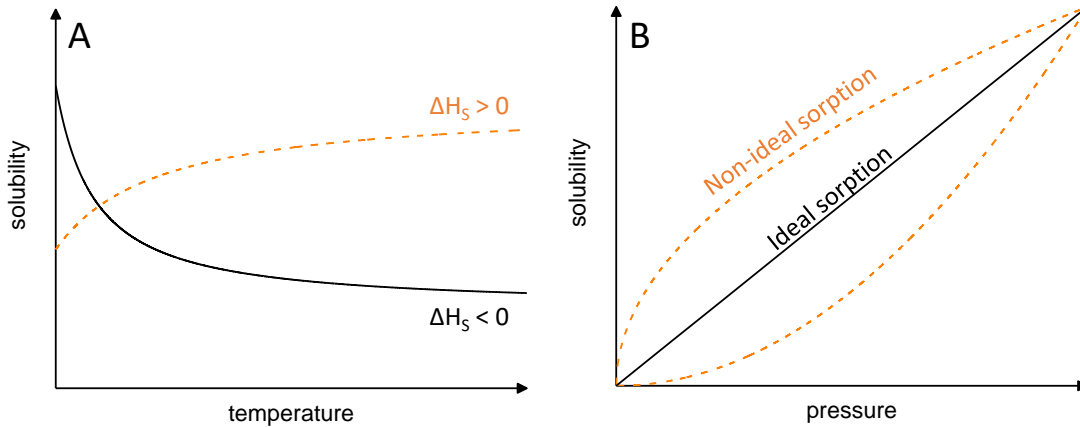


**Figure 1.2:** Schematic representation of the solubility of gases in the polymer matrix as a function of **A:** temperature and **B:** pressure calculated according to equation (1) respectively (2).

**Figure 1.2 A** shows the solubility of the blowing agent in the polymer matrix as a function of temperature. For most gases like  $\text{CO}_2$ ,  $\Delta H_s$  has a negative value which means that the solubility decreases with increasing temperature. Some gases, for example  $\text{N}_2$ ,  $\Delta H_s$  also have a positive value, which means that the solubility increases with increasing temperature.<sup>[85]</sup> As already mentioned, the solubility curve as a function of pressure **Figure 1.2 B** shows a linear relationship in the case of ideal sorption. Especially at very high gas pressures, however, positive or negative deviations from the ideality can occur.<sup>[28]</sup>

A practical investigation of the solubility respectively the maximum absorption of a gas by a polymer sample can be performed in a high-pressure autoclave. For this purpose, the sample is saturated to equilibrium at the desired pressure. After the sample is taken out of the autoclave the mass loss due to diffusion of the gas is measured continuously over time. From the initial weight of the sample  $W_{ini}$  and the weight at the measured time  $t$   $W_t$ , the quantity of gas absorbed  $M_t$  at the time  $t$  can be calculated using the following equation:<sup>[86,87]</sup>

$$M_t = \frac{W_{ini} - W_t}{W_{ini}} \cdot 100 \% \quad (3)$$

To determine the saturation concentration  $M_0$ ,  $M_t$  is plotted against the square root of the desorption time. By extrapolating the fit curve, the saturation concentration can be derived from the Y-axis intercept.

In addition to the solubility, the diffusivity of the blowing agent in the polymer matrix plays a decisive role. The diffusivity is determined by the chemical structure of the polymer, its chain mobility, packing and morphology.<sup>[88]</sup> Furthermore, process parameters such as temperature, pressure and concentration of the gas have an influence on it. The temperature dependence of the diffusion coefficient  $D$  can be described by the following equation:<sup>[89]</sup>

$$D = D_0 \cdot e^{\frac{-\Delta E_D}{R \cdot T}} \quad (4)$$

Where  $D_0$  represents the maximal diffusion coefficient at infinite temperature and  $\Delta E_D$  the activation energy for diffusion. Consequently, the diffusion increases with rising temperature and thus a better homogenization of the blowing agent in the polymer phase can be achieved at higher temperatures.

A final aspect of blowing agents is their plasticizing effect on the polymer. As they are small molecules, they can intercalate between the polymer chains, thus reducing their interactions, which increases the mobility of the chains and reduces the glass transition of the material. According to the model developed by Chow<sup>[90]</sup> there is a linear relationship between the blowing agent concentration and the decrease of the glass transition temperature.<sup>[91,92]</sup> By lowering the  $T_g$  the viscosity of the material gets reduced which promotes faster formation and growth of foam cells leading to a reduction in cell size and density. In addition, with a reduced viscosity a processing at lower temperatures is possible, which has a positive effect not only on foam formation due to reduced coalescence, but also on the economic aspects.<sup>[7]</sup> Is the blowing agent added to the polymer at the solid state, the modulus gets reduced. The reduction is necessary to enable foaming of solid polymers like for example in batch foaming. Here it is required that the polymer can be deformed by the resulting pressure inside the emerging cells. The constant outgassing during the foaming process reduces the plasticizing effect and the foam cells can be stabilized effectively. Under these conditions it is possible to generate very small cells. Finally, the crystallization of semi-crystalline polymers is also delayed by the plasticizing effect of the blowing agents.<sup>[93,94]</sup> The delay can have a beneficial effect on foam formation, as the polymer crystallizes very quickly, solidifying the polymer and thus preventing further expansion.

## 1.2.2 Cell nucleation

The next step of the foaming process is to expose the polymer/gas mixture to a thermodynamic instability to start the nucleation of the cells. This instability is caused by the sudden reduction of gas solubility due to pressure and/or temperature changes. The supersaturated system is attempting to lower its free energy as gas molecules assemble into cell nuclei. By further diffusion of the gas into the cells the free energy of the system is reduced furthermore. The formation of cell nuclei is an extremely important part of the foaming process, as it influences the morphology of the cells and thus determines the properties of the final foam.<sup>[7]</sup> The classical nucleation theory is the most used theory to describe the process of cell nucleation and growth in polymeric foams. It distinguishes in two different types: homogenous and heterogeneous nucleation. The course of the Gibbs free energy as a function of the radius of the nucleus is shown for both types in **Figure 1.3** and is explained in more detail separately.

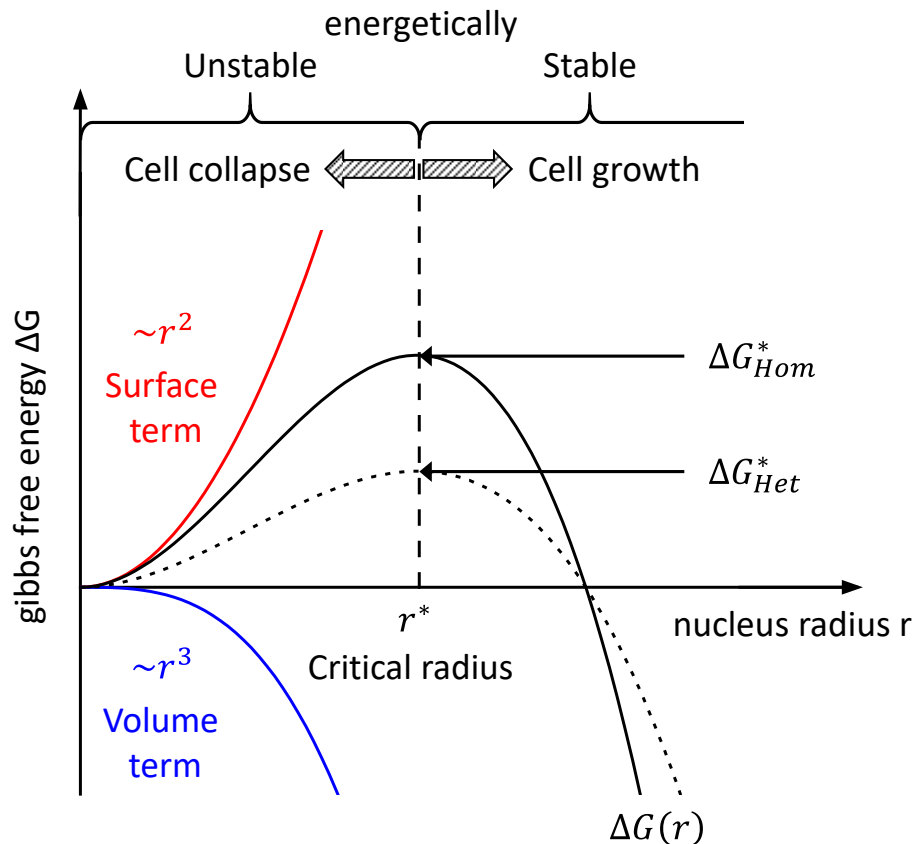


**Figure 1.3:** Course of the Gibbs free energy  $\Delta G$  as a function of the nucleus cell radius  $r$  for homogeneous and heterogeneous nucleation calculated according to (5).<sup>[95,96]</sup>

### Homogenous nucleation

Homogenous nucleation means the spontaneous and random formation of bubbles without any external nuclei. In most cases, nucleation is initiated by minimal pressure or temperature differences in the melt. For a newly build cell to grow without collapsing, it is necessary to reach the critical radius  $r^*$  and thus exceed the energy maximum of the free energy barrier  $\Delta G_{Hom}^*$ . Furthermore, the stability of the cell depends on the pressure difference inside the cell and the ambient pressure, as well as the interfacial energy. Taking all these factors into consideration, Gibbs free energy  $\Delta G(r)$  can be expressed as follows:<sup>[95,96]</sup>

$$\Delta G(r) = -\frac{4}{3}\pi r^3 \Delta P + 4\pi r^2 \gamma_{\alpha\beta} - \Delta V_{free\ vol} \quad (5)$$

With the interfacial energy  $\gamma_{\alpha\beta}$ ,  $\Delta P$  the pressure difference and  $\Delta V_{free\ vol}$  as term for the free volume of the additives, which can be ignored for homogenous nucleation.

If the system is at the maximum of Gibbs free energy, the cells have reached exactly the critical radius  $r^*$  and it applies:

$$r^* = \frac{2\gamma_{\alpha\beta}}{\Delta P} \quad (6)$$

Accordingly, the homogenous Gibbs free energy barrier  $\Delta G_{Hom}^*$  can be expressed as:

$$\Delta G_{Hom}^* = \frac{16\pi\gamma_{\alpha\beta}^3}{3\Delta P^2} \quad (7)$$

### Heterogeneous nucleation

Heterogeneous nucleation is caused by defects, such as impurities or additives that act as nuclei, which drastically reduces the required activation energy. The extent of the reduction strongly depends on the surface and geometry of the additives. For example, a planar surface is assumed for platelet-shaped nucleating agents and smooth equipment walls. However, for most of the nucleating agents this approximation does not apply since they and their agglomerates have rough surface geometries in micro- or nanoscale (nano-fibers, talc, nano-silica, etc.). Therefore, it is appropriate to see the surface of the additives as a conical cavity.<sup>[79]</sup> A schematic representation of the heterogeneous foam cell nucleation on the surface of the additives is shown in **Figure 1.4**.

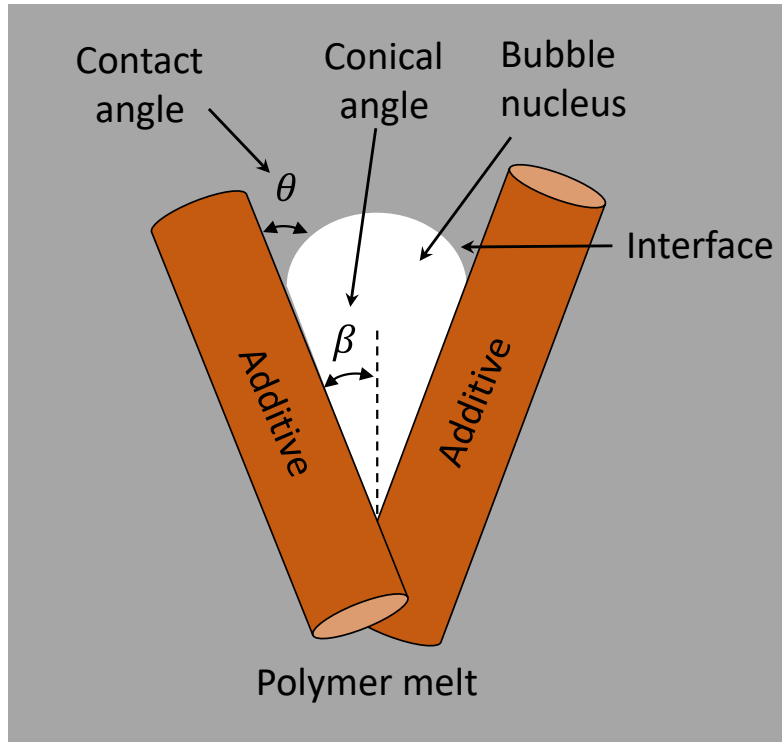


**Figure 1.4:** Heterogeneous foam nucleation at the additive surface in the polymer melt. Visualization of the conical angle  $\beta$  and the contact angle  $\theta$ . Adapted from [79].

If the nucleation is caused by a heterogeneous nucleus, equation (7) must be extended with the so-called shape factor  $F$ :<sup>[97,98]</sup>

$$G_{Het}^* = G_{Hom}^* \cdot F(\theta, \beta) = \frac{16\pi\gamma_{\alpha\beta}^3}{3\Delta P^2} \cdot F(\theta, \beta) \quad (8)$$

Whereby  $F$  is dependent on the wetting of the bubble on the additive, respectively the contact angle  $\theta$  and the conical angle  $\beta$ .

$$F(\theta, \beta) = \frac{1}{4} \left[ 2 - 2 \sin(\theta - \beta) + \frac{\cos\theta \cos^2(\theta - \beta)}{\sin\beta} \right] \quad (9)$$

According to equation (9), the shape factor is decreasing with increasing the contact angle  $\theta$ . In addition, a reduction of the conical angle  $\beta$  also leads to a reduction of the shape factor  $F$ . Therefore, a better wetting of the additive by the bubble nucleus and a tight angle  $\beta$  leads to a huge depletion of the Gibbs free energy which is necessary for a stable nucleus. Consequently, by selecting suitable foam nucleating agents it is possible to form stable nuclei much faster and therefore more cells are generated which increases the cell density in the final foam.

### 1.2.3 Bubble growth and stabilization

Once nucleation has taken place and the nucleus has exceeded the critical radius, the cell is able to grow driven by the pressure inside the cell. In contrast the viscosity of the polymer itself and the surface tension of the gas bubble hinder this expansion. To describe the growth process of the bubble, the classic “single bubble growth model” is often used. Here, however, it is assumed that each bubble has an infinite volume of gas available for growth, which is not the case in a foaming process.<sup>[99,100]</sup> For this reason, the model was further developed into the so-called “cell model” and is schematically shown in **Figure 1.5**.<sup>[101,102]</sup>

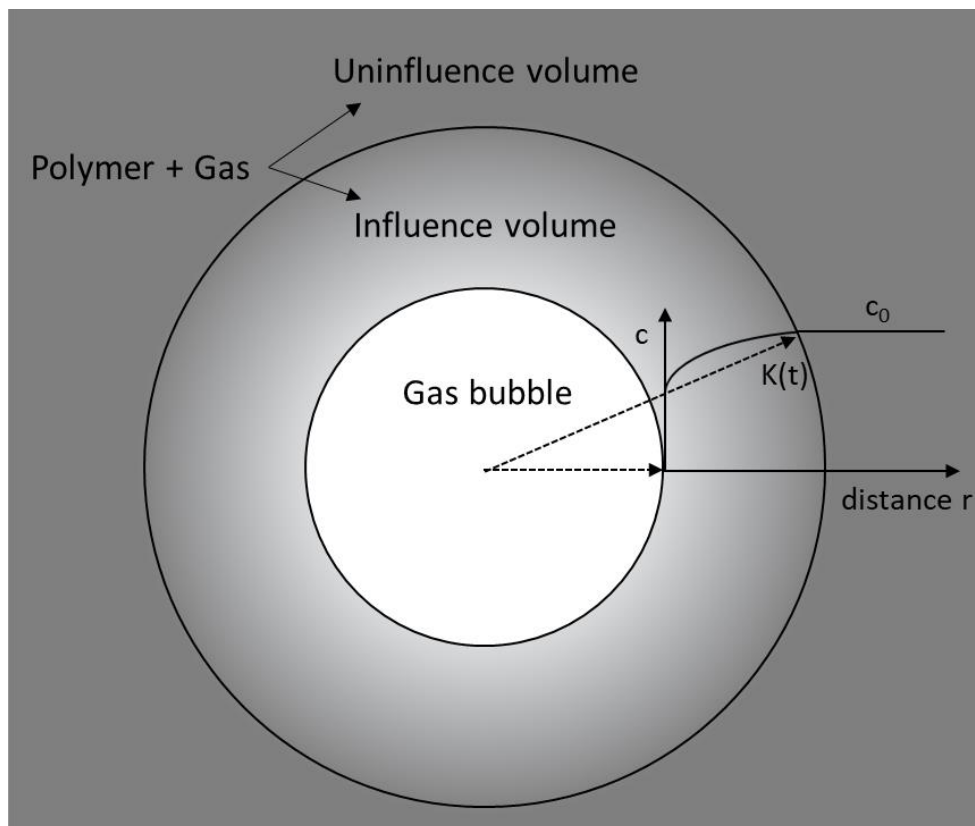


**Figure 1.5:** Schematic representation of the gas bubble and its surrounding volume. Adapted from <sup>[103]</sup>.

It is assumed that each cell is surrounded by a finite amount of gas loaded melt, referred to as influence volume in the figure. It is further assumed that both the cell and the influence volume are spherical and remain so over the entire growth period. The concentration of the blowing agent in the uninfluenced volume remains constant over the entire period of time at  $c_0$ .

When approaching the bubble, the gas in the polymer melt begins to diffuse into the interior of the bubble from a radius  $K(t)$  onwards, causing a concentration gradient. The growth of the cell continues until either all the dissolved gas has diffused into the cell or an equilibrium between the energy required for the

## Introduction

---

expansion of the surface and the necessary volume work has been reached. This equilibrium can be expressed by the following equation:

$$\gamma_0 \cdot dA = p_0 \cdot dV \quad (10)$$

Here  $\gamma_0$  stands for the surface tension,  $p_0$  for the partial pressure in the cell,  $dA$  and  $dV$  for the change of the surface and the volume respectively. Since the assumption of a spherical bubble was made, the change in surface and volume can be formulated via the radius  $r$  of the bubble:

$$\gamma_0 \cdot 8\pi r \cdot dr = p_0 \cdot 4\pi r^2 \cdot dr \quad (11)$$

The partial pressure within a cell with radius  $r$  is thus:

$$p_0 = \frac{2 \cdot \gamma_0}{r} \quad (12)$$

Accordingly, at a constant surface tension the partial pressure in a smaller cell is always greater than in a larger cell. Therefore, when two cells of different sizes collide, the blowing agent will diffuse from the smaller to the larger cell leading to a shrinkage and finally to a cell collapse.<sup>[104]</sup> This cell deterioration mechanism is named cell coarsening<sup>[79]</sup>. If there is an inhomogeneous distribution of cell sizes at the beginning of the stabilization process, this inhomogeneity gets even more pronounced by cell coarsening, leading to a poor final foam morphology. This is another reason why undissolved gas in large bubbles during the foaming process has an extremely negative effect on the resulting foam quality.

In addition to cell coarsening, cell coalescence is also important factor. If two foam cells grow next to each other, the cell wall between them is subjected to biaxial stretching. As a result, the cell wall may rupture. Although this is desired in the production of open-cell foams, the quality of closed-cell foams is greatly reduced by the inhomogeneous foam structure that is created. The phenomenon of cell coalescence occurs mainly in foams produced with polymers having a low melt strength. Polypropylene foams are to be mentioned here in particular. One way to reduce or even eliminate cell coalescence is to branch the polymer. By using long-chain-branched PP in foam extrusion, it is possible to significantly increase the cell density and the foam density compared to linear PP.<sup>[105,106]</sup> Further possibilities to prevent cell coalescence include the use of suitable additives which are oriented towards the cell walls and thus increase the melt

strength.<sup>[107]</sup> It is also possible to reduce the melt temperature during foaming. If the temperature during foaming is too high, the bubbles may shrink to smaller cells due to the lower viscosity or cell coalescence may occur before the foam can be stabilized. On the other hand, if the temperature is too low, the foam will be stabilized too quickly during cooling and the cells will not grow to their maximum size. Therefore it is important to find the optimal foaming window for each process.<sup>[108]</sup> Excessive tearing of the cell walls can cause the whole foam to collapse. So, it is necessary to stabilize the foam beforehand by appropriate measures. The easiest way is to increase the viscosity, for example by cooling, building up molecular weight or by stress hardening. In addition, stabilization can be achieved by reducing the surface tension and by increasing the free energy with increasing the surface area.<sup>[109]</sup>

### 1.3 Different foaming techniques

For the implementation of the above described principles, various methods can be utilized. The four most commonly used foaming techniques are batch foaming, extrusion foaming, bead foaming and foam injection molding. The former is usually a small-scale process while the other three are large scale processes used in industry. In the following chapters, the individual techniques will be explained in more detail and their advantages as well as the areas of application will be listed.

#### 1.3.1 Batch foaming

The so-called batch foaming is a batch-wise process that is carried out in a closed vessel such as a high-pressure autoclave and can be divided into two sub-categories. They are distinguished in which way the thermodynamic instability is induced, which causes the foaming of the sample. The process is called either temperature-induced or pressure-induced batch foaming.

##### Temperature-induced batch foaming

Using this method, the thermodynamic instability is caused by a rapid change in temperature throughout the material. A schematic representation of the entire process is shown in **Figure 1.6**.

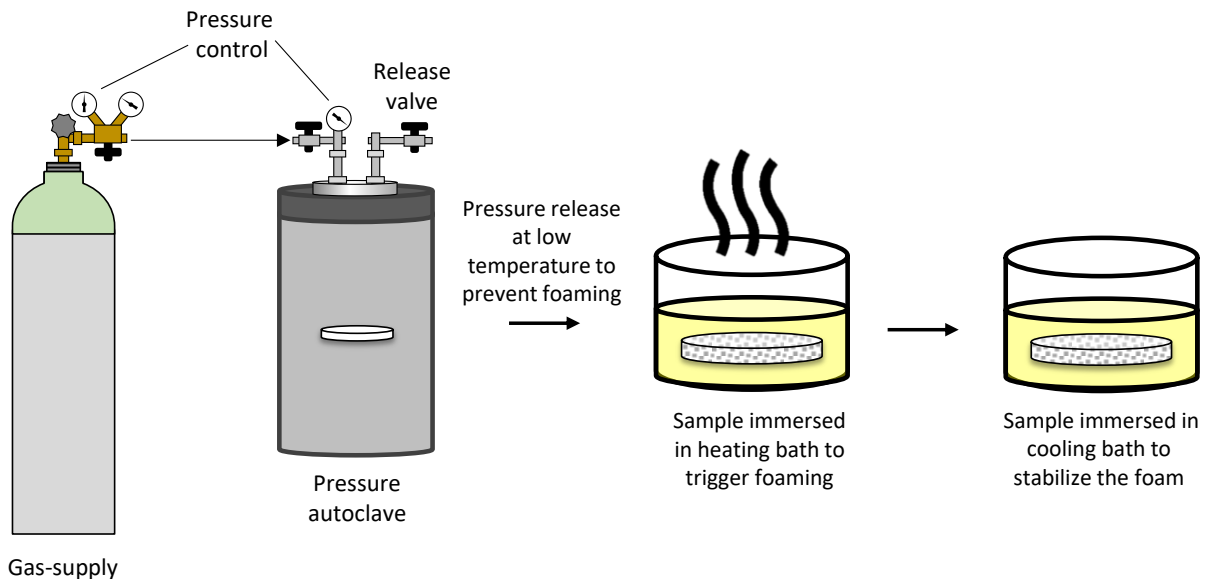


**Figure 1.6:** Schematic illustration of the temperature-induced batch foaming process.

First, the sample is placed in a high-pressure autoclave. The sample itself should not be too thick to ensure a quick and uniform saturation. Afterwards the sample is charged with the desired blowing agent, which is performed at relatively low temperatures and high pressures. When the equilibrium saturation is reached after a certain time, the pressure is released slowly, and the sample is taken out of the autoclave.

Since the samples are still far below the glass transition temperature no foaming occurs. In a second step the sample is now placed in a heating bath. The temperature rises above the  $T_g$  of the polymer/blowing agent mixture, increases the chain mobility significantly, allowing the stored gas to expand and subsequently start cell nucleation and growth. To stop the foaming process and to stabilize the structure, the sample is transferred from the hot bath to a cold bath, which solidifies the polymer matrix.

This type of batch foaming is mainly used for amorphous polymers, as the blowing agent can easily penetrate into the spaces between the polymer chains. Decisive parameters influencing the foaming result are mainly the dissolved amount of blowing agent, determined by type, loading time, temperature and pressure as well as the temperature and residence time in the heating bath. As these parameters can be set independently of each other, good process control is guaranteed.<sup>[110–112]</sup>

### Pressure-induced batch foaming

This type of batch foaming uses a rapid pressure drop to nucleate the cells and to start the expansion of the foam. The process is shown schematically in **Figure 1.7**.

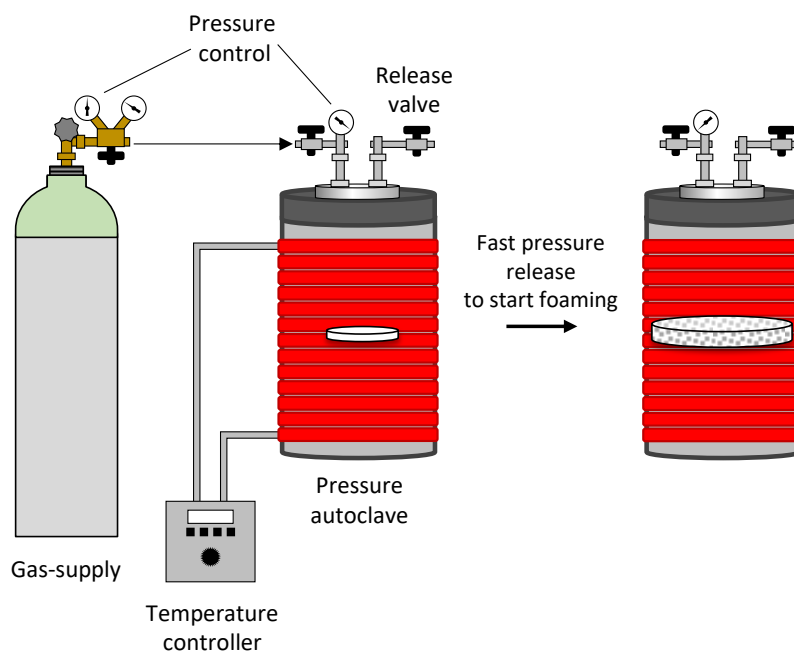


**Figure 1.7:** Schematic illustration of the pressure-induced batch foaming process.

Similarly, the sample is first placed in a high-pressure autoclave where it is loaded with the desired propellant under high-pressure. In this case, however, this is carried out at elevated temperatures. Once the sample is loaded with the desired amount of blowing agent, rapid depressurization to atmospheric pressure takes place. This pressure drop immediately lowers the solubility of the blowing agent in the

polymer melt, causing the supersaturated sample to nucleate and grow cells. The cooling to stabilize the final cell structure can be done either at air or in an extra cooling bath.

With this process as well, the final foam structure depends on various factors. Similar to temperature-induced batch foaming, the dissolved blowing agent is of great importance. In addition, the pressure drop or the pressure drop rate is the most important parameter. Increased depressurization also increases the level of supersaturation and thus the driving force for cell nucleation (see Equation (7) and (8)). In addition, the diffusion of the blowing agent is limited by a shorter pressure drop, which favors cell nucleation over cell growth.<sup>[113]</sup>

In conclusion, both batch foaming processes are laboratory-scale experiments, they are therefore used especially in the field of research and development. This enables not only to validate the effects of the individual process parameters, but also to investigate the influence of additives, for example. The results obtained can be used both to clarify structure-property relationships and as a basis for a possible up-scaling towards industry-relevant processes.

### 1.3.2 Extrusion foaming

Foam extrusion has been used to produce large quantities of polymer foams on an industrial scale since the 1970's.<sup>[7]</sup> Today, the enormous demand of foams, especially in building and construction, packaging and lightweight applications, is driving the desire to use a continuous process whereby it is possible to achieve enormously high throughput rates. In addition, it is an easy-to-control process that can be used for a wide range of different polymers which feature a sufficient high melt strength. Typical materials are polystyrene, polyvinyl chloride and polyurethanes, with polyolefins gaining in importance in recent years.<sup>[114]</sup> Most foam extrusion in the industry is performed on tandem lines. Compared to the single, tandem lines offer the advantage of better temperature control and better homogenization of all components. **Figure 1.8** shows an example of such an extrusion line used for foam extrusion.

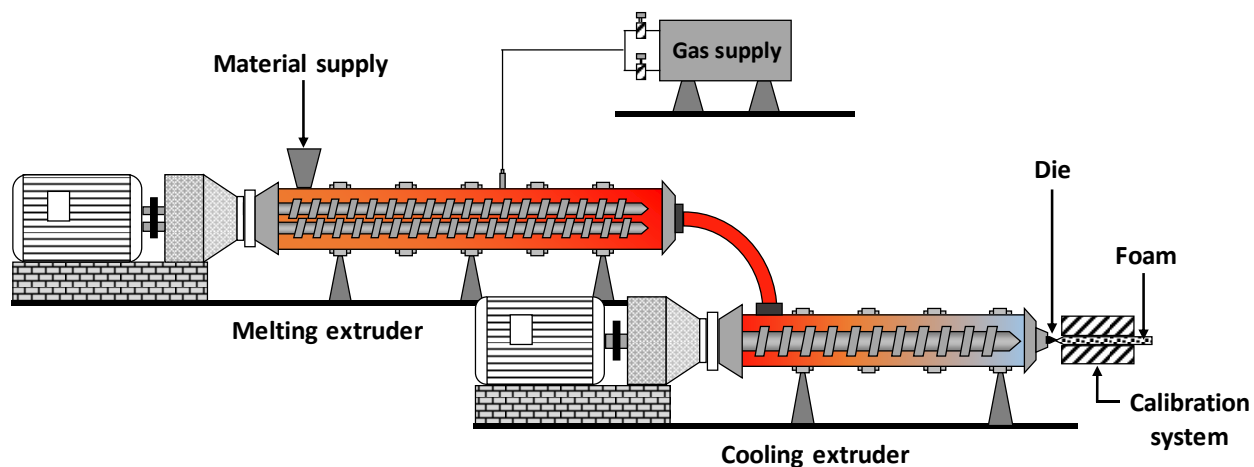


**Figure 1.8:** Schematic illustration of a foam extrusion process using a tandem extrusion line.

At the beginning of the process the system is continuously loaded with the desired polymer. In the first extruder, often called melt or melting extruder, the material is first heated and melted at high temperatures and pressures. The blowing agent is subsequently injected into the first extruder. In order to achieve a good homogenization of polymer, blowing agent and possible additives, a twin-screw extruder is often used. The screw configuration allows the melt flow, pressure and shear rate to be varied.<sup>[115]</sup> At the end of the first extruder there should ideally be a single-phase system that is transferred to the second extruder. Here the gas loaded melt is slowly cooled down to the desired foaming temperature. For this reason, this is often referred to as the cooling extruder. The cooling process increases both the pressure and the viscosity. At the end of the second extruder is the die, where a rapid pressure drop occurs, which triggers cell nucleation and growth. The cells continue to grow until the polymer solidifies. Often a calibration unit is attached to the end of the die, which makes it possible to thaw the foam strand and give it the desired shape.

The ability of a polymer whether it can be processed with the foam extrusion process depends on its crystallinity and its crystallization rate, among other things. Depending if a polymer is amorphous, semi-crystalline or crystalline, it has a correspondingly large process or foaming window. This is the temperature range in which foaming of the desired material is possible in terms of viscosity and melt strength. The lowest possible temperature is called the extrusion limit. If the melt is cooled down below this limit, the pressure in the extruder becomes too high due to the increase in viscosity resulting in an emergency shut down of the machines. Furthermore, it is possible for the die to freeze if the temperature is too low, which means that the process must also be stopped. The highest possible temperature that the melt can exhibit during foaming is called the foaming limit. If this temperature is exceeded, the polymer no longer has a

sufficiently high viscosity and melt strength, causing cell collapse and the resulting foam to shrink. A visualization of the foaming window for the materials with a different crystallinity is shown in **Figure 1.9**.

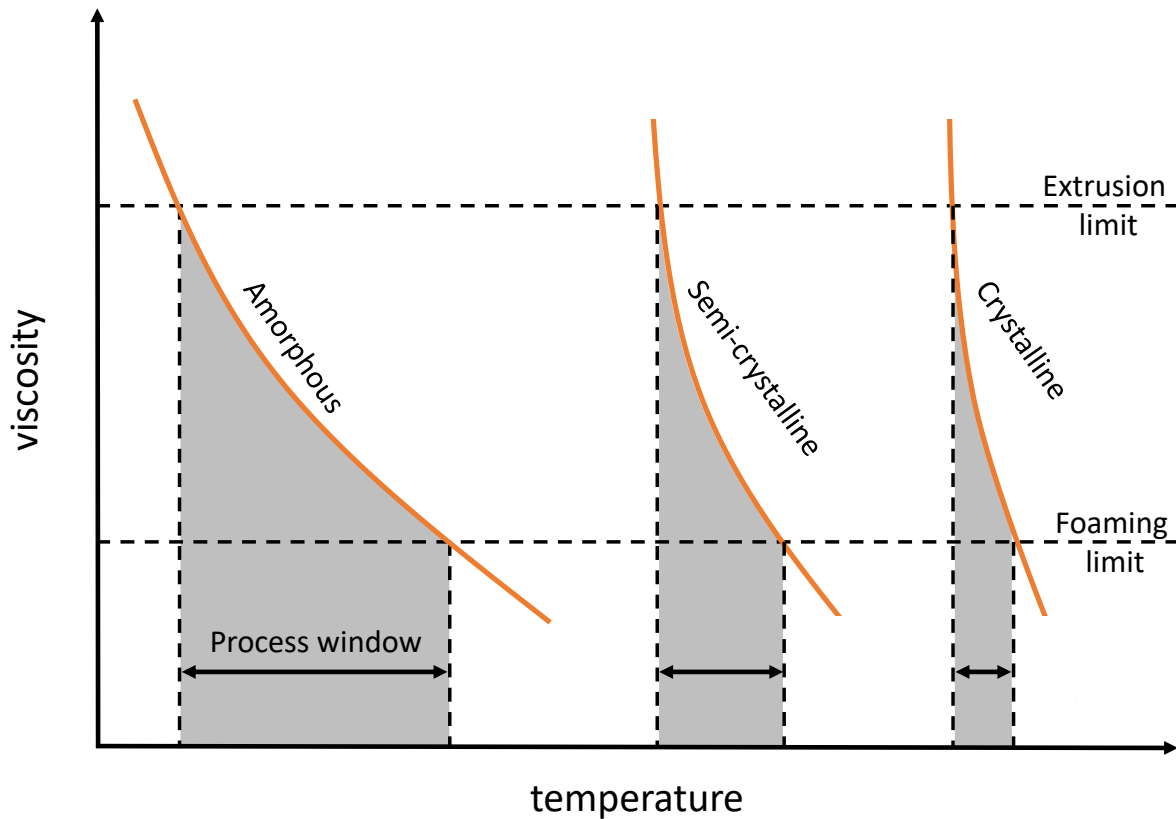


**Figure 1.9:** Schematic representation of the process window for amorphous, semi-crystalline and crystalline polymers. Adapted from [7].

While the viscosity of amorphous polymers decreases almost continuously with increasing temperature, in semi and crystalline materials this transition occurs very abruptly with crystallization or melting of the crystallites. The higher the crystallinity and the faster a polymer crystallizes, the narrower the foaming window. For amorphous polystyrene, the processing window is around 50 °C, while for semi-crystalline PP it is only 4 °C.<sup>[116]</sup> A common method to increase the foamability is by using chain extender. This allows a molecular weight increase by branching or chain elongation, which has a positive effect on the melt strength. In this way it is possible to significantly improve the foamability for example of PP<sup>[117,118]</sup>, polylactic acid (PLA)<sup>[119]</sup> or polybutylene terephthalate (PBT)<sup>[120]</sup>.

### 1.3.3 Bead foaming

Bead foams are a multitude of foamed polymer particles that have been welded together to create almost any desired shape. This is also the biggest advantage of bead foams, because in this way lightweight parts with very complex geometries can be produced, which are in no way inferior in their properties to extruded foams. Bead foams made of PS, PE and PP have the largest market share.<sup>[121]</sup> Basically there are two different types of beads, expandable beads and expanded beads. The former are particles which contain blowing agent but have not yet been foamed. This is basically only possible with amorphous polymers, as these are able to retain the blowing agent over a longer period of time even in solid state. By means of a so-called pre-expansion step, these are later foamed and welded to the desired component. The enormous advantage of this type of beads is the much more efficient transport and storage possibility of the unfoamed particles. In addition, the pre-expansion step allows the part-manufacturer to control the density of the beads himself. The latter refers to particles that are already foamed. These usually consist of semi-crystalline polymers, as the crystalline domains make it impossible to store the blowing agent in a solid state for a long time. **Figure 1.10** shows the different ways of producing both types.

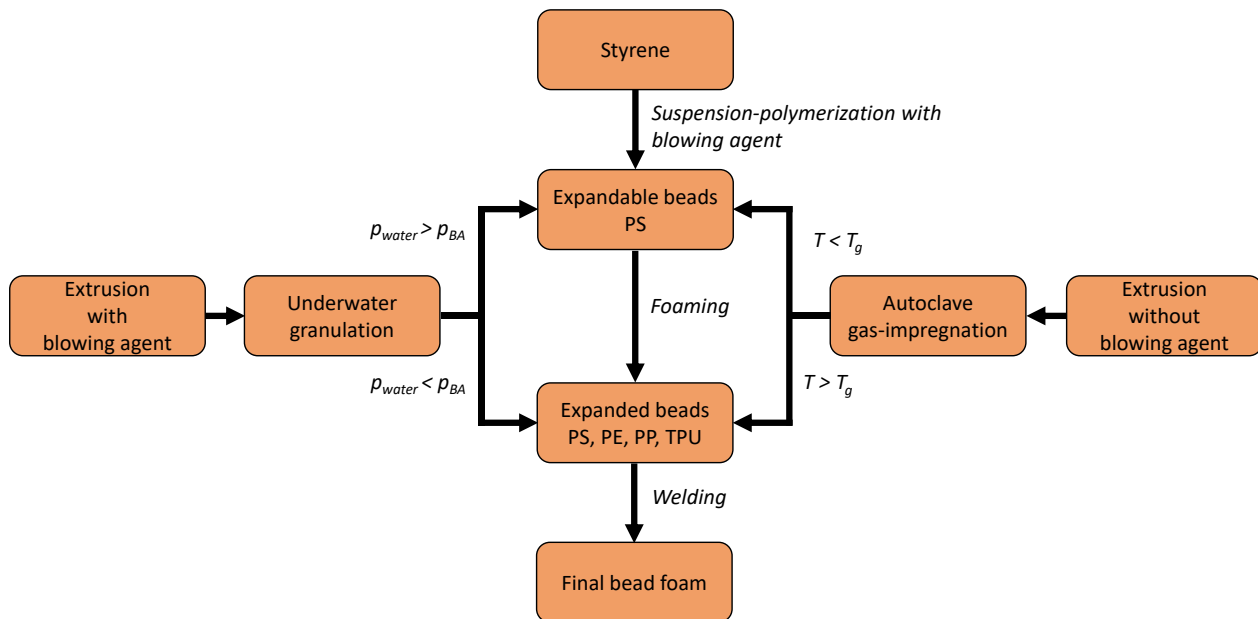


**Figure 1.10:** Different techniques for the production of expanded and expandable beads as well as further processing to the final bead foam.

There are three different techniques to produce expandable beads, predominantly out of polystyrene. The most common way is to introduce the blowing agent directly into the polymer during a suspension polymerization of styrene.<sup>[122]</sup> First the PS particles are formed and afterwards the desired blowing agent, in most cases pentane, can be introduced.<sup>[123]</sup> To prevent agglomeration, the particles are coated with an

## Introduction

---

antistatic agent. In order to obtain a homogeneous size distribution they are also sieved.<sup>[122]</sup> The disadvantage of this method, however, is that it is difficult to utilize additives. Since the additive must not change the polymerization process and the surface tension of styrene and water.<sup>[124]</sup>

Another possibility is the extrusion with the desired blowing agent and downstream underwater pelletizing.<sup>[125]</sup> The extrusion step is carried out analogous to the foam extrusion process described before. The difference is that there is a hole plate instead of the die, which extrudes the polymer strand into a stream of water and cuts it into small particles with rotating knives. If the water pressure is greater than the vapor pressure of the blowing agent, the latter remains trapped in the solidified polymer and expandable beads are obtained. If the water pressure is not sufficient, the pressure difference causes foaming and expanded beads are generated. The big advantage of this production method is that it is a continuous process and therefore large quantities can be produced quickly. Furthermore, it is possible to dose the blowing agent and, if necessary, additives precisely.

Finally, the beads can also be loaded with the blowing agent at a later point in the production process. For this purpose, the micro pellets are first produced by extrusion without a blowing agent. In a second step, the granulate can now be loaded in an autoclave. If the loading takes place at a temperature below the glass transition of the polymer used, foaming can be suppressed. In this way expandable beads can be produced from amorphous polymers. If the blowing agent is loaded at a temperature above the  $T_g$ , the particles foam at the pressure drop and expandable beads are created. This is the main production of polypropylene particles.<sup>[126]</sup>

The expanded particles, whether directly during extrusion or in a pre-expansion step, are then welded into the desired component. This is done in a so-called steam-chest molding process. The particles are placed in a special mold and heated under high-pressure with steam. The surface of the particles gets melted or softened and polymer chains diffuse into adjacent beads. This results in cohesion between the various particles.<sup>[127]</sup> A good cohesion together with a low percentage of macro-voids is required to ensure good mechanical properties of the resulting foam.

### 1.3.4 Foam injection molding

Foam injection molding is a special form of the conventional injection molding process. The major difference is that the material is mixed with a blowing agent, which allows the specimens to foam in the mold. Depending in which form and at what state the loading is carried out, different processes are distinguished. If the loading of the granulate takes place outside of the extruder either in the feed hopper or in an extra autoclave, the process is called ProFoam respectively KUZ process. If the gas is injected directly into the melt in the extruder, it is referred to as the MuCell or CellMould process.<sup>[128]</sup> Regardless at what state in the process the gas loading takes place, the process is nevertheless almost identical. The structure of a system that operates according to the CellMould process is shown schematically in **Figure 1.11**.

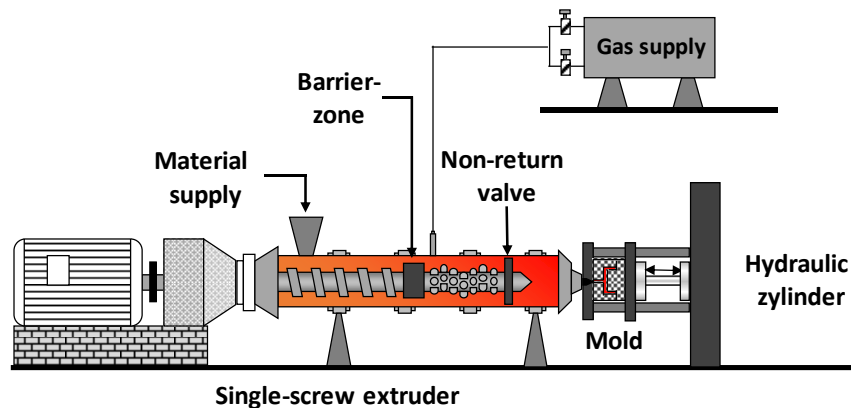


**Figure 1.11:** Schematic illustration of a foam injection molding system using the CellMould process.

First, the supplied material is melted in the extruder. A distinctive feature compared to foam extrusion is that the screws do not move the melt forwards but backwards. Due to a special design of the screw together with non-return valve it is possible to generate a well homogenized gas/polymer melt at the end of the extruder. This melt is injected into the cavity of the mold. A distinction is made between two different types of injection methods, namely the low-pressure and the high-pressure approach.<sup>[109]</sup> In **Figure 1.12** the two possibilities are shown schematically.

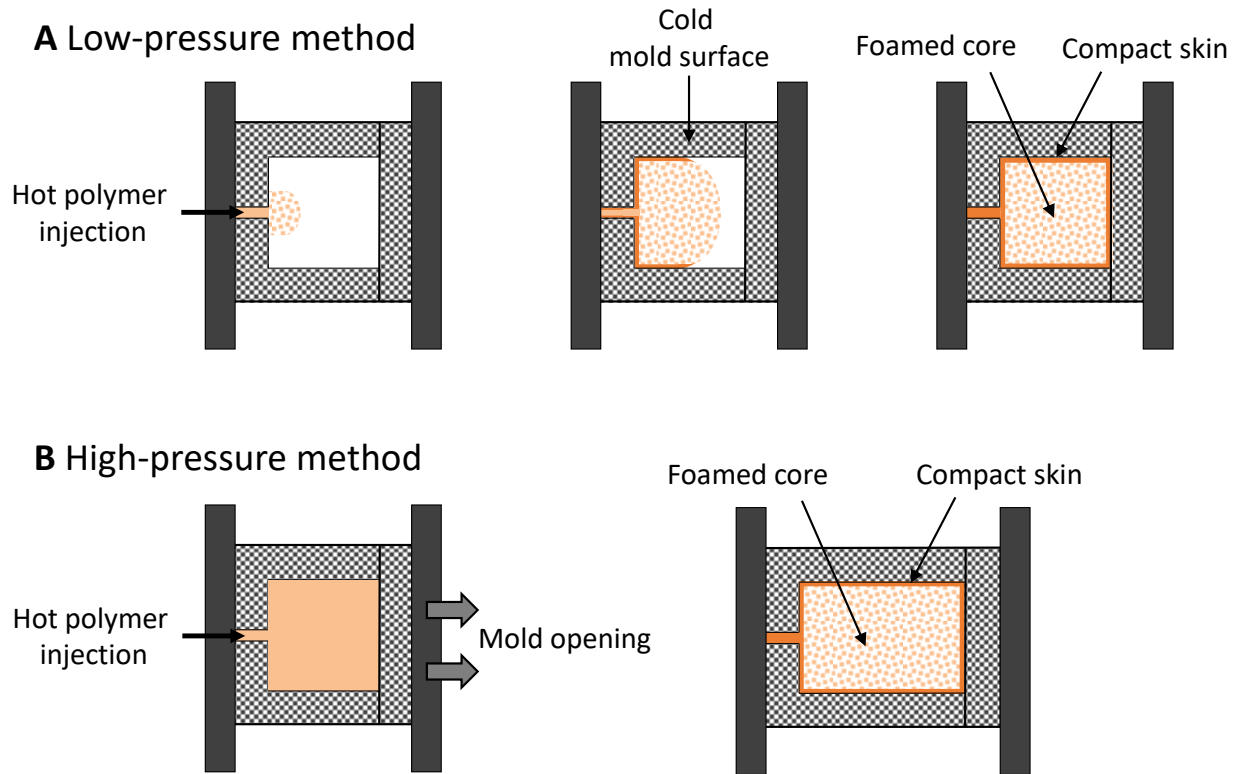


**Figure 1.12:** Schematic illustration of two methods of filling the mold in foam injection molding: **A:** low-pressure method using a normal mold and **B:** high-pressure method for a breathing mold. Adapted from <sup>[109]</sup>

In the low-pressure method, a pressure drop occurs directly when injecting the gas-charged melt, resulting in foaming of the sample. Since the walls of the mold are significantly colder than the hot polymer, solidification occurs immediately and an unfoamed compact outer skin is formed. This isolates the rest of the subsequent melt, which allows it to flow and foam for longer period of time. With this method, the cavity is not completely filled with gas-charged melt. Nevertheless, the foaming of the material fills the entire component.

In the high-pressure method the mold is completely filled under high-pressure to suppress foaming. The mold is then slowly opened to the desired thickness. The newly gained volume and the resulting pressure drop causes the sample to foam. The mold required in this method is called a breathing mold.<sup>[69]</sup>

Both methods lead to components with a compact skin and a foamed core. This type of foams is also called integral foams. Due to the sandwich structure these foams have better specific mechanical properties than their non-foamed counterparts.<sup>[129]</sup> Foam injection molding is mainly used to reduce the weight of components, which is accompanied by a reduction of the required material, leading to a reduction of the costs ultimately. A further advantage of the foam injection molding process compared to conventional injection molding is the reduced material shrinkage and less warpage due to the internal pressure of the

expanding blowing agent. In addition, the introduction of a blowing agent lowers the viscosity of the melt, which results in a reduction of the injection pressure and thus the required clamping force of the machines is reduced. A problem that often occurs in foam injection molding is the deterioration of the optical properties of the components. Early foaming at the flow front generates foam bubbles which get dragged towards the inner wall of the mold. Here they solidify and crack due to the continuous mold movement. The resulting streaks are called silver marks or silver streaks.<sup>[130,131]</sup> To reduce the occurrence of these defects, a counterpressure can be applied in the mold to prevent premature foaming, or dynamic cooling of the mold can be implemented. In this case the wall of the cavity is heated, so that prematurely foamed cells do not solidify on the wall but are smoothed.<sup>[109]</sup>

### 1.4 Classification and properties of polymer foams

There are numerous different polymer foams which cover an enormously large spectrum of properties. Of course, the matrix material itself has the biggest influence. But even foams made from the same polymer can have extremely different features. In the following different possibilities to classify polymer foams and the most important characteristics and their effects on the resulting properties will be explained.

#### 1.4.1 Classification of polymer foams

To be able to compare and distinguish polymer foams more easily, it is useful to classify them according to different considerations. The most common distinction is by their cellular structure, hardness, density or volume expansion ratio and the size of the foam cells.

##### Cellular structure

The cellular structure is the type and manner in which the individual cells are connected within the foam. It is called a closed-cell foam when the individual cells are completely separated from each other by walls. This leads to higher rigidity and strength. In addition, the permeability is greatly reduced, making these materials very suitable for the use in thermal insulation.<sup>[132]</sup> If, on the other hand, the neighboring cells are connected by pores in the cell walls, it is considered as an open-cell foam.<sup>[133]</sup> It should be noted that it is also referred to a closed-cell foam having up to 10 % of interconnected cells.<sup>[134]</sup> An extreme form of this is a reticulated foam, in which only a skeletal structure of the cells is left and no cell walls are present.<sup>[79]</sup>

The open-celled ratio of a foam is greatly determined by the degree of expansion during extrusion. At higher degrees of expansion, the probability of cell walls breaking is higher, resulting in more open cells. One possibility to determine the open cell content is to measure the adsorption or permeation of water.<sup>[15]</sup> The following table briefly lists the advantages and disadvantages of open cell foams:

**Table 1.1:** Advantages and disadvantages of open-celled foams.<sup>[15]</sup>

<b>Advantages of open-cell foams</b>	<b>Disadvantages of open-cell foams</b>
Fast gas exchange possible	Weak isolation properties
Less blowing agent residuals	Reduced mechanical properties
Good acoustic isolation	Lower buoyancy
Higher liquid adsorption and desorption	Lower energy absorption capacity
	Lower dimensional stability

Since the properties of foams can vary greatly depending on their cellular structure, i.e. the open or closed cell content, it is very useful to classify them according to this aspect. The majority of the foams produced have a mainly closed cell structure, thus it is necessary especially for open cell foams to specify their cellular structure.<sup>[28]</sup>

### Hardness

Classifying the foams in terms of their stiffness creates three different groups. The subdivision is based on the resistance of the substance to being deformed elastically, i.e. the elastic modulus, at 23 °C and 50 % relative humidity:<sup>[135]</sup>

<b>Description</b>	<b>Elastic modulus [MPa]</b>
• Flexible foams (soft)	< 68.6
• Semi-flexible foams (semi-rigid)	68.6 – 686
• Rigid foams	> 686

If the polymer foam has an elastic modulus of less or equal than 68.6 MPa, it is referred to as a soft or flexible foam. Examples are soft polyvinyl chloride<sup>[136]</sup>, polyvinyl formal (PVF)<sup>[137]</sup> und PP<sup>[138]</sup> foams. With an elastic modulus of 68.6 – 686 MPa the foam is called semi-flexible or semi-rigid. Characteristic for this area are semi-hard polyurethane<sup>[139,140]</sup> foams. If the elastic modulus is greater than 686 MPa it is a rigid foam, such as hard PU<sup>[141]</sup>, PS<sup>[142]</sup> or phenolic foams<sup>[143]</sup>. As already shown in the examples, the rigidity of the foam is determined by the polymer matrix used, but foam density, morphology and cellular structure also play a major role. The rigidity increases with density and decreases with open-cell content.

### Foam density or volume expansion ratio (VER)

The density is one of the most basic properties of a foam, therefore it is reasonable to subdivide based on this aspect as well. To compare foams made of different materials a distinguishing regarding the volume expansion ratio is also possible.

<b>Description</b>	<b>Volume expansion ratio</b>
• High-density foams	< 4
• Medium-density foams	4 – 10
• Low-density foams	11 – 40
• Very low-density foams	> 40

## Introduction

---

If the foam has a VER of less or equal to four, it is a high-density foam. Is it higher than four but less than ten it is referred to as a medium-density foam and is the volume expansion ratio higher than ten the foam is called low-density. In addition, it is sometimes reported that foams are very low-density foams with values greater than 40.<sup>[79]</sup> With a classification based on the VER, it is particularly easy to compare foams across different polymers, as this is independent of the material used. The method and which process parameters are used have the biggest influence in this case. For example, there are polystyrene foams with low-, medium- and high-density, all of them with different properties and therefore various applications.

### Mean cell size

Nowadays in particular, foams are often classified according to their average cell size. This is since, foams with cells in the micro or even nanoscale range can show a drastic improvement in their properties. A possible classification is shown below:<sup>[144]</sup>

<b>Description</b>	<b>Mean cell size [<math>\mu\text{m}</math>]</b>
• Macro-cellular foams	> 300
• Fine-celled foams	11 – 300
• Micro-cellular foams	0.1 – 10
• Nano-cellular foams	> 0.1

One refers to a macro-cellular foam if its cells are larger than 300  $\mu\text{m}$ . If the cells have a size between 300 and 11  $\mu\text{m}$ , it is a fine-celled foam. If the cells get even smaller and are in the range of 10  $\mu\text{m}$  to 100 nm, the foam is called microcellular foam. All foams with cell sizes below 100 nm are declared as nano-cellular.

### 1.4.2 Foam structure and morphology characterization

In order to describe a polymer foam, one should explain its foam structure and morphology in detail. This is because these ultimately determine the final properties of the foam. The most important characteristics are:

#### Foam density and volume expansion ratio

The first and most basic characteristic necessary to qualify a foam is the amount of material it actually contains. This characteristic is known as the density ( $\rho_{foam}$ ) of the foam and has typically the unit  $\text{kg m}^{-3}$ . The density is commonly determined with the help of the Archimedes' principle. Accordingly, the statistical buoyancy of a body in a medium is as great as the weight of the medium displaced by the body.<sup>[145]</sup> So by measuring the weight of the sample in air ( $m_{air}$ ) and in water ( $m_{water}$ ), together with the density of water ( $\rho_{water}$ ) at the measurement temperature the foam density can be calculated:

$$\rho_{foam} = \frac{m_{air}}{m_{air} - m_{water}} \cdot \rho_{water} \quad (13)$$

In addition to the density, the relative density ( $\rho_{rel}$ ) or the VER is often stated. These two quantities describe the relationship between the density of the foam and that of the unfoamed polymer ( $\rho_{bulk}$ ) as shown in equation (14):

$$VER = \frac{\rho_{bulk}}{\rho_{foam}} = \frac{1}{\rho_{rel}} \quad (14)$$

They are therefore independent of the raw polymer used, which makes it possible to compare foams made from different materials.

A further specification used is the so-called void fraction ( $V_f$ ) or porosity. It is a measurement of the empty spaces in a foam, and has a value between 0 and 1, or 0 % and 100 %. It can be calculated from the relative density using equation (15):

$$V_f = 1 - \rho_{rel} \quad (15)$$

When measuring porosity by means of gas adsorption, it must be noted that only the surface can be measured in the case of closed cell foams. For this reason, the term "accessible void" is often used. Further possibilities for measuring are for example optical methods or computed tomography.<sup>[146]</sup>

## Introduction

---

### Mean cell size and its distribution

The next crucial parameter to describe the microstructure of the foam is the size of his cells and the associated cell size distribution. The most common method to determine the sizes of the individual cells is by optical methods such as scanning electron microscopy (SEM). With the help of an image analysis software the area of the individual cells ( $A_{cell}$ ) can be determined and converted into the nominal diameter ( $\phi$ ) using the following equation:

$$\phi = 2 \cdot \sqrt{\frac{A_{cell}}{\pi}} \quad (16)$$

The mean cell size ( $\phi_m$ ) is determined by forming the arithmetic mean value of all measured cells. In order to specify as exact as possible, a larger number of cells should be measured. The exact procedure and evaluation is described in detail at 5.2 in the experimental part.

Since the mean cell size by itself does not provide information about the homogeneity of the foams, this value must be considered with caution. For this reason, the standard deviation and, even better, a cell size distribution should be provided. A possible way to characterize the cell morphology of a foam is, for example, a histogram of the cell sizes. Furthermore, by plotting the cumulative area of the cells against the corresponding cell size, a good insight into the cellular composition of the foam can be gained. This is particularly useful for inhomogeneous foams.

### Cell density

In addition to the cell size, the cell density of the foam ( $N_v$ ) is often stated. It describes the number of cells ( $n$ ) in a certain volume unit, usually one  $\text{cm}^3$ :<sup>[147,148]</sup>

$$N_v = \left( \frac{n \cdot M_{mic}^2}{A_{mic}} \right)^{\frac{3}{2}} \quad (17)$$

This value can also be determined very well by optical methods. In a SEM micrograph with a certain magnification ( $M_{mic}$ ) the number of cells on the micrograph is determined and then extrapolated from the area ( $A_{mic}$ ) of the image section to the corresponding volume. The exact determination is shown at 5.2 in the experimental part.

It should be noted that the mere indication of the cell density does not allow any predictions to be made about the homogeneity of the foam. This can be very misleading, especially in the case of inhomogeneous cell distribution, for example. In addition, when determining the cell density, incomplete cells are also counted, which leads to a certain error.<sup>[149]</sup> Thus, the cell density should rather be regarded as a guide value.

#### Cell nucleation density

Another variable used to describe the foam morphology is the cell nucleation density ( $N_0$ ). It refers to the number of cells in one cubic centimeter of unfoamed material and can be calculated from the void fraction and the cell density:<sup>[149]</sup>

$$N_0 = \left( \frac{N_v}{1 - V_f} \right) \quad (18)$$

A requirement, however, is that no cell coalescence has occurred during the processing stage and that the cells are all spherical.

#### Foam anisotropy

The last structural property to be discussed is the anisotropy in foams. If it is not ensured during the expansion process that growth in all directions is equally possible, anisotropy in the foam structure may occur. This can be the case, for example, during foam extrusion. Due to the direction of extrusion and the shear at the die, the cells may exhibit lateral distortion.<sup>[16]</sup> Also in foam injection molding it is possible that the cells receive a preferential orientation through the injection direction. This anisotropy can cause the physical properties of the foam to differ depending on the direction measured. For this reason, it is often stated in the specifications of the parameters whether the measurement was made in the direction of extrusion or perpendicular to it.

### 1.4.3 Thermal conductivity

The major field of application for polystyrene foams is their use as insulation material. Whether in the building and construction sector as wall, floor and pipe insulation, in the transport industry in refrigerated trucks or as appliances, for example in refrigerators. Due to the superior properties, they have the highest growth rate compared to conventional insulation materials such as mineral wool.<sup>[5]</sup> These properties include better insulation, no water adsorption and easier handling.<sup>[150]</sup>

The overall thermal conductivity ( $\lambda_t$ ) of a polymeric foam is composed of four different factors:

- Heat conduction through the solid polymer  $\lambda_s$
- Heat conduction through the gas within the cells  $\lambda_g$
- Heat convection through the cells  $\lambda_c$
- Radiation across voids and through cell walls  $\lambda_r$

The relationship between the individual factors is shown in equation (19) and a schematic illustration of the way in which they occur in a polymeric foam is given in **Figure 1.13**:

$$\lambda_t = \lambda_s + \lambda_g + \lambda_c + \lambda_r \quad (19)$$

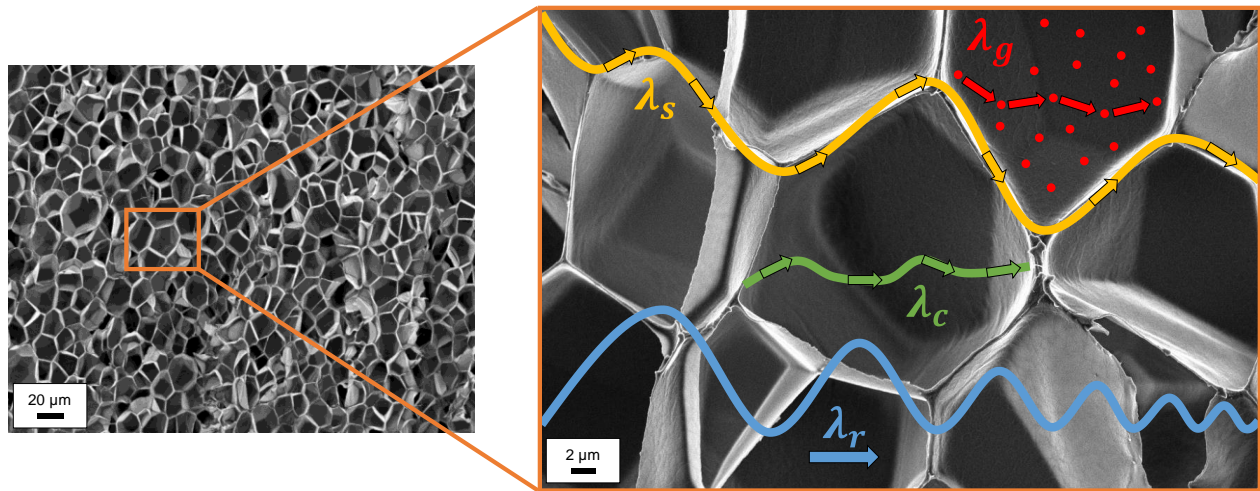


**Figure 1.13:** SEM Micrograph a polystyrene foam including a magnification with a schematic presentation of the occurring thermal conductivities during heat transfer:  $\lambda_s$ : Heat conduction through the solid polymer;  $\lambda_g$ : Heat conduction through the gas;  $\lambda_c$ : Heat convection through the cells;  $\lambda_r$ : Radiation across voids and through cell walls.<sup>[68]</sup>

In the following, the individual contributions will be explained in more detail and the foam parameters affecting them will be reviewed.

### Heat conduction through the solid polymer - $\lambda_s$

Part of the heat transfer takes place along the cell walls and struts of the polymer foam. With equation (20) this contribution can be calculated:<sup>[151]</sup>

$$\lambda_s = (1 - V_f) \left( \frac{2 - f_s}{3} \right) \lambda_{bulk} \quad (20)$$

$$f_s = \frac{V_{struts}}{V_{struts} + V_{walls}} \quad (21)$$

$V_f$  refers to the void fraction,  $f_s$  to the strut fraction which describes the ratio of the volumetric fraction of the struts ( $V_{struts}$ ) and the cell walls ( $V_{walls}$ ), as well as the thermal conductivity of the bulk material used ( $\lambda_{bulk}$ ). **Figure 1.14** shows the exemplary course of  $\lambda_s$  as a function of foam density and cell size.

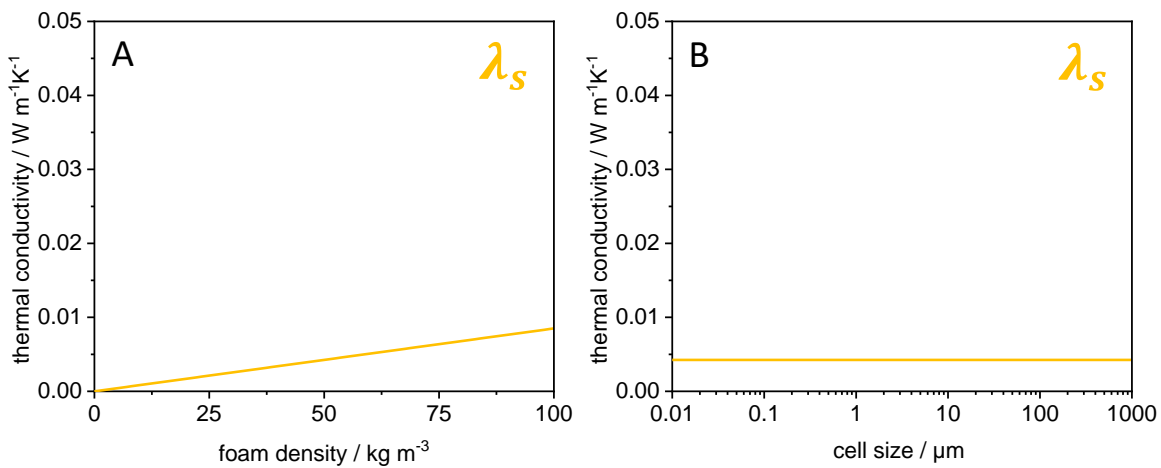


**Figure 1.14:** Representative course of  $\lambda_s$  as a function of **A:** the foam density (cell size set to 100  $\mu\text{m}$ ) and **B:** the cell size (foam density set to 50  $\text{kg m}^{-3}$ ) calculated according to (20).

The thermal conductivity via the solid polymer increases with increasing density. An increase in density means that the foam consists of more material, therefore more heat can be transferred through the matrix. Furthermore, the size of the cells has no influence on this factor. In summary, to reduce  $\lambda_s$ , a density as low as possible is aspired and, in addition, a material should be chosen which itself has a low thermal conductivity.

## Introduction

---

### Heat conduction through the gas within the cells - $\lambda_g$

The second term of total thermal conductivity  $\lambda_g$  deals with the transfer of heat via the gas located in cell cavities. The calculation is done via equation (22):<sup>[65]</sup>

$$\lambda_g = \frac{V_f}{1 + 2\tau Kn} \cdot \lambda_{g0} \quad (22)$$

$$Kn = \frac{l_{mean}}{\phi} \quad (23)$$

Here  $\tau$  is the efficiency factor of the energy transfer from the gas molecules to the cell walls and has a value of about 2 for polymeric foams.  $\lambda_{g0}$  describes the thermal conductivity of the gas in the cells (0.026 W m<sup>-1</sup>K<sup>-1</sup> for air) and  $Kn$  denotes the so-called Knudsen number, which is the quotient of the mean free path of the gas and the cell size (Equation (23)). The exemplary course of  $\lambda_g$  is plotted against foam density and cell size in **Figure 1.15**.

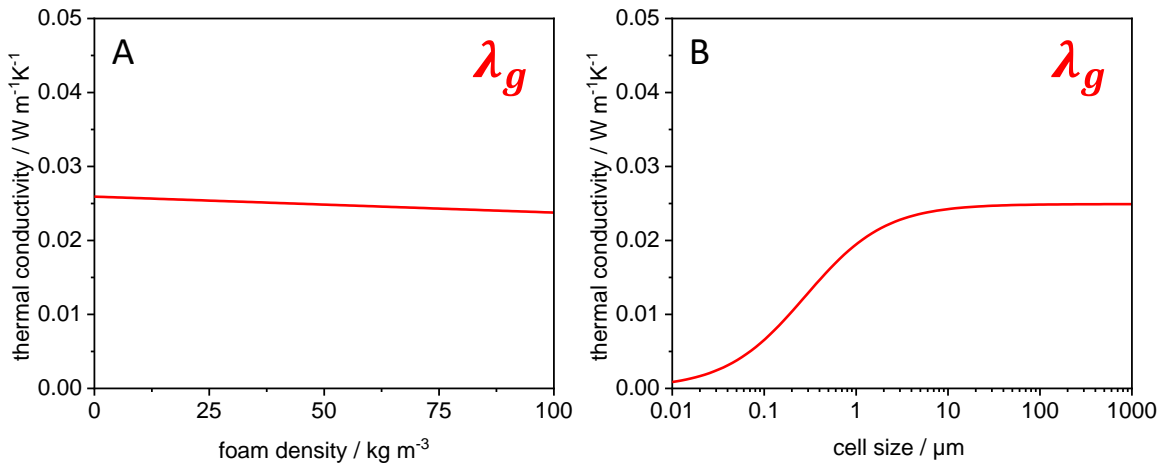


**Figure 1.15:** Representative course of  $\lambda_g$  as a function of **A:** the foam density (cell size set to 100  $\mu$ m) and **B:** the cell size (foam density set to 50 kg m<sup>-3</sup>) calculated according to (22).

In contrast to the transfer via the polymer matrix,  $\lambda_g$  shows an almost independent progression with regard to density. However, in this case the cell size has a considerable influence on the resulting thermal conductivity. The reason for this is the so-called "Knudsen effect". It describes the contribution of gas molecules which are located in a confined space to the thermal conductivity. It comes into play when the cell size in the foam is about as large as or smaller than the average free path of the gas (around 70 nm for air) within the cells. Due to the fact that the gas molecules constantly collide with the cell walls, they no

longer have enough power to transfer the energy in case of collision, which disturbs the transfer from the gas molecules to the cell walls.<sup>[152]</sup> The reduction of the cell size to 1  $\mu\text{m}$  already leads to a reduction of the thermal conductivity of the gas phase by more than 12 %. The reduction is even more drastic for foams with cells in the nanometer range. For example, at a cell size of 200 nm,  $\lambda_g$  can be reduced by almost 50 %. The fact that the Knudsen effect occurs in both micro-cellular<sup>[65]</sup> and nano-cellular<sup>[152,153]</sup> foams was proven in published works.

A further possibility to reduce the thermal conductivity across the gas phase is the substitution of the air in the cells by gases which have an even lower natural conductivity  $\lambda_{g0}$ . This was exploited in the past by using CFCs (see chapter 1.2.1) as blowing agents. In addition to the already discussed enormous ecological damage caused using such blowing agents, there is also an exchange of the gas with the environment through diffusion over time, whereby the thermal insulation performance steadily decreases.

#### Heat convection through the cells - $\lambda_c$

Convection describes the heat transfer by bulk movement of molecules in fluids like gases or liquids. It has been shown several times that convection has a significant effect only in cells larger than 4 mm. Since most commercial and the foams discussed in this thesis have much smaller cells, convection in the cells can be neglected.<sup>[154–156]</sup>

#### Radiation across voids and through cell walls - $\lambda_r$

The final parameter influencing the overall thermal conductivity is the thermal radiation inside the cell voids and through the walls of the foam. This contribution can be described by the Rosseland equation (24):<sup>[152,157]</sup>

$$\lambda_r = \frac{16 \cdot n_{ref}^2 \cdot \sigma \cdot T^3}{3 \cdot K_R} \quad (24)$$

Here  $n_{ref}$  describes the effective index of refraction ( $\approx 1$  for polymeric foams),  $\sigma$  the Stefan-Boltzmann constant,  $T$  the mean temperature and  $K_R$  the Rosseland mean extinction coefficient which can be calculated approximately by equation (25):

$$K_R = K_{struts} + K_{walls} \cdot K_{solid} \quad (25)$$

## Introduction

In this equation  $K_{struts}$ ,  $K_{walls}$  and  $K_{solid}$  describe the extinction coefficients for the struts, walls and the solid polymer correspondingly. The former two can be calculated with equation (26) and (27) respectively.<sup>[158]</sup> The latter is determined by measurements for the each individual polymer. For polystyrene the value was determined to be  $80 \text{ cm}^{-1}$ .<sup>[159]</sup>

$$K_{struts} = 4.10 \cdot \frac{\sqrt{f_s \frac{\rho_{foam}}{\rho_{bulk}}}}{\phi} \quad (26)$$

$$K_{walls} = (1 - f_s) \cdot \frac{\rho_{foam}}{\rho_{bulk}} \quad (27)$$

The following figure shows an example of  $\lambda_r$  in dependence of the foam density and the cell size.

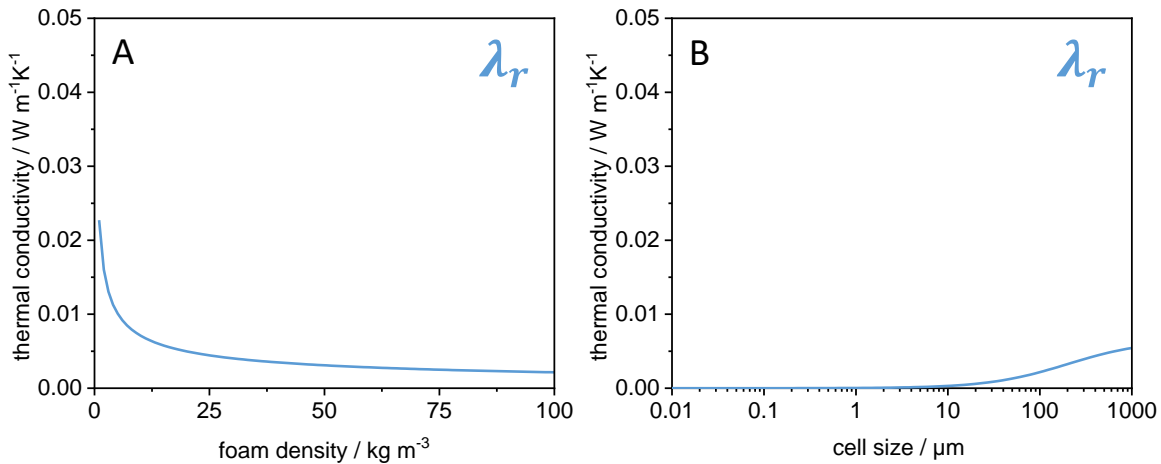


**Figure 1.16:** Representative course of  $\lambda_r$  as a function of **A:** the foam density (cell size set to 100  $\mu\text{m}$ ) and **B:** the cell size (foam density set to 50  $\text{kg m}^{-3}$ ) calculated according to (24).

The contribution of  $\lambda_r$  initially increases continuously with decreasing density but changes abruptly at very low-densities. This is due to the fact that with decreasing density the cell walls also become thinner, which leads to an increase in transparency for the radiation. The heat radiation can therefore pass through the foam more unimpeded. One way to reduce this is for example by introducing IR absorbers such as thermally reduced graphite oxide (TRGO).<sup>[27]</sup>

Looking at the progression regarding the cell sizes, it becomes apparent that  $\lambda_r$  does not contribute significantly to total thermal conductivity up to a size of about 10  $\mu\text{m}$ . Due to the very small cells, internal reflection from cell walls occurs very often and thus the heat radiation is extinguished. However, if the cells become larger, the rays are reflected less frequently and  $\lambda_r$  increases drastically.

### Overall thermal conductivity $\lambda_t$

To summarize the influence of the individual components to the total thermal conductivity and to explain its behavior,  $\lambda_t$  is shown in **Figure 1.17** as a function of foam density and cell size.

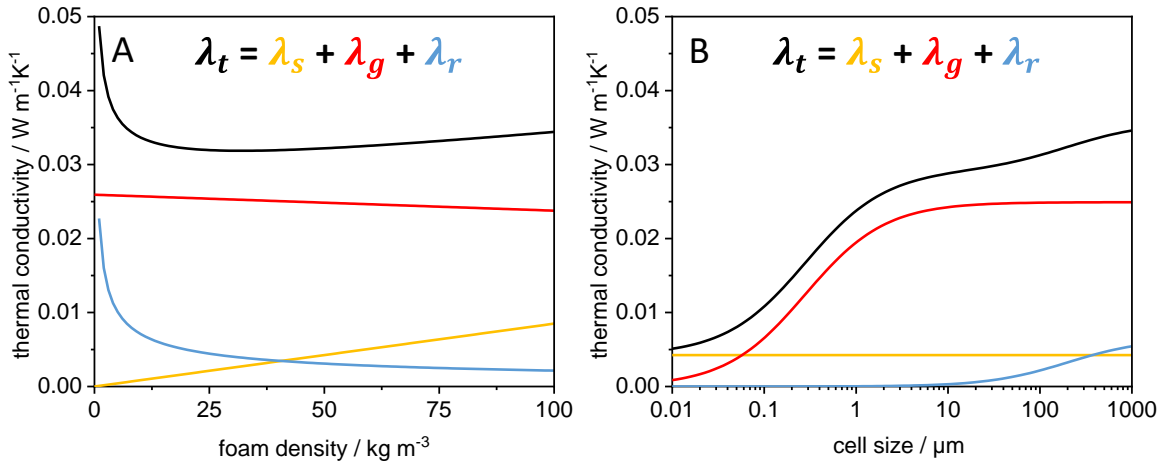


**Figure 1.17:** Representative course of  $\lambda_t$  as the superposition of  $\lambda_s$ ,  $\lambda_g$  and  $\lambda_r$  in dependence of **A:** the foam density (cell size set to  $100 \mu\text{m}$ ) and **B:** the cell size (foam density set to  $50 \text{ kg m}^{-3}$ ) calculated according to (20), (22) and (24).

Since the curves of  $\lambda_s$  and  $\lambda_r$  show opposite trends with respect to density, the total thermal conductivity has a minimum. It is therefore necessary to find a good compromise between lowering the density and still featuring a very low transparency of the cell walls. However, the influence of these two factors on the total thermal conductivity is relatively small. By far the greatest contribution is made by the transfer through the gas in the cells. Since this is largely independent of the density of the foam, there is no further possibility of improvement with respect to the density.

In contrast, the trend of  $\lambda_t$  differs regarding cell size. By reducing the cell size, it is possible to reduce both the heat transfer via the gas phase and the thermal radiation, which in turn reduces the overall thermal conductivity. From cells with a size of about  $10 \mu\text{m}$  the influence of  $\lambda_r$  can be reduced to nearly 0. In addition, the influence of the Knudsen effect begins at this point, which greatly reduces  $\lambda_g$ . To produce foams with excellent thermal insulation properties, the goal is therefore to reduce the size of the cells as much as possible.

### 1.5 Self-assembly and supramolecular additives

Supramolecular chemistry is a section of chemistry that deals with the assembly of molecules into larger structures. In contrast to molecular chemistry, which deals with covalent bonds, supramolecular chemistry is mainly concerned with intermolecular bonds. Jean-Marie Lehn, awarded the Nobel Prize together with Donald J. Cram and Charles J. Pederson in 1987 for their work related to supramolecular chemistry, describes it as "the chemistry of the non-covalent bond" or "the chemistry beyond the molecule".<sup>[160]</sup> A histogram with the amount of publications per year containing the keyword "supramolecular" shows that this is a very ambitious and rapidly growing field of research.

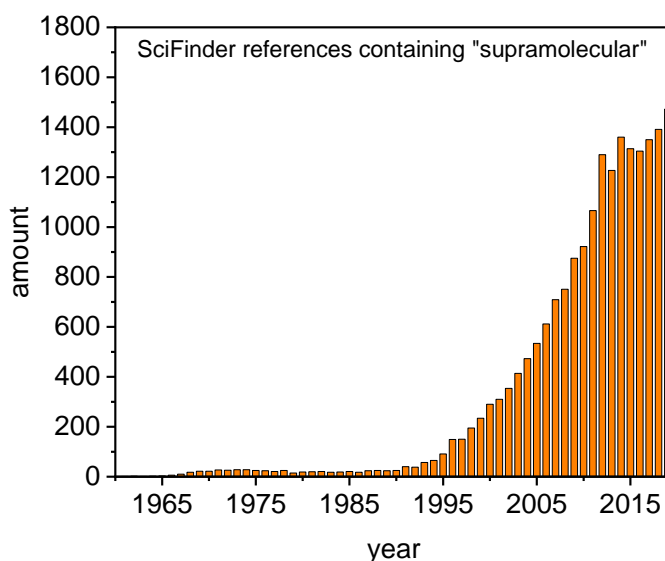


**Figure 1.18:** References of the SciFinder search "supramolecular" per year. Date: 20.03.2020.

The steady and significant increase illustrates the enormous potential that researchers envision in self-assembled systems. In the sheer endless number of supramolecular systems, only those which are used as additives in polymers are addressed in this work. In the following, the different applications and modes of interaction are explained in more detail.

### 1.5.1 The self-assembly process

The main characteristic of supramolecular chemistry is the self-assembly of molecules into superstructures through intermolecular non-covalent interactions. Non covalent-bonds range from coordinative bonds with a strength of several  $100 \text{ kJ mol}^{-1}$  to weak Van der Waals interactions with a few  $\text{kJ mol}^{-1}$ . Among the coordinative bonds, ion-ion are the strongest, followed by ion-dipole and dipole-dipole interactions.<sup>[161]</sup> As a special form of dipole-dipole interactions, hydrogen bonds (H-bond) are the most frequently used in supramolecular chemistry.<sup>[162]</sup> According to the International union of pure and applied chemistry (IUPAC) they are defined as “an attractive interaction between a hydrogen atom from a molecule or a molecular fragment X–H in which X is more electronegative than H, and an atom or a group of atoms in the same or a different molecule, in which there is evidence of bond formation.”<sup>[163]</sup> Depending on the corresponding donor and acceptor, the geometry and length, H-bonds exist in different strengths. Typically, they have a moderate strength of  $4 - 60 \text{ kJ}\cdot\text{mol}^{-1}$ , with donor groups mostly consisting of C-H, N-H, O-H and S-H and acceptor groups mainly containing N, O, P, S, halogens, aromatic  $\pi$ -clouds and transition metals.<sup>[164]</sup>

In order to assemble a molecule into supramolecular aggregates, some requirements have to be met. It must be guaranteed that the individual building blocks can move. For molecules in solution, this is almost always the case due to Brownian molecular movement. Furthermore, the molecules must carry the corresponding information, either geometrical or electronic, for self-assembly after synthesis in their structure. Finally, it must be possible to reversibly form and break the resulting bonds. This means that through a thermodynamic control poorly defined or damaged structures can be repaired.<sup>[161,162,165]</sup>

A well-known class of molecules, which are able to form supramolecular objects via hydrogen bonds by self-assembly processes, are for example 1,3,5-benzene trisamides. Using this class of molecules, the underlying self-assembly process from individual building blocks to macroscopic objects will be explained and is schematically illustrated in **Figure 1.19**.

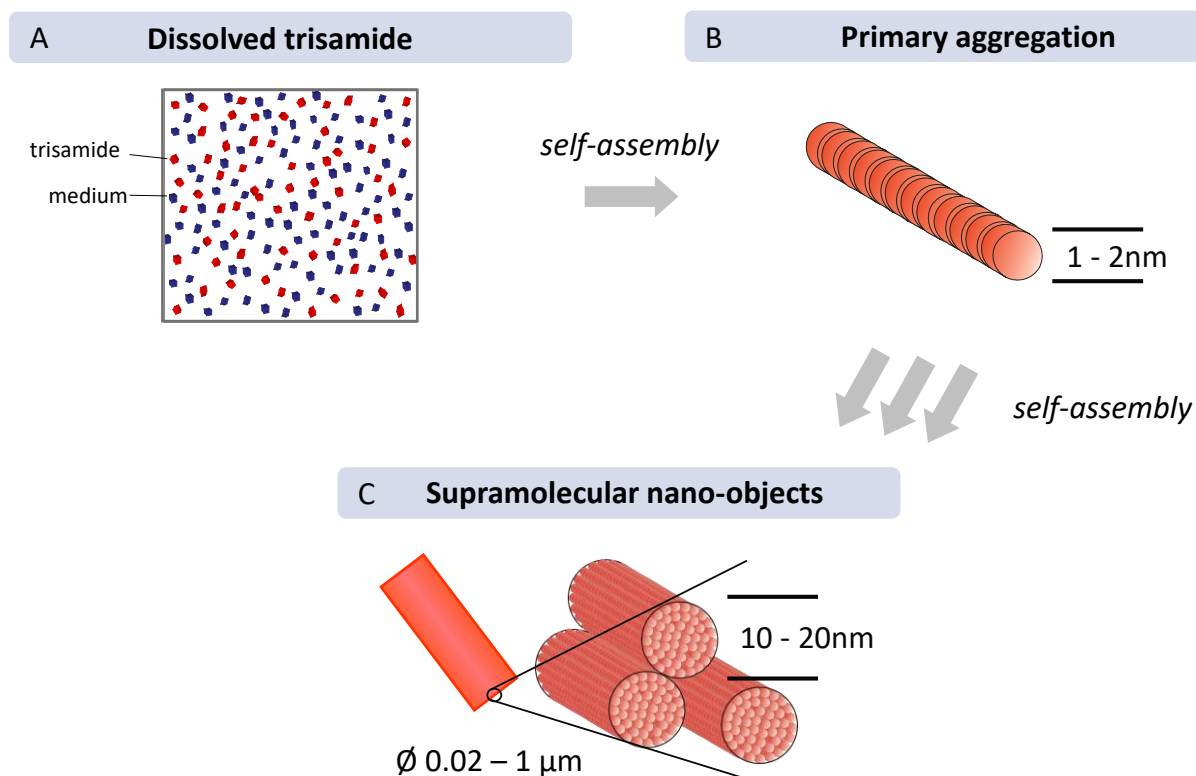


**Figure 1.19:** Schematic representation of the self-assembly process on the example of benzene trisamides. **A:** BTAs are soluble in the matrix. **B:** Self-assembly into primary aggregates. **C:** Further self-assembly into supramolecular nano-objects. Source: University of Bayreuth; Macromolecular Chemistry I.

The most common method to initiate the self-assembly process is upon cooling. Therefore, the benzene trisamide is dissolved in the desired medium (solvent, polymer, etc.) through heating (**A**). In solution, the molecularly dissolved BTA will be distributed homogeneously in the solution medium by diffusion. The self-assembly process begins with the cooling of the solution, i.e. the reduction of the solubility (**B**). Individual aggregates form columns and ultimately merge into supramolecular objects (**C**).<sup>[166]</sup> Of decisive importance is that this is a reversible process. By heating again, the formed objects can be dissolved and by cooling them down, they can be formed again. It should be noted that this process is influenced by other factors in addition to the molecular structure of the benzene trisamide itself. It is required that the temperature, the heating and cooling rates, the concentration and the medium in which the benzene trisamide is dissolved are well matched to achieve the best possible results for the desired application.

### 1.5.2 Supramolecular polymer additives

The ability to form supramolecular objects with a high aspect ratio predestines benzene trisamides for the use as additives in polymers. In addition, they offer another major advantage over conventional inorganic additives such as talc or nanoparticles, as there is no need for extensive dispersion of the additive. By adapting the structure and concentration of the additive to the respective polymer, it is possible to dissolve it molecularly and distribute it homogeneously by diffusion. On cooling, the self-assembly process produces finely distributed supramolecular objects which can for example nucleate the polymer. Together with their good chemical and thermal stability, benzene trisamides have been successfully used as nucleating agents for a number of semi-crystalline polymers. These include, for example, poly(vinylidene fluoride) (PVDF)<sup>[167]</sup>, poly(butylene terephthalate)<sup>[168]</sup> and isotactic polypropylene<sup>[169]</sup>. In the case of PP, the  $\beta$ -phase could be nucleated by the addition of the benzene trisamides, which improved the mechanical properties.<sup>[170,171]</sup> By influencing the crystallization behavior, it was possible for selected benzene trisamides to act as clarifiers and significantly improve the optical properties of PP.<sup>[169]</sup>

In addition to the benzene trisamides there are other classes of compounds which are used as supramolecular additives in polymers. An example are dibenzyl sorbitol derivatives that have been developed as supramolecular additives for the nucleation and clarification of PP.<sup>[172–176]</sup> Due to their very good solubility in polypropylene, the additive can be distributed evenly in the polymer matrix. Upon cooling, a three-dimensional fiber network is formed which is able to nucleate PP with its high surface area. There are also some bisamide-based molecules, which are able to nucleate polypropylene<sup>[177,178]</sup> and to improve their charge storage properties.<sup>[179]</sup> Finally, it is also possible to induce the  $\beta$  phase of the PP with these additives.<sup>[180]</sup>

### 1.5.3 Supramolecular additives as foam nucleating agents

As an extension to their use as additives to nucleate polymers, supramolecular additives can also be used in the foam industry. The function of these additives will be explained with reference to the general formation of foams (see topic 1.2 and **Figure 1.1**).

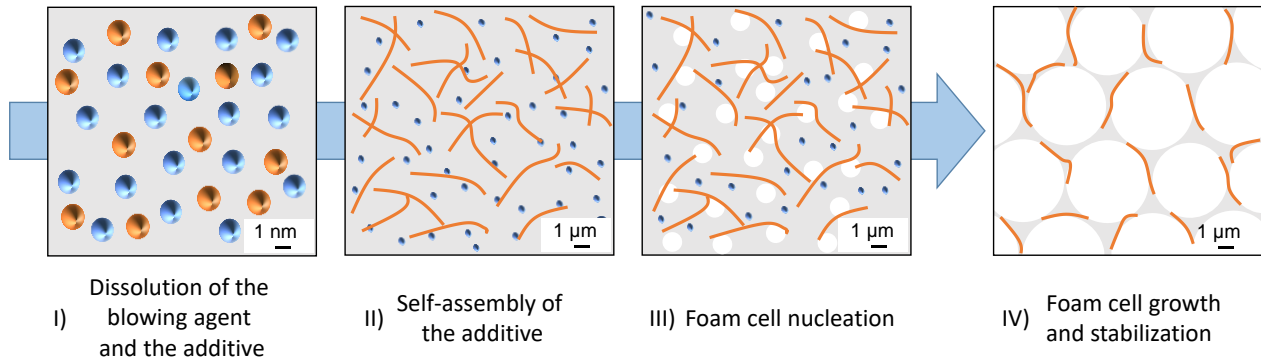


**Figure 1.20:** Schematic representation of the general steps in the foaming process of polymer materials with supramolecular additives (blue: blowing agent; orange: additive; grey: polymer phase; white: foam cells). Source: University of Bayreuth; Macromolecular Chemistry I and Polymer Engineering.

In the first step **I**, both the blowing agent and the supramolecular additive are dissolved at the molecular level in the polymer matrix during the extrusion. In order to develop its optimum effect, it is essential to ensure a complete dissolution of the additive in the melt so a homogenous distribution can be assured. It is therefore important to adapt the additive to the corresponding polymer and select a suitable concentration range. The temperature used during extrusion also has a decisive influence on the solubility of the additive. The higher this temperature, the better the additive can dissolve. Obviously, possible decomposition of the polymer or the additive must be taken into account. In the next step **II**, the self-assembly process is initiated by reducing the temperature and the additive crystallizes into the desired supramolecular objects. It is necessary that the temperature at the beginning of the crystallization is above the foaming temperature, otherwise the objects would not have formed yet. In the third step **III** the foam formation is initiated by a thermodynamic instability and the supramolecular objects act as heterogeneous nuclei for the foam cells. Due to the heterogeneous nucleation, all foam cells are formed simultaneously and can thus grow evenly. In the fourth step **IV** they keep on growing till the polymer has cooled down sufficiently and the cell structure has been stabilized. Ultimately, the additive is located inside the cell walls and cell struts.

Benzene trisamides have successfully been used as foam nucleating agents in semi-crystalline polypropylene so far. By using these supramolecular additives in foam injection molding, cell sizes could be reduced from 120 μm to 20 μm featuring a homogeneous cell size distribution. Tensile tests and Charpy

impact tests showed a dependence on the width of the cell struts of the foams, which could be influenced by different additives.<sup>[69]</sup> Also in foam extrusion of PP, a morphology control could be achieved by addition of benzene trisamides. The foams showed a more homogeneous cell size distribution and an improved compression modulus compared to the talc-added samples.<sup>[70]</sup>



## 2 Aim of the thesis

The insulation of houses and buildings plays an important role in view of the climate change and CO<sub>2</sub> reduction, because a very large amount of the world's energy consumption can be attributed to heating and cooling of these buildings. To reduce energy demand of buildings, insulation is indispensable today with polystyrene foams being one of the most widely used insulation materials. Due to continuous further improvements, this material class shows the highest growth rate compared to other isolation materials. The thermal conductivity of polystyrene foams depends primarily on its density and morphology. Controlling the foam morphology plays a key role, which can be realized in a straightforward manner by the use of additives. Therefore, this work aims to reveal and comprehensively study supramolecular additives as efficient foam nucleating agents. Supramolecular additives have the unique feature to self-assemble in polymer melts to supramolecular nanostructures through directed non-covalent interactions. These supramolecular objects are capable of nucleating the foam bubbles and thereby control the morphology. To obtain an optimal effect of the additive, they must be carefully adapted to the polymer used. Especially their solubility and self-assembly behavior are of great importance. So far, this concept has only been successfully utilized in PP foams<sup>[69,70]</sup> and should now be transferred to tailor the morphology of amorphous polystyrene foams.

Therefore, the aim of the work is to establish this concept with two known C<sub>3</sub>-symmetric benzene trisamides and to evaluate their potential to nucleate and control the morphology of amorphous low-density polystyrene foams with respect to smaller cell sizes and their homogenous distribution.

On this basis, a novel class of supramolecular bisamides is being designed to tailor their solubility and self-assembly behavior directly for polystyrene to further improve their effectiveness as foam nucleating agents.

### *Foaming polystyrene with supramolecular benzene trisamides*

For the foam nucleation experiments two different BTAs should be explored for its potential to function in polystyrene. Besides a commercially available BTA, which serves as a reference, a second BTA with a lower melting point and therefore probably a better solubility should be studied. While the first BTA is based on a 1,3,5-triaminobenzene with three *t*-butyl side groups, the second additive consists of 1,3,5-benzenetricarboxylic acid with three *i*-pentyl side groups, which should result in a better solubility.

To study the self-assembly process 500 ppm of the additives should be dissolved at elevated temperatures in xylene which serves as model solvent mimicking the chemical structure of polystyrene. After cooling to

room temperature, the formed supramolecular objects can be isolated and investigated with scanning electron microscopy with respect to their shapes and sizes.

To gain a better understanding of the behavior of the additives in polystyrene, they should be compounded in various concentrations and processed into small sample plates by injection molding. These specimens should then be investigated with respect to haze and clarity.

To screen the additives and optimize the foaming conditions a *temperature induced batch foaming process* is used. This batch foaming process should be adapted and first optimized for the neat polystyrene with respect to the CO<sub>2</sub> content, the foaming temperature and the foaming time. With these optimized conditions both additives should be investigated for their foam nucleating potential. The resulting foams should be analyzed with respect to their density and morphology by means of scanning electron microscopy, which allows to reveal the influence of the different additives.

The findings should then be transferred to a *foam extrusion process*, which is of more industrial relevance. For these experiments, the commercially available BTA should be used in three selected concentrations to prove the concept of supramolecular additives as efficient foam nucleating agents. An important aspect is the visualization of the supramolecular nanostructures present in the resulting polymer foams. For this a method should be developed. The resulting extrusion foams should be investigated with respect to density, morphology and the thermal conductivity in order to clarify the effects of morphology control by the supramolecular foaming agent.

Since the solubility and self-assembly behavior of the supramolecular additives plays a major role and the fact that the solubility of the BTA is limited in the polystyrene matrix, the next step should be to develop and establish a new class of supramolecular additives to overcome this drawback.

### *Foaming polystyrene with supramolecular bisamides*

A possible way to increase the solubility in polystyrene might be the utilization of *bisamides* instead of BTAs as supramolecular additives. Therefore, a series of kinked and more flexible bisamides should be synthesized and investigated with respect to serving as foam nucleating agents for polystyrene. To tailor the solubility and the self-assembly behavior this new class of kinked bisamides consists of a two benzene units connected by a methylene spacer as the central unit. The two amide groups are located in para position on both sides and carries a benzyl, cyclohexyl, n-butyl or t-butyl peripheral substituent to further control the properties of the additive. In addition, a methyl or ethyl group can be introduced at all four

ortho positions to the amide group at the aromatics, to fine-tune the solubility of the additive in the polymer. As reference compounds, two simple C<sub>2</sub> symmetric bisamides should be used and evaluated.

All bisamides should be examined with regard to their self-assembly behavior, the solubility and should ultimately be used in different concentrations in the *temperature induced batch foaming process*. In order to investigate the effects of the individual adjusting screws of the additive class, all foams should be examined with regard to their density and morphology.

To demonstrate the potential as foam nucleating agents of this class, one suitable derivative should be selected, synthesized in larger quantities and used in two industrial relevant large scale foam processes, i.e., *foam extrusion and foam injection molding*. The same methods and procedures should be used to analyze the resulting polymer foams.

Finally, a comparison should be made between the corresponding foams containing BTAs and kinked bisamides, respectively. One aspect should be the capability of controlling the morphology towards smaller and homogeneously distributed cell sizes. The other aspect should cover the actual appearance of the additives in the foams.



### 3 Foaming polystyrene with benzene trisamides

The most common class of trisamides which are also used in this work are the 1,3,5-benzenetrisamides. The general structure of this class is shown in **Figure 3.1**.

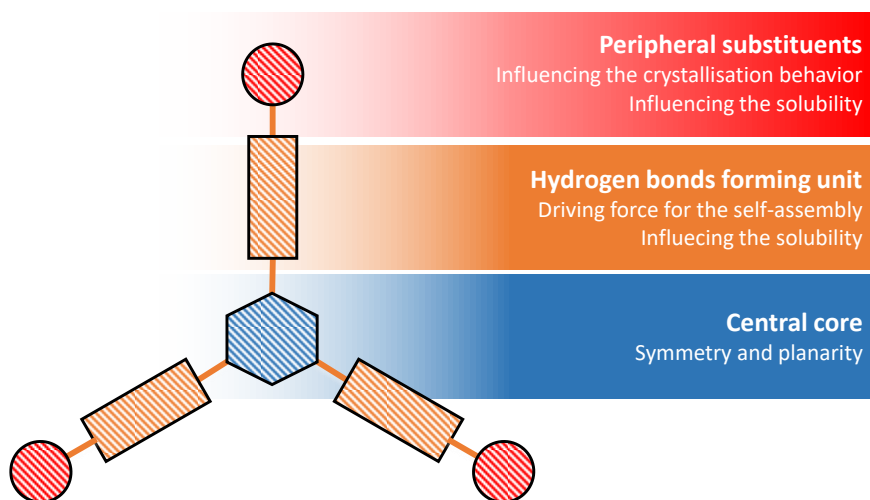


**Figure 3.1:** Schematic structure of the 1,3,5-benzenetrisamides.

In general, they consist of three parts. In the middle is a central core which determines the symmetry and planarity of the molecule. In positions 1, 3 and 5 hydrogen bonding units in the form of amides are attached to the core. Through these the molecules are able to organize themselves via intermolecular forces and are capable of building supramolecular objects. The amide group can be linked either with its C-atom or with its N-atom to the core. By varying this centering, the hydrogen bond patterns can be changed, which affects the solubility of the molecule and makes it a useful tool for tuning the properties.<sup>[181]</sup> In the periphery, certain substituents can be incorporated. These mainly influence the crystallization behavior, the solubility and the thermal properties.<sup>[169,182,183]</sup> By varying this residue the self-assembly process can be controlled decisively. Among other things, the size of the residue plays an important role, as it defines the distance between the columns and thus the interactions between the macrodipoles.<sup>[184]</sup> Further variations of the peripheral groups result in an enormous spectrum of compounds which can have completely different chemical properties. By introducing short linear and branched alkyl chains, for example, solid materials with a high melting point are created.<sup>[181,182]</sup> If the benzene trisamides have longer linear alkyl chains (hexyl or higher) they show a thermotropic liquid crystalline behavior.<sup>[185]</sup> In addition, polar side chains make it even possible to form organogels and hydrogels.<sup>[186]</sup> Via crown ethers<sup>[187]</sup> or acid groups<sup>[188]</sup> it is even feasible to make the compounds water compatible. Benzene trisamides have been successfully used as foam nucleating agents in semi crystalline PP and are now to be tested in completely amorphous PS.

### 3.1 Synthesis and properties of the selected benzene trisamides

In this work two BTAs were used as foam nucleating agents. One is the commercially available supramolecular additive N,N',N''-benzene-1,3,5-triyltris(2,2-dimethylpropanamide) - **1** also known as Irgaclear XT 386, serving as a reference. Second, N,N',N''-tris(3-methylbutyl)-1,3,5-benzenetricarboxamide - **2** which is specially adapted to the polymer matrix. The structures of the two substances are shown in **Figure 3.2**.

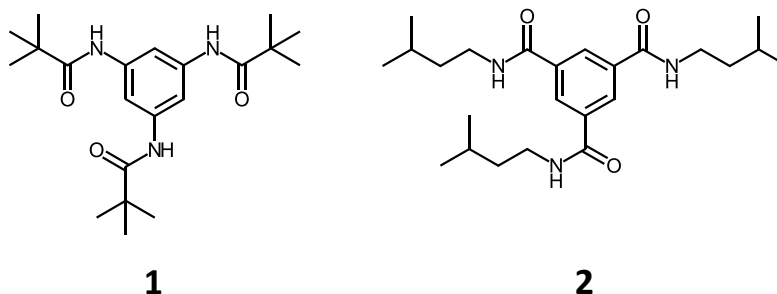


**Figure 3.2:** Chemical structure of N,N',N''-Benzene-1,3,5-triyltris(2,2-dimethylpropanamide)] – **1** and N,N',N''-Tris(3-methylbutyl)-1,3,5-benzenetricarboxamide – **2**.

#### 3.1.1 Synthesis and characterization

Additive **1** was not directly synthesized as it is commercially available. A possible synthesis route of the commercial available additive **1** is the amidation of 1,3,5-triaminobenzene with 2-methylpropionyl chloride and is shown in **Figure 3.3**.<sup>[169]</sup>

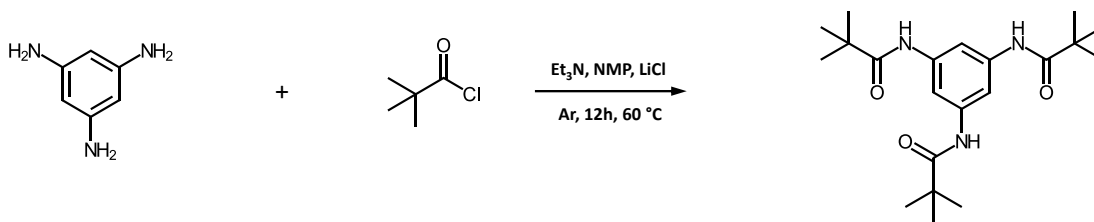


**Figure 3.3:** Reaction scheme of 1,3,5-triaminobenzene with 2-methylpropionyl chloride to N,N',N''-benzene-1,3,5-triyltris(2,2-dimethylpropanamide) – **1**.

The synthesis of **2** is carried out via the solvent-free reaction of trimethyl 1,3,5-benzenetricarboxylate with an excess of isopentylamine. After washing with water, the final product can be obtained as a white powder with very high purity and good yields.<sup>[169]</sup> The reaction scheme is showed in **Figure 3.4**.

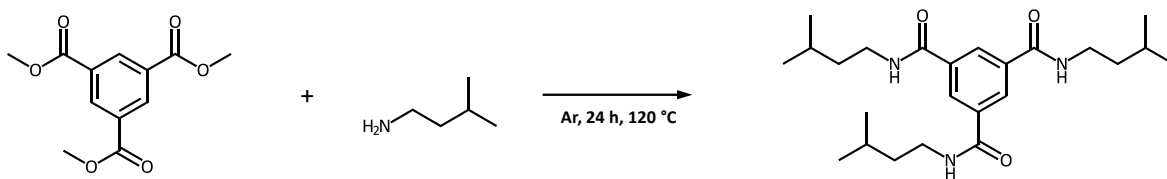


**Figure 3.4:** Reaction scheme of trimethyl 1,3,5-benzenetricarboxylate with isopentylamine to N,N',N''-Tris(3-methylbutyl)-1,3,5-benzenetricarboxamide – **2**.

The thermal analysis via differential scanning calorimetry (DSC) and thermogravimetric analysis (TGA) revealed that additive **1** shows no melting point over the entire measured temperature range in the DSC. At a temperature of 350 °C, 5 % of the material has decomposed. BTA **2** has a melting point of 269 °C and is comparably stable with a  $T_{-5wt. \%}$  of 360 °C. Due to their high stability, both compounds can be used without any concerns in foam extrusion.

A detailed description of the synthesis and the further characterization by proton nuclear magnetic resonance ( $^1\text{H}$  NMR), mass spectra (MS) and infrared (IR) can be found at 5.4.1 in the experimental part.

### 3.1.2 Self-assembly behavior

An important aspect is the morphology of the supramolecular objects, which may act as nucleating sites for the cell formation. To get insight how the morphology and shape of the supramolecular objects may develop in a nonpolar polymer melt, self-assembly experiments were performed at elevated temperatures using a nonpolar solvent, because solvents allow for a straightforward isolation of the objects and their subsequent investigation by microscopic techniques. Xylene was chosen as a nonpolar model solvent, since it features structural similarities to the PS repeating unit and a reasonable high boiling point. For these screening experiments, 500 ppm was selected as concentration to ensure complete solubility at elevated temperatures. The applied self-assembly protocol includes dissolving the additive at elevated temperatures until an optically clear solution was obtained. Subsequent cooling to room temperature resulted in a turbid dispersion indicating the supramolecular object formation. Evaporation of the solvent allows for the isolation of the supramolecular structures and subsequent characterization by SEM. The obtained images are shown in **Figure 3.5**.

It should be noted that the values given can only be considered as rough guidelines and cannot be transferred one to one to the application in the polystyrene melt. On the one hand, PS can only be compared with xylene as a solvent to a limited extent and, on the other hand, the conditions during extrusion and injection molding are significantly harsher.

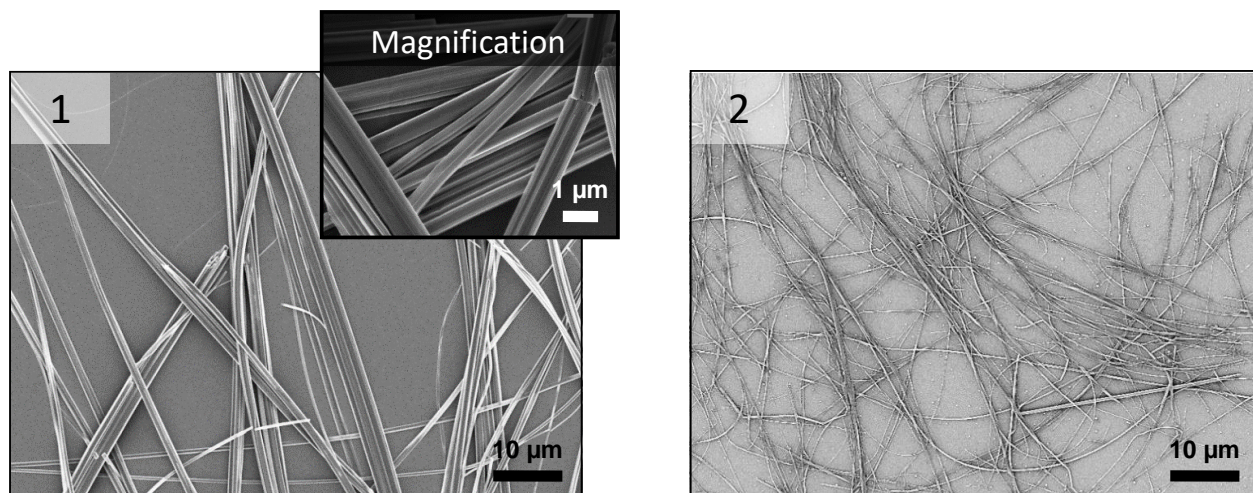


**Figure 3.5:** SEM micrographs of 500 ppm additive **1** and **2** self-assembled upon cooling in xylene. If necessary, another SEM micrograph of the corresponding additive with higher or lower magnification is provided.

Both additives form fine fibers. The fibers of **1** have a thickness between 250 to 1500 µm. It is visible that the larger fibers consist of several small fibers arranged together. This is additionally shown in the extra magnification. Additive **2** creates much thinner fibers which are in the range of 100 to 250 µm. The above-mentioned agglomeration is also visible with additive **2**, but much less pronounced.

### 3.1.3 Solubility in polystyrene

To provide initial information on the solubility of the additives in the polystyrene matrix, the haze values of the injection molded test specimens with different concentrations of the additive were determined and are shown in **Figure 3.6**.

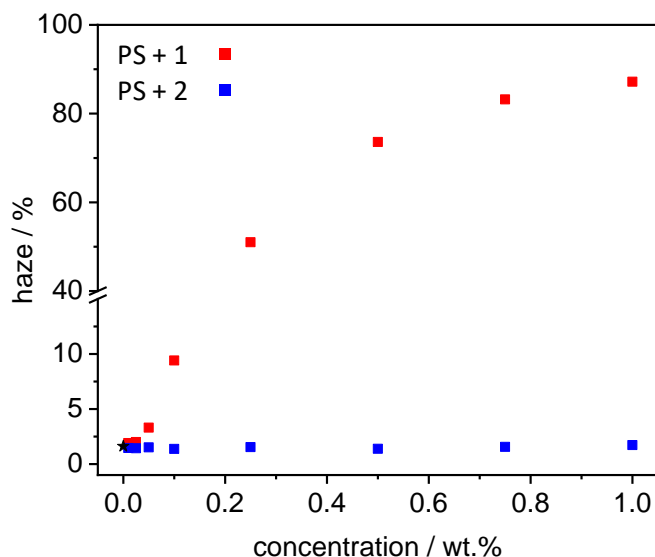


**Figure 3.6:** Haze values of the injection molded specimen in dependence of various concentrations of **1** and **2** in polystyrene. The black star represents the haze value of neat PS.

From a concentration of 0.1 wt.% onwards, it is clearly visible that additive **1** leads to an enormous increase in haze. This means that there are objects in the test specimens which are larger than the wavelength of visible light and therefore scatter the light. This can be an indication of large aggregates in the sample due to incomplete dissolution. These aggregates can have a negative effect on the foam nucleating effect as the additive is no longer homogeneously dispersed in the polymer matrix. In addition, the undissolved residues also act as nuclei for the crystallization of the dissolved additive, which further promotes inhomogeneous distribution and further increases the size of the aggregates. By further increasing the concentration, the haze value increases accordingly.

In the case of additive **2** there is no clouding of the platelets even at a concentration of 1.0 wt.%. Accordingly, even at the highest concentration, there are no objects or aggregates in the sample present that can scatter the light. This is an indication that additive **2** has a good solubility in the polystyrene melt probably caused by the higher mobility compared to the *t*-butyl of additive **1**. Consequently, many nuclei for the formation of foam bubbles can be introduced homogeneously distributed in the polymer.

### 3.2 Batch Foaming

This section of the thesis deals with the batch foam process, which enables a large number of parameters to be set and various additives to be tested as foam nucleating agents on a small scale. In this way, first insights into the behavior and effectiveness of the additives in the foaming process shall be gained. As polystyrene is a completely amorphous polymer, the temperature induced method was selected for foaming.

#### 3.2.1 Foam sample preparation

The different processing steps from the commercial polymer granulate to the finished batch foam and the associated parameters will be described in detail below.

##### Production of the specimen

The first step is the grinding of the polymer granulate into a fine powder with a cryo-mill which is necessary to enable easier filling of the micro-extruder and to ensure good distribution of the additive in the powder/powder blends. After grinding, the powder is dried. The additive is then mixed with the polymer powder. To break down any aggregates or larger crystalline structures of the additive, the mixture is pestled. The mixture is then thoroughly mixed for at least 24 h in an overhead shaker at medium speed of rotation.

The well homogenized mixture is then fed into a micro-extruder and melted at 260 °C. The relatively high temperature of 260 °C selected for the extruder is necessary to ensure that the additive at best completely dissolves in the polymer melt and thus optimum dispersion can be achieved. A residence time of five minutes and a screw speed of 50 rotations per minute were selected to homogenize the mixture.

The melt is then transferred to a micro injection molding machine. Here the melt is pressed into a surface polished mold to obtain round specimens with a diameter of 27 mm and a thickness of 1.1 mm. With this thickness a homogeneously and complete loading with the blowing agent within a reasonable time is ensured. Furthermore, the entire test specimen can uniformly be foamed and almost no unfoamed core remains. The surface polished mold allows the optical properties of these platelets to be investigated. The different additive concentrations can be realized in the extrusion step by a dilution series.

The injection molding process causes internal stress in the material, which are caused by the different cooling rates at the contact surface of polymer and mold as well as inside the specimens. The birefringent strains can be illustrated with two crossed polarizers (**Figure 3.7** left). This internal stress causes the material to deform along these strains during the foaming step. (**Figure 3.11** right). To ensure a uniform

foaming, the standard procedure<sup>[189]</sup> had to be optimized. Therefore, the specimens are annealed at a temperature over the glass transition allowing the material to relax due to the given chain mobility. The sprue was cut off and they were put into an iron mold with the exact dimensions of the test samples in order to retain its shape. In comparison the stress-free sample is shown in **Figure 3.7** on the right side.

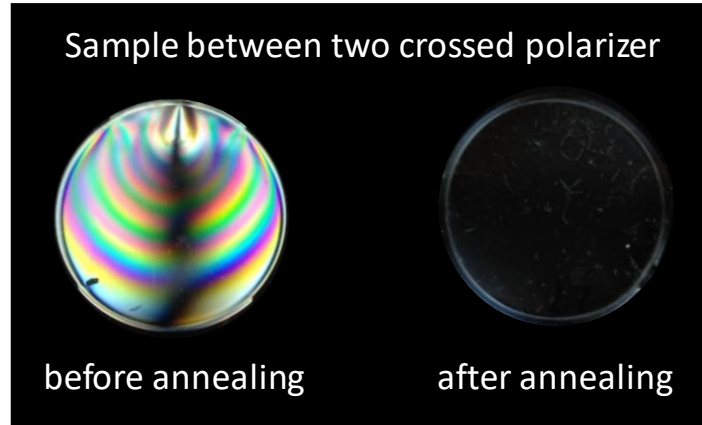


**Figure 3.7:** Injection molded sample between two crossed polarizers; left: before annealing; right: after annealing at 135 °C for 4 h.

Saturation process

The saturation of the samples with the blowing agent, takes place in a high-pressure autoclave and the samples are loaded with 50 bar CO<sub>2</sub> at room temperature. To ensure complete saturation, they remain in the autoclave for at least 24 h. In order to determine the CO<sub>2</sub> content  $M_t$  in the samples as described in 1.2.1, they are weighed before loading ( $W_{ini}$ ) and after opening the autoclave after certain time intervals ( $W_t$ ).  $M_t$  can thus be calculated using formula (3). By plotting  $M_t$  against the square root of time and then extrapolating to 0, the maximum CO<sub>2</sub> uptake can be obtained at the Y-axis intercept. This is shown in

**Figure 3.8** for three different polystyrene samples without additives.

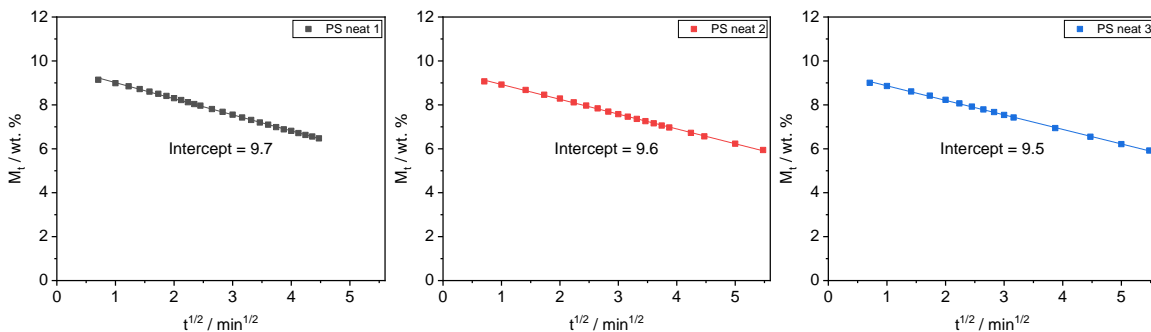


**Figure 3.8:** CO<sub>2</sub> content over the square root of time with a linear fit for three different polystyrene samples without additives.

Averaged over the three acquired values, a maximum CO<sub>2</sub> absorption of the polystyrene grade under these test conditions is determined to be 9.6 wt.%. In order to make further statements about the desorption behavior of the CO<sub>2</sub> out of the polystyrene, the CO<sub>2</sub> content as a function of time for pure and for PS with a tris- and a bisamide is shown in **Figure 3.9**.

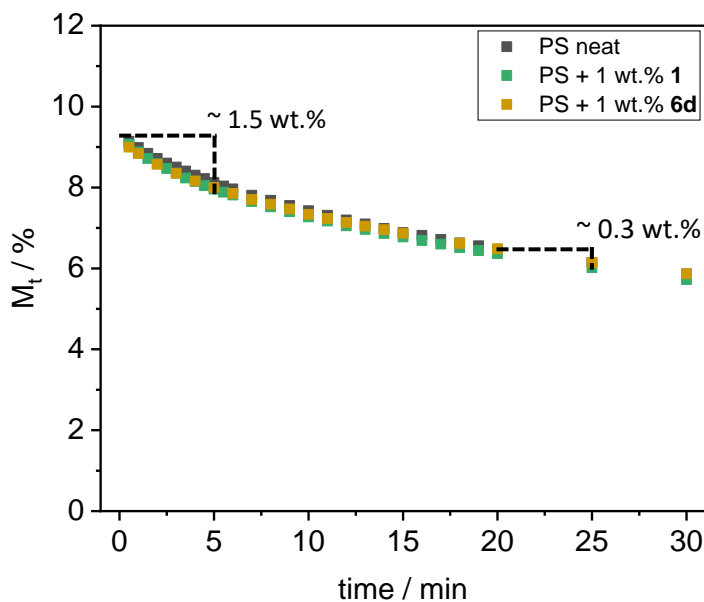


**Figure 3.9:** CO<sub>2</sub> desorption over time for neat polystyrene as well as polystyrene with 1.0 wt.% additive **1** and **6d**.

It becomes evident that the additives do not influence the absorption and desorption of CO<sub>2</sub> in the polystyrene. Furthermore, the desorption of CO<sub>2</sub> shortly after opening the autoclave is much faster than at a later stage. Thus, the samples lose about 1.5 wt.% of CO<sub>2</sub> in the first five minutes, whereas in the section of 20 - 25 minutes after opening the autoclave only 0.3 wt.% CO<sub>2</sub> is released out of the sample.

To ensure an almost identical CO<sub>2</sub> content for all samples foamed directly in succession, the samples were stored for a desorption time of 18 minutes in air prior to the foaming process. This results in a CO<sub>2</sub> content of approximately 6.5 wt.% for each sample.

### Foaming parameters

The temperature-induced batch foaming process is used to foam the samples, as mentioned above. After the samples have reached the desired CO<sub>2</sub> content, they are placed in the hot oil bath and remain there for the specified foaming time. To avoid temperature differences due to the introduction of the still cold polymer sample and its surroundings, a good mixing of the oil bath must be provided. Furthermore, it is important to ensure an unhindered and uniform foaming of the sample in all directions to prevent anisotropic effects.

The decisive experimental parameters of this process are the temperature of the heating bath and the duration of the exposure to the heating medium. To investigate the effect of these two factors, the temperature of the oil bath was varied between 125 and 140 °C in 5 °C steps and different foaming times between 10 and 35 s were investigated. These screening tests were performed with a sample containing 1.0 wt.% **6b**. The results obtained are shown in **Figure 3.10**.

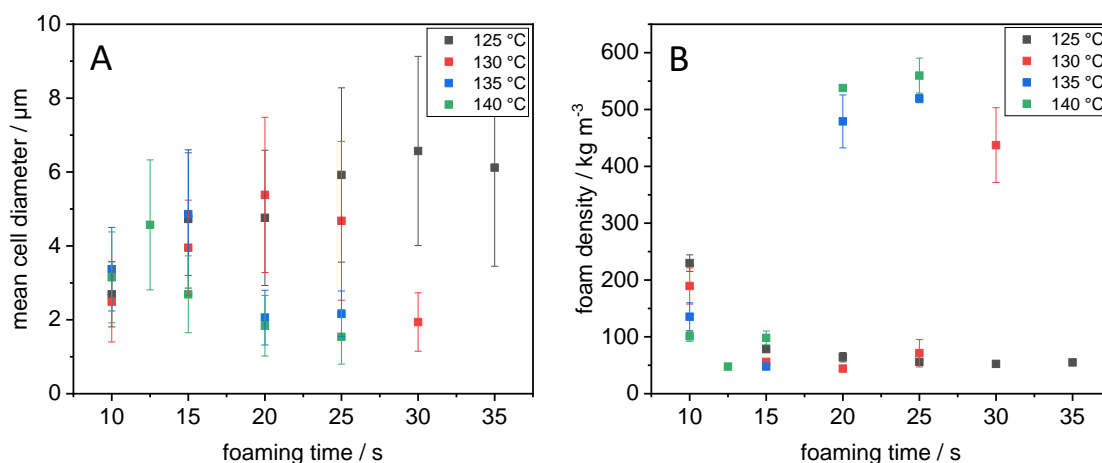


**Figure 3.10:** **A:** Mean cell diameter and **B:** densities of foams containing 1.0 wt.% **6b** in dependence of the foaming time at four different temperatures.

Looking first at the progression of the cell sizes with increasing foaming time for the individual temperatures, it becomes clear that there is a maximum for each temperature. In agreement with this, the corresponding foams show a minimum in their foam density at the same foaming time. This maximum of cell size or minimum of foam density therefore reflects the highest possible expansion under the set process conditions. If the sample is exposed to the hot medium for a longer period of time, the cell collapse begins, and the cells shrink leading to a density increase. While the largest cells are reached after about 12.5 s at 140 °C, about 30 s are required at 125 °C. The increase in temperature reduces the viscosity and

thus the melt strength of the polymer. The higher the temperature, the stronger the plasticization, which makes it easier to foam the sample. The reduced melt strength not only promotes foaming but also cell collapse. While at moderate temperatures the transition from foaming to cell collapse takes a long time, it takes a considerably shorter time at high temperatures. For this reason, a foaming temperature of 130 °C was chosen. The foaming time selected was 15 s, as cell collapse can be excluded and small cells can be obtained at a low-density.

To stabilize the obtained foam structure, the samples are placed in a cold oil bath immediately after the corresponding foaming time has passed. By cooling below the glass transition, the mobility of the chains is frozen and thus further foaming is prevented. The produced foams are then washed with soap to remove any adhering oil and dried in air for at least 24 h to ensure that all the blowing agent has diffused out of the foams. **Figure 3.11** shows the visual appearance of the foams produced in this way. On the left side of the picture a foam is shown which has been tempered as described and in comparison, on the right side a foamed sample which has not been tempered before foaming.

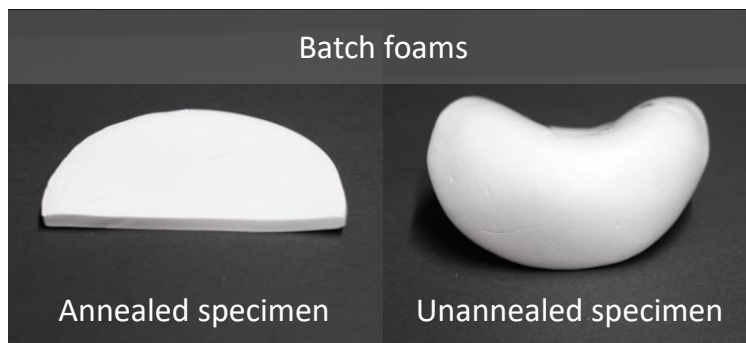


**Figure 3.11:** Resulting PS batch foams of a **left:** annealed specimen and **right:** unannealed specimen produced by the temperature-induced batch foaming.

It can be clearly seen that the annealed specimen is able to foam uniformly in all directions without hindrance. In the unannealed specimen, however, expansion is influenced by the stress in the material. On the one hand, this reduces the homogeneity of the entire foam and, on the other hand, the uneven shape makes further characterization problematic. To summarize, the following table lists all process parameters set for the batch procedure:

**Table 3.1:** Summary of the parameters for the temperature-induced batch foam process.

Pre-treatment	Saturation	Foaming
<p><b>Annealing time:</b> 4 h</p> <p><b>Annealing temperature:</b> 135 °C</p>	<p><b>Saturation CO<sub>2</sub> pressure:</b> 50 bar</p> <p><b>Saturation time:</b> &gt; 24 h</p> <p><b>Saturation temperature:</b> 25 °C</p> <p><b>Desorption time:</b> 18 min</p> <p style="text-align: center;">→ CO<sub>2</sub>-Content: ≈ 6.5 wt.%</p>	<p><b>Foaming temperature:</b> 130 °C</p> <p><b>Foaming time:</b> 15 s</p>

### 3.2.2 Production of neat references

First, foams without additives were produced which serve as a reference for the possible improvement by the addition of supramolecular additives. To compensate the relatively large fluctuations which occur in foams without additives, a total of four foams were produced under the same conditions. Each foam was characterized and the results obtained were combined to give an average value.

The characterization was carried out with focus on density and morphology of the foams. The density was determined by the Archimedes buoyancy method utilizing small cuboids cut out of the foams. To obtain a reliable value, the density was measured at different spots within the sample and an average value was calculated for all of them. The very thin compact outer skin was not removed before the measurements.

The characterization of the morphology includes the calculation of the average cell size and the associated standard deviation, which can be used as a measure of the homogeneity of the foam, as well as an assessment of the foam structure on a macroscopic level, if necessary. The cell sizes are determined by means of SEM micrographs, whereby it is assumed that the cells are spherical. To obtain a reliable value, a large number of cells were measured.

The results of the density measurement and the cell size evaluation of the four unadditivated foams are summarized in **Figure 3.12** and **Figure 3.13**.

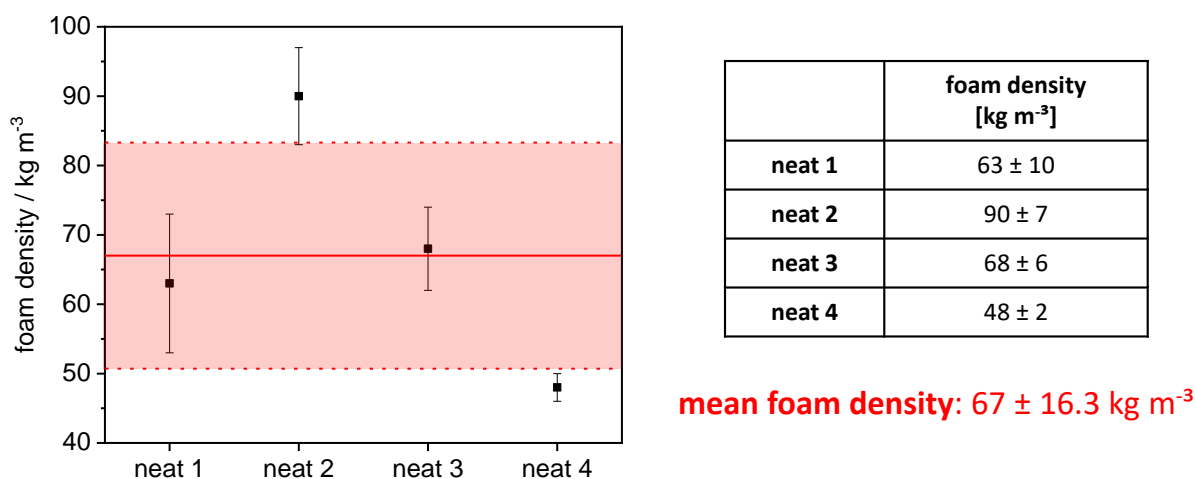


**Figure 3.12:** Foam density of the four different neat PS foams. The red line and area correspond for the mean foam density over all four samples and its corresponding error.

Considering the specific densities of the individual unadditivated foams first, it becomes apparent that these show a very large deviation. The lowest measured value is 48 kg m<sup>-3</sup> and the highest measured

density is with  $90 \text{ kg m}^{-3}$ , almost twice as high. It can also be seen that the foams are sometimes affected by a very large variation in density within this range. This suggests that there is non-uniform foaming not only across the samples but also within a sample. To form a fixed value for pure polystyrene batch foams, all measurements were averaged, resulting in a mean density of  $67 \pm 16.3 \text{ kg m}^{-3}$ .

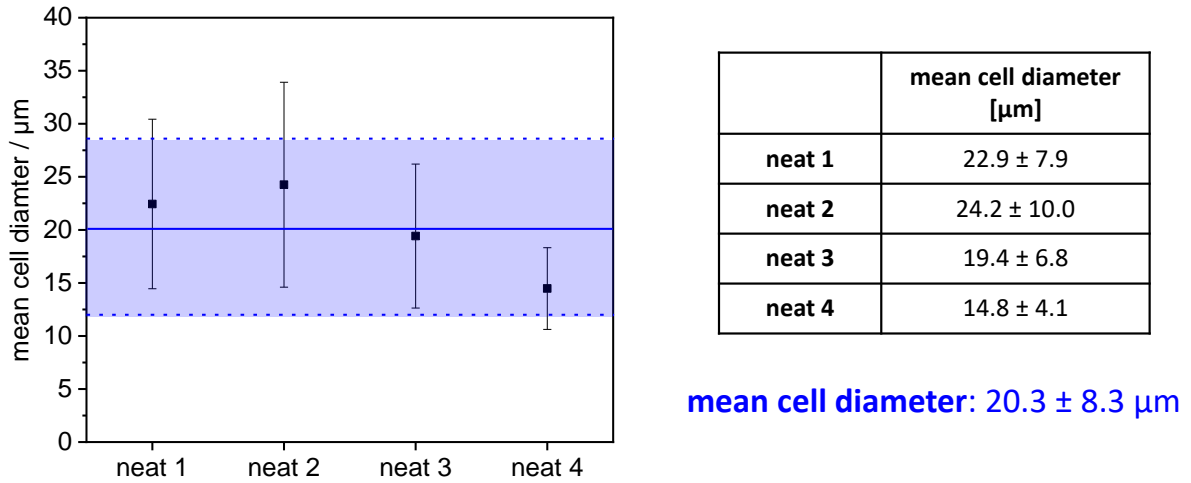


**Figure 3.13:** Mean cell diameter of the four different neat PS foams. The blue line and area correspond for the mean cell diameter over all four samples and its corresponding error.

A similar picture emerges considering the cell diameter. It is also subject to a very large variation of 14.8 to 24.2 μm. In addition, the standard deviations of the cell sizes within the individual foams are also relatively high. The reference cell size for unadditivated foams in the batch foam process was also calculated as the mean value of all four foams and determined to be 20.3 μm.

In summary, foaming of the polystyrene samples without additive is associated with very large fluctuations in both density and cell size. Due to the absence of nucleating agents, the system lacks the necessary process control, which can lead to the described variations.

### 3.2.3 Foaming with benzene trisamides

In this section, the effect of the commercial and the selected BTA as foam nucleating agents will be investigated. For this purpose, both additives are introduced into the test specimens in a concentration range of 0.01 to 1.0 wt.% through the described dilution series and foamed with the temperature-induced batch foam method. Analogous to the previously described experiments without additives, the resulting foams are characterized with respect to their density and cell morphology.

In **Figure 3.14** the results for the commercial additive **1** are shown in the diagrams **A** and **B**. For better understanding, the measured haze values of the used specimens (**C**) as well as the histogram and the SEM micrograph of the self-assembly experiments (**D**) are shown below, once again.

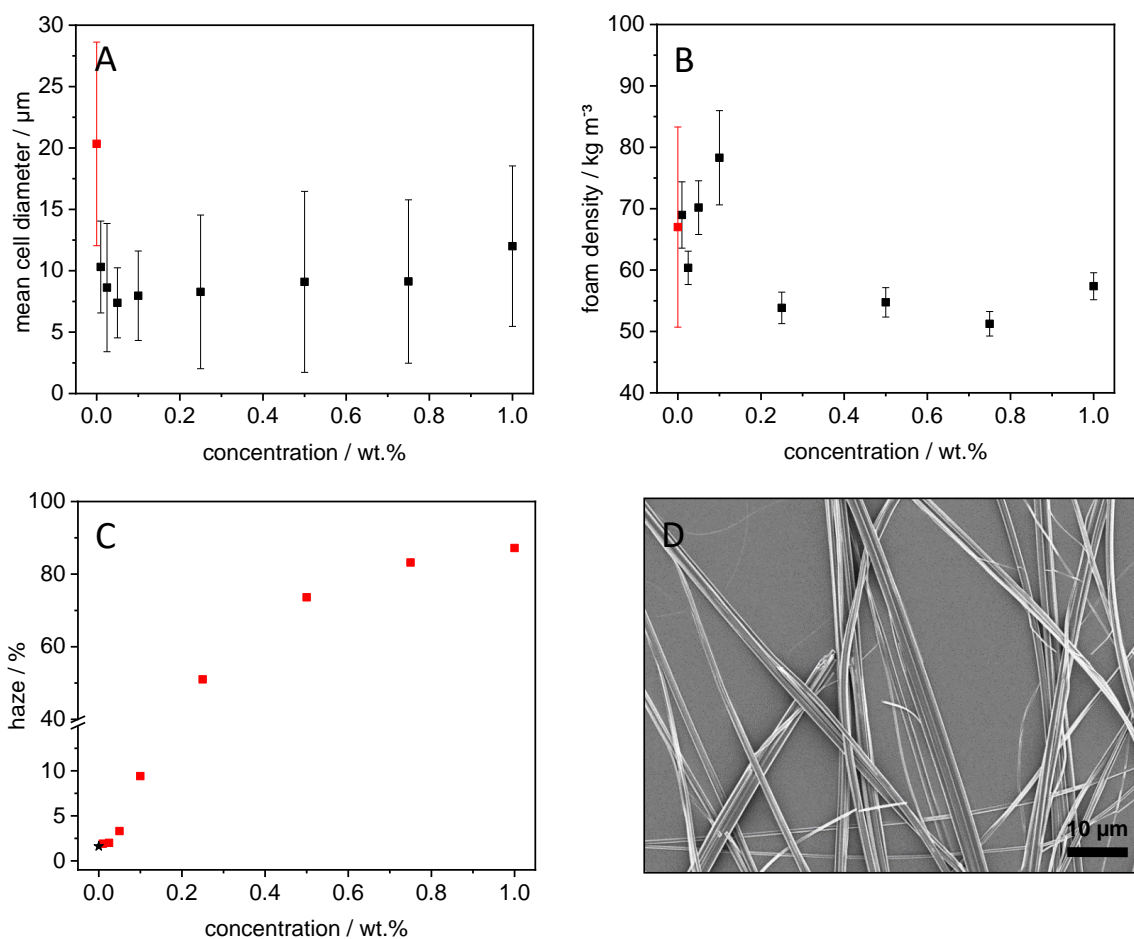


**Figure 3.14:** **A:** Mean cell diameter of the foams with different concentrations of **1**. The red square represents the mean value of neat PS. **B:** Density of the foams with different concentrations of **1**. The red square indicates the mean value of neat PS. **C:** Haze values of the specimen used for the foaming. The black star represents the haze value of neat PS. **D:** SEM micrograph of 500 ppm **1** self-assembled upon cooling in xylene.

It is shown that above a certain concentration the morphology of the foam changes from a homogeneous to an inhomogeneous cell size distribution (see **Figure 6.2**). These two morphologies will be explained briefly using the foams with 0.05 and 0.5 wt.% BTA **1**. For this purpose, a histogram of both foams was prepared with the cell sizes and the cumulative area as a function of the cell sizes. Together with a corresponding SEM micrograph these results are shown in **Figure 3.15**.

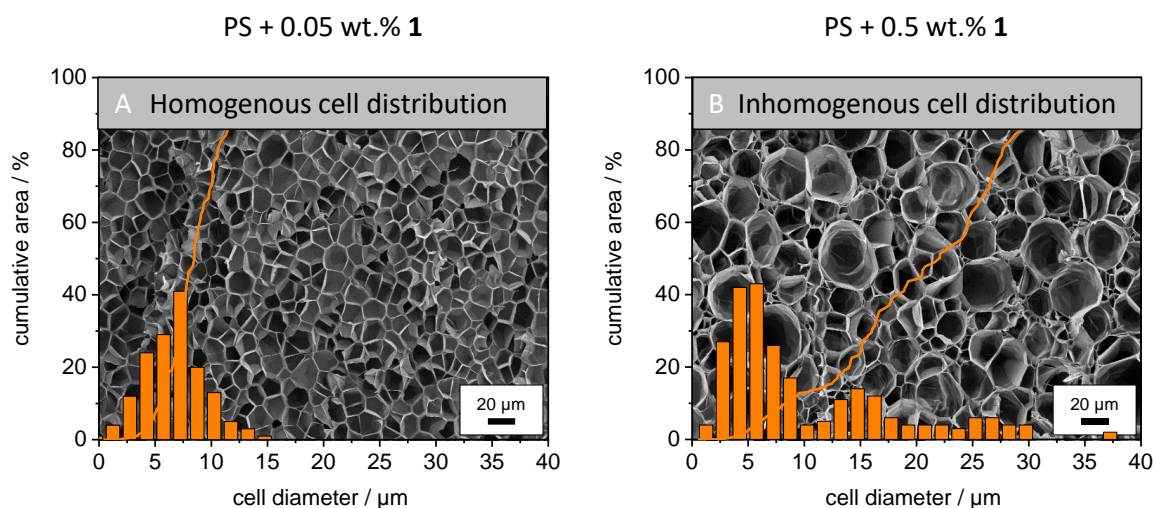


**Figure 3.15:** **A:** SEM micrograph showing the homogeneous cell distribution of the PS foam with 0.05 wt.% **1** together with a histogram featuring the cell size as well as the cumulative area in dependence of the cell size. **B:** SEM micrograph showing the inhomogeneous cell distribution of the PS foam with 0.5 wt.% **1** together with a histogram featuring the cell size as well as the cumulative area in dependence of the cell size.

On the SEM micrograph and in the histogram, you can see that with a concentration of 0.05 wt.% of additive **1** a foam is formed which has relatively uniform cell sizes. The mean determined cell size corresponds to  $7.4 \pm 2.9 \mu\text{m}$  and reflects approximately the peak in the histogram. The cumulative area shows an almost continuous growth over the cell sizes and reaches 100 % already at cell sizes below 15  $\mu\text{m}$ . This means that the total area of the considered region is made up of cells smaller than 15  $\mu\text{m}$ . If one looks at the foam with a concentration of 0.5 wt.% of BTA **1**, a completely different morphology is apparent. The inhomogeneity of cell sizes can be clearly seen in the SEM micrograph and the corresponding histogram. On the one hand, cells between 1 – 10  $\mu\text{m}$  in size, as in the previous example, and on the other hand those with a diameter larger than 11 up to 40  $\mu\text{m}$ . Although the foam has a much larger number of small cells, these make up only about 14% of the total area of the section under consideration. The rest is made up by the large cells.

Nevertheless, the foams containing additive **1** in very low concentrations ranging from 0.01 to 0.05 wt.% show a significant reduction of the average cell size down to  $7.4 \pm 2.9 \mu\text{m}$ . The fiber network formed by this BTA thus offers a very large number of potential nucleation sites that can nucleate the bubble growth.

However, the number of fibers introduced in this way is very limited due to their low solubility in the polystyrene melt. If the amount of additive is increased, the foams begin to form an inhomogeneous cell distribution. This is exactly in line with the increase of the haze value due to a possible incomplete dissolution of the additive in the polymer melt. A closer look reveals that the larger cells also accommodate large additive aggregates as shown in the following figure.

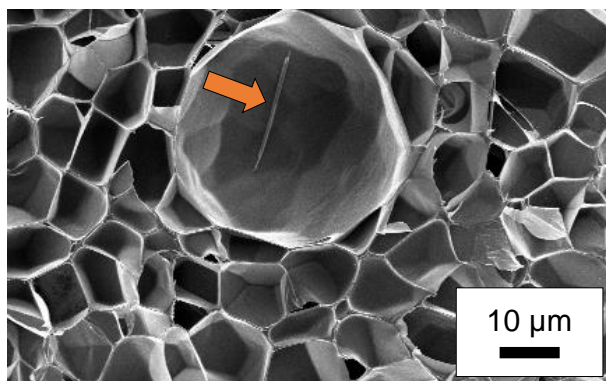


**Figure 3.16:** SEM micrograph of the inhomogeneous foam structure of the PS foam containing 0.1 wt.% **1** showing an additive aggregate in its large cell (marked with an orange arrow).

Due to the incomplete dissolution during compounding, aggregates as they were formed in from the synthesis remain in the melt. This leads to an inhomogeneous distribution of the additive. In addition, these aggregates act as nuclei for the crystallization of the dissolved benzene trisamide, causing them to grow in size and further promote an inhomogeneous distribution of the additive. Consequently, an additive-poor area is formed around the aggregates, which prevents heterogeneous nucleation and thus allows the single cell to grow further. At a concentration of 0.1 wt.%, only very few of these large cells exist, making them easily distinguishable from normally nucleated cells. This is also evident when looking at the very small standard deviations of the specific cell sizes. By increasing the concentration, the number of large cells increases very quickly. In addition, during bubble growth large cells collide directly with each other, which disturbs their unhindered propagation and thus causes stagnation of further growth.

Looking at the densities of the produced foams, it is noticeable that especially at the higher concentrations a stronger density reduction takes place compared to the samples without additive. In addition, these also show a lower standard deviation. In the concentration range from 0.01 to 0.1 wt.% the values fluctuate quite strongly around the average value of the pure PS foams but have a proportionately smaller error than these.

In direct comparison to the reference additive **1** just described the effects of BTA **2** will be explained in more detail. This additive has been directly adapted to the polystyrene matrix regarding its solubility and

can therefore be used in a much greater concentration range. The obtained results and all needed information's are summarized in **Figure 3.17**.

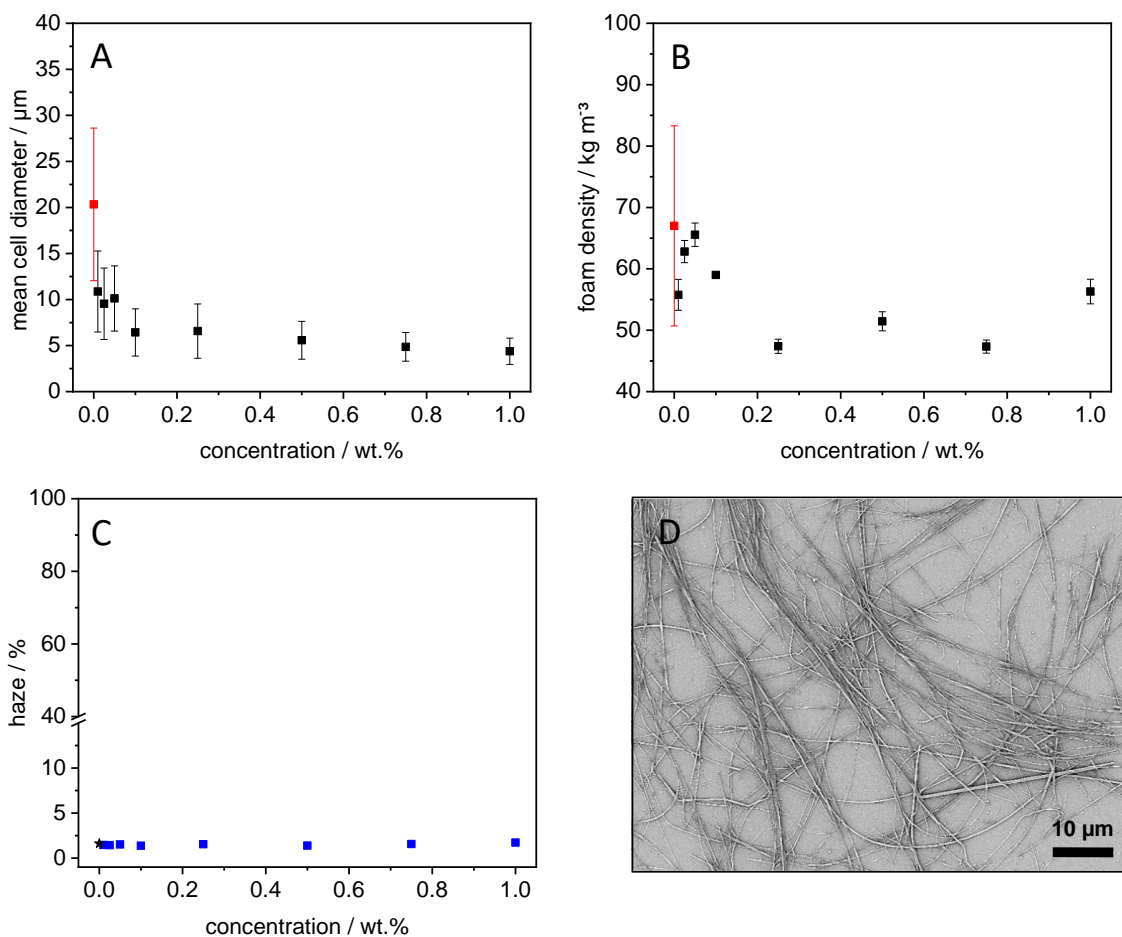


**Figure 3.17:** **A:** Mean cell diameter of the foams with different concentrations of **2**. The red square represents the mean value of neat PS. **B:** Density of the foams with different concentrations of **2**. The red square indicates the mean value of neat PS. **C:** Haze values of the specimen used for the foaming. The black star represents the haze value of neat PS. **D:** SEM micrograph of 500 ppm **2** self-assembled upon cooling in xylene.

It is shown that additive **2** features a homogenous cell distribution over the entire investigated concentration range, which confirms the good solubility (see **Figure 6.3**). Despite its good solubility, BTA **2** still forms supramolecular objects when the polymer melt is cooled down. Even at a concentration of only 0.01 wt.%, a halving of the cell size compared to unadditivated foams can be observed. The decisive factor here is also the crystallization of the additive in a very fine fiber network, which provides an enormous number of potential nuclei for the formation of the foam bubbles. In contrast to additive **1**, it is possible to introduce more supramolecular fibers into the system by simply increasing the concentration. This consequently increases the number of available nuclei, resulting in a steady reduction of the average cell

## **Foaming polystyrene with benzene trisamides**

---

size. With a concentration of 1.0 wt.% the cells can be reduced by a factor of 4.5 to a size of  $4.4 \pm 1.4 \mu\text{m}$ . Furthermore, the mean cell sizes show a relatively small deviation, which indicates a high homogeneity of the foams. Regarding density, all foams have a lower density than the unadditivated reference. Again, the foams are very homogeneous, as the difference in density between the different measured spots is very small. Similar to additive **1**, more pronounced density reductions can be observed at higher concentrations.

### 3.3 Foam extrusion

In this section the concept of supramolecular additives as foam nucleating agents will be transferred to foam extrusion. Foam extrusion is one of the large-scale processes used to produce polystyrene foams. The resulting foams have a very low thermal conductivity, which empowers them to be used as insulating material in the building and construction sector. A widely used approach to further improve the insulating performance of these materials is to control the foam morphology to very small foam cells to further reduce thermal conductivity. An extremely efficient way to achieve this is by using additives. In the following, the commercially available BTA **1** is used to control the morphology of the generated polystyrene foams and thus significantly enhance the thermal conductivity.

#### 3.3.1 Foam sample preparation

The foam extrusion experiments on a pilot scale were performed on a tandem extrusion line. This consists of a twin-screw extruder and a single-screw extruder. The first extruder is supplied with the mixture of pure polymer and masterbatch via a dosing system. The systematically selected concentrations of 0.1, 0.2 and 0.5 wt.% can be precisely adjusted via the flow rates of the two materials. In the first part of the extruder, the polymer granulate is melted and compounded with the additives. The temperature was set to 260 °C to ensure complete dissolution of the additive (0.1 and 0.2 wt.%) in the polymer melt. Subsequently, 4 wt.% CO<sub>2</sub> as blowing agent and 3 wt.% EtOH as co-blowing agent are introduced under pressure. The ratio of blowing agents were taken from a study, which revealed an optimized blowing agent ratio of CO<sub>2</sub> and ethanol for PS foam extrusion.<sup>[66]</sup> Ethanol was used as a co-blowing agent to further enhance plasticization to produce low-density foams as described in the literature.<sup>[66]</sup>

It is important to ensure that the pressure is sufficient high for the propellants to be in a supercritical state. At the end of the first extruder there is in the best case a homogeneous polymer/blowing agent mixture which is transferred to the second extruder, where it gets cooled down. By cooling down to the foaming temperature the melt strength increases, which prevents cell collapse during foaming and also results in further pressure build-up. In addition, cooling reduces the solubility of the additive in the melt significantly, causing it to crystallize into fine nano-objects in a self-assembly process. However, if the temperature is reduced too much, the plasticization of the polystyrene is insufficient, leading to clogging of the die and consequently to an enormous increase in pressure. If the temperature is excessively high, cell collapse and outgassing of the blowing agent occurs as a result of the low melt strength. Both restrictions result in a foam window of 106 to 130°C for the foam extrusion process. At the end of the extruder there is a slit die where the rapid pressure drop occurs. The associated supersaturation leads to the foaming of the material.

For the same reasons as for the temperature in the second extruder, there is also a temperature range for the die in which foams can be produced. In this series of experiments, it was in the range of 123 – 132 °C. It should be noted that the exact temperatures at which the foams were produced are always included in the characterization. The experimental setup used is shown schematically in **Figure 3.18**.

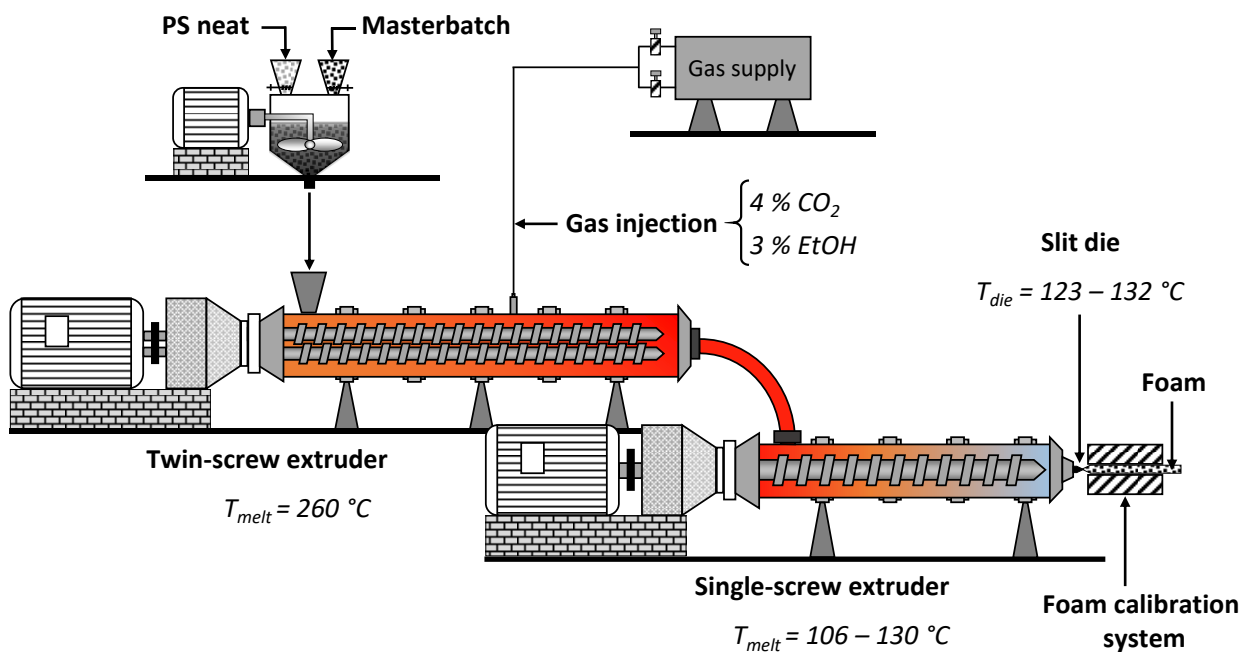


**Figure 3.18:** Experimental setup of the foam extrusion line consisting of a twin-screw extruder and a colder single-screw extruder. The first gets filled with the polymer by a dosing unit and the melt is loaded with the blowing agents. The second is equipped with a slit die and a foam calibration system.

Directly after the nozzle there can be a calibration unit to dam up the resulting foams and bring them into the desired shape if it is needed. In order to analyze the effects of the additive precisely, pure polystyrene was foamed under the same conditions as a reference. The exact process parameters can be found at 5.3.3 in the experimental part.

### 3.3.2 Foaming with the selected benzene trisamide

In order to test the use of supramolecular additives as foam nucleating agents for polystyrene in foam extrusion, the commercially available BTA **1** was used. Since the solubility of the additive is of great importance for our conceptual approach, a further investigation with optical light microscopy was carried out.

Therefore, a film of the PS with the corresponding concentration of additive **1** is pressed between two glass slides and tempered with a hot-stage at a controlled heating or cooling rate of 10 K min<sup>-1</sup>. With the two crossed polarizers of the microscope it is possible to make the birefringent crystalline structures of

the additive in the amorphous polystyrene melt visible. First, the sample is heated until the complete additive is dissolved completely. During the subsequent cooling process, the temperature at which the first birefringent self-assembled supramolecular objects of the additive occur is determined. This temperature is called the self-assembly temperature and is different for each concentration. Once the sample has cooled down to room temperature and all additive has crystallized, the sample is heated in a controlled manner. The second decisive temperature is the temperature at which all supramolecular objects were dissolved in the polymer melt. This is known as the dissolution temperature which is also concentration dependent. **Figure 3.19** shows exemplary the polarization microscope images for the concentration of 0.1 wt.% **1** in polystyrene during cooling and heating.

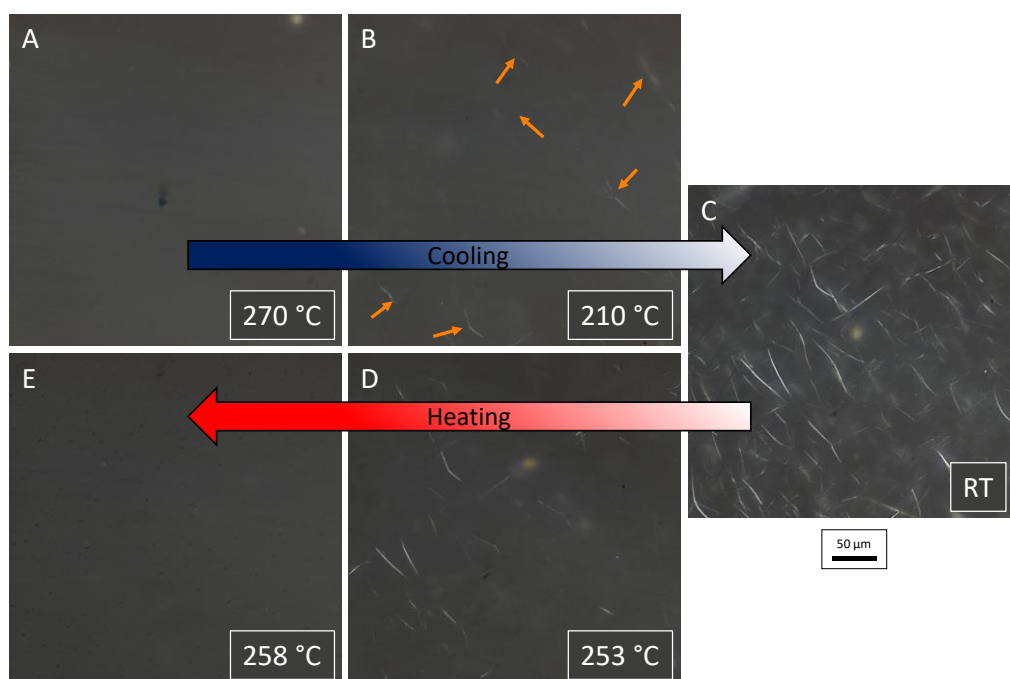


**Figure 3.19:** Polarized optical microscopy images of a PS film with 0.1 wt.% **1**: (A-C) micrographs taken at various temperatures during cooling step (orange arrows indicate the first appearance of self-assembled supramolecular objects; (C-E) micrographs taken at various temperatures during heating step. When all self-assembled supramolecular objects are dissolved in the polymer melt the dissolution temperature is reached.

Micrograph **A** shows the amorphous PS melt in which the entire additive is dissolved. During cooling, the additive begins to crystallize and forming supramolecular objects by a self-assembly process at a temperature of around 210 °C (micrograph **B**). These objects continue to grow through continuous cooling until the entire additive is finally crystallized (micrograph **C**). After the film is cooled down to room temperature the heating step can be conducted. At a certain temperature, the structures slowly begin to disappear, micrograph **D**, up to the dissolution temperature at 258 °C, micrograph **E**, at which all of the supramolecular objects have been dissolved again.

The dissolution and self-assembly temperatures for each sample having different concentrations in the range of 0.05 to 0.5 wt.% were plotted in **Figure 3.20**.

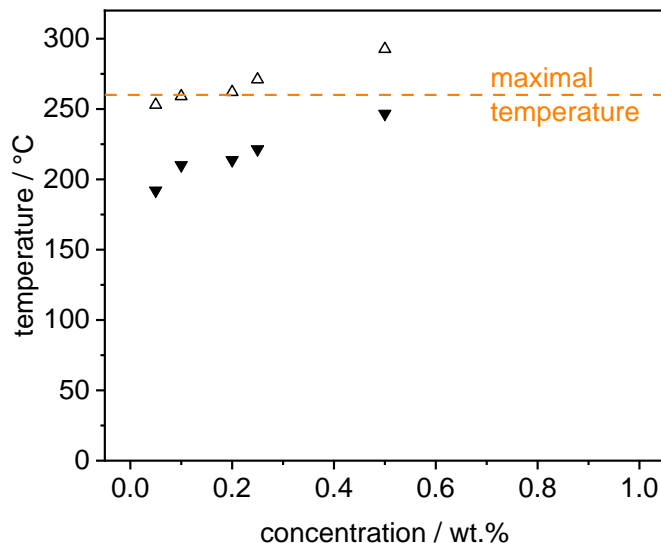


**Figure 3.20:** Dissolution ( $\Delta$ ) and self-assembly ( $\blacktriangledown$ ) temperatures of additive **1** in PS depending on the concentration, determined with polarized light microscopy (The dashed line at 260 °C indicates the maximal temperature during the foam extrusion process). Reprinted with permission of <sup>[67]</sup> ©SAGE journals.

In the case of the dissolution behavior, it can be seen that for 0.05 wt.% a temperature of 250 °C is required to dissolve all the supramolecular structures formed by additive **1**. At concentrations lower than 0.05 wt.% the determination of the solubility or self-assembly temperature was not possible. This might be due to the smaller diameter of the supramolecular objects than the wavelength of visible light, and thus they could not be observed under the light microscope. This is in accordance with the determined haze values. The dissolution temperature increases with increasing concentration and reaches a value of approx. 262 °C for 0.2 wt.%. This temperature corresponds to the maximal temperature (260 °C) as it is used during the foam extrusion process. At a concentration of 0.5 wt.%, dissolution of **1** occurs at approx. 300 °C. This is attributed to the maximal soluble concentration of **1** in PS, since the PS starts to decompose above these temperatures.<sup>[190]</sup> These findings may seem to slightly differ from the solubility limits stated at the batch foaming process. But during the production of the foamable test specimens in the micro compounder, a temperature of 260 °C was set at the heating elements indeed, but this is not quite reached by the polymer melt. It is therefore likely that the melt temperature of 258 °C required for dissolving 0.1 wt.% of BTA **1** was not reached in the micro compounder. The temperature at which self-assembly occurs upon cooling is also shown in **Figure 3.20**. In all cases, these temperatures are approximately 50 °C below the dissolution

temperature. However, these temperatures are fairly above the foaming temperature of approximately 115 °C. Therefore, the presence of solid supramolecular objects is ensured in the foaming step. We note that during the foaming process several additional factors such as pressure, blowing agents and shear forces are present, which could not be taken into account by these studies. However, it was expected that the solubility and self-assembly temperatures differ only slightly during foam extrusion process.

Based on these findings, three concentrations were selected to determine the effect of additive **1** concentration systematically on the final morphology of the extruded foams. As already mentioned, it is possible to completely dissolve 0.2 wt.% of the additive in the polymer melt at a temperature of 262 °C. Due to the relatively long processing time in foam extrusion, the high shear forces, the lowered glass transition temperature and the blowing agent content, it should be possible at the temperatures used to dissolve this amount of benzene trisamide at a molecular level and thus distribute it homogeneously. This concentration is therefore considered the optimum concentration for foam extrusion. In addition to this, 0.1 wt.% was selected to evaluate the effects of reducing the fiber quantity and 0.5 wt.% as a negative example to study the consequences of the partial insolubility of the additive. The foams are then to be characterized regarding to the morphology and its modification by the addition of the additive and the associated changes in their thermal properties. The term morphology refers to cell size, cell density and homogeneity, i.e. the distribution of cell sizes, in the XPS foams. In addition to these characteristics, density also plays a major role in the final thermal conductivity and is therefore examined as well.

### Morphology and density

The foam morphologies of the neat PS, PS with 0.1, 0.2 and 0.5 wt.% additive **1** together with the cell size distributions, mean cell sizes, cell densities, foam densities as well as the processing temperatures are displayed in **Figure 3.21**.

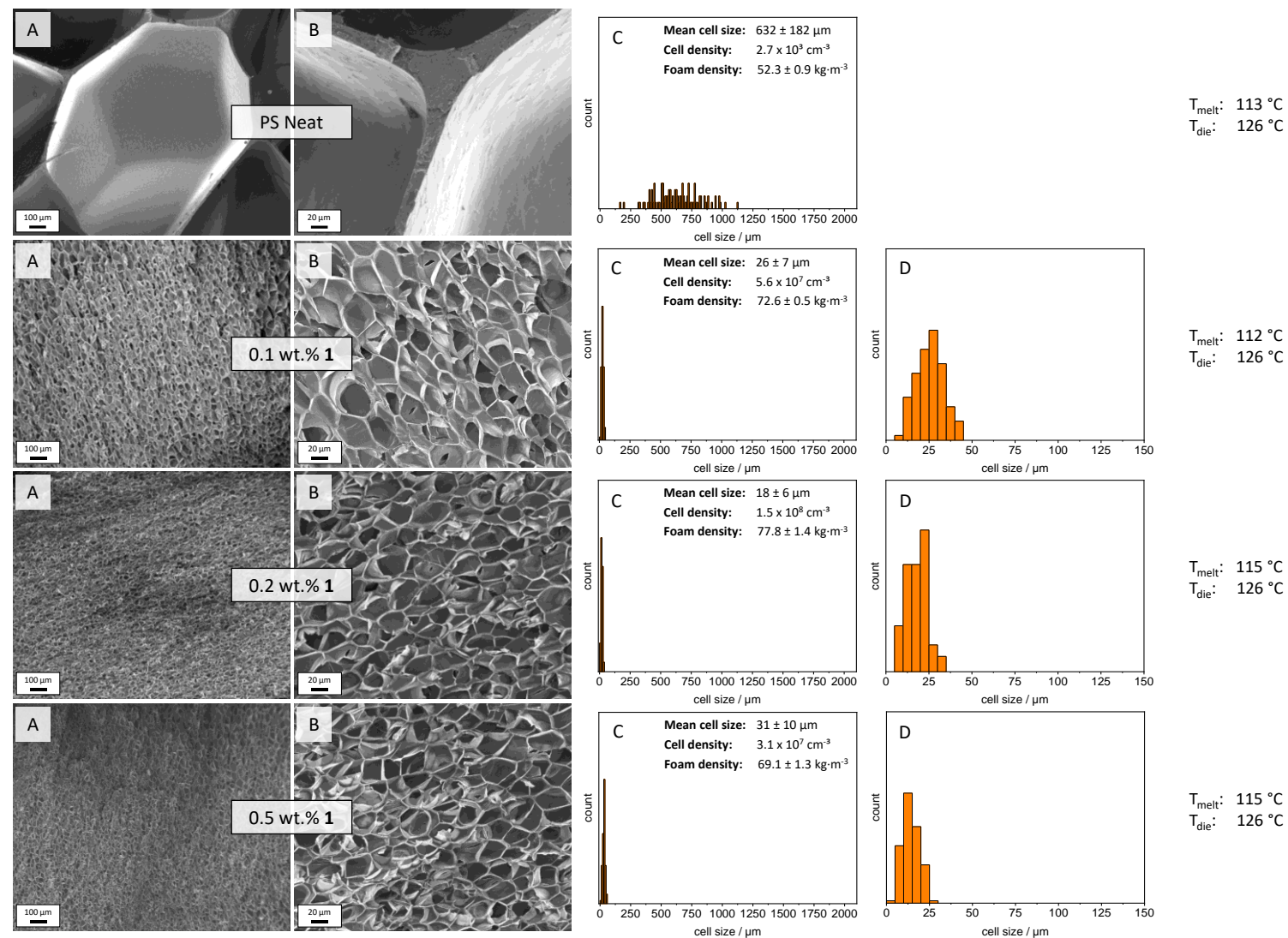


**Figure 3.21:** Comparison of the neat extrusion PS foam and the foams prepared with different concentrations of additive **1**. SEM micrographs **A**: overview and **B**: higher magnification. **C**: Corresponding histograms of the cell sizes, including mean cell size, cell density and foam density. **D**: Section of the histogram. Reprinted with permission of <sup>[67]</sup> ©SAGE journals.

The neat PS foam has a closed cell macro-cellular structure with an average cell size of  $632 \pm 182 \mu\text{m}$  and a cell density of  $2.7 \times 10^3 \text{ cells per cm}^3$ . The corresponding histogram also shows its broad variation of the cell size ranging from  $150 \mu\text{m}$  to over  $1000 \mu\text{m}$ . In comparison the XPS processed with additive **1** lead at the lowest concentration of 0.1 wt.% already to a cell size reduction of  $26 \pm 7 \mu\text{m}$  and an increase in the cell density to  $5.6 \times 10^7 \text{ cm}^{-3}$ . This clearly demonstrates the formation of supramolecular objects acting as foam nucleation sites which generates foams with a homogenous morphology and very small cells as seen in the corresponding histogram. By increasing the additive concentration to 0.2 wt.% the cell size get as small as  $18 \pm 6 \mu\text{m}$  and the cell density also reaches its highest amount with  $1.5 \times 10^8 \text{ cm}^{-3}$ . As stated before, this is the highest concentration at which all of the additive can be soluble in the polystyrene matrix and thus the maximum number of foam nucleation sites is available resulting in a 35 times cell size reduction. By increasing the additive amount to 0.5 wt.% the solubility limit of the additive during the extrusion process is exceeded. For this reason, partially insoluble additive in the form of aggregates is present in the melt. These can serve as nuclei for the further self-assembly of the additive during cooling. This leads to a formation of larger objects and thus to a reduction of the number of available foam nucleation sites. Due to the incomplete dissolution, the homogenous dispersion is no longer given, which can also have a negative effect on the foam morphology. All this leads to an increase of the cell size to  $31 \pm 10 \mu\text{m}$  and a decrease of the cell density to  $3.1 \times 10^7 \text{ cm}^{-3}$  compared to the XPS foams with 0.2 wt.% **1**.

Looking at the foam densities an increase with decreasing the cell size is observed. The neat XPS foams show the lowest density with  $52.3 \pm 0.9 \text{ kg m}^{-3}$  while the foams with 0.2 wt.% additive exhibits a density of  $77.8 \pm 1.4 \text{ kg m}^{-3}$ . This small increase could be due to the strongly increased inner surface of the micro-cellular foams. Consequently, significantly more cell walls and cell struts have been formed than in the macro-cellular neat foam.

To confirm the validity of our concept and to show the existence of the supramolecular objects in the foam structure its visualization is of great interest. So far, this was only possible in PBT and PP. Richter et al. succeeded in revealing the supramolecular structures of selected BTAs within the PBT matrix. Certain parts of the PBT were hydrolyzed with the use of NaOH, which allowed the nanoobjects to be exposed.<sup>[168]</sup> Furthermore, Kersch et al. were able to prove the presence of supramolecular objects of self-assembled benzene trisamides in a PP matrix. The samples were treated with a solution of potassium permanganate in a mixture of sulfuric acid and phosphoric acid. Preferably the amorphous part was etched to reveal the crystalline structures.<sup>[171]</sup>

For the first time, the structures of supramolecular additives were also detected and visualized in a polystyrene foam. For this purpose, the plasma etching technique was used. Since the objects are highly crystalline and amorphous PS is easily degradable under plasma power, it was possible to remove the PS faster than the crystalline additive.

First, the required exposure time of the O<sub>2</sub>-plasma was determined. For this purpose, extrusion foams containing 0.1 wt.% additive **1** were treated for different times. **Figure 3.22** shows the corresponding SEM micrographs after 15, 30, 60 minutes and an untreated sample as reference.

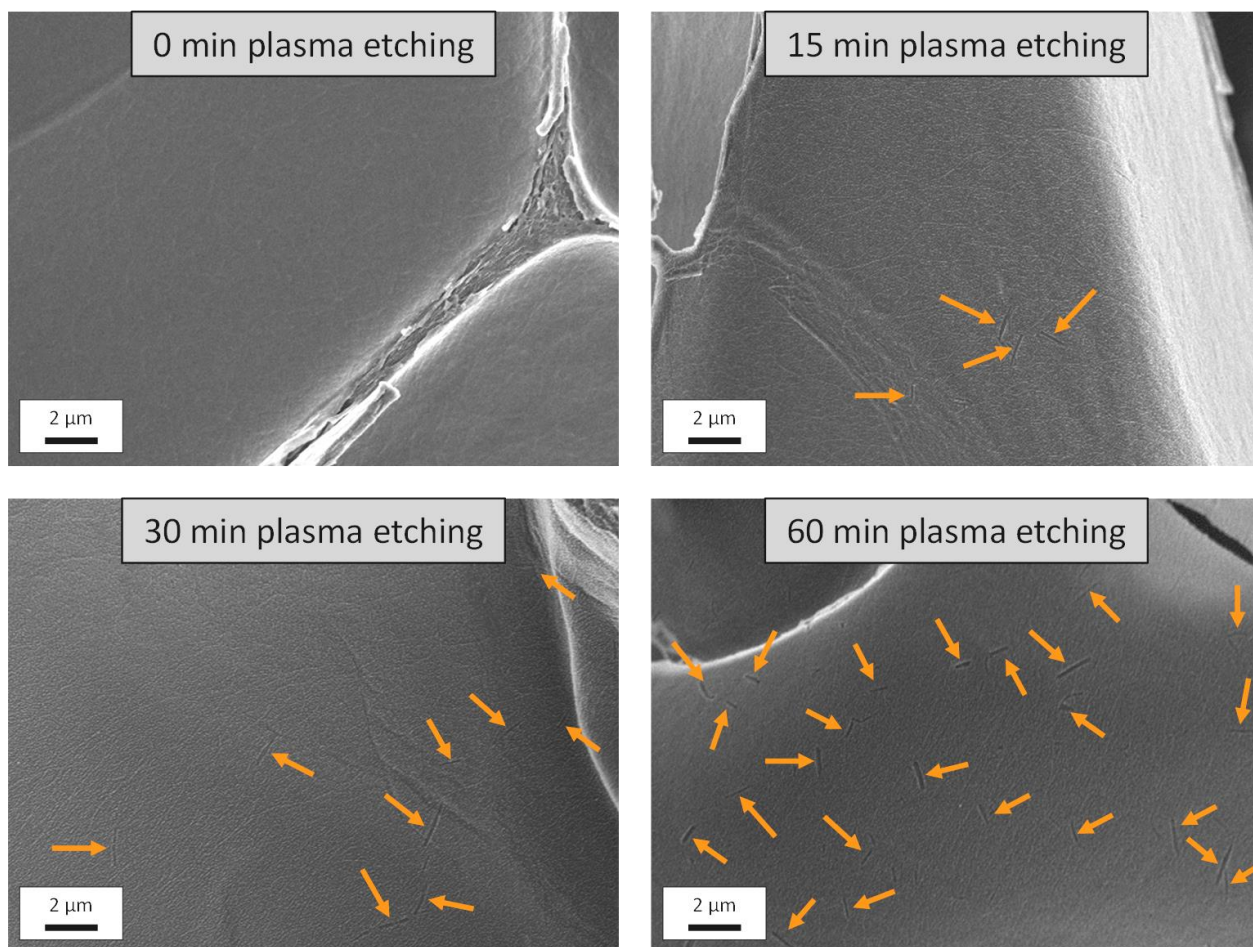


**Figure 3.22:** SEM micrographs of PS extrusion foams containing 0.1 wt.% additive **1** after 0, 15, 30 and 60 min O<sub>2</sub>-plasma etching. Orange arrows indicate the holes in which the additive objects were present before the plasma etching.

While no evidence of the supramolecular additives can be seen in the untreated sample, some distinct features can be detected after only 15 minutes of plasma etching. We attribute these holes to the former presence of the supramolecular objects in the extrusion PS foams. Thus, the width of the holes corresponds to the supramolecular objects diameter. By increasing the exposure time to 30 respectively

60 minutes, a larger part of the amorphous polystyrene layer is removed, thus exposing more additive holes. Since the already very thin cell walls of the foams are severely stressed by this etching process and excessive tearing of the cell structures should be avoided, the exposure time was not increased further. Consequently, an etching duration of 60 minutes was selected for the subsequent experiments.

The SEM micrographs of the etched XPS foams having 0.1, 0.2 and 0.5 wt.% **1** with the distributions of its supramolecular objects diameter are shown in **Figure 3.23**.

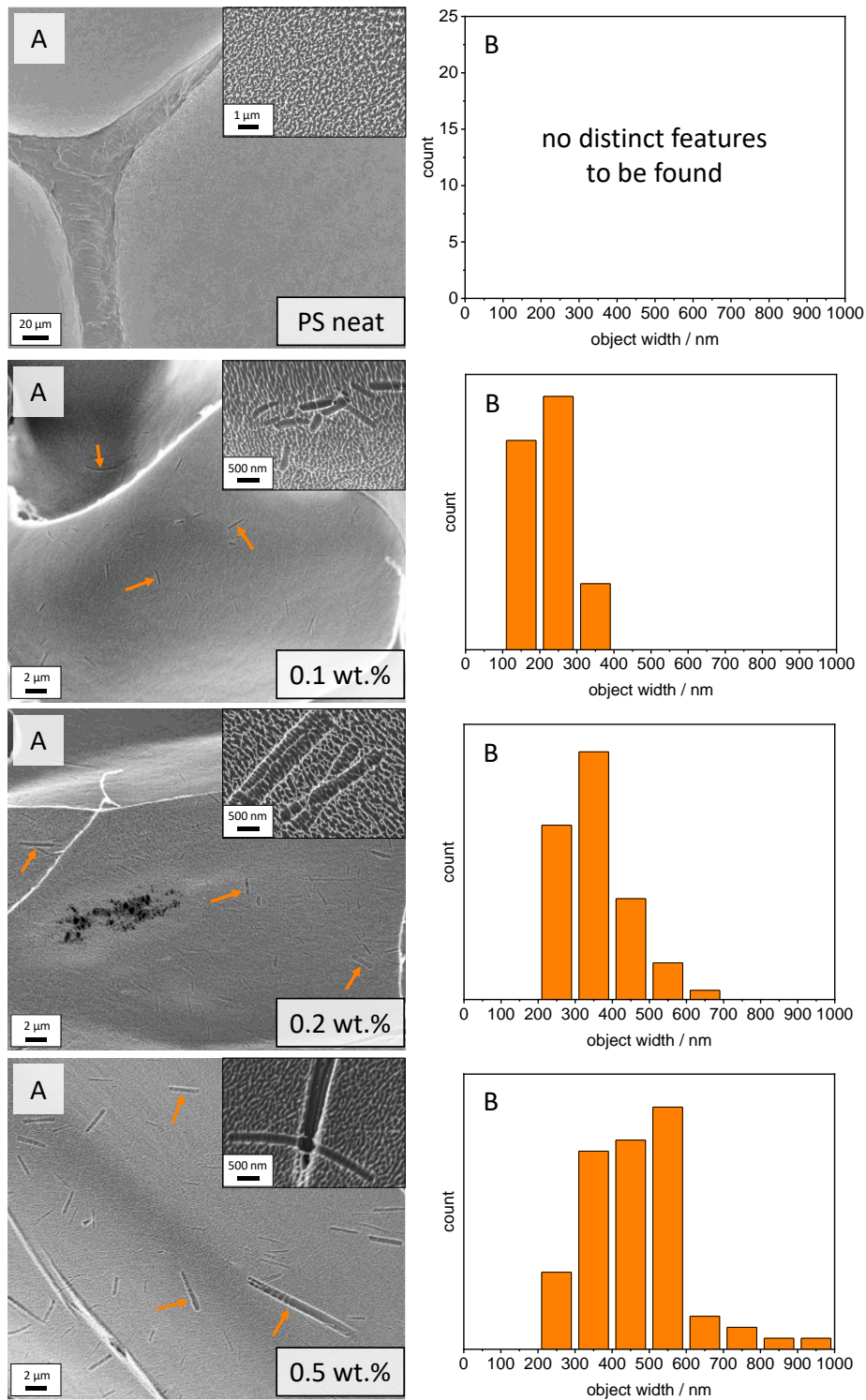


**Figure 3.23:** A: SEM micrographs of PS extrusion foams without additive and with 0.1, 0.2 and 0.5 wt.% **1** after 60 min O<sub>2</sub>-plasma treatment. Orange arrows indicate some of the holes in which the additive objects were present before the plasma etching. Inserts with larger magnification also show some example holes. B: Histograms of the width of the holes corresponding to the diameter of the objects (note the different scale bar for neat PS foams). Reprinted with permission of <sup>[67]</sup> ©SAGE journals.

The SEM Micrographs taken after 60 minutes of plasma etching show a significant difference between foams with and without additive. The samples with 0.1, 0.2 and 0.5 wt.% **1** exhibit distinct features which do not occur in pure PS foams. Most of the objects in the foams with 0.1 wt.% additive possess a diameter in the range of 200 to 300 nm. The foams with 0.2 wt.% additive exhibited objects having mostly a diameter around 300 – 400 nm, while the supramolecular objects in the foams with 0.5 wt.% additive show a diameter particularly between 500 and 600 nm. In addition, these foam features also very large objects ranging up to 1  $\mu\text{m}$  which are attributed to the undissolved aggregates during the extrusion process. As already mentioned, these aggregates are probably responsible for the cell size increase of the XPS foams with 0.2 to 0.5 wt.%.

The increase in size of the supramolecular objects diameter with increasing concentration is consistent with the found haze increase as already described in **Figure 3.6**. At concentrations below 0.1 wt.%, almost all additive nano-objects have a diameter below 380 nm and are therefore smaller than the wavelength of visible light. By increasing the amount to 0.1 wt.% some of the nano-objects grow up to 400 nm and are accordingly able to scatter the light and increase the haze value to around 9 %. By further increasing the amount of additive, the supramolecular objects also grow in their size. At a concentration of 0.2 wt.% around half of them are bigger than 380 nm and consequently the haze value goes up to around 50 %. At a concentration of 0.5 wt.% **1** at which the additive exhibits incomplete solubility at the processing temperature, not only the already thickened supramolecular objects increase the haze value dramatically but also the undissolved fiber shaped aggregates.

### Thermal conductivity

For a large number of applications, like in buildings and constructions, the thermal conductivity plays a decisive role. Therefore, the change in thermal conductivity caused by the morphology control via the supramolecular additives is now to be investigated. In **Figure 3.24** the measured thermal conductivities of the four extrusion foams are plotted against the additive concentration.

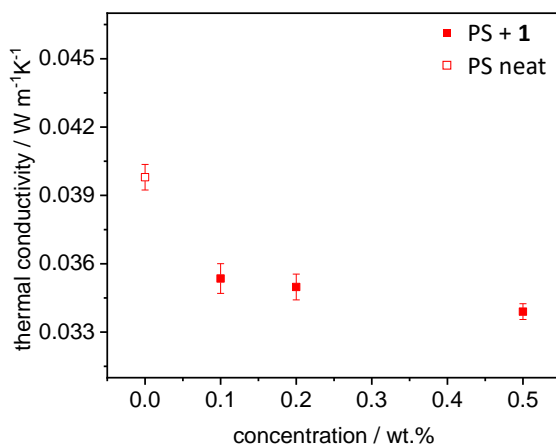


**Figure 3.24:** Thermal conductivity of the PS extrusion foams without and with different concentrations of additive **1**.<sup>[68]</sup>

For all applied concentrations of additive **1**, there is a significant reduction of the thermal conductivity. The lowest value was measured for the foam with 0.5 wt.% **1** to be 0.0339 W m<sup>-1</sup>K<sup>-1</sup>, which equals a reduction of 17 % compared to the pure polystyrene extrusion foam. When using 0.1 and 0.2 wt.% of the additive, a reduction of 11 and 12 % can be achieved. Contrary to expectations, it is not the foam with the smallest average cell size that has the lowest thermal conductivity. As already explained in 1.4.3, the total thermal conductivity does not only depend on the cell size of the foam, but also on the density. To illustrate these dependencies, **Figure 3.25** shows the thermal conductivity plotted against both foam density and cell size.

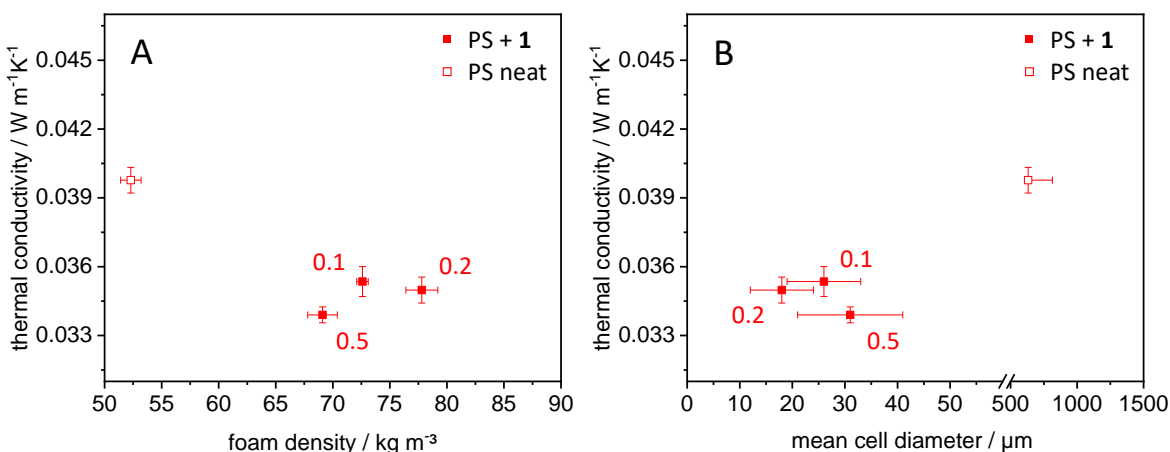


**Figure 3.25:** Thermal conductivity of the PS extrusion foams without and with additive **1** in dependence of **A**: foam density and **B**: mean cell diameter. The red numbers indicate the corresponding additive concentration.<sup>[68]</sup>

By considering the neat polystyrene foam, it is evident that controlling the morphology has the bigger influence on thermal conductivity compared to the increase in density which takes place by the addition of BTA **1**. Although the neat PS foam has the lowest density, it still has a much higher thermal conductivity than the additivated foams. This is due to the fact that with very large cells, a big amount of heat transport occurs within the foam via radiation. This amount can be drastically reduced by downsizing the cell size and clearly outweighs the increase in heat transport over the solid phase due to the increased density (see **Figure 1.17**). Especially for small cells (> 50 μm) the influence of radiation is not as significant and therefore the density becomes more important. So, foams with 0.5 wt.% additive **1** exhibit the lowest thermal conductivity, which is attributed to the optimal compromise between cell size reduction and increase in foam density. Unfortunately, foams with 0.2 wt.% additive exhibit the highest cell size reduction as well as the highest increase in density, which means that the total thermal conductivity cannot be reduced as much.

Various approaches are conceivable to further improve the overall thermal conductivity of the extrusion foams. One possibility, for example, would be to reduce the density of the foams through process optimization to allow the cell size reduction to develop its full potential. Relevant parameters would be the melt temperatures in the first and second extruder, the pressure and the pressure drop rate, the blowing agent and its quantity and the die temperature as well as its geometry. By optimizing all these parameters, it should be possible to generate foams which do not have an increased density despite the enormous cell size reduction. Another possibility would be the use of even more efficient additives, which are able to reduce the size of the cells even further. With further diminishing cell sizes, it would be possible

## **Foaming polystyrene with benzene trisamides**

---

to significantly limit the heat transfer via the gas phase due to the so-called Knudsen effect, which consequently reduces the overall thermal conductivity.

### 3.4 Conclusion

To establish the concept of the morphology control of amorphous polystyrene with supramolecular additives two BTAs have been used. The first additive consists of 1,3,5 triaminobenzene-based core with three *t*-butyl side groups - **1**. The second additive comprises of 1,3,5-benzenetricarboxylic acid with three *i*-pentyl side groups - **2**.

First it was shown that both selected benzene trisamides are capable of forming supramolecular fibers via a self-assembly process from xylene as a model solvent. While the fibers of additive **1** have a huge variety in their diameter ranging from 250 to 1500 nm, the fibers of BTA **2** are in the range of only 100 to 250 nm.

An analysis of the haze values of the injection molded specimen with different concentrations of both additives in polystyrene suggested a better solubility of additive **2** since the platelets show no increased haze value even with the highest concentration of 1 wt.%.

To investigate the benzene trisamides as foam nucleating agents and to optimize the foaming conditions a *temperature-induced batch foaming process* was used. The optimization of the foaming conditions showed that 18 minutes after the pressure was released from the autoclave the saturation of CO<sub>2</sub> reached 6.5 wt.%, which was used for all experiments. After the screening of the foaming time and temperature, the batch foaming parameters were set to 15 seconds and 130 °C resulting in low density foams. Ultimately it was found that an annealing step of the specimen prior to the saturation is needed to remove the internal stress in the material caused by the injection molding process to ensure a uniform foaming.

By foaming the specimen containing additive **1** and **2** under these conditions, it was possible to significantly reduce the cell sizes of all generated foams. However, the decisive difference is the different solubility of the substances in polystyrene. While additive **1** can only be dissolved up to a very limited concentration under the prevailing conditions, additive **2** offers the possibility of introducing a higher amount of additive homogeneously dispersed into the polymer matrix. In addition, the supramolecular objects of **2** have a much higher aspect ratio which significantly increased the number of potential nuclei. It is thus possible to nucleate more bubbles and thus almost halve the size of the resulting cells down to 4.4 μm in comparison with additive **1**.

Due to the access to large quantities of additive **1**, it was utilized in a *foam extrusion process* on pilot-scale. Therefore, foams with a concentration of 0.1, 0.2 and 0.5 wt.% of additive **1** were produced. A concentration of approximately 0.2 wt.% was determined to be the highest amount of the additive, which can be completely dissolved in the polystyrene at the given conditions and therefore is regarded as the

optimal concentration. With this amount of additive, the foams showed the smallest average cell size of only 18  $\mu\text{m}$ , which is a factor of 35 smaller than those of the neat polystyrene reference foams. However, the foam density slightly increases from 52.3  $\text{kg m}^{-3}$  to 78.8  $\text{kg m}^{-3}$ . At the lowest concentration of 0.1 wt.%, the number of possible nuclei is reduced, leading to a lower nucleation effect. By increasing the concentration up to 0.5 wt.%, no further decrease of the mean cell size was observed. This is attributed to the incomplete solubility of the additive, which was also demonstrated by the solubility study.

Furthermore, it is possible to visualize the supramolecular nanostructures of the additives in the foams with the plasma etching technique. Since the surface of the amorphous polystyrene is faster removed than the crystalline structures of the additives it was found by means of SEM that the trisamides are located in the cell walls and cell struts.

Moreover, it was also possible to identify the influence of the additive concentration on the resulting fiber diameter. By increasing the concentration of additive **1** from 0.1 to 0.5 wt.%, the diameter of the nano-objects increases from 200 to 500 nm. In addition, at a concentration of 0.5 wt.% huge aggregates of additive **1** have been found in the foams, which is also an indication of incomplete solubility.

To ultimately investigate the effects of the morphology control of the foams, the thermal conductivity of all samples was measured. Although the reduction in the cell size achieved by 0.5 wt.% of additive **1** was less distinct than with 0.1 wt.% and 0.2 wt.%, the lowest thermal conductivity of 0.0339  $\text{W m}^{-1}\text{K}^{-1}$  was measured here. This corresponds to a reduction of 17 % compared to that of the neat polystyrene foam. Consequently, the foam with 0.5 % BTA **1** exhibits the optimum compromise between the competing effects from cell size and foam density. While the higher foam density increases the heat transfer over the solid phase, the smaller cell sizes reduce the heat transfer over the gas phase as well as by radiation.

To further improve the foam nucleating ability, it was our aim to find supramolecular additives, whose fiber diameters are smaller and in addition shows a better solubility in polystyrene. Therefore, we explored bisamides and in particular a novel class of kinked bisamides as foam nucleating agents for polystyrene.

## 4 Foaming polystyrene with bisamides

The bisamides<sup>[191]</sup> used in this thesis have a similar structure as the benzene trisamides described in the previous chapter. The schematic structure is shown in **Figure 4.1**.

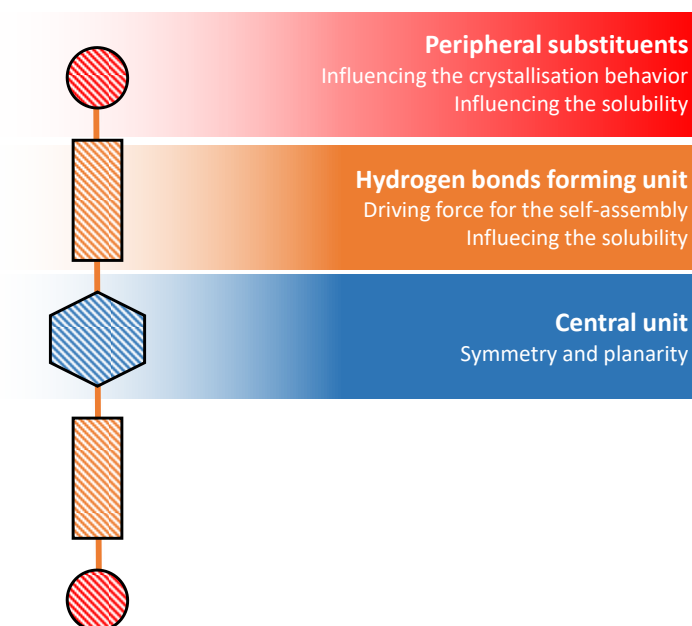


**Figure 4.1:** Schematic structure of the used benzene bisamides.

They also consist of the three components central unit, hydrogen bonding unit and a peripheral residue. The main difference is that these additives only have two hydrogen bonding units. The tasks and effects of the individual components are identical, as described in section 3. In addition to the variation of the peripheral residues and orientation of the amide bond, different central units were introduced in this chapter. In addition to a simple benzene and naphthalene core, a novel kinked central unit was introduced. It consists of two benzene rings, which are connected by a methylene spacer. This greatly increases the mobility of the compounds, which improves the solubility in the polystyrene matrix. Additionally, both benzene rings can be substituted with further methyl or ethyl groups. The steric hindrance thus introduced leads to a torsion of the amide groups and consequently results in increased phase transitions of the kinked bisamides. By adapting the different adjustment screws, it is possible to adapt these novel foam nucleating agents perfectly to the polystyrene matrix and thus achieve outstanding nucleation properties.

This type of bisamide has already been used in the clarification of polypropylene compounds<sup>[192]</sup> and is now to be used as a supramolecular foam nucleating agent in amorphous polystyrene.

## 4.1 Synthesis and properties of the selected bisamides

Besides the recently explained benzene trisamides, 14 different bisamides including the novel class of kinked bisamides were used as foam nucleating agents in this work. As reference additives N,N'-1,4-phenylenebis[cyclohexanecarboxamide] - **3a** and the commercially available N,N'-dicyclohexyl-2,6-naphthalene dicarboxamide - **3b** also known as NJSTAR NU-100 were used.

The kinked bisamides consist of two benzene rings connected by a methylene-linker as the central unit, followed by two N-centered amide bonds and a substituent on both sides in the periphery. The two benzene rings of the central unit can also be substituted with the group  $R_1$  on positions 2 and 6 on both sides. In this case,  $R_1$  consists either of only a proton, a methyl group or an ethyl group. Accordingly, groups **4**, **5** and **6** are formed. The two groups  $R_2$  in the periphery consist either of a phenyl, cyclohexane, *t*-butyl or *n*-butyl and extend the four groups by **a** - **d**. The structural formula of the two references and the composition and identification of the twelve kinked bisamides is shown in **Figure 4.2**.

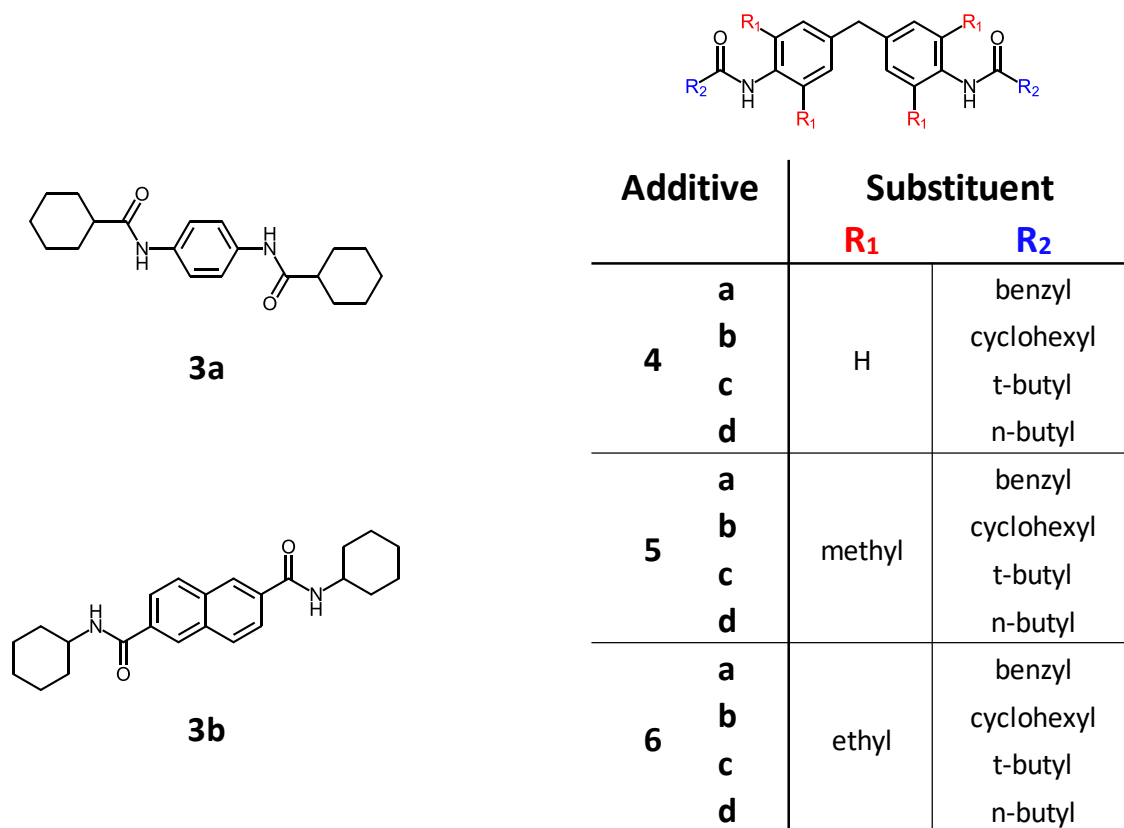


**Figure 4.2:** Chemical structure of N,N'-1,4-Phenylenebis[cyclohexanecarboxamide] – **3a**, N,N'-dicyclohexyl-2,6-naphthalene dicarboxamide - **3b** and the composition as well as the nomenclature of the twelve kinked bisamides **4a** - **6d**.

#### 4.1.1 Synthesis and characterization

The synthesis of **3a** accomplished by the reaction of 1,4-phenylenediamine with cyclohexanecarbonyl chloride in N-methyl-2-pyrrolidone (NMP) and pyridine. After the product has been precipitated in water and recrystallized from dimethyl formamide (DMF), **3a** can be obtained with high purity and high yields. The reaction scheme can be seen in **Figure 4.3**.

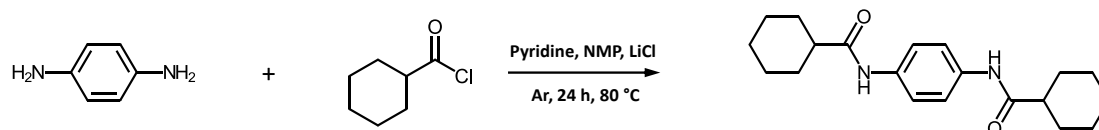


**Figure 4.3:** Reaction scheme of 1,4-phenylenediamine with cyclohexanecarbonyl chloride to N,N'-1,4-Phenylenebis[cyclohexanecarboxamide] - **3a**.

The second reference bisamide **3b** was not directly synthesized as it is commercially available. One possible synthesis route can be via the reaction of dimethyl 2,6-naphthalendicarboxylate with cyclohexylamine in an autoclave.<sup>[193]</sup> The reaction scheme is shown in **Figure 4.4**.

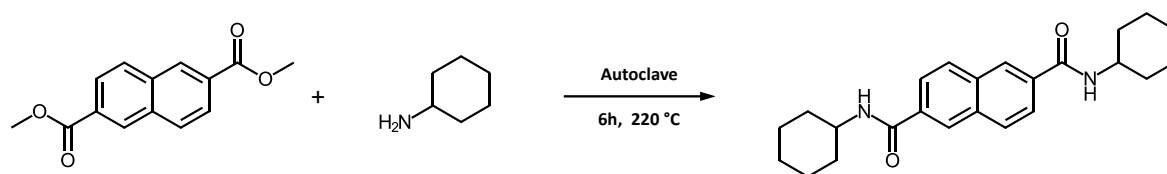


**Figure 4.4:** Reaction scheme of dimethyl 2,6-naphthalendicarboxylate with cyclohexylamine to N,N'-dicyclohexyl-2,6-naphthalene dicarboxamide - **3b**.

The synthesis of the kinked bisamides is achieved by the reaction of the corresponding substituted kinked diamine central unit with the desired acyl chloride. To ensure sufficient solubility of the products THF or NMP was used as solvent and a tertiary amine such as trimethylamine or pyridine was used as hydrogen chloride scavenger. The reaction scheme is shown schematically in **Figure 4.5**.

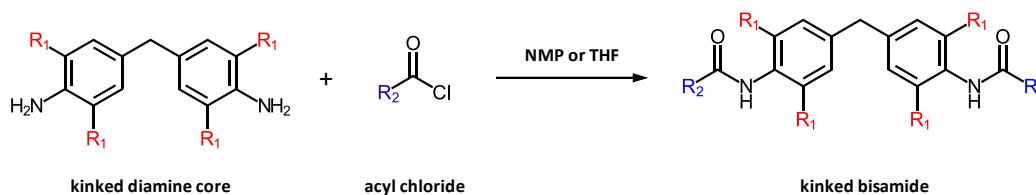


**Figure 4.5:** Basic reaction scheme of the kinked diamine central unit with the corresponding acyl chloride to form the respective kinked bisamide.

In This way, all twelve bisamides can be produced with yields between 56 - 95 % and a high purity. The TGA measurement revealed a tendency for the thermal stability with regard to the structure of the kinked

bisamides. Therefore, the  $T_{-5\text{wt.}\%}$  of each bisamide sorted by the residue  $R_2$  is graphically shown in **Figure 4.6**.

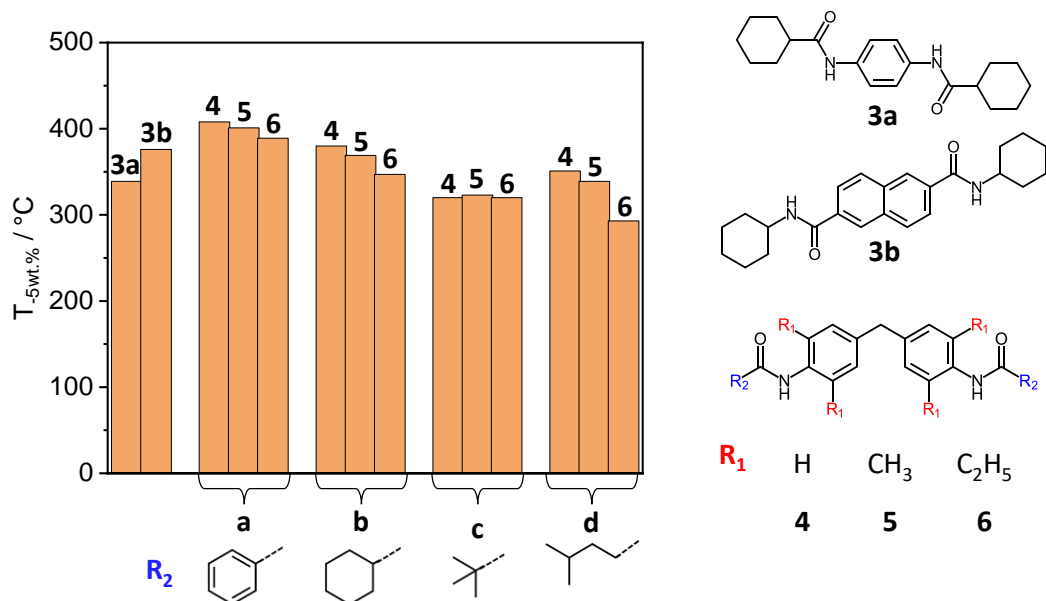


**Figure 4.6:**  $T_{-5\text{wt.}\%}$  of the two reference bisamides as well as all kinked bisamides sorted by the residue  $R_2$  measured by TGA.

The additive **3a** is thermally not as stable as the second reference additive **3b**, but still features a  $T_{-5\text{wt.}\%}$  far above 300 °C which makes them useable in the extrusion process without any considerations.<sup>[191]</sup>

Looking at the kinked bisamides, it is observed that the derivatives of group **4**, without substitution at the center, have a slightly higher temperature stability than the corresponding derivatives of groups **5** and **6**. The reason for this is presumably based on the fact that the substitution leads to a steric hindrance of the hydrogen bonds and thus weakens them. Consequently, this effect increases from methyl to the ethyl substitution, giving the compounds of group **6** the lowest thermal stability compared to their corresponding counterparts. Within the groups it is found that the species with a benzene residue in the periphery have the highest thermal stability. Thus, a weight loss of 5 wt.% of additives **4a** and **5a** only occurs at temperatures above 400 °C. Compounds with a cyclohexane residue come in second place, where the decomposition temperature is about 30 °C lower. The additives with t-butyl residues have the lowest temperature stability in group **4** and **5**, but in group **6** the compound with n-butyl residue has the lowest value with only 293 °C. However, this temperature is still high enough to use this additive in the extrusion process without problems. A detailed description of the synthesis and further characterization by  $^1\text{H}$  NMR, MS and IR can be found at 5.4.2 in the experimental part.

### 4.1.2 Self-assembly behavior

Analogous to the BTAs used, all bisamides were tested for their self-assembly behavior. The SEM images of the two references are shown in **Figure 4.7**.

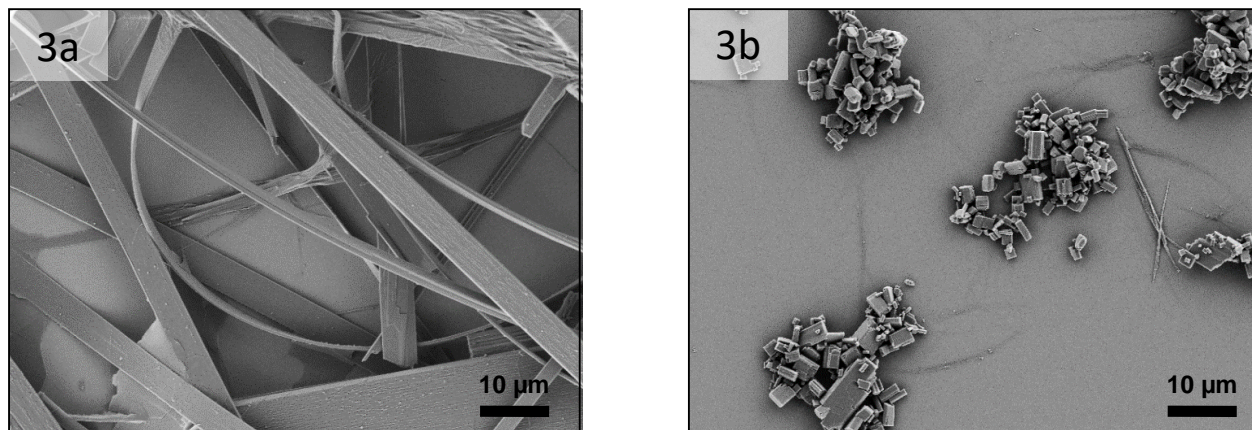


**Figure 4.7:** SEM micrographs of 500 ppm additive **3a** and **3b** self-assembled upon cooling in xylene.

The bisamide **3a** is crystallizing from the xylene solution in a ribbon-like structure. The width of the ribbons varies in a very wide range between 1500 nm and over 5000 nm. However, the width within a band remains constant over the object. The commercial bisamide **3b** is not completely soluble in the xylene solution even at a concentration of just 500 ppm. Nevertheless, the dispersion was investigated in the same way as the other substances. It is observed that **3b** forms highly aggregated 3-dimensional small building blocks. These aggregated clusters are distributed with different sizes over the whole sample.

Subsequently, the kinked bisamides will be characterized for their self-assembly behavior. For this purpose, they will first be analyzed in groups and then structural property relationships will be determined for all kinked bisamides. **Figure 4.8** shows SEM images of the four representatives of the first group, **Figure 4.9** shows the second group and **Figure 4.10** the third group.

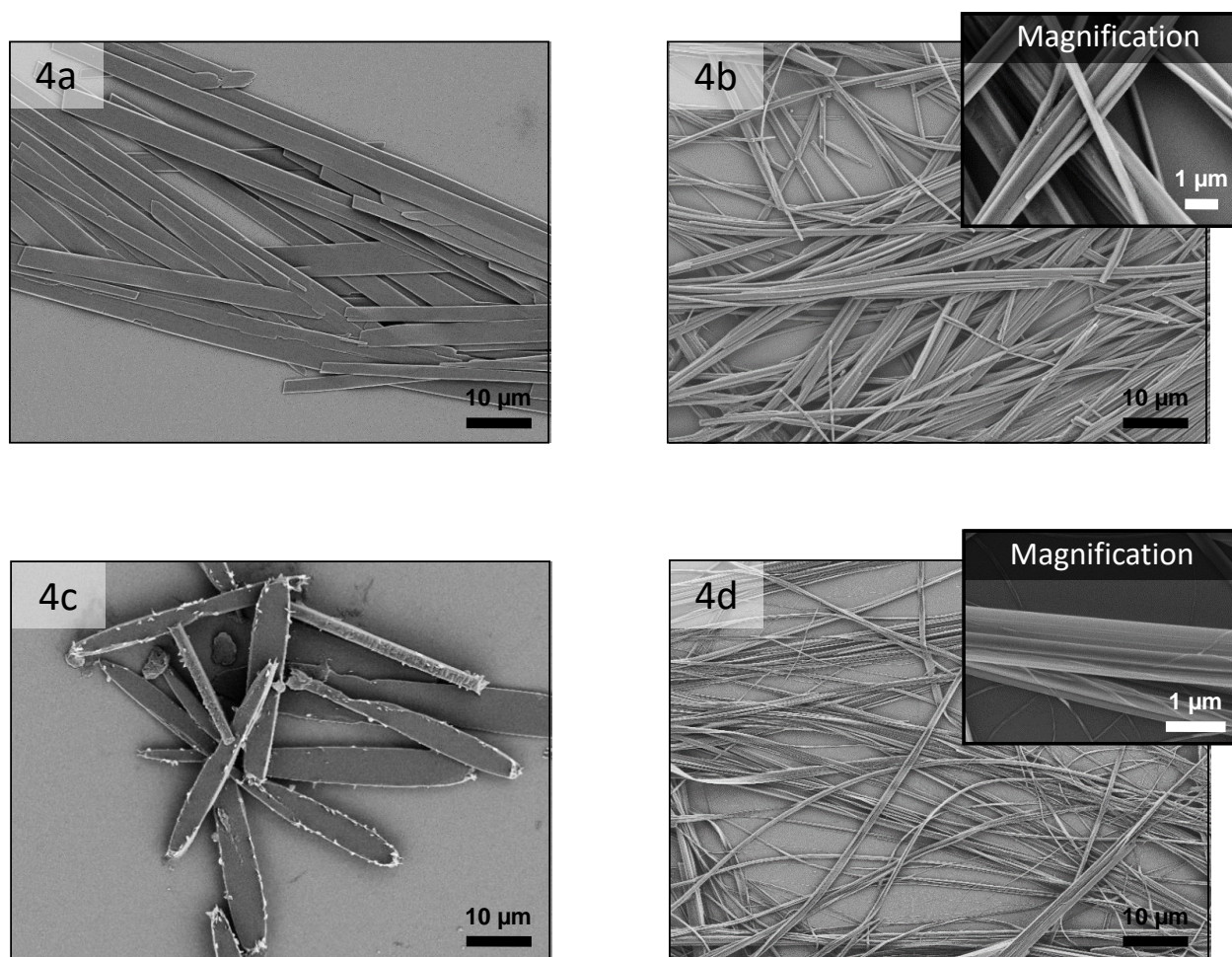


**Figure 4.8:** SEM micrographs of 500 ppm additive **4a** – **4d** self-assembled upon cooling in xylene. If necessary, another SEM micrograph of the corresponding additive with higher or lower magnification is provided.

Additive **4a** forms a clearly visible ribbon-like structure. The width of the bands varies between 800 and 3800 nm, whereby it always remains the same within the band, similar to **3a**. Another noticeable feature is the completely straight linearity of the objects. Additive **4b** crystallizes in the form of fibers with widths of 200 to 1300 nm. It is observed that the larger fibers are formed by several smaller ones, as indicated by the additional SEM micrograph at higher magnification. Therefore, the actual average fiber diameter is expected to be smaller. The additive **4c** forms a platelet shaped geometry during its self-assembly process. These objects have a width between 2000 nm up to 5000 nm and are on average 20 to 30  $\mu\text{m}$  long. The appearance of additive **4d** in the recorded SEM micrographs is similar to that of **4b** with widths between 200 to 1500 nm. At very high magnification, it can also be seen that there are even smaller fibers on top of the surface of the fibers and the silicon wafer.<sup>[191]</sup>

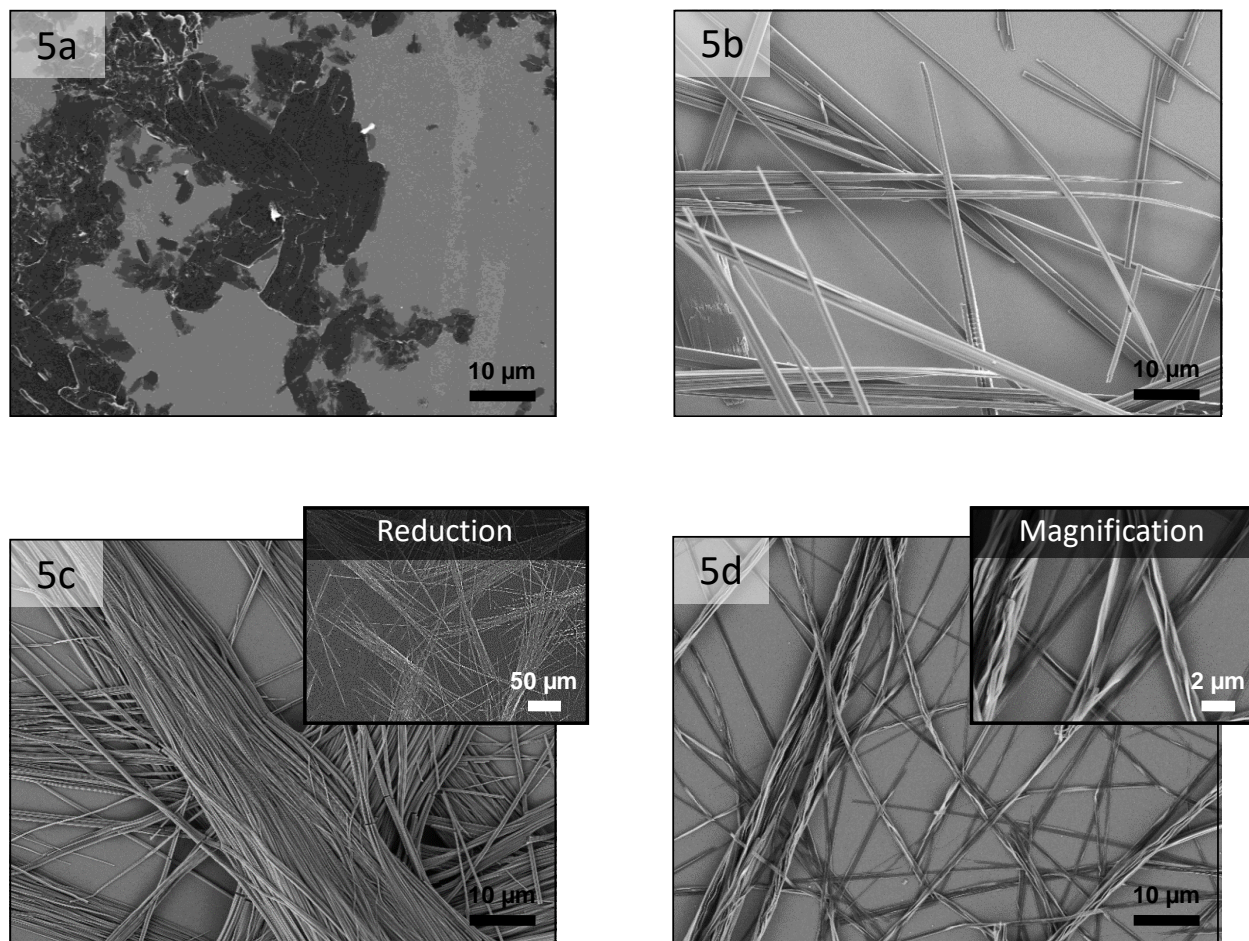


**Figure 4.9:** SEM micrographs of 500 ppm additive **5a** – **5d** self-assembled upon cooling in xylene. If necessary, another SEM micrograph of the corresponding additive with higher or lower magnification is provided.

Upon cooling, bisamide **5a** forms micrometer-sized less-defined plate-like structures. The objects of crystallized additive **5b** have a fibrous structure, although there are some larger objects that are more like ribbons. Many of the objects have an average size of 500 nm. However, there are also some supramolecular objects with a width of more than 4500 nm. The compound **5c** forms very fine fibers with diameters between 200 and 1500 nm. These fibers are strongly bundled together, which gives them a certain platelet character as shown in the extra SEM micrograph with a lower magnification. Additive **5d** also forms thin fibers within a range of 300 to 1600 nm. Certainly, these have a special feature compared to the fiber-like structures discussed so far, because they do not have a smooth and even surface, but a highly corrugated shape. The surface is shown in the additional picture with a higher magnification.<sup>[191]</sup>

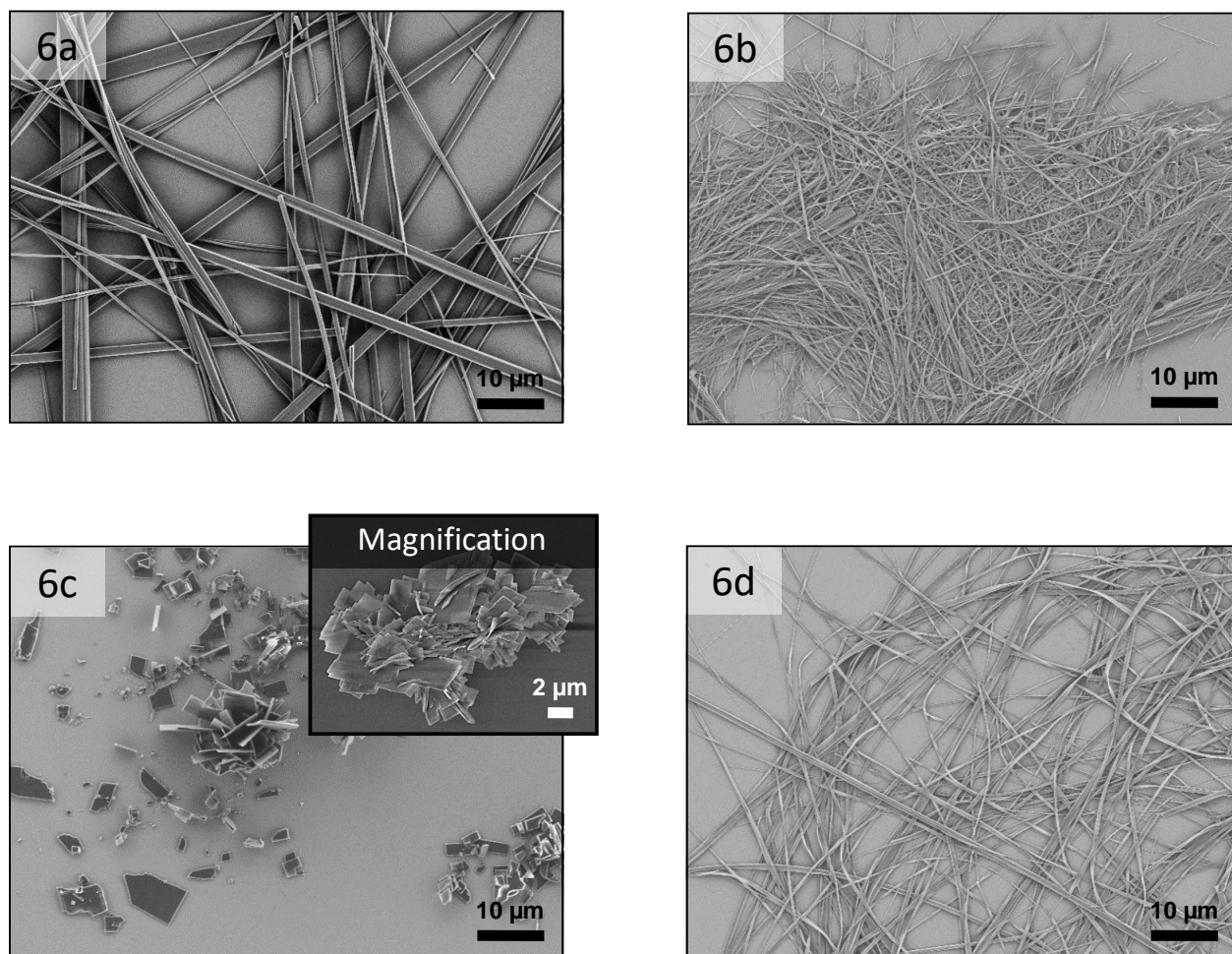


**Figure 4.10:** SEM micrographs of 500 ppm additive **6a** – **6d** self-assembled upon cooling in xylene. If necessary, another SEM micrograph of the corresponding additive with higher or lower magnification is provided.

The objects of additive **6a** show similar ribbon-like structures as those of **4a**, although they have a significantly smaller width and are not subject to strong fluctuations. Thus, the objects are in the range of 300 to 3800 nm. The kinked bisamide **6b** forms fibers with diameters between 100 and 600 nm. Additive **6c** forms platelets with a very low aspect ratio which reach sizes of up to 10  $\mu\text{m}$  in length and width. Most of these platelets are agglomerated and form a rose flower-like superstructure like **5a**. The last bisamide **6d** forms fibers similar to **6b**. The structures range from 100 to 1000 nm.<sup>[191]</sup>

From these observations, structure-property relationships of the kinked bisamides will be determined. It seems that the substitution at the central unit of the bisamides by  $R_1$  has no noticeable influence on the self-assembly behavior of the additives, because in all three groups there are different manifestations of the crystallized objects. Also, the dimensions of these are not related to the change at the central unit.

This is different with the influence of the peripheral residue  $R_2$ . By varying it, it is possible to influence the crystallization behavior in a certain way. The introduction of a benzene group leads to the formation of a ribbon-like or platelet-like structure. If this is exchanged by a *t*-butyl group, preferably platelet-like structures are formed. If the residue is cyclohexane or *n*-butane, the self-assembly process mainly produces fibers. However, no statements can be made about the diameter of the fibers.

#### 4.1.3 Solubility in polystyrene

The haze value was also measured from the bisamide containing injection-molded specimens. The results are shown in **Figure 4.11**.

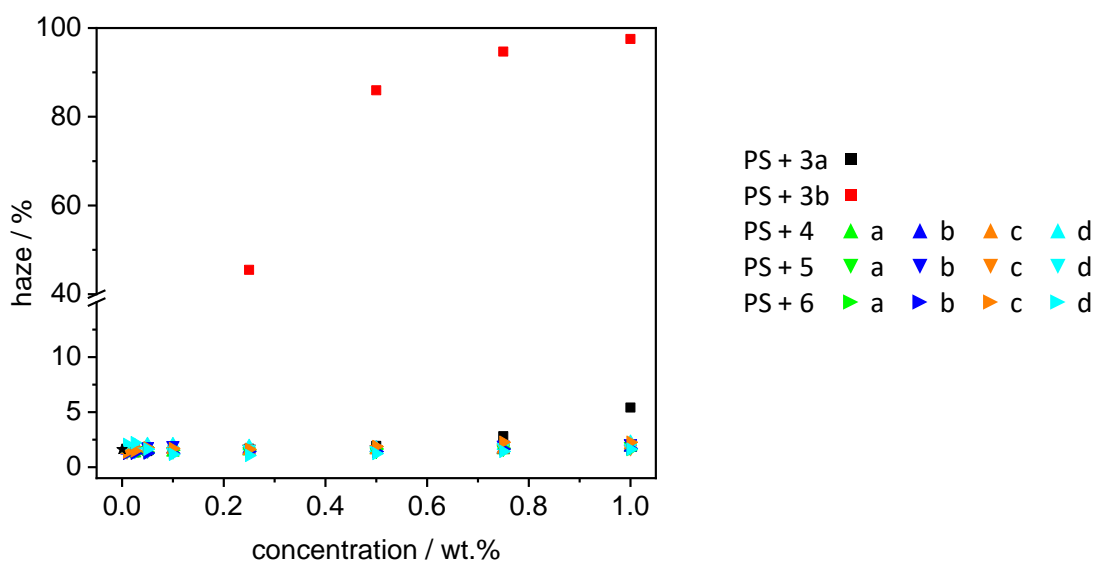


**Figure 4.11:** Haze values of the injection molded specimen in dependence of various concentrations of **3a** and **3b**; **4a - 4d**; **5a - 5d** and **6a - 6d** in polystyrene. The black star represents the haze value of neat PS.

The bisamide **3a** shows a slightly increased haze value from a concentration of 0.75 wt.% up to 5.4 % at a concentration of 1.0 wt.%. The commercial additive **3b** starts to have a strong turbidity effect on the sample even at a concentration of 0.25 wt.%. By further increasing the concentration, this becomes even more pronounced with the haze reaching a value of 97 % at the highest concentration. Analogous to additive **1**, this is an indication that the two additives cannot be dissolved in larger quantities in the polystyrene matrix and are therefore present in aggregates which result in clouding of the sample. For this reason, a homogeneous dispersion of the additives is no longer guaranteed, which can have a negative effect on the foam nucleating effect.

## Foaming polystyrene with bisamides

---

The situation is different with the kinked bisamides. For all substances used, the haze value of the test specimens does not change even at the highest concentrations. This means that there are no large objects or aggregates capable of scattering light in the sample. This suggests a significantly better solubility of the kinked bisamides compared to the other two bisamides **3a** and **3b**.

It should be noted that the small fluctuations of haze above and below the value of pure polystyrene are caused by streaks in the sample or other small defects on the surface.

## 4.2 Batch foaming

Similar to the benzene trisamides, the selected bisamides will in this section be investigated for their effectiveness as additives for foam nucleation. For this purpose, first the two references will be described in more detail, followed by the novel class of the kinked bisamides. The foam sample preparation was done with the exact same procedure as described in 3.2.

### 4.2.1 Foaming with the reference bisamides

The analysis of the generated foams containing additive **3a** is summarized in **Figure 4.12**.

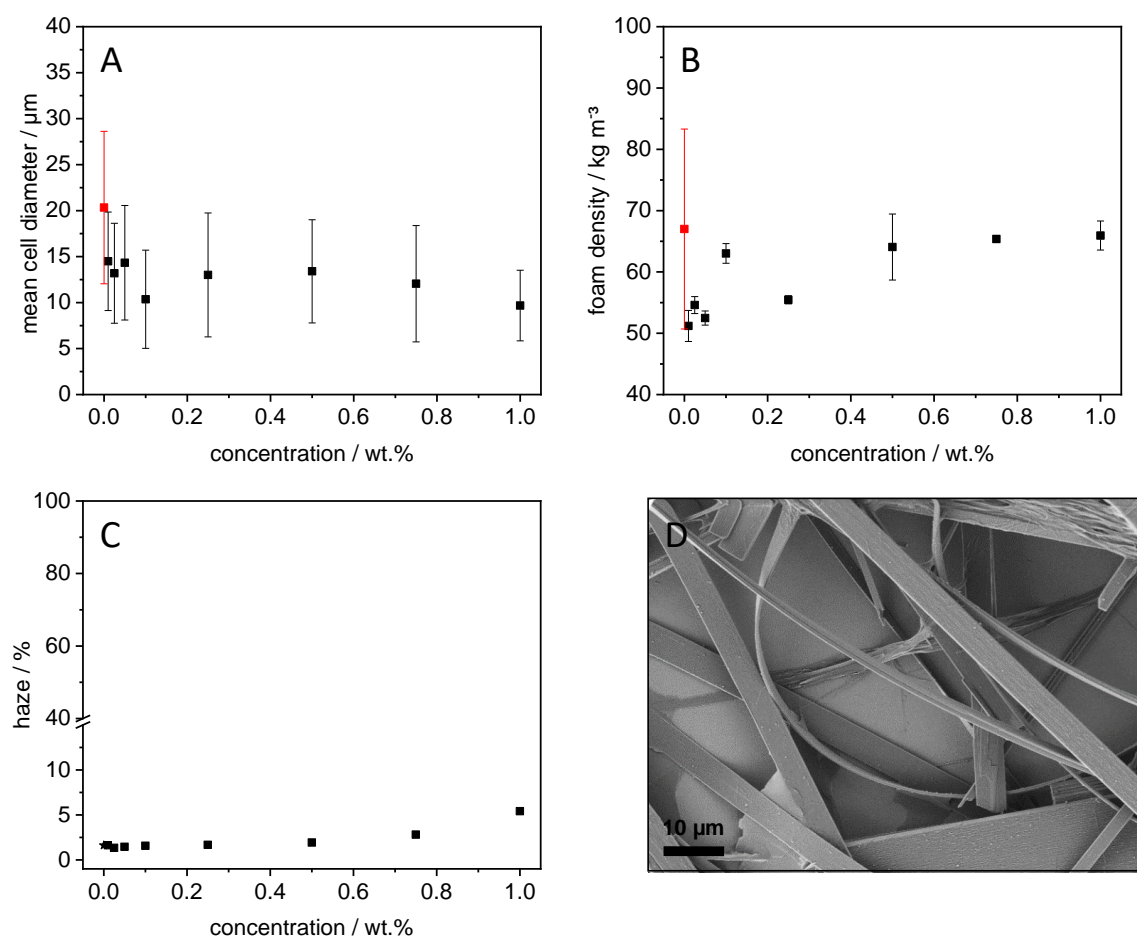


**Figure 4.12:** **A:** Mean cell diameter of the foams with different concentrations of **3a**. The red square represents the mean value of neat PS. **B:** Density of the foams with different concentrations of **3a**. The red square indicates the mean value of neat PS. **C:** Haze values of the specimen used for the foaming. The black star represents the haze value of neat PS. **D:** SEM micrograph of 500 ppm **3a** self-assembled upon cooling in xylene.

The reference additive **3a** shows a relatively low solubility in the polystyrene matrix which is expressed by the formation of inhomogeneous foam structures above a concentration of 0.1 wt.% (see **Figure 6.4**). The solubility limit is therefore lower than expected due to the increase in haze values at concentrations of

0.5 wt.% and above. The reason for the unchanged haze values at the corresponding concentrations can probably be explained by the size of the supramolecular objects. Despite the insolubility, the remaining aggregates are not of a sufficient size to scatter the light and thus increase the haze. In the concentration range from 0.01 to 0.05 wt.% homogenous foams are generated. However, the reduction of the cell size and thus the nucleating effect of this additive is rather weak. The smallest determined average cell size is  $13.2 \pm 5.4 \mu\text{m}$  at a concentration of 0.025 wt.%. The inferior nucleating effect is presumably due to the ribbon-like structure of the self-assembled objects of this supramolecular additive. These have a significantly lower surface-to-volume ratio and thus offer a greatly reduced number of possible nucleation nuclei for the same amount of additive. The densities of the foams are below the value for pure polystyrene for all used concentrations. Moreover, except for the foam containing 0.5 wt.%, these have a relatively low variance.

The results of the second reference bisamide **3b** are shown in **Figure 4.13**.

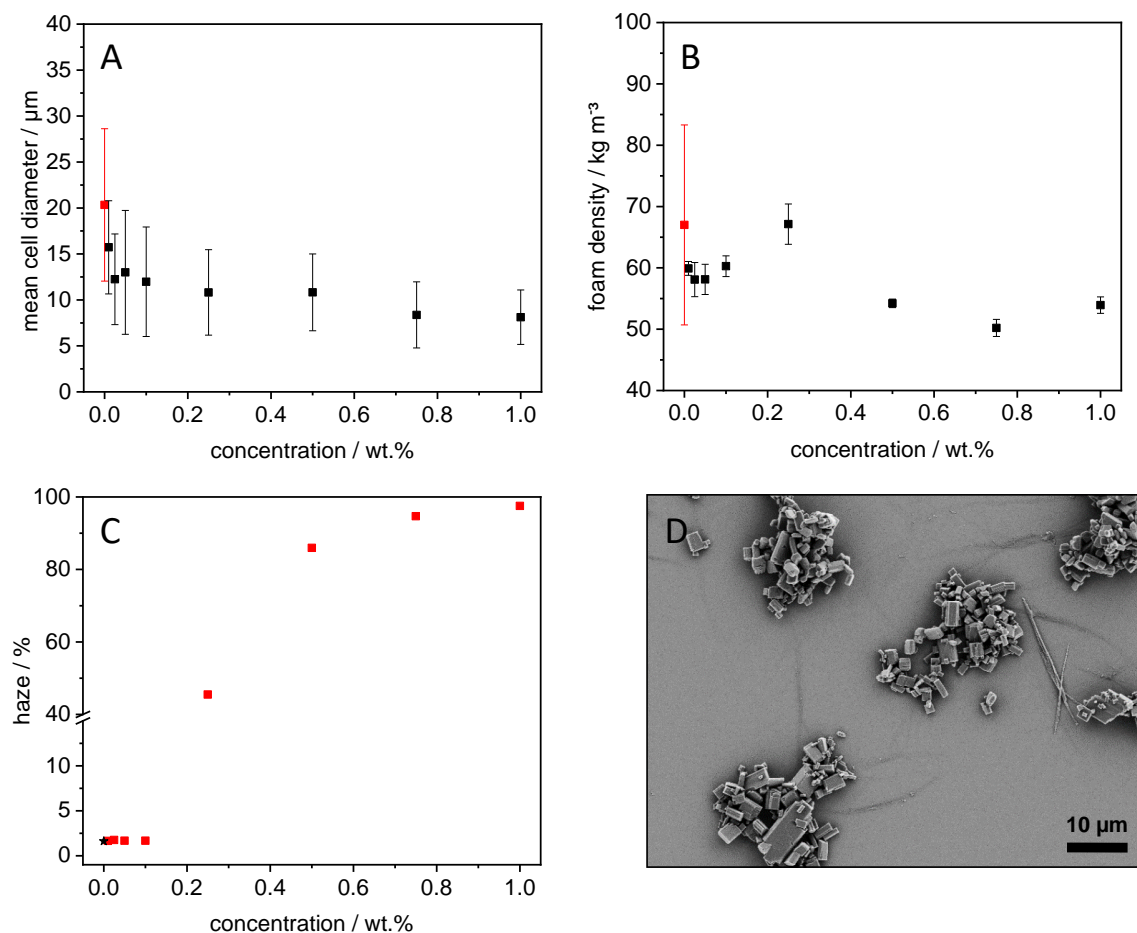


**Figure 4.13:** **A:** Mean cell diameter of the foams with different concentrations of **3b**. The red square represents the mean value of neat PS. **B:** Density of the foams with different concentrations of **3b**. The red square indicates the mean value of neat PS. **C:** Haze values of the specimen used for the foaming. The black star represents the haze value of neat PS. **D:** SEM micrograph of 500 ppm **3b** self-assembled upon cooling in xylene.

Even in the case of **3b**, an inhomogeneous cell distribution is formed at a concentration above 0.25 wt.% (see **Figure 6.5**) and is thus in exact accordance with the solubility limit of this bisamide in the polystyrene matrix based on the increased haze values. At lower concentrations, the foam nucleating effect is similarly weak as for the reference additive **3a**. The smallest mean cell size was determined to be  $12.0 \pm 6.0 \mu\text{m}$  for foams with a concentration of 0.1 wt.%. Again, the low nucleating effect is probably related to the geometry of the crystallized supramolecular objects. The three-dimensional building blocks that are formed have a small surface-to-volume ratio, so that only a relatively small number of nuclei are available. This number of nuclei cannot be further increased by increasing the concentration due to the limited solubility of the additive in the polystyrene melt. In addition, the building blocks are most likely highly

aggregated, which also limits the nucleating effect. The densities of the foams are all, with one exception, in a range between 50 and 60 kg m<sup>-3</sup> and thus below the density for pure polystyrene foams. The measured values also show a small standard deviation, which suggests that the foams could be foamed evenly.

### 4.2.2 Foaming with the kinked bisamides without a substitution at the central unit

These two reference bisamides are now compared with the twelve representatives of the novel class of the kinked bisamides. The evaluation and discussion of the results will be shown first individually and then in the groups determined by the substitution at the nucleus. Finally, all data will be summarized, discussed, and evaluated across the groups.

The kinked bisamide without substitution of the central unit and with a benzyl residue in the periphery is the first one to be discussed. The results are shown in **Figure 4.14**.

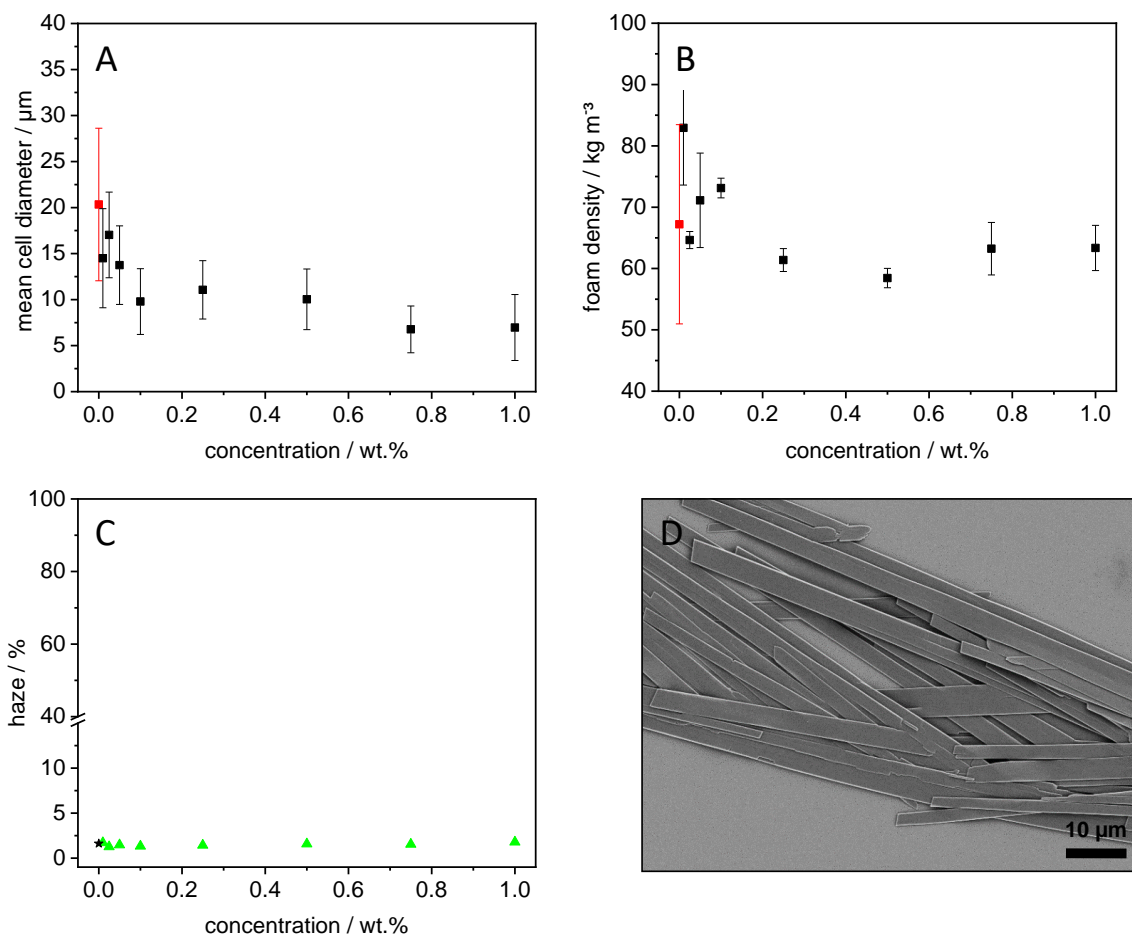


**Figure 4.14:** **A:** Mean cell diameter of the foams with different concentrations of **4a**. The red square represents the mean value of neat PS. **B:** Density of the foams with different concentrations of **4a**. The red square indicates the mean value of neat PS. **C:** Haze values of the specimen used for the foaming. The black star represents the haze value of neat PS. **D:** SEM micrograph of 500 ppm **4a** self-assembled upon cooling in xylene.

This additive has a better solubility in the polymer melt compared to the two references, as an inhomogeneous morphology is only formed at concentrations higher than 0.75 wt.% (see **Figure 6.6**) even though the test samples do not show any increase in the haze value at these high concentrations. The smallest cells with a homogenous distribution were obtained at a concentration of 0.1 wt.% with a size of  $9.8 \pm 3.6 \mu\text{m}$ . The moderate foam nucleation is probably also due to the band-like structure of the supramolecular objects. This offers a reduced nuclei amount for the formation of foam bubbles. Nevertheless, a reduction of the average cell size can be seen for the entire concentration range compared to pure polystyrene foams indicating that a sufficient number of nucleating sites is still present. The density

of the foams is subjected to relatively large fluctuations and is sometimes even above the average density for pure PS. Especially at higher concentrations, however, the foam density tends to remain constant.

The obtained results of the bisamide with cyclohexyl residue in the group with unsubstituted central unit are summarized in **Figure 4.15**.

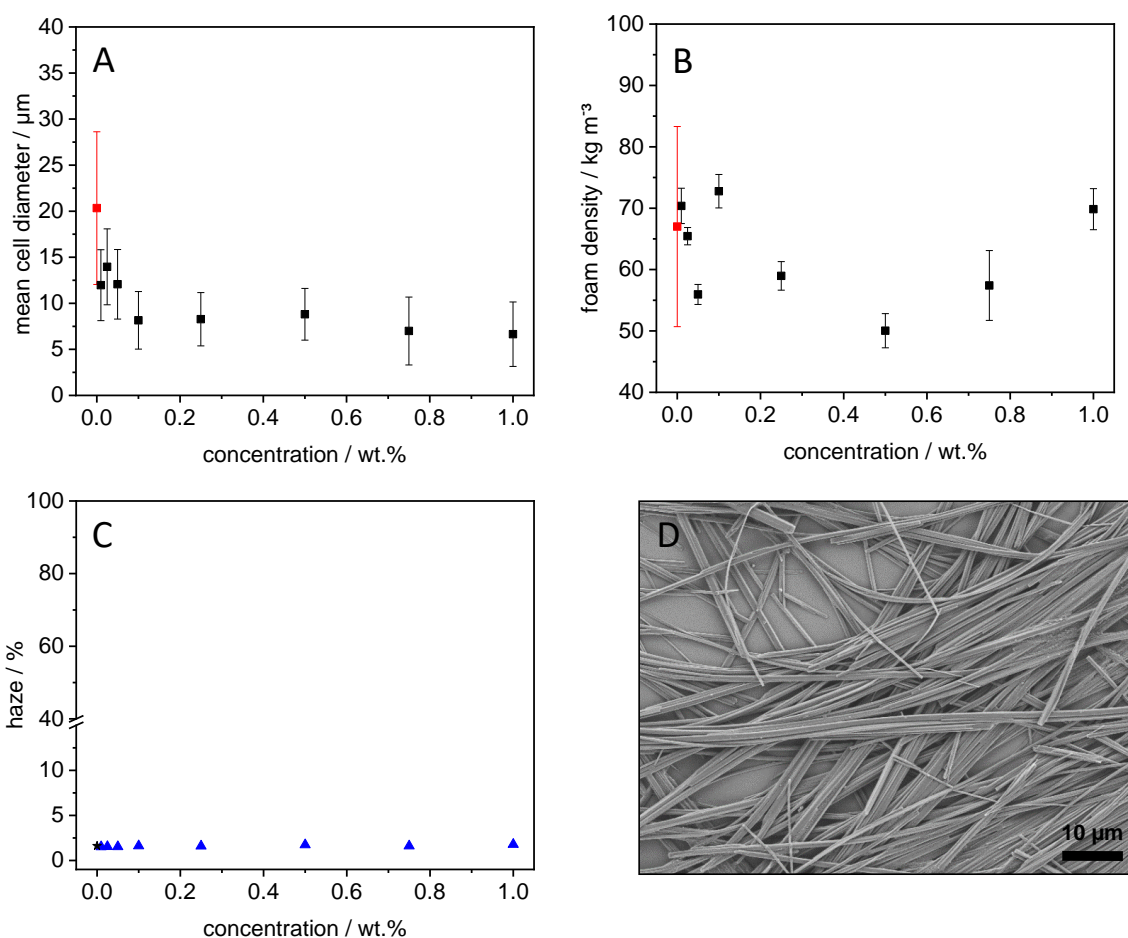


**Figure 4.15:** **A:** Mean cell diameter of the foams with different concentrations of **4b**. The red square represents the mean value of neat PS. **B:** Density of the foams with different concentrations of **4b**. The red square indicates the mean value of neat PS. **C:** Haze values of the specimen used for the foaming. The black star represents the haze value of neat PS. **D:** SEM micrograph of 500 ppm **4b** self-assembled upon cooling in xylene.

As with the previous additive, an inhomogeneous cell distribution is formed starting at a concentration of 0.75 wt.% (see **Figure 6.7**). As with all kinked bisamides, injection molded specimens still show no increase in haze even at the highest concentrations. In the homogenous range, the smallest calculated mean cell diameter has a size of  $8.1 \pm 3.1 \mu\text{m}$  at a concentration of 0.1 wt.%. Because the additive forms relatively fine fibers during crystallization, a large number of potential nuclei are available which can nucleate the foam bubbles. The densities of the foams with different concentrations shows a large fluctuation and there

is no recognizable system underlying it. Nevertheless, most of them are below the density of the pure polystyrene foam.

The next bisamide in this series is the one with a *t*-butyl residue at the amide function. The corresponding illustrations are shown in **Figure 4.16**.

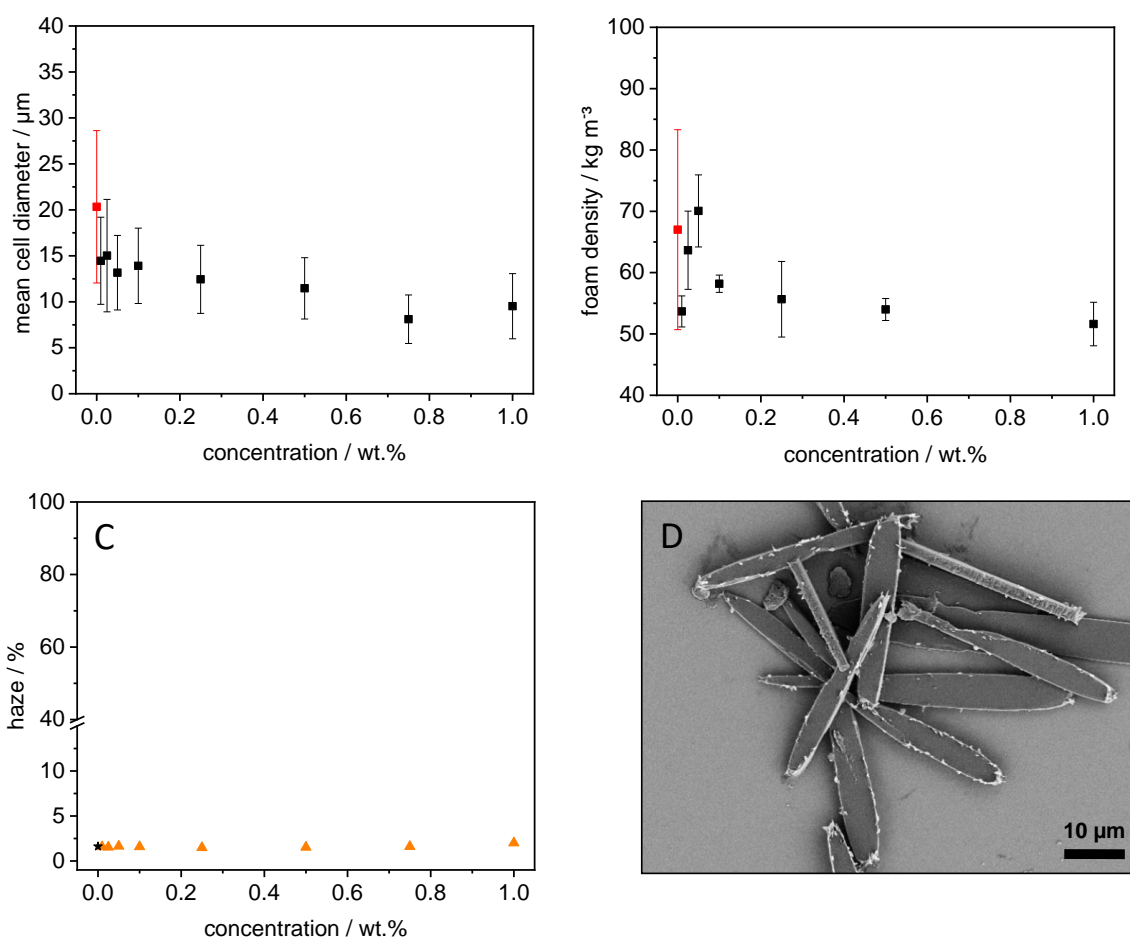


**Figure 4.16:** **A:** Mean cell diameter of the foams with different concentrations of **4c**. The red square represents the mean value of neat PS. **B:** Density of the foams with different concentrations of **4c**. The red square indicates the mean value of neat PS. **C:** Haze values of the specimen used for the foaming. The black star represents the haze value of neat PS. **D:** SEM micrograph of 500 ppm **4c** self-assembled upon cooling in xylene.

Additive **4c** is the first bisamide which generates homogenous foams over the entire concentration range (see **Figure 6.8**). Due to the *t*-butyl group, the molecule is very well soluble in the polystyrene melt, even with an unsubstituted central unit, and can thus be homogeneously distributed even at 1.0 wt.%. The foam nucleating effect of this additive is rather weak, especially at low concentrations. The reason is probably the platelet-like structure of the self-assembled objects, which can only provide a small surface area for the bubble nucleation. However, because large quantities of the additive can be dissolved, it is still possible

to reduce the cell size to  $8.1 \pm 2.6 \mu\text{m}$  with a concentration of 0.75 wt.%. With one exception, the densities of the foams are all below the red line. Here, too, there is a trend towards greater density reduction, especially in foams with higher additive concentrations.

Bisamide **4d** has an *n*-butyl residue in the periphery and is the last member of the first group. The characterization of the foams and the other relevant data are shown in **Figure 4.17**.

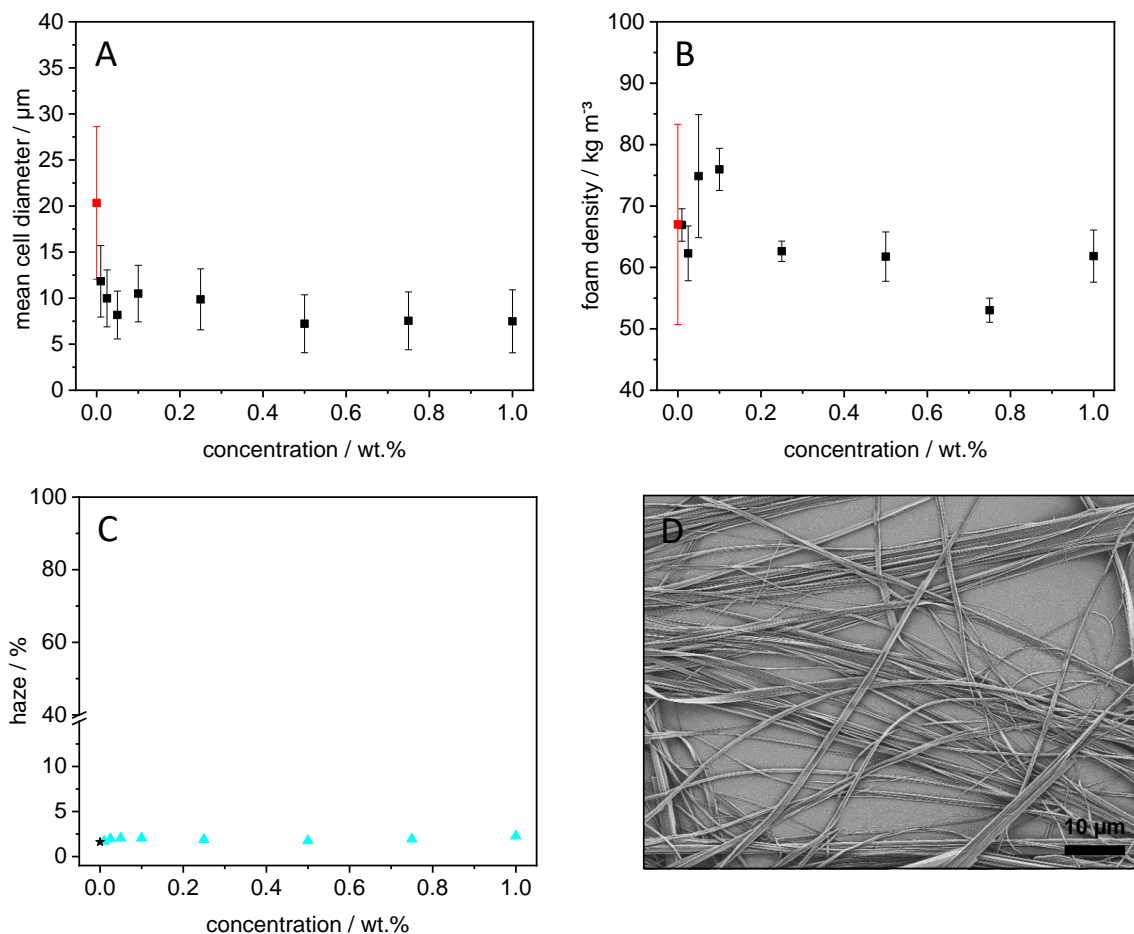


**Figure 4.17:** **A:** Mean cell diameter of the foams with different concentrations of **4d**. The red square represents the mean value of neat PS. **B:** Density of the foams with different concentrations of **4d**. The red square indicates the mean value of neat PS. **C:** Haze values of the specimen used for the foaming. The black star represents the haze value of neat PS. **D:** SEM micrograph of 500 ppm **4d** self-assembled upon cooling in xylene.

The kinked bisamide **4d** shows an inhomogeneous cell distribution already at a concentration of 0.5 wt.% (see **Figure 6.9**) and is therefore quite insoluble in comparison. As this compound forms a relatively fine fiber network during the self-assembly process, the foam nucleating effect is relatively good even at lower concentrations. Thus, the average cell size can be reduced to  $8.1 \pm 2.6 \mu\text{m}$  at a concentration of only

0.05 wt.%. The measured densities of the foams are relatively close to the ones of pure PS. Especially the foams with higher concentration show a higher density reduction and are more homogeneous.

#### 4.2.3 Foaming with the kinked bisamides with the methyl substitution at the central unit

In group **5**, both benzene rings of the central unit were substituted with a methyl group at position 2 and 6. The variation of the groups in the periphery remains unchanged analogous to the previous group.

The results of the first additive **5a** are summarized in **Figure 4.18**.

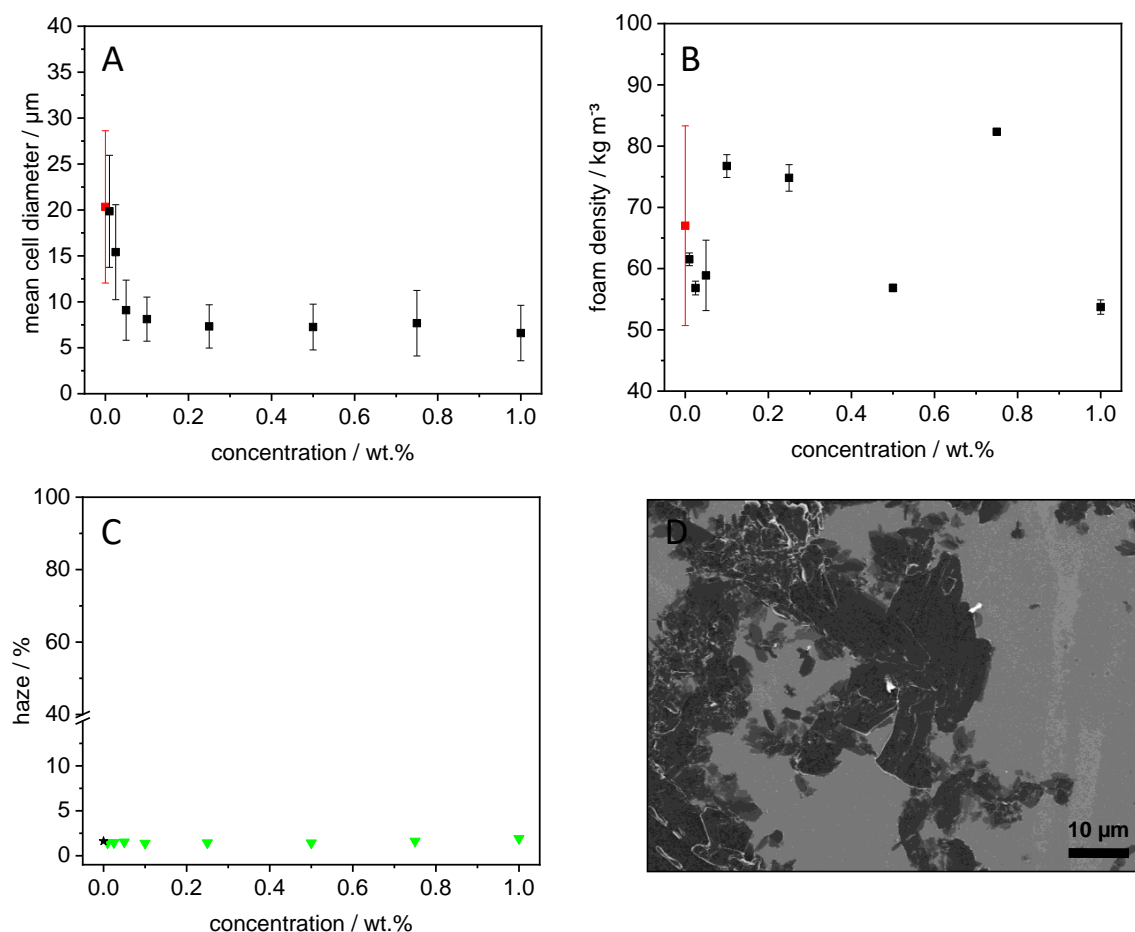


**Figure 4.18:** **A:** Mean cell diameter of the foams with different concentrations of **5a**. The red square represents the mean value of neat PS. **B:** Density of the foams with different concentrations of **5a**. The red square indicates the mean value of neat PS. **C:** Haze values of the specimen used for the foaming. The black star represents the haze value of neat PS. **D:** SEM micrograph of 500 ppm **5a** self-assembled upon cooling in xylene.

Like its representative from group **4**, additive **5a** forms an inhomogeneous cell distribution at a concentration of 0.75 wt.% and above (see **Figure 6.10**). Although these additive forms platelets during crystallization, it still has a good foam nucleating effect, contrary to expectations. For example, at a

concentration of 0.5 wt.%, the cells can be reduced in size down to  $7.3 \pm 2.5 \mu\text{m}$ . It is possible that a different morphology is formed in the polystyrene matrix or that a relatively large number of possible nucleation sites are formed between the crossing points due to the aggregation of the additive. The density of the foams fluctuates very strongly above and below the red line, whereby no pattern can be detected.

**Figure 4.19** shows the results of the next additive **5b**.

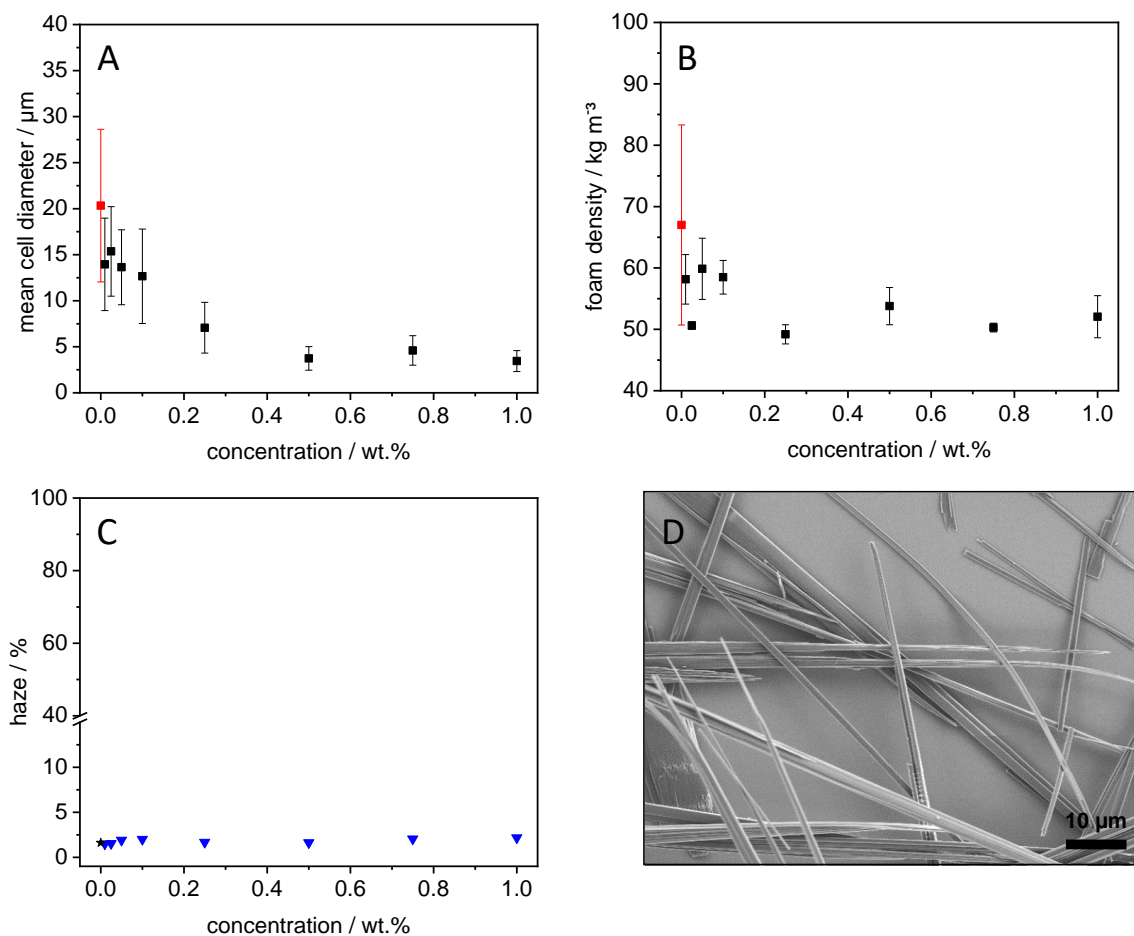


**Figure 4.19:** **A:** Mean cell diameter of the foams with different concentrations of **5b**. The red square represents the mean value of neat PS. **B:** Density of the foams with different concentrations of **5b**. The red square indicates the mean value of neat PS. **C:** Haze values of the specimen used for the foaming. The black star represents the haze value of neat PS. **D:** SEM micrograph of 500 ppm **5b** self-assembled upon cooling in xylene.

In contrast to additive **4b**, this kinked bisamide is now soluble over the entire investigated concentration range, resulting in the formation of foams with a homogeneous cell morphology throughout (see **Figure 6.11**). The foam nucleating effect is particularly noticeable at lower additive concentrations. However, due to the good solubility, higher concentrations can be used, which is associated with an

enormous cell size reduction. With an addition of 1.0 wt.% **5b** it is therefore possible to reduce the size of the cells by a factor of almost 6 to a value of  $3.5 \pm 1.1 \mu\text{m}$ . If only half of this amount is used, a reduction to  $3.7 \pm 1.3 \mu\text{m}$  is still possible. In addition to the enormous reduction of cell sizes, these foams also have very homogeneous cell distributions, which is evident from the very small standard deviations. Looking at the densities of the generated foams, a significant reduction can be seen for all concentrations used.

**Figure 4.20** shows the results for kinked bisamide **5c** which carries a *t*-butyl group in the periphery.

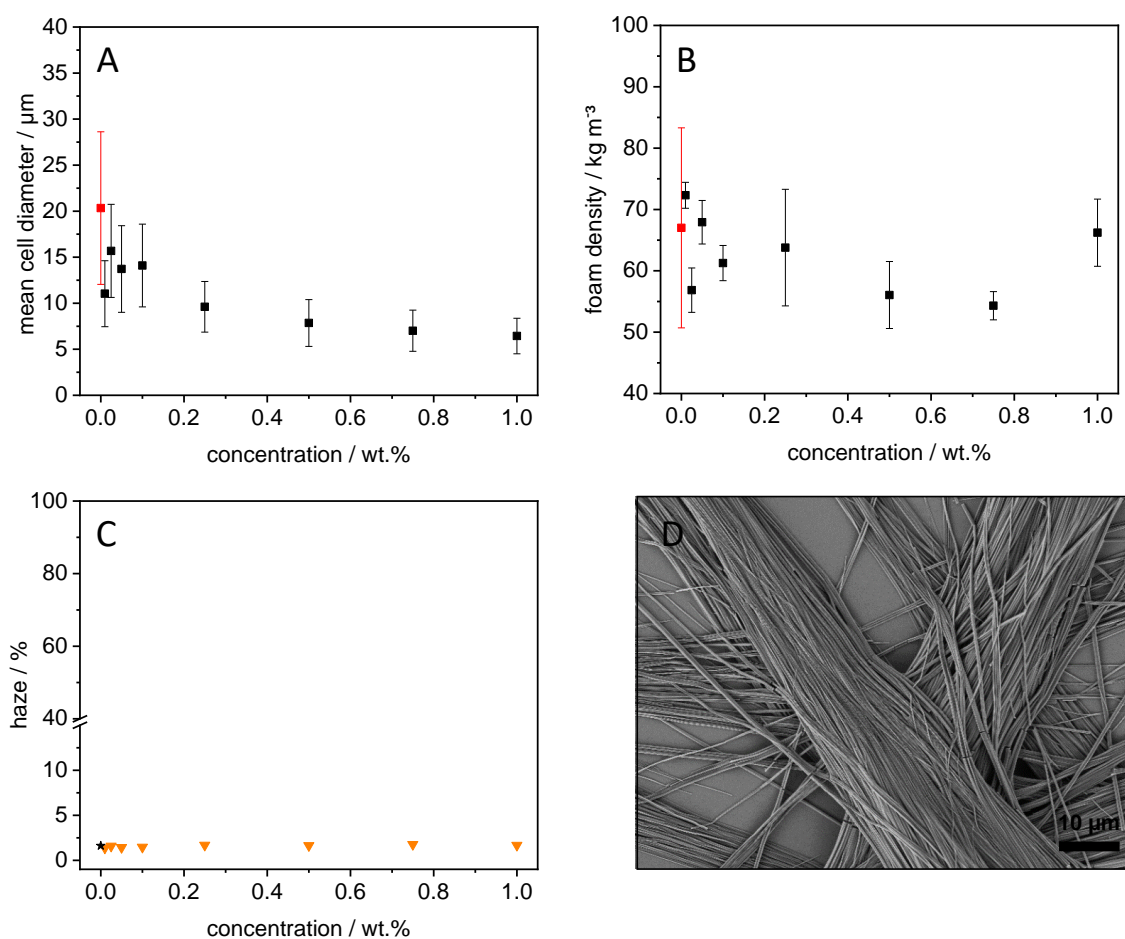


**Figure 4.20:** **A:** Mean cell diameter of the foams with different concentrations of **5c**. The red square represents the mean value of neat PS. **B:** Density of the foams with different concentrations of **5c**. The red square indicates the mean value of neat PS. **C:** Haze values of the specimen used for the foaming. The black star represents the haze value of neat PS. **D:** SEM micrograph of 500 ppm **5c** self-assembled upon cooling in xylene.

Like its corresponding representative from group **4**, this additive possesses a high solubility in the polystyrene matrix and homogeneous foams can be formed over the entire concentration range (see **Figure 6.12**). The foam nucleating effect is rather weak for low concentrations, which is probably due to the bundled structure of this additive. However, because a large amount of additive can also be used, it is

possible to significantly increase the effect. Thus, cells with an average size of only  $6.4 \pm 1.9 \mu\text{m}$  can be generated. A glance at the density shows that this is in the range of unadditivated foams or even below. A clear trend cannot be found.

The additive with *n*-butyl **5d** is the last additive in this group and the results are summarized in **Figure 4.21**.

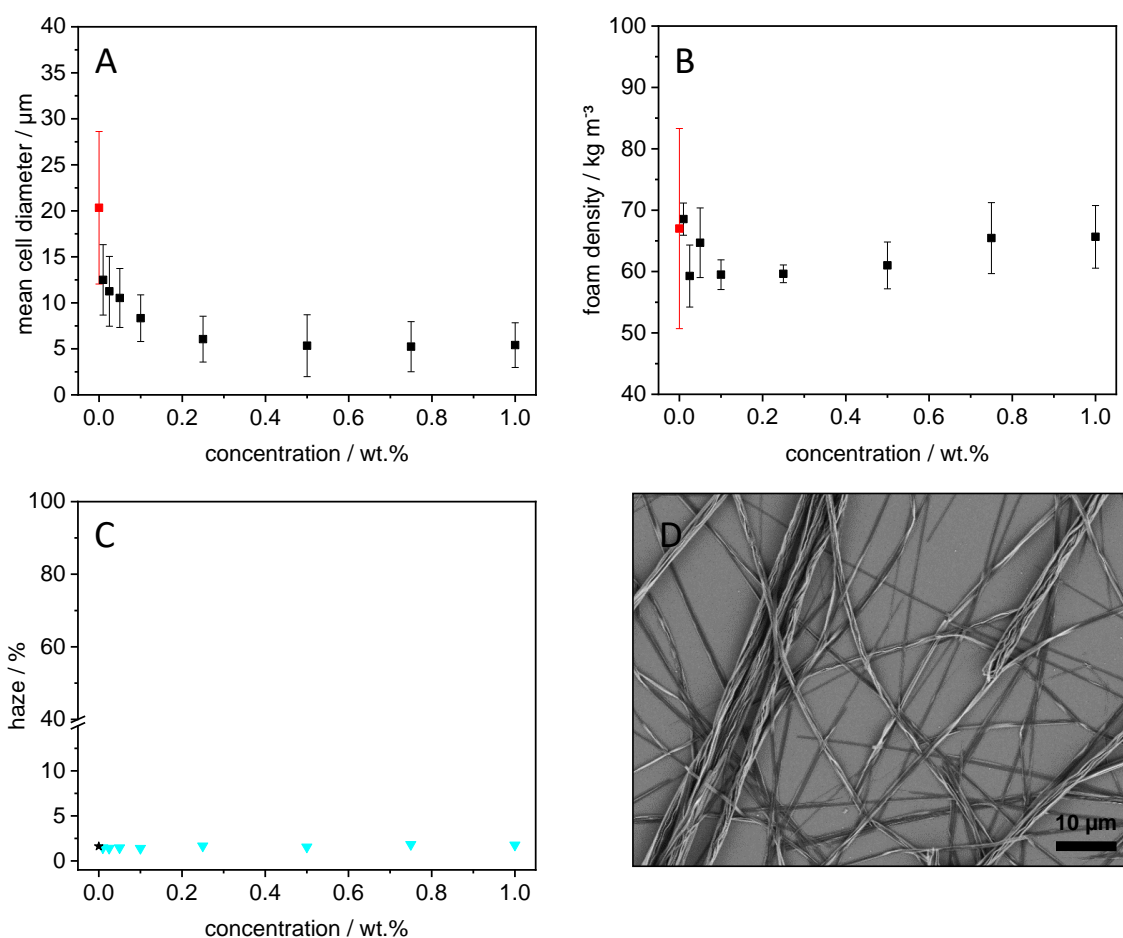


**Figure 4.21:** **A:** Mean cell diameter of the foams with different concentrations of **5d**. The red square represents the mean value of neat PS. **B:** Density of the foams with different concentrations of **5d**. The red square indicates the mean value of neat PS. **C:** Haze values of the specimen used for the foaming. The black star represents the haze value of neat PS. **D:** SEM micrograph of 500 ppm **5d** self-assembled upon cooling in xylene.

Like its corresponding analogue in group **4**, additive **5d** forms an inhomogeneous cell morphology above a concentration of 0.5 wt.% (see **Figure 6.13**). The bisamide **5d** with its supramolecular fibers has a good foam nucleating effect. Thus, with a concentration of only 0.25 wt.% it is possible to reduce the cell sizes down to  $6.1 \pm 2.5 \mu\text{m}$ . Further remarkable are the relatively small deviations in cell size, which is an indication for the homogeneity of the foams. The density reduction in comparison to pure polystyrene is relatively low with this additive.

#### 4.2.4 Foaming with the kinked bisamides with the ethyl substitution at the central unit

The final group consists of the bisamides which carry four ethyl groups at their central unit. The variation of  $R_2$  remains unchanged.

The results of the first additive of group 6 are shown in **Figure 4.22**.

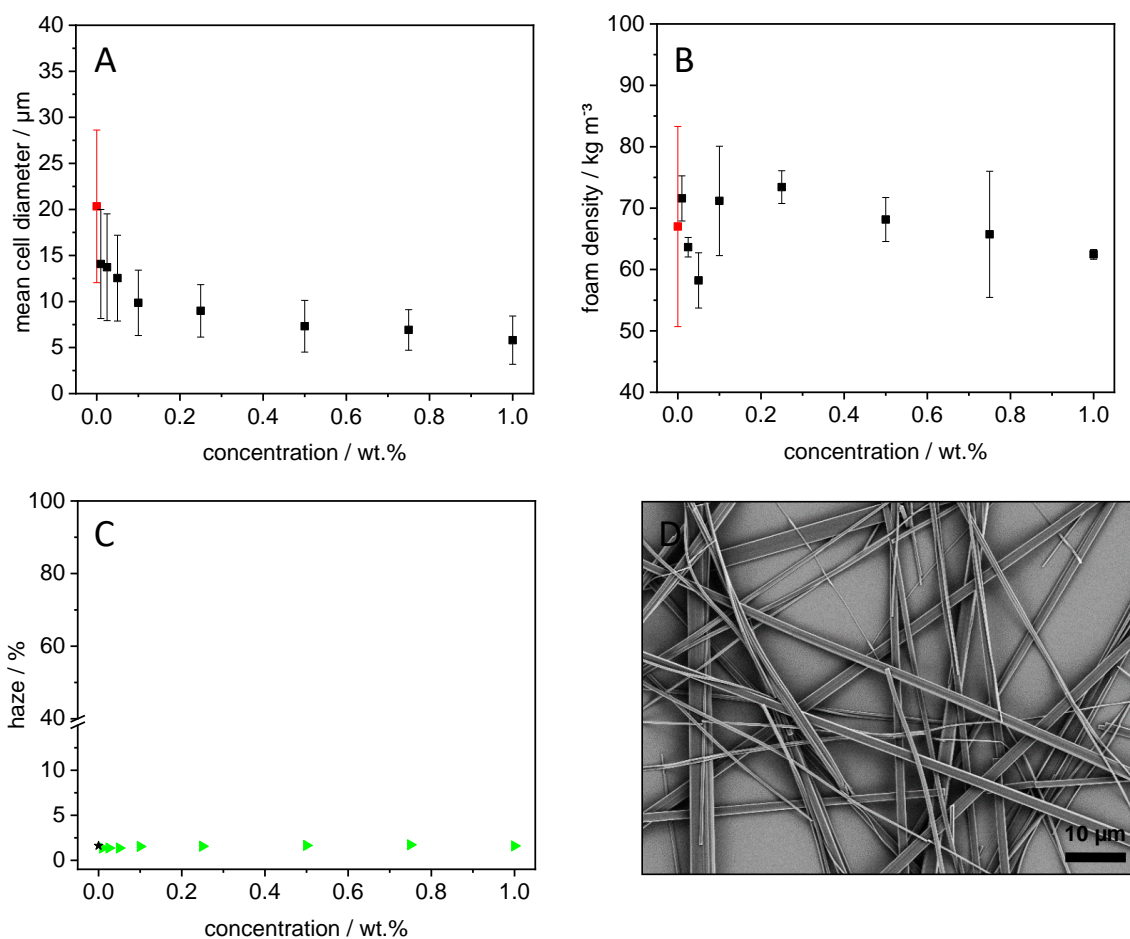


**Figure 4.22:** **A:** Mean cell diameter of the foams with different concentrations of **6a**. The red square represents the mean value of neat PS. **B:** Density of the foams with different concentrations of **6a**. The red square indicates the mean value of neat PS. **C:** Haze values of the specimen used for the foaming. The black star represents the haze value of neat PS. **D:** SEM micrograph of 500 ppm **6a** self-assembled upon cooling in xylene.

As its two members in group **4** and **5**, additive **6a** also forms inhomogeneous structures starting at a concentration of 0.75 wt.% (see **Figure 6.14**). By adding 0.5 wt.% of this additive, the corresponding foam cells could be reduced to  $7.3 \pm 2.8 \mu\text{m}$  with a uniform cell distribution. The relatively thin ribbon-like supramolecular objects therefore provide a relatively high number of nuclei for the foam nucleation. The densities of the foams exhibit relatively large fluctuations and are both above and below the value for pure polystyrene. A correlation with the concentration is not apparent here either.

The next bisamide in the series is **6b** which carries cyclohexane in the periphery. The evaluation of foams with this additive is given in **Figure 4.23**.

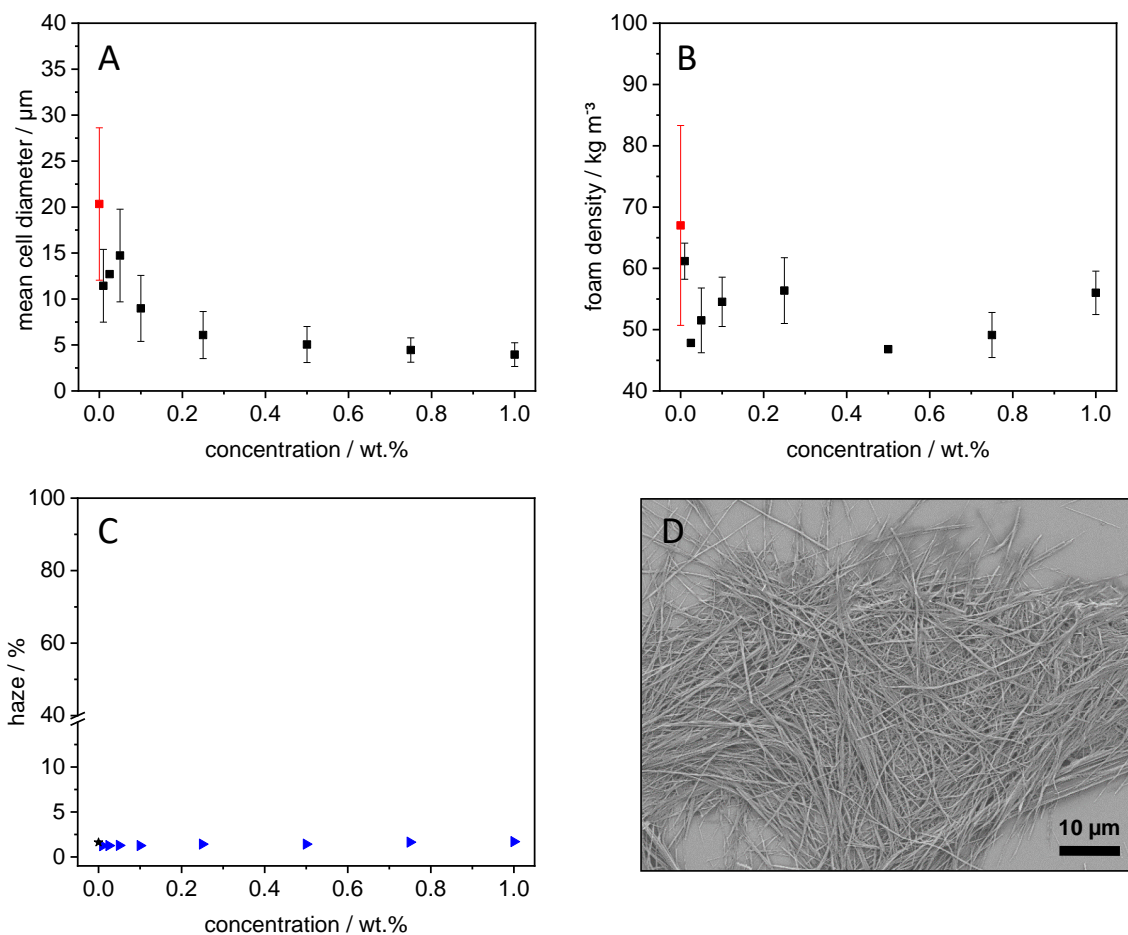


**Figure 4.23:** **A:** Mean cell diameter of the foams with different concentrations of **6b**. The red square represents the mean value of neat PS. **B:** Density of the foams with different concentrations of **6b**. The red square indicates the mean value of neat PS. **C:** Haze values of the specimen used for the foaming. The black star represents the haze value of neat PS. **D:** SEM micrograph of 500 ppm **6b** self-assembled upon cooling in xylene.

Additive **6b** exhibits high solubility in the polystyrene matrix and forms uniform foams over the entire investigated concentration range (see **Figure 6.15**). Since bisamide **6b** forms the thinnest supramolecular fibers of all used bisamides, it is not surprising that it has an excellent foam nucleating effect. Thus, with a concentration of 1.0 wt.% it is possible to reduce the average cell size of the foam to  $3.9 \pm 1.3 \mu\text{m}$ . The very low standard deviation also emphasizes the homogeneity of these foams. However, the density of the foams containing this additive does not improve significantly and is, with irregular fluctuations, in the range for pure polystyrene foams.

The results of additive **6c**, which has a *t*-butyl residue at the amide function, is depicted below.

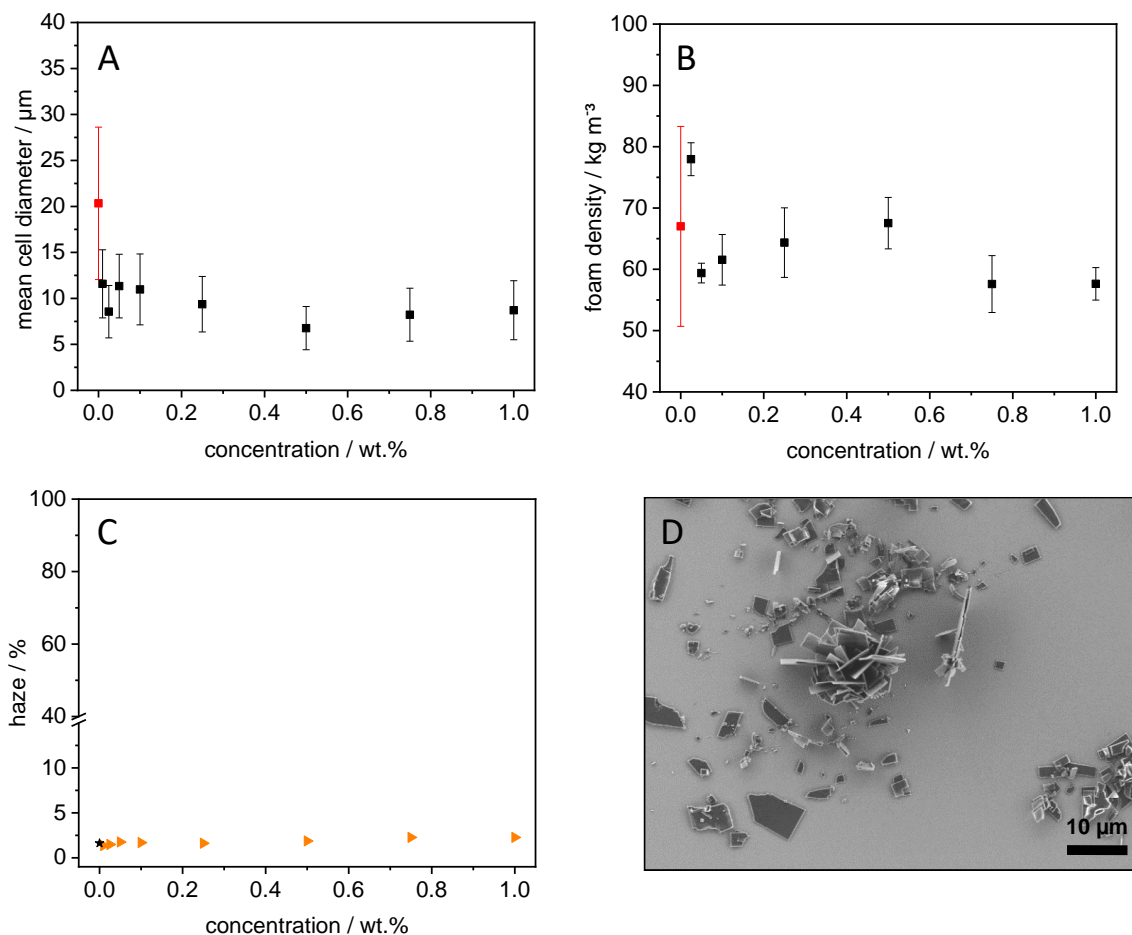


**Figure 4.24:** **A:** Mean cell diameter of the foams with different concentrations of **6c**. The red square represents the mean value of neat PS. **B:** Density of the foams with different concentrations of **6c**. The red square indicates the mean value of neat PS. **C:** Haze values of the specimen used for the foaming. The black star represents the haze value of neat PS. **D:** SEM micrograph of 500 ppm **6c** self-assembled upon cooling in xylene.

Like the preceding two bisamides with *t*-butyl, this additive also has a very high solubility in polystyrene and only forms foams with homogeneous cell distributions (see **Figure 6.16**). Although the additive crystallizes in a platelet-shaped geometry, it is still able to reduce the foam cells to  $6.8 \pm 2.3 \mu\text{m}$  with a concentration of 0.5 wt.%. Another noticeable effect of this additive is that an increase in concentration to 0.75 or 1.0 wt.% results in an increase in the average cell size. One possible reason could be a stronger agglomeration of the supramolecular objects, which reduces rather than increases the number of nuclei. The densities of the foams are mostly below the value of pure polystyrene foam. A stronger density reduction is observed at the two highest concentrations.

The final additive is **6d**, which has been provided with *n*-butyl. The results of the foams are summarized in **Figure 4.25**.

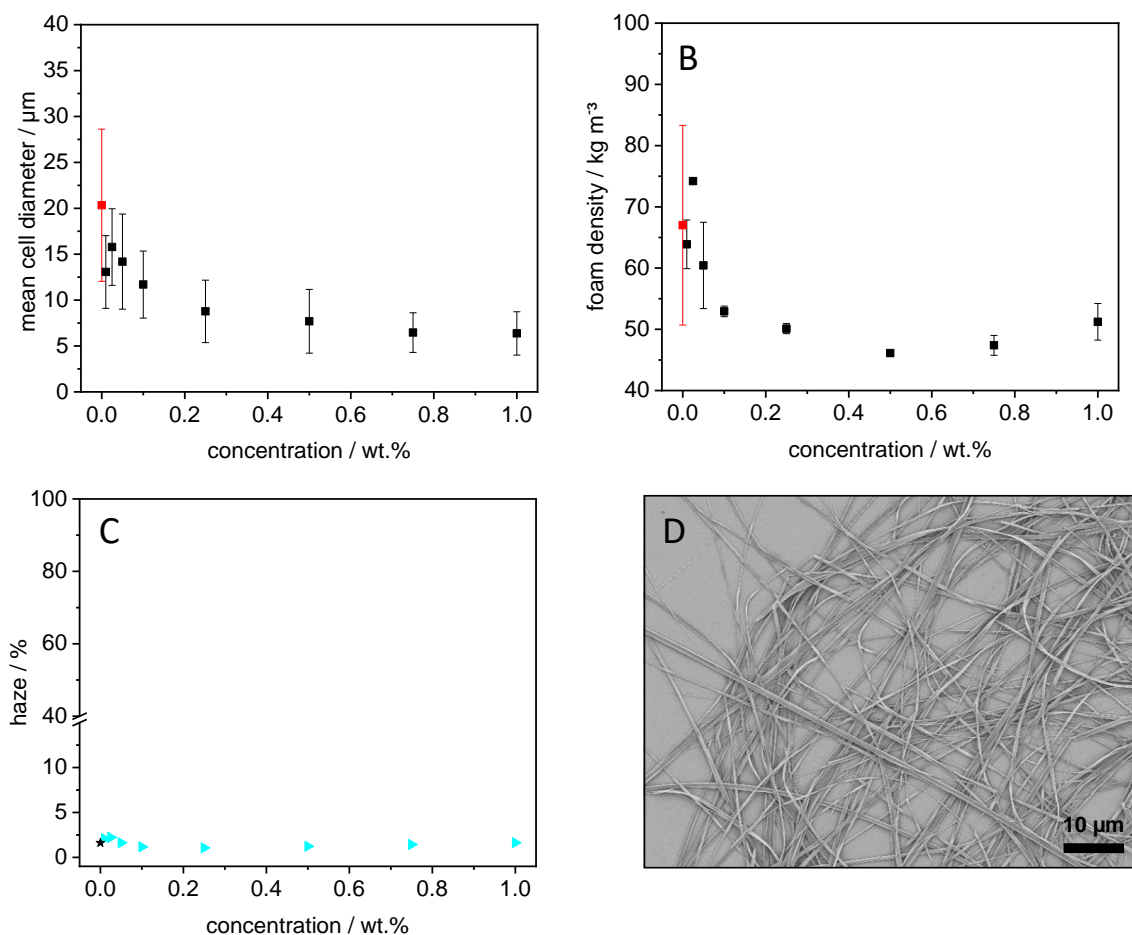


**Figure 4.25:** **A:** Mean cell diameter of the foams with different concentrations of **6d**. The red square represents the mean value of neat PS. **B:** Density of the foams with different concentrations of **6d**. The red square indicates the mean value of neat PS. **C:** Haze values of the specimen used for the foaming. The black star represents the haze value of neat PS. **D:** SEM micrograph of 500 ppm **6d** self-assembled upon cooling in xylene.

In contrast to the two additives **4d** and **5d**, bisamide **6d** is soluble in the polystyrene melt over the entire investigated concentration range and resulting in homogenous cell size distributions (see **Figure 6.17**). Due to the increased solubility, more of the supramolecular fibers can be introduced into the PS matrix, which allows the average cell diameter to be steadily reduced. The smallest cells were measured in the foam with 1.0 wt.% of additive **6d** with a value of  $6.4 \pm 2.4 \mu\text{m}$ . Furthermore, a very large density reduction to  $46 \text{ kg m}^{-3}$  can be observed. The strong density reduction occurs especially at higher concentrations.

### 4.3 Foam extrusion

Similar to the benzene trisamides, a selected bisamide will be tested in a pilot-scale foam extrusion. The preparation and production of the foams took place in the same way as described in 3.3.1.

#### 4.3.1 Foaming with the selected bisamide

In addition to the commercially available BTA **1**, a kinked bisamide specially adapted to the polystyrene matrix is now to be used as a foam nucleating agent. Therefore, the bisamide **6b** was selected, due to its excellent results in batch foaming and the associated optimal solubility. Upscaling the synthesis to handle the large quantities required for the extrusion process on a pilot plant scale proved to be unproblematic. To ensure the comparability with the BTA used, the additive concentrations were kept at 0.1, 0.2 and 0.5 wt.%. In addition, polystyrene foams without any additives were again produced in this extrusion series, which will be used as a reference. Furthermore, the melt temperature of the second extruder and the die temperature were varied and their effects on the foam morphology were investigated. The foams were produced in the same way as described in 3.3.1.

The characterization of the extrusion foams was also carried out with regard to morphology and density and the resulting thermal conductivity.

### Morphology and density

First, the effects of the melt temperature in the second extruder and the die temperature on the densities of the neat and additivated foams are described. **Figure 4.26** shows the density of the neat polystyrene foam (A) and of the modified foams (B) at different melt temperatures. The die temperature was kept constantly at 126 °C.

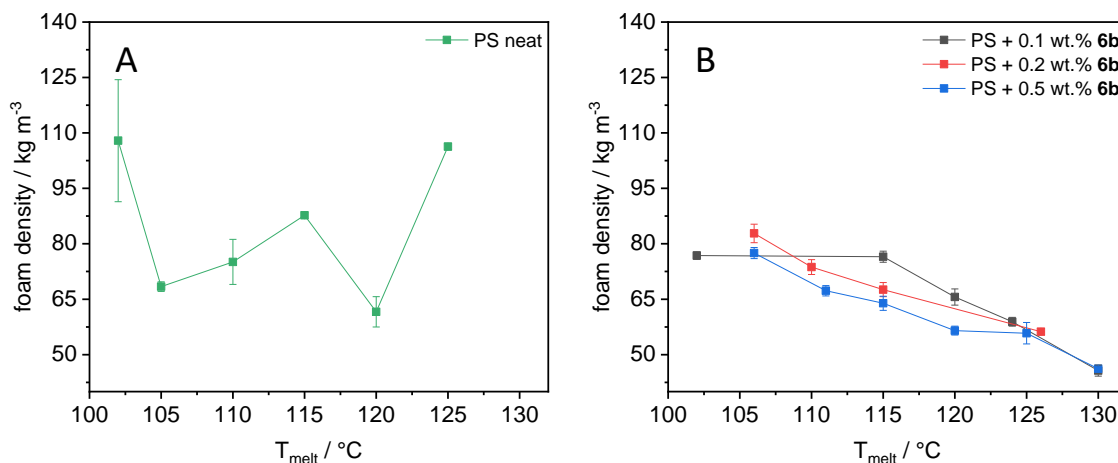


**Figure 4.26:** Resulting foam densities at different melt temperatures ( $T_{\text{melt}}$ ) at a constant die temperature ( $T_{\text{die}}$ ) of 126 °C for **A:** neat PS and **B:** Foams with 0.1, 0.2 and 0.5 wt.% **6b**. The connections between the points are only eye guidelines.

It is apparent that the neat polystyrene foams exhibit a relatively large variance in density and do not follow any discernible trend with increasing the melt temperature. The situation is different with the additivated foams since the density decreases continuously with increasing the melt temperature. The increase in  $T_{\text{melt}}$  reduces the melt strength of the polystyrene, which makes the material expand more easily. However, if the temperature is increased too much and the melt strength becomes too low, the resulting foam cells can no longer be stabilized and cell collapse occurs. While this was already observed with pure polystyrene foams at a melt temperature of 125 °C, the use of additives made it possible to obtain homogeneous foams even at these temperatures.

The next step is to investigate the effect of the die temperature on the foam density. The melt temperature was therefore kept constant at 115 °C.

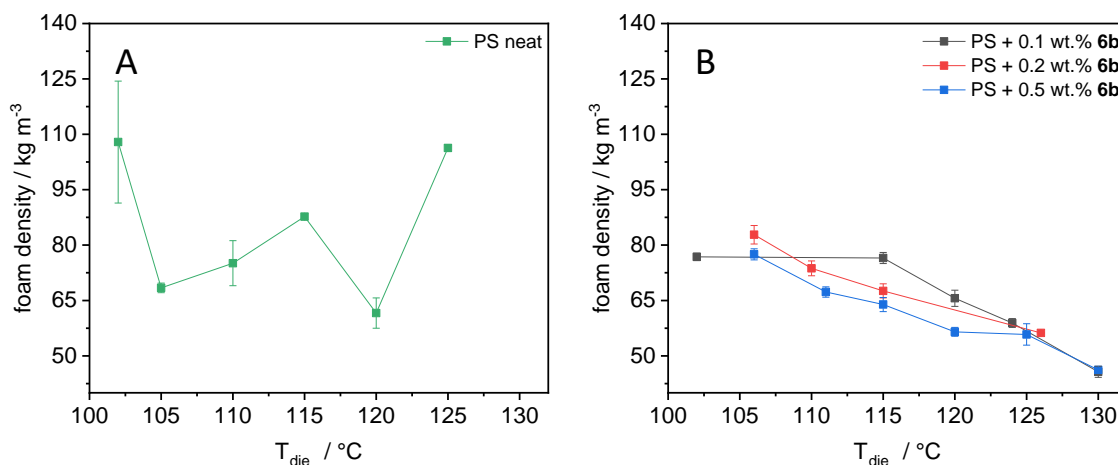


**Figure 4.27:** Resulting foam densities at different die temperatures ( $T_{die}$ ) at a constant melt temperature ( $T_{melt}$ ) of 115 °C for **A:** neat PS and **B:** Foams with 0.1, 0.2 and 0.5 wt.% **6b**. The connections between the points are only eye guidelines.

The pattern is similar here as well. While the neat polystyrene foams are subject to very strong fluctuations and do not follow any discernible trend, the additivated foams show an almost constant density over all investigated nozzle temperatures. This suggests that the nozzle temperature has no significant influence on the density of the resulting foams.

In addition to these two aspects, it is also apparent that the foam extrusion process with pure polystyrene is subject to very large fluctuations and can only be controlled with difficulty. In this context, the additives act not only as foam nucleating agents but also as excellent process stabilizers.

The actual effects of the different concentrations of the kinked bisamide on the morphology and density will be investigated. For this purpose, the results of the again foamed neat polystyrene as well as those of the foams with 0.1, 0.2 and 0.5 wt.% of additive **6b** are summarized in **Figure 4.28**. In addition to the morphology, the graph also contains the cell size distributions, mean cell sizes, cell densities, foam densities as well as the processing temperatures of the generated foams. It should also be noted that for all concentrations (0.0 - 0.5 wt.%) of all generated foams (different processing temperatures), those with the smallest average cells are considered here.

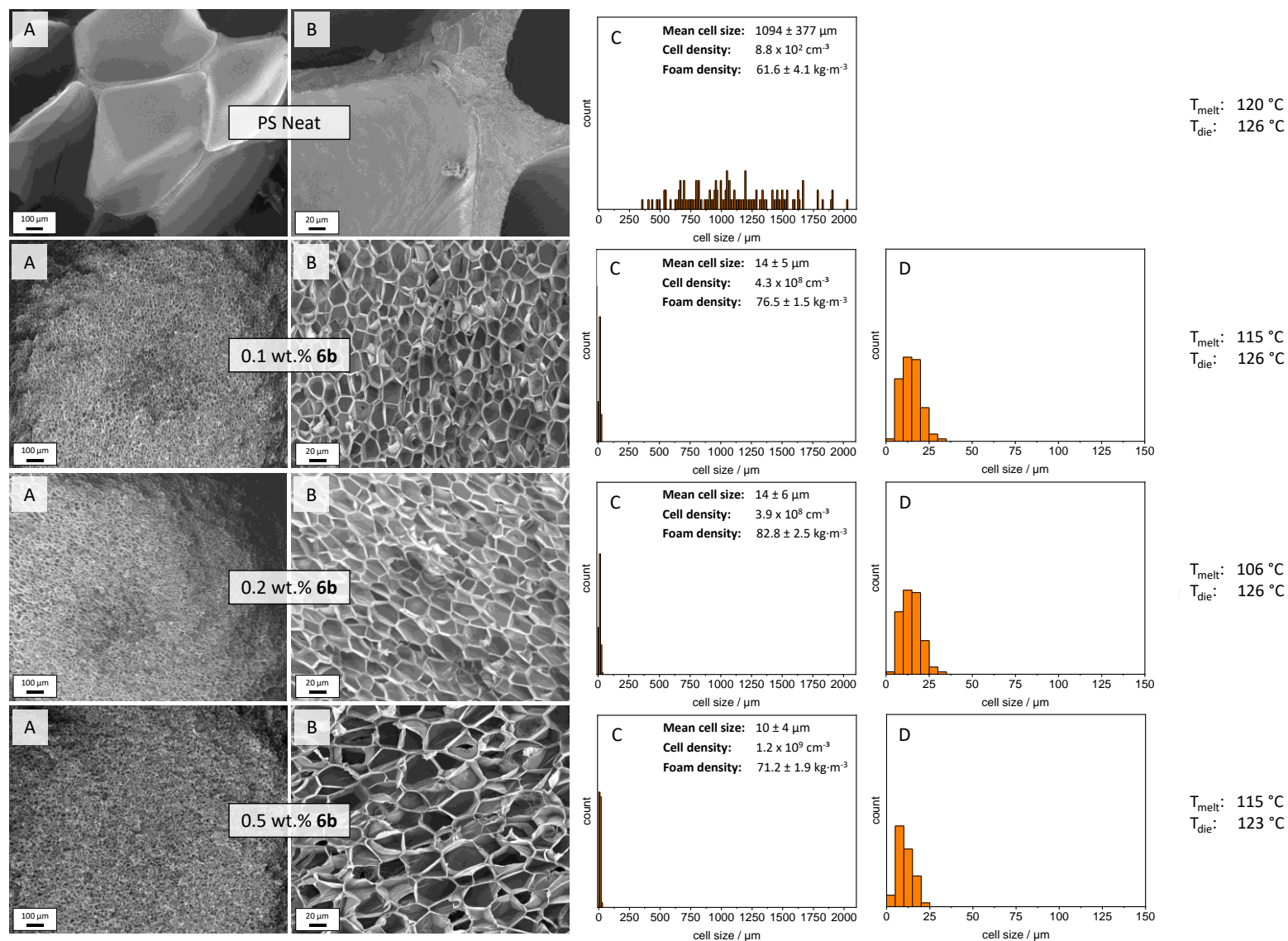


**Figure 4.28:** Comparison of the neat extrusion PS foam and the foams prepared with different concentrations of additive **6b**. SEM micrographs **A**: overview and **B**: higher magnification. **C**: Corresponding histograms of the cell sizes, including mean cell size, cell density and foam density. **D**: Section of the histogram.

All foams have a closed cell structure with a homogenous distribution. In the case of the newly foamed pure polystyrene, it can be seen that this is a macro-cellular foam. This time, however, it has an average cell size of  $1084 \pm 377 \mu\text{m}$  and a cell density of  $8.8 \times 10^2 \text{ cm}^{-3}$ . The corresponding histogram also shows the very broad distribution of cell sizes ranging from  $300 \mu\text{m}$  to over  $2000 \mu\text{m}$ . By adding only 0.1 wt.% of the additive **6b**, the cells can be reduced to an average size of  $14 \pm 5 \mu\text{m}$  and the cell density can be increased up to  $4.3 \times 10^8 \text{ cm}^{-3}$ . This equals a 77 times cell size reduction and an increase in cell density in 6 orders of magnitude. It is therefore beyond question that this additive is also able to form supramolecular fibers in the foam extrusion process, which nucleate the foam cell formation. Furthermore, a look at the histograms of the cell size distribution shows the homogeneity of the generated foams. The increase of the concentration to 0.2 wt.% did not show any significant changes in the foam morphology. However, by increasing the additive amount to 0.5 wt.% it was possible to reduce the average cell size to only  $10 \pm 4 \mu\text{m}$ . A cell density of up to  $1.2 \times 10^9 \text{ cm}^{-3}$  was calculated. Due to the adjusted solubility of this additive to the polymer used, it is possible to introduce larger amounts into the polymer matrix without worrying about homogeneous dispersion. Thus, more nucleation sites can be provided for the generation of foam bubbles, which makes it possible to control the morphology of the resulting foams even better.

Looking at the densities of the foams, an increase caused by the additives can be observed. While the foam without additives exhibits a density of  $61.4 \pm 4.1 \text{ kg m}^{-3}$ , the foam with 0.2 wt.% of additive **6b** shows a density of  $82.8 \pm 2.5 \text{ kg m}^{-3}$ . The densities of the foams with 0.1 wt.% and 0.5 wt.% exhibit values of  $76.5 \pm 1.5 \text{ kg m}^{-3}$  and  $71.2 \pm 1.9 \text{ kg m}^{-3}$  respectively. Again, the increase is probably due to the enormous increase of the inner surface of the microcellular foams, which means that considerably more cell walls and cell struts have to be created than in the macro-cellular neat foam.

In order to confirm the presence of the supramolecular fibers in the cell walls and cell struts and to detect any differences, these extrusion foams were also treated with the plasma etching technique. The recorded SEM images together with the histograms of the corresponding distribution of the width of the supramolecular objects are shown for all plasma etched foams in **Figure 4.29**.

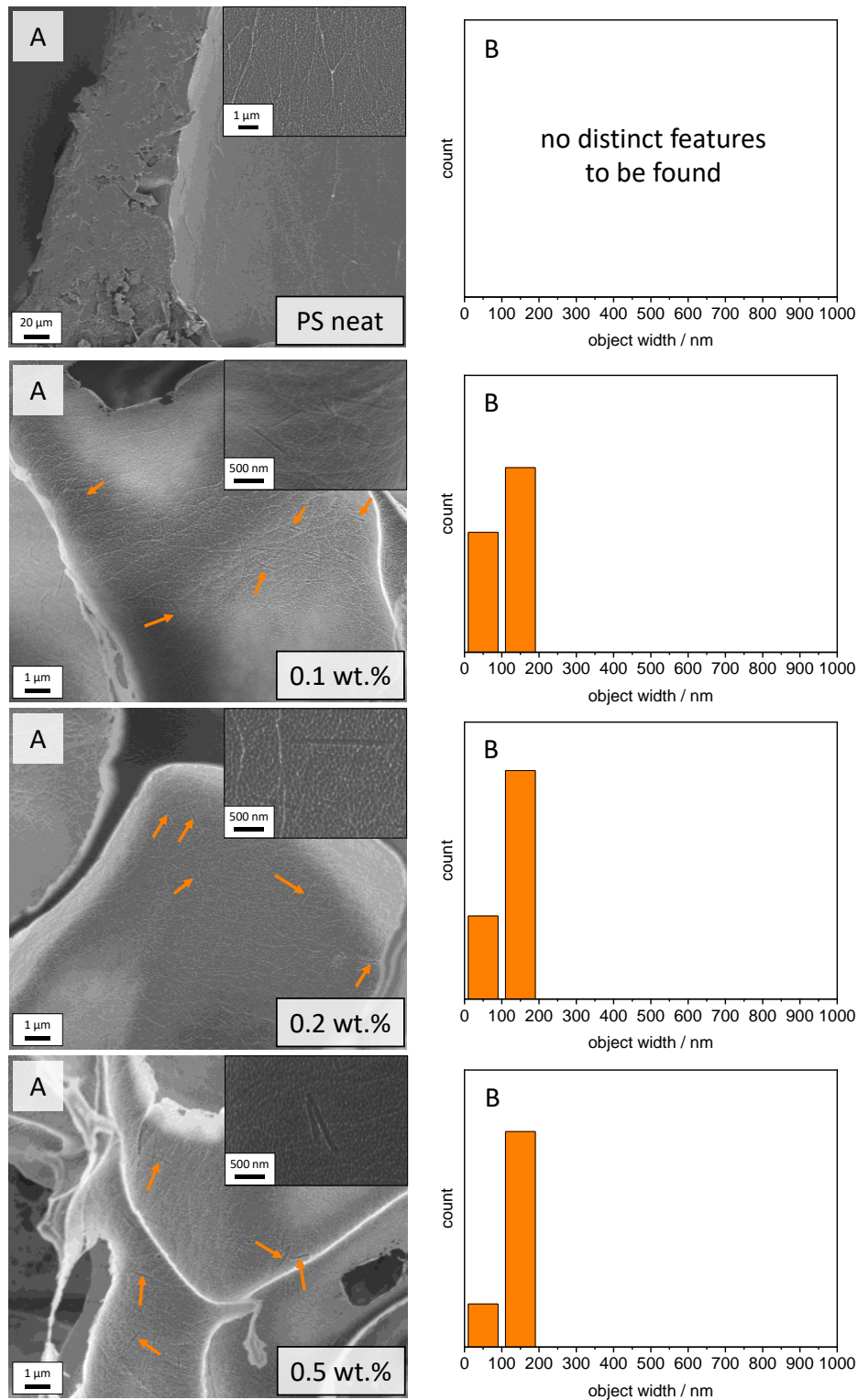


**Figure 4.29:** **A:** SEM micrographs of PS extrusion foams without additive and with 0.1, 0.2 and 0.5 wt.% **6b** after 60 min O<sub>2</sub>-plasma treatment. Orange arrows indicate some of the holes in which the additive objects were present before the plasma etching. Inserts with larger magnification also show some example holes. **B:** Histograms of the width of the holes corresponding to the diameter of the objects. (note the different scale bar for neat PS foams).

Here, too, the situation is similar to that of plasma-etched foams with BTA **1**, where the holes in the cell walls in which the additives were found are clearly visible. However, there is also a decisive difference. The holes found and thus the diameters of the supramolecular fibers remain approximately the same for all used concentrations and range between 100 and 200 nm. This also explains why there is no increase in haze value when using this additive even at higher concentrations. A further discussion on this and the direct comparison with the found fiber diameters of additive **1** will be done in the next chapter.

### Thermal conductivity

The foams produced in this extrusion series were also examined with regard to their thermal conductivity. The measured values of the foams with additive **6b** and the newly produced neat reference are shown in **Figure 4.30**.

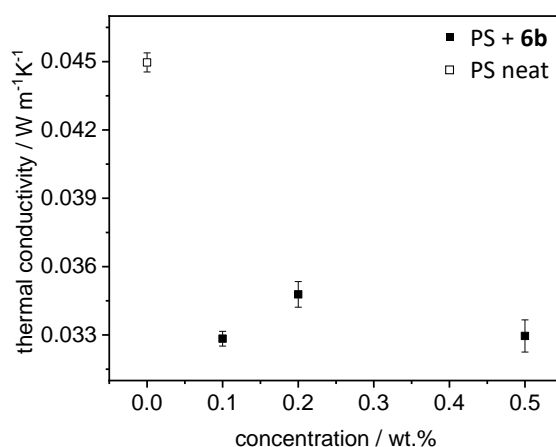


**Figure 4.30:** Thermal conductivity of the PS extrusion foams without and with different concentrations of additive **6b**.

It is apparent that the additive foams have a significantly reduced thermal conductivity. The thermal conductivity of the neat PS foam from this extrusion series has a value of 0.0450 W m<sup>-1</sup>K<sup>-1</sup>. By adding 0.1 or 0.5 wt.% **6b**, this could be reduced to 0.0328 W m<sup>-1</sup>K<sup>-1</sup> and 0.0329 W m<sup>-1</sup>K<sup>-1</sup> respectively. This corresponds to a reduction of more than 26 % in both cases. For the foams with 0.2 wt.% a reduction of still more than 22 % was measured. In order to investigate the effects of density and morphology changes in more detail, the thermal conductivity as a function of foam density and cell size is shown in **Figure 4.31**.

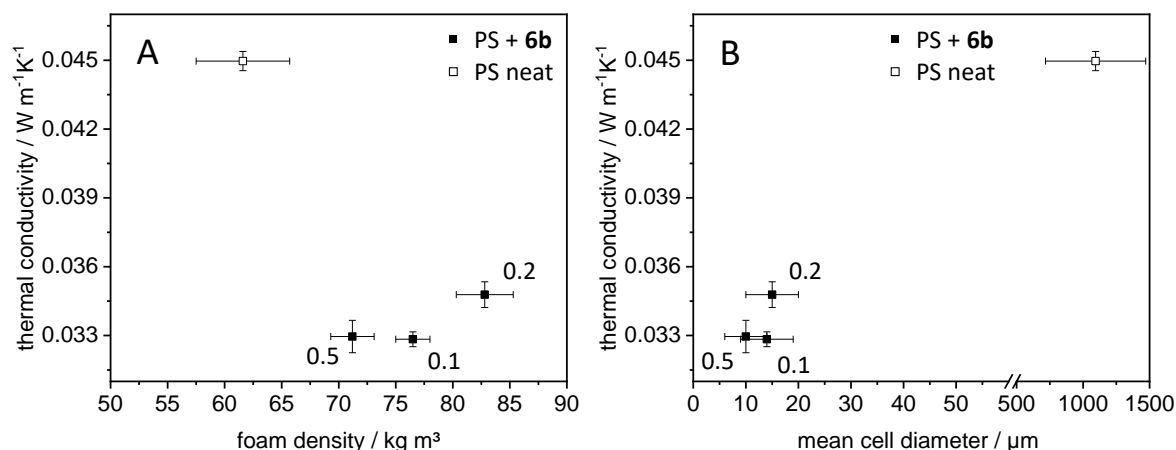


**Figure 4.31:** Thermal conductivity of the PS extrusion foams without and with additive **6b** in dependence of **A:** foam density and **B:** mean cell diameter. The black numbers indicate the corresponding additive concentration.

It is obvious that the strong reduction of the thermal conductivity from the pure to the additivated foams is caused by the controlled reduction of the cell sizes. Looking at the foams with 0.1 and 0.2 wt.% of kinked bisamide **6b**, the influence of the density becomes evident. Both foams have cells of the same size, but the foam with 0.2 wt.% has a higher density, which is most likely the reason for the increased thermal conductivity. The situation is different when considering the foams with 0.1 and 0.5 wt.% of the additive. Although a lower density and even smaller cell sizes were determined for the former, both foams still exhibit the same thermal conductivity. A possible explanation for this is the relatively large variance of the thermal conductivity measurement of the foam with 0.5 wt.% **6b**. In addition, as already mentioned, the influence of cell size reduction in these dimensions is no longer quite as pronounced. Only with a reduction further below  $10 \mu\text{m}$  a considerable improvement through the Knudsen effect is conceivable.

One possible way to further improve thermal conductivity, is a process optimization of the extrusion series with this additive in order to reduce the density of the obtained foams while maintaining the same cell size reduction. It would also be possible to increase the concentration of the additive even more, since the solubility limit has not yet been reached at the concentrations used. In this way it would be possible to increase the number of potential nucleation seeds even further. In addition, when using the kinked bisamide, an increase in the concentration does not affect the diameter of the supramolecular fibers, and they therefore have an excellent surface-to-volume ratio even at very high concentrations.

### 4.3.2 Comparison of the trisamide and the bisamide as foam nucleating agents

To compare the findings of both foam extrusion, the results obtained with the commercial benzene trisamide **1** and kinked bisamide **6b** are correlated to each other. It should be noted that for both extrusion tests a reference without additive was prepared in each case, which is why two values for pure polystyrene foams are always given in the subsequent figures.

First of all, the cell size reduction and the change in foam density depending on the additive and its quantity should be assessed. The two graphs are shown in **Figure 4.32**.

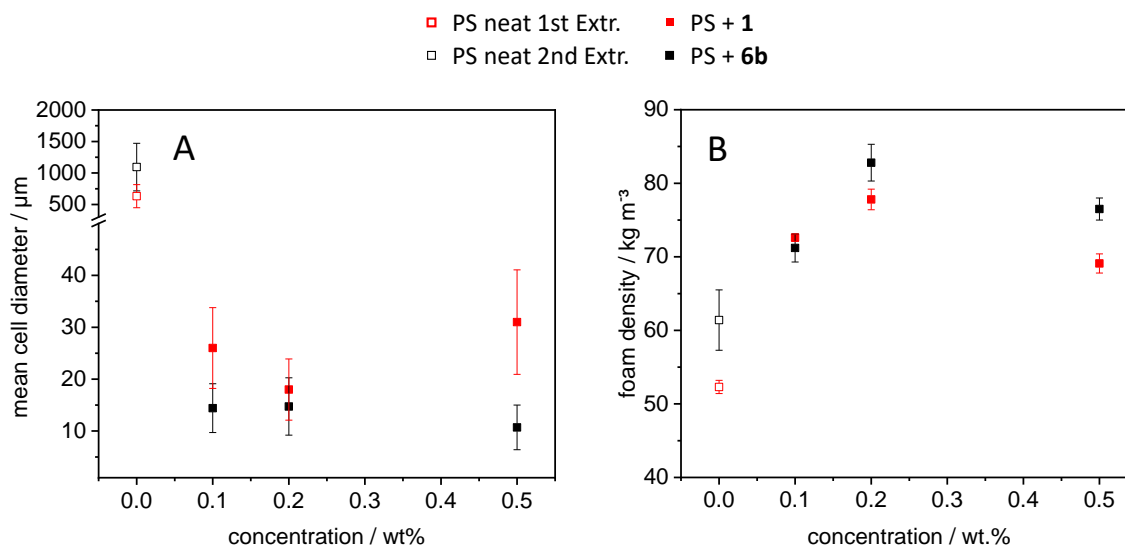


**Figure 4.32:** **A:** mean cell diameter and **B:** foam density of the extrusion foams without and with additive **1** and **6b** in dependence of the concentration.

Considering first the effects of the additive addition on the cell sizes of the foams, it can be seen that the kinked bisamide reduces the foam cells even further in comparison to the commercial benzene trisamide **1** and thus exhibits a better foam nucleation efficiency. One reason for this is the solubility of additive **6b**, which is adapted to the polymer matrix. This makes it possible to use larger quantities and thus significantly increase the potential nuclei amount. While the solubility limit for additive **1** is already reached at a concentration of 0.2 wt.%, it would be conceivable to use the kinked bisamide even at concentrations exceeding 0.5 wt.%.

Furthermore, plasma etching experiments have shown that an increase in the concentration of additive **1** leads to an increase in the diameter of the supramolecular fibers. Consequently, this leads to a lower surface-to-volume ratio and thus to a comparatively lower nucleus count. However, by increasing the concentration of additive **6b**, the diameter of the fibers remains constant even if the additive quantity is

increased fivefold. For illustration, the fiber histograms of the two additives for all concentrations are shown in **Figure 4.33**.

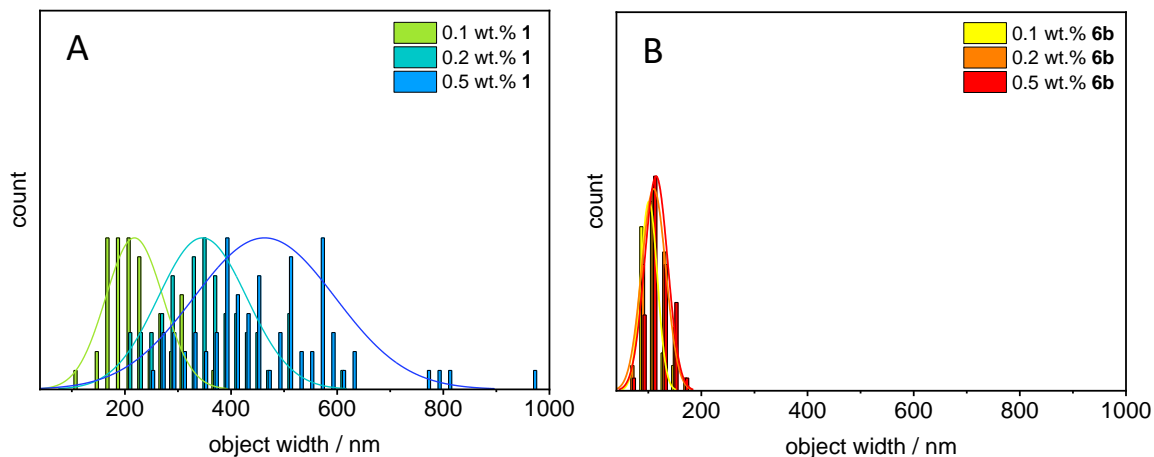


**Figure 4.33:** Histograms of the detected width of the objects formed by additive **A: 1** and **B: 6b** at different concentrations.

In addition to the increase in size, it is apparent that even at a concentration of 0.1 wt.%, the fibers of additive **1** have a diameter almost twice as large and thus have a significantly inferior surface-to-volume ratio. This can affect the nucleating effect as already described.

Unfortunately, the strong reduction in cell size is accompanied by an increase in density due to the increased inner surface. Since additive **6b** reduces the size of the cells even further, the increase in density is slightly higher than with additive **1**.

Considering the determined values for cell size and foam density of the two references without additives, very large deviations from each other are evident. This shows that the overall extrusion process without additives has no process control.

These identified conditions of density and morphology are decisive for the thermal conductivity of the foams. The determined values as a function of cell size are shown for both additives and both references in **Figure 4.34**.

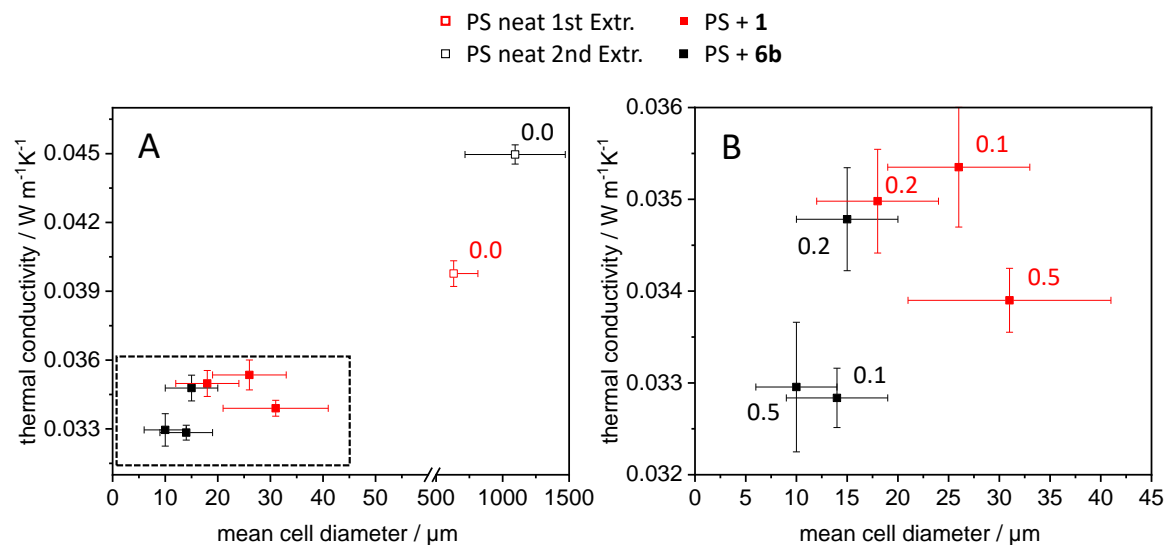


**Figure 4.34:** **A:** Thermal conductivities of the PS extrusion foams without and with additive **1** and **6b** respectively in dependence of the mean cell diameter. **B:** section of A marked with the dashed square. The red (**1**) and black (**6b**) numbers indicate the corresponding additive concentration in both cases.

With these findings, the great influence of cell size on thermal conductivity is apparent. For example, the reference foam from the first extrusion series has significantly smaller cells and thus also a lower thermal conductivity than the corresponding foam from the second extrusion series. Furthermore, there is also a clear advantage in the use of the different additives. Due to the better nucleating effect of additive **6b** and the resulting smaller cell morphology of the foam, the thermal conductivity can be further reduced compared to additive **1**. The only exception is the extrusion foam with 0.2 wt.% **6b**, which has a slightly increased thermal conductivity compared to the other two foams with the same additive due to the increased density.

In summary, by specifically adapting the solubility of additive **6b** to the polymer matrix used, and by expertly adjusting the molecular structure and the associated influence on the self-assembly process, the already excellent results from the commercial BTA **1** can be further improved.

### 4.4 Foam injection molding

In order to confirm the general functionality of the supramolecular additives also in other large-scale industrial processes, they were conclusively used in the foam injection molding process. This process is mainly used to reduce the weight and thus the costs of the generated parts without deteriorating the mechanical properties. Another advantage over conventional injection molding is that the internal pressure of the blowing agent prevents material shrinkage and causes less warpage.

#### 4.4.1 Foam sample preparation

The CellMould process was used for the production of injection molded foams. In order to investigate the effects on the morphology and the concentration influence of the additives, pure polystyrene foams and foams with 0.1 and 0.5 wt.% of the additive were produced. A concentration of 0.2 wt.% was waived, as it was found in foam extrusion that increasing from 0.1 to 0.2 wt.% has only a very small effect. Since the additives cannot be added via a masterbatch in the manufacturing line, they were added to the polystyrene in an additional external compounding step. To take into account the thermal stresses of this step, pure polystyrene was also processed in the same way. To start up the extruder and to find suitable process parameters, however, untreated PS as purchased from the manufacturer was used.

These materials are added and melted at 240 °C in the first part of the single-screw extruder, the plasticizing section. In the second part of the extruder, the polymer melt is loaded with 0.7 wt.% N<sub>2</sub> as the blowing agent. This area is separated from the former by a barrier zone. The special screw design of the CellMould process divides the melt flow into many individual streams, ensuring homogeneous distribution of the blowing agent and producing a single-phase mixture. A non-return valve enables the generation of pressure necessary to dissolve the blowing agent. The homogeneous melt is then pressed into mold which has a temperature of 40 °C. By quenching the melt at the edge of the mold, foaming is suppressed at this point and the outer skin which is typical for foam injection molding is formed. In the high-pressure process, a breathing mold with an initial wall thickness of 2 mm is used. Once the mold is completely filled, it is enlarged to 3.5 or 5.5 mm in a controlled manner. This results in a pressure drop which induces the foaming. The exact process parameters can be found at 5.3.4 in the experimental part.

#### 4.4.2 Foaming with the selected bisamide

Since the kinked bisamide **6b** has already proven to be extremely efficient in foam extrusion, it was also selected for the use in foam injection molding. As these experiments mainly aim to confirm the concept of supramolecular additives for morphology control, the characterization of these foams is primarily focused on homogeneity, cell sizes and densities. For a more detailed analysis, the foam samples were divided into three different positions which is shown schematically in **Figure 4.35**.

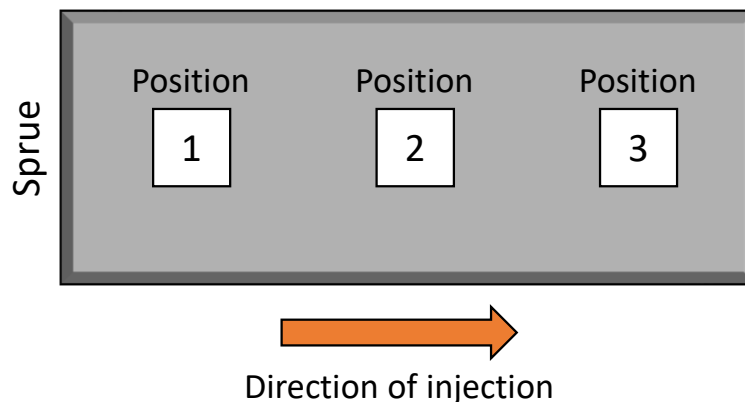


**Figure 4.35:** Schematic visualization of the different measuring points of the foam injection molded samples.

The density was measured several times at these three positions and the mean values are given. The SEM micrographs were taken in the direction of extrusion at position 2 on a cryo broken edge.

As already mentioned, a breathing mold is used in the high-pressure process, which was expanded from an initial 2 mm to 3.5 and 5.5 mm. The uncompounded pure polystyrene as supplied by the manufacturer was used to initiate the process and to set suitable parameters. These settings were kept constant for the entire production process to ensure the comparability of the results. Unfortunately, in retrospect, it became apparent that the materials which had undergone the additional compounding step had defects at the macroscopic level. To make these defects visible, the foams were irradiated by a light source. The obtained images for pure PS without and with the additional compounding step are contrasted in **Figure 4.36**.

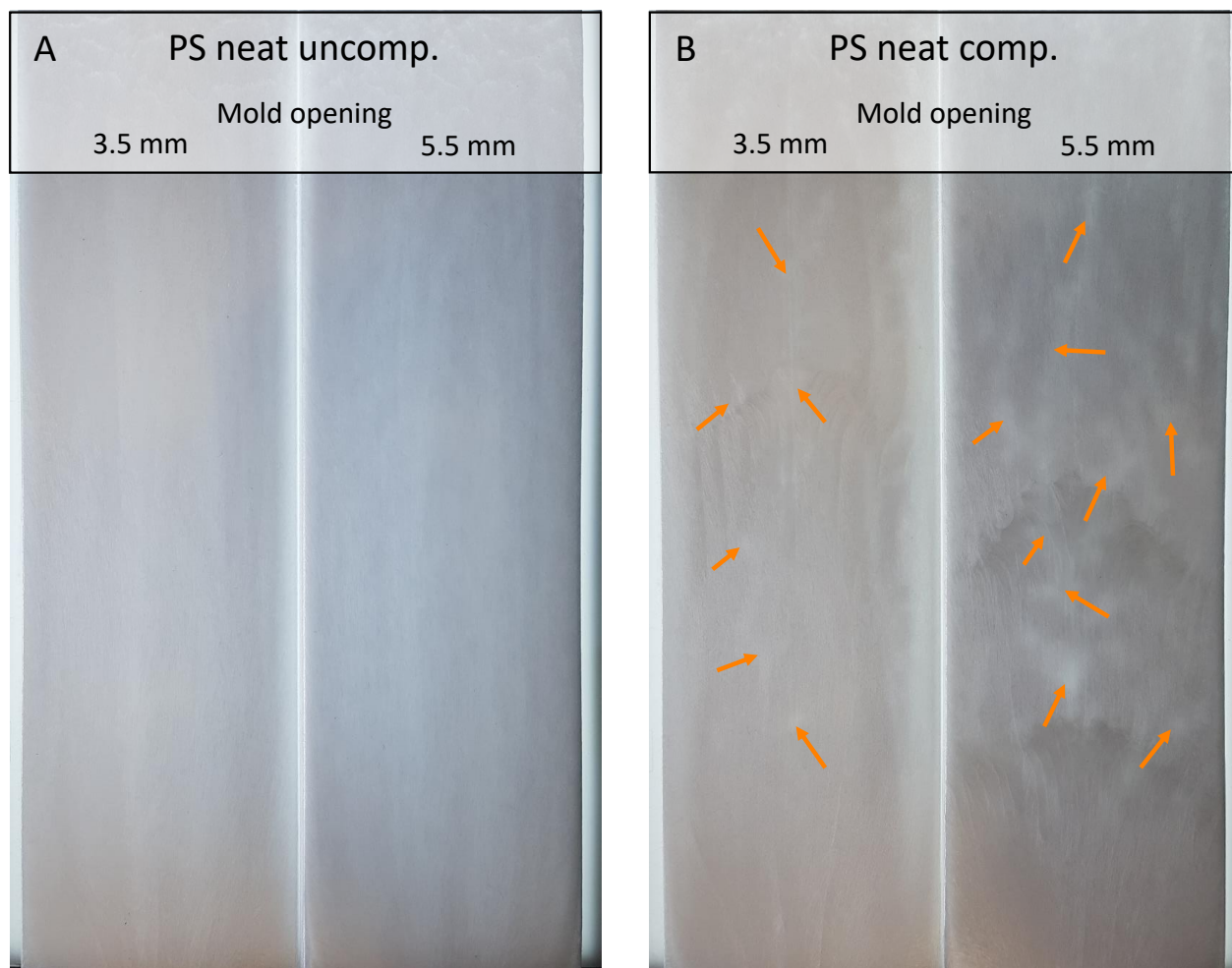


**Figure 4.36:** A: Neat un-compounded and B: compounded polystyrene injection molded foams with a mold opening of 3.5 and 5.5 mm transmitted by a light source. Orange arrows indicate some of the macroscopic defects in the samples.

While the un-compounded polystyrene is completely filled throughout the entire sample, the foams with the already compounded material show obvious defects in the form of large holes. Furthermore, an increase of these defects from the samples with 3.5 mm mold opening to 5.5 mm can be seen. Exactly the same picture is obtained when examining the additivated foams. This indicates that the external compounding and the associated increased thermal stress is responsible for this. A SEC measurement revealed that the molecular weight decreased from initially 340 to 277 kg mol<sup>-1</sup> (same PDI) due to the high temperatures and the enormous shear forces caused by the external compounding. The reduction of the molecular weight results in a decrease of the melt viscosity of the polystyrene. This is likely to result in the cells inside the foams no longer being able to be stabilized and eventually lead to cell collapse.

Nevertheless, the foams were examined for their density and morphology. It was ensured that samples were only taken from flawless parts. The measured average density at the respective positions for all foamed materials are summarized in **Figure 4.37**.

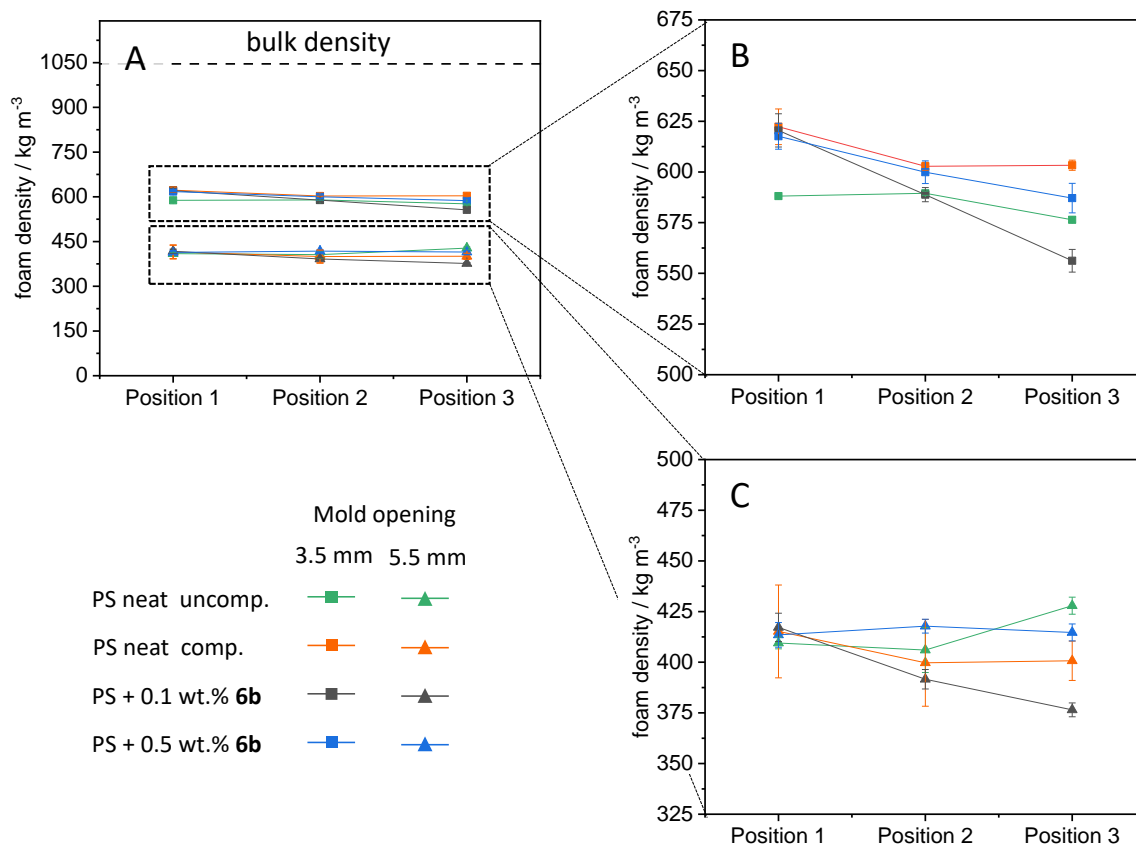


**Figure 4.37:** **A:** Density of the foam injection molded samples produced using the high-pressure method with 3.5 and 5.5 mm mold opening at different positions. The dashed black line represents the bulk density of the polystyrene. **B:** Section of **A** regarding the samples with a mold opening of 3.5 mm. **C:** Section of **A** regarding the samples with a mold opening of 5.5 mm. The connections between the points are only eye guidelines.

The foams in which the mold has been opened to 5.5 mm show a greater reduction in density, as the material has more space to expand. In comparison to the bulk density of polystyrene, it was possible to reduce the density from 1040 to an average of 400 kg m<sup>-3</sup>, which corresponds to a density reduction of more than 60 %. In the case of foams where the mold has been opened by only 3.5 mm, an average density reduction of 40 % is achieved.

A closer look at the densities at the different positions shows the trend of increasing density in the area of the sprue and decreasing towards the end of the component. A definite influence of the additive on the

density itself cannot be seen. However, the high variance in the density of the foam made of pure compounded polystyrene with a mold opening of 5.5 mm is noteworthy.

Considering the morphology of the foams, the influence of the additive is clearly visible again. **Figure 4.38** presents the SEM micrographs of all samples and **Table 4.1** summarizes the calculated mean cell diameters and cell densities.

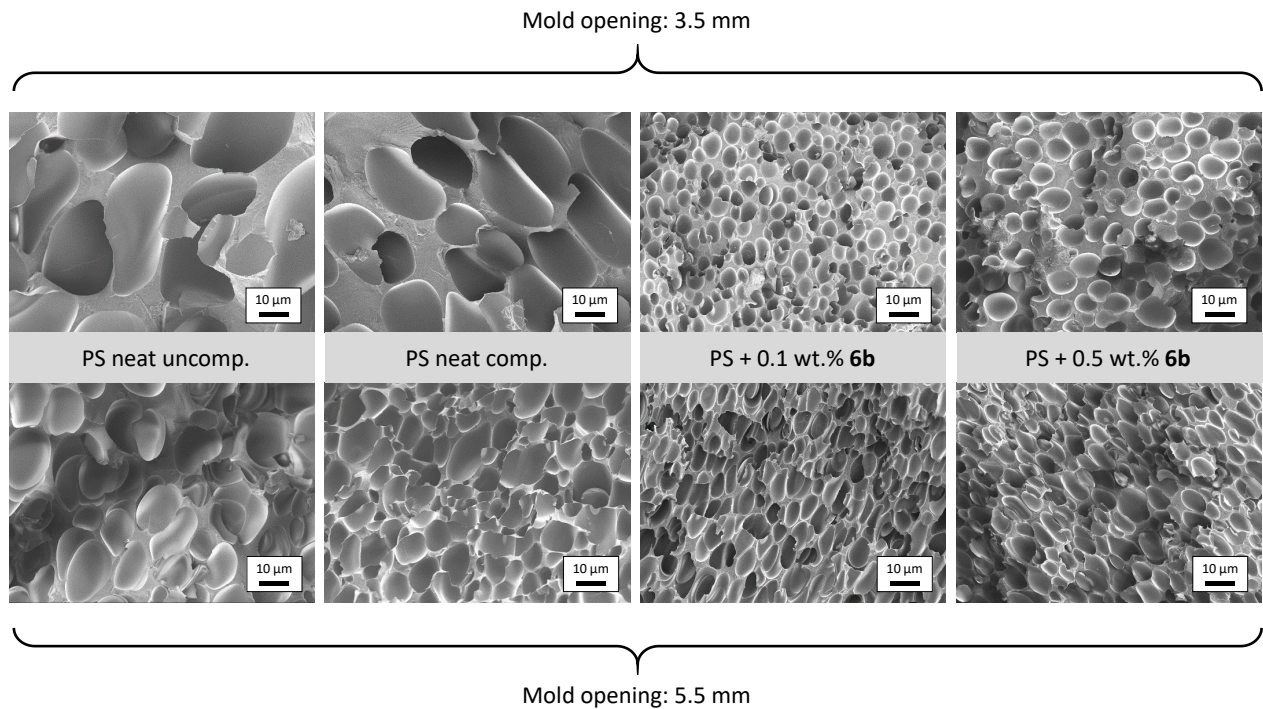


**Figure 4.38:** SEM micrographs of each injection molded foam produced by utilizing the high-pressure method with 3.5 mm and 5.5 mm mold opening.

The SEM images show firstly that the proportion of cell webs and cell walls is significantly reduced by further opening of the mold. This reflects the previously explained higher density reduction. Secondly, the cell size is drastically reduced by the addition of the additives.

**Table 4.1:** Mean cell diameter and cell density of each injection molded foam produced utilizing the high-pressure method with 3.5 and 5.5 mm mold opening.

Mold opening		PS neat uncomp.	PS neat comp.	PS + 0.1 wt.% 6b	PS + 0.5 wt.% 6b
3.5 mm	Mean cell size [ $\mu\text{m}$ ]	$106 \pm 47$	$72 \pm 26$	$17 \pm 6$	$12 \pm 4$
	Cell density [ $\text{cm}^{-3}$ ]	$7.1 \times 10^5$	$2.5 \times 10^6$	$1.8 \times 10^8$	$3.6 \times 10^8$
5.5 mm	Mean cell size [ $\mu\text{m}$ ]	$77 \pm 35$	$41 \pm 13$	$17 \pm 6$	$12 \pm 4$
	Cell density [ $\text{cm}^{-3}$ ]	$2.1 \times 10^6$	$2.3 \times 10^7$	$2.9 \times 10^8$	$5.5 \times 10^8$

Considering the cells of the foams without additive and with a mold opening of 3.5 mm, it is evident that they have very large cells with an average diameter of  $106 \pm 47$  and  $72 \pm 26 \mu\text{m}$  respectively. By adding only 0.1 wt.% **6b**, the cells can be reduced in size to as little as  $17 \pm 6 \mu\text{m}$ . By increasing the concentration to 0.5 wt.%, the number of potential nuclei can be increased, reducing the average cell size further to  $12 \pm 4 \mu\text{m}$ . The reduction is a clear proof that even at the extremely high cooling rates during the injection molding process, supramolecular objects are formed which can nucleate the bubble formation very efficiently. Opening the mold to 5.5 mm results in a slight reduction of the average cell size of pure PS foams to  $77 \pm 35 \mu\text{m}$  and  $41 \pm 13 \mu\text{m}$ , respectively. Looking at the additivated foams, it is evident that the mean cell sizes have not changed. Nevertheless, a certain change in morphology can be seen here as well. Thus, the cell densities increase from  $1.8 \times 10^8$  to  $2.9 \times 10^8 \text{ cm}^{-3}$  for the foam with 0.1 wt.% **6b** and from  $3.6 \times 10^8$  to  $5.5 \times 10^8 \text{ cm}^{-3}$  for the sample with 0.5 wt.% **6b**. Although the mean cell size remains unchanged, the number of cells increases significantly. This increase is enabled by the reduction of the cell struts and cell walls, which is reflected in the density reduction mentioned above. Of course, the cell density also increases in neat foams due to the enlarged mold opening. This increase is more pronounced, since the cells also become smaller.

In summary, the supramolecular additive **6b** is able to control the morphology of the foams and to significantly improve their cell size and homogeneity also in the foam injection molding. Regardless whether an additive is used, the foams with an additional compounding step showed numerous defects in the form of voids at a macroscopic level. In order to prevent this, the additive addition might be carried out via a masterbatch, similar to the foam extrusion process described above. This would avoid the

additional thermal stress and thus prevent a reduction in molecular weight. However, it is also conceivable to counteract the reduced melt viscosity by adjusting the injection molding parameters to precisely the material used, so that these defects do not occur in the first place. With defect-free specimens the mechanical properties should be investigated to determine if the morphology control achieves the desired effect.

## 4.5 Conclusion

In this chapter, it was successfully demonstrated that the class of kinked bisamides, consisting of a 4,4'-diphenylmethane central unit and peripheral side groups linked via amide functions, is highly efficient as supramolecular foam nucleating agents for polystyrene. In addition, two reference bisamides based on 1,4-benzene and 1,8-naphthalene central unit have also been deployed.

By systematically varying the molecular design, the solubility as well as the self-assembly behavior of the kinked bisamides in PS can be fine-tuned. Therefore, it was possible in self-assembly experiments with xylene as model solvent mimicking polystyrene to realize nano-objects from plate-like to ribbon to fiber shape. Upon cooling they form homogeneously dispersed nano-objects, providing a large number of nucleation sites contributing in the foam cell nucleation. Moreover, haze measurements reveal that the kinked bisamides exhibit a better solubility in PS than the reference bisamides.

A series of temperature-induced batch foaming experiments gave an indication about the solubility of each bisamide. If the deployed concentration exceeds the solubility limit in the polymer, the homogenous distribution is no longer given, which result in inhomogeneous foam morphologies. In the following table, the resulting cell morphologies of the foams are summarized.

**Table 4.2:** Overview of the resulting foam morphologies with all used bisamides in the investigated concentration range.

Additive	concentration / wt.%							
	0.01	0.025	0.05	0.1	0.25	0.5	0.75	1.0
3a	homogeneous			inhomogeneous				
3b	homogeneous				inhomogeneous			
4a	homogeneous						inhomogeneous	
4b	homogeneous						inhomogeneous	
4c	homogeneous							
4d	homogeneous					inhomogeneous		
5a	homogeneous						inhomogeneous	
5b	homogeneous							
5c	homogeneous							
5d	homogeneous					inhomogeneous		
6a	homogeneous						inhomogeneous	
6b	homogeneous							
6c	homogeneous							
6d	homogeneous							

The two reference additives have a relatively low solubility in the polystyrene melt. Due to the planarity and rigidity of the central units and the strong hydrogen bonds a completely solution on the molecular level is hampered. By introducing the methylene bridge between the two aromatics in the central unit, the solubility of the kinked bisamides is significantly increased. It was found that the solubility increases from the bisamides featuring no substitution at the central unit  $R_1$  (**4a** - **4d**) over to the methyl substituted ones (**5a** - **5d**) to the ones with ethyl groups (**6a** - **6d**). Furthermore, it was revealed that the substituent  $R_2$  at the amide groups has also an impact on the solubility. For example, bisamides with a benzyl (**a**) group are not as soluble as derivatives with a cyclohexyl (**b**) and or t-butyl (**c**) substituent.

Looking at their nucleation capability, the foam cell nucleation and ultimately the ability to control the morphology of the foams, it was found that two kinked bisamides can generate foams with a cell size below  $4\ \mu\text{m}$ . This includes the bisamides with cyclohexane side groups and methyl substituents in ortho positions to the amide groups - **5b** which forms a foam with a homogenous cell distribution with an average cell size of only  $3.5\ \mu\text{m}$  and a foam density of  $52\ \text{kg m}^{-3}$ . This equals almost a reduction by the factor 6 compared to the neat PS batch foams. The second additive is, the kinked bisamide with the same peripheral substituent but ethyl groups at the central unit - **6b**. Here homogenous foams with an average cell size of  $3.9\ \mu\text{m}$  and a density of  $56\ \text{kg m}^{-3}$  were generated.

Consequently, the kinked bisamide **6b** was selected as additive for a continuous foam extrusion process on pilot scale analogous to BTA **1**. All generated polystyrene extrusion foams show comparable foam densities in the range of 67 to  $80\ \text{kg m}^{-3}$ . Due to its better solubility compared to additive **1** even a concentration of 0.5 wt.% of **6b** could be completely dissolved in the polystyrene melt and hence providing a larger number of potential nuclei for the foam nucleation. Therefore, the lowest mean cell size was determined to be only  $10\ \mu\text{m}$  with a concentration of 0.5 wt.% **6b**. In addition, by the plasma etching technique we found that unlike trisamide **1** the diameter of the self-assembled supramolecular fibers of bisamide **6b** are independent of the concentration deployed. This further increases the possible amount of nucleation sites during the foaming process. Ultimately, no larger amount of non-dissolved additive aggregates were found in the plasma etched foams even at the highest concentration which confirms the better solubility of this additive in polystyrene.

Due to the decrease in the cell size a further reduction of the overall thermal conductivity was measured. The foams containing 0.1 and 0.5 wt.% bisamide **6b** feature a thermal conductivity of  $0.0328\ \text{W m}^{-1}\text{K}^{-1}$  and  $0.0329\ \text{W m}^{-1}\text{K}^{-1}$  respectively, which equals an outstanding reduction of 26 % compared to the corresponding foam without additives.

Finally, the kinked bisamide **6b** was also tested in a foam injection molding setup. In this process a morphology control of the additive was also observed, resulting in foams with drastically reduced cell size and an improved overall homogeneity. Unfortunately, the produced injection molded foams showed defects on a macroscopic level which is attributed to polymer degradation during processing regardless if an additive was used or not. Therefore, the thermal conductivity could not be determined.



## 5 Experimental part

### 5.1 Polymer and chemicals

The polystyrene grade used is PS 168N manufactured by INEOS Styrolution (Frankfurt am Main, Germany) and supplied in form of 3 mm cylinder granules (3 x 2 mm). According to the manufacturer, it is a high-molecular weight, heat resistant grade with high mechanical strength. Furthermore, it is stated that the grade is suitable for chemical and physical foaming.<sup>[190]</sup> **Table 5.1** lists the most important data as specified by the manufacturer.

**Table 5.1:** Summary of the relevant properties of the used polystyrene grad PS 168N as stated by the manufacturer.<sup>[190]</sup>

	Value	Unit	Standard
<b>Rheological properties:</b>			
Melt Volume Rate (200 °C, 5 kg)	1.5	cm <sup>3</sup> 10 <sup>-1</sup> min <sup>-1</sup>	ISO 1133
<b>Thermal properties:</b>			
Glass transition temperature (10 K min <sup>-1</sup> )	101	°C	ISO11357-1/-2
Thermal conductivity	0.17	W m <sup>-1</sup> K <sup>-1</sup>	DIN 52612-1
<b>Optical properties:</b>			
Haze	2	%	ASTM D 1003
Light transmission (550 nm)	89	%	ASTM D 1003
<b>Other properties:</b>			
Density	1040	kg m <sup>-3</sup>	ISO 1183

Since it is a high-molecular polystyrene, it has a very low melt volume rate and therefore a high melt strength. This predestines it for the application in foaming processes. The glass transition temperature of this amorphous thermoplastic is 101 °C, which results in a relatively wide service temperature range below this temperature. Furthermore, the low thermal conductivity of polystyrene itself makes it ideal for use in thermal insulation applications. Due to its completely amorphous structure, the grade has a haze of 2 % and a light transmission of 89 %. This makes it possible to detect even small concentrations of additional substances in the polystyrene, as long as they are in the detectable size range. The density of the bulk material has a value of 1040 kg m<sup>-3</sup> and serves as a reference value for the determination of the density reduction or the volume expansion ratio. The molecular weight was determined with a size exclusion chromatography to be 340 kg mol<sup>-1</sup> with a polydispersity index of 2.3.

## Experimental part

---

The synthesis of the bisamides were carried out by Doris Hanft, Sandra Ganzleben and Jutta Failner at the chair Makromolekulare Chemie I University of Bayreuth. Characterization, analysis and evaluation were performed by myself.

The commercially available trisamide N,N',N''-Benzene-1,3,5-triyltris(2,2-dimethylpropanamide) also known as Irgaclear XT 386 was kindly provided by Ciba Specialty Chemicals. The commercially available bisamide N,N'-dicyclohexyl-2,6-naphthalene dicarboxamide also known as NJSTAR NU-100 was purchased from New Japan Chemical Co.

The silicone oil M100 medium viscosity purchased from Carl Roth GmbH + Co. KG was used as the oil bath for foaming the samples.

All chemicals were commercially available and used without further purification.

CO<sub>2</sub> with a purity of 99.995 % was supplied by Rießner Gase GmbH.

## 5.2 Analytical methods

- <sup>1</sup>H NMR** The <sup>1</sup>H NMR spectra were measured on a Bruker AC spectrometer (300 MHz). The solvent was either DMSO-d<sub>6</sub> or CDCl<sub>3</sub>/CF<sub>3</sub>COOD and served as an internal standard. The chemical shift is given in ppm and the multiplicity of the signals is indicated by s (singlet), d (doublet), t (triplet), q (quartet), qi (quintet) and sx (sextet).
- DSC** Differential scanning calorimetry (DSC) were carried out using a Mettler Toledo DSC 2. Therefore about 6–12 mg of the substance were weight into a high-pressure pan (30 μL). The additives **4a–4d**, **5a**, **5d**, **6a** and **6d** were measured in a temperature range from 25–300 °C and the additives **1**, **2**, **3a**, **3b**, **5b**, **5c**, **6b** and **6c** in a temperature range of 25–350 °C with a rate of 10 K min<sup>-1</sup> respectively. Every heating and cooling step was repeated three times. The reported melting points are taken from the second heating step, the glass transition of the second cooling step.
- MS** Mass spectra (MS) were carried out using electron spray ionization on a FINNIGAN MAT 8500 spectrometer from Thermo-Fisher scientific.
- IR** Infrared (IR) spectra were measured on a PerkinElmer Spectrum 100 FT-IR using the attenuated total reflection (ATR) method. The spectra were recorded in a range of 4000 to 650 cm<sup>-1</sup>. The signal intensity is indicated by w (weak), m (medium) and s (strong).
- TGA** Thermogravimetric analysis (TGA) were carried out on a Mettler Toledo TGA/SDTA 851e with a TS0800GC1 Gas Controller and a Mettler Toledo DSC3+ with auto sampler. Around 5 to 10 g of each additive were weight in a TiO<sub>2</sub> crucible and heated from 30–700 °C with a rate of 10 K min<sup>-1</sup> under nitrogen atmosphere. The temperature at which a weight loss of 5 % occurred is indicated.
- SEC** Size exclusion chromatography (SEC) was performed utilizing a Waters 515 HPLC pump and THF as eluent at a flow rate of 0.5 mL min<sup>-1</sup>. A volume of 100 μL of polymer solution (1–2 mg mL<sup>-1</sup>) was injected with a 707 Watersauto-sampler into a column setup comprising a guard column (ResiPore Guard, 5 × 0.75cm, particle size 3 μm) and two separation columns (ResiPore,

30 × 0.75 cm, particle size 3 μm). Polymer size distributions were monitored with a Waters 998 photodiode array detector at 254 nm and a Waters 414 refractive index detector. Narrow distributed polystyrene standards were used for calibration and 1,2-dichlorobenzene as an internal reference.

**Hazemeter** The haze and the clarity values were measured according to ASTM D-1003 on injection molded specimen with a BYK Gardener Haze Guard plus. The average of at least three samples is recorded.

**SEM** Scanning electron microscopy (SEM) pictures were taken with a Zeiss LEO 1530 with an acceleration voltage of 3 kV using an in-lens or a SE2 detector. Therefore, the foam samples were cryo fractured with liquid nitrogen and the breaking edges were sputtered with 2 nm platinum under argon atmosphere using a Cressington Sputer Coater 208HR. The samples were additionally wrapped with a copper foil prior to the sputter process to ensure a better conductivity.

**PolMic** The polarization microscope (PolMic) used in this work was a Nikon DIAPHOT 300. The pictures were recorded with a Nikon DS Ri2 digital camera with the software NiS-Elements. For the dynamic thermal experiments, a Mettler Toledo HS1 hot stage controller and HS82 hot stage were used. The heating and cooling rates were set to 10 K min<sup>-1</sup>.

**Thermal conductivity** The thermal conductivities of the foam samples were measured by the heat flow meter LaserComp FOX 50 from TA Instruments. Foam samples were cut into cylinders with a diameter of 60 mm and thicknesses (L) between 3 and 8 mm depending on the extruded foam thickness. The samples were positioned between two temperature-controlled plates. These plates established a temperature difference (ΔT) of 10 °C across the samples by setting the upper plate as 30 °C, while the lower plate was set as 20 °C. The resulting heat flux (Q/A) through samples was measured by two proprietary thin film heat flux transducers. Thermal conductivities (λ<sub>t</sub>) were calculated according to **Equation (28)**:

$$\lambda_t = \frac{Q \cdot L}{A \cdot \Delta T} \quad (28)$$

At least five samples from each foam at different positions were measured and average values of the thermal conductivities were determined.

### Density

Foam density was calculated by the water-displacement method (ISO 1183) predicated on the Archimedes principle using a Mettler Toledo XP 205 with density kit. Therefore, small rectangles were cut out of the sample and weight in air ( $m_{air}$ ). Afterwards the boost of samples was determined under water ( $m_{water}$ ;  $\rho_{water}$ : Density of water at measurement temperature) The resulting density ( $\rho_{foam}$ ) was calculated with the following equation:

$$\rho_{foam} = \frac{m_{air}}{m_{air} - m_{water}} \cdot \rho_{water} \quad (13)$$

Each measurement was performed with three different rectangle of the corresponding sample and the mean value is reported.

### Morphology

The morphology of the foamed samples was examined via SEM micrographs. The area ( $A_{cell}$ ) of at least 70 cells of each sample were taken into account. Assuming a circular shape of the cells the following equation was used to determine the size( $\phi$ ) of each individual cell:

$$\phi = 2 \cdot \sqrt{\frac{A_{cell}}{\pi}} \quad (16)$$

The arithmetic average ( $\phi_m$ ) of all calculated cells is stated for each foam.

The cell density ( $N_v$ ) was calculated by Kumar's theoretical approximation.<sup>[112]</sup> Therefore the total number of cells (n) in a known area ( $A_{mic}$ ) in the SEM micrograph has to be evaluated. Together with the magnification ( $M_{mic}$ ) the cell density can be estimated with the equation below:

$$N_v = \left( \frac{n \cdot M_{mic}^2}{A_{mic}} \right)^{\frac{3}{2}} \quad (17)$$

For the determination of the cell size and cell density the image-processing program ImageJ was used.

### 5.3 Experimental procedures

#### 5.3.1 Self-assembly and solubility of the additives

To determine the shape of the supramolecular objects in which the additives crystallize, self-assembly experiments were performed. For this purpose, 500 ppm of the corresponding additive were dissolved in xylene at 130 °C for 30 minutes. After the complete dissolution, the mixture was slowly cooled down to room temperature. The precipitating additives were applied to a silicon wafer and the solvent evaporated. The silicon wafer was applied to a SEM stub using adhesive carbon foil and sputtered with a Cressington Sputter Coater 208HR under argon atmosphere with 2 nm platinum. The SEM micrographs were taken with a Zeiss LEO 1530 with an acceleration voltage of 3 kV.

The diameter of at least 70 objects of the respective additive was measured with the program AxioVision, summarized in histograms and plotted with a normal distribution.

The solubility of **1** in PS at different concentrations was determined with the optical light microscope Nikon Diaphot300 equipped with crossed polarizers and a hot-stage FP82TM from Mettler. For this purpose, about 10 mg of the corresponding extruded sample (as explained in 5.3.2.1) were melted between two microscope slides and pressed into films with a thickness of 50 – 100  $\mu\text{m}$ . First, the films were heated up to 300 °C with a heating rate of 10 K  $\text{min}^{-1}$  to determine the solubility temperature of the additive at which all supramolecular objects were dissolved in the polymer matrix. Subsequently, the films were cooled down to room temperature with a cooling rate of 10 K  $\text{min}^{-1}$  to determine the self-assembly temperature, at which the first self-assembled supramolecular objects appear.

## 5.3.2 Batch foaming

### 5.3.2.1 Preparing the polymer/additive-compounds

#### Preparation of the powder-powder masterbatches

Therefore, the polymer granulate was grounded with the ultra-centrifugal mill Retsch ZM200 with a mesh size of 1000  $\mu\text{m}$  and a rotation speed of 18000 rpm to ensure further incorporation and distribution of the additive. During the grinding process the polymer was cooled with liquid nitrogen.

The ground PS was mixed with 1.0 wt.% of the corresponding additive to generate the powder-powder masterbatch. To ensure a good distribution the masterbatch was mixed with a Heidolph Reax 2 overhead shaker for 24 h with 50 rpm

#### Compounding and Injection molding

The compounding was done with the co-rotating twin screw-compounder DSM Xplore 15 mL. The materials got compounded for 5 minutes with a screw speed of 50 rpm at a temperature of 260 °C under nitrogen atmosphere. After that, the melt was discharged into the injection molding barrel for 2 min.

Since it is time-consuming to empty the extruder completely and a defined dead volume remains, it is advantageous to prepare a dilution series to enable different concentrations. At the beginning, the extruder is filled with 13.5 g of the corresponding material. Around 8.1 g can be transferred into the injection molding barrel while 5.4 g are left behind in the compounder. With this knowledge it is possible to realize the desired concentrations. Compounds with the following concentrations were produced with all additives: 1.0, 0.75, 0.5, 0.25, 0.1, 0.05, 0.025 and 0.01 wt.%. At the beginning a cleaning run was carried out for each additive.

The Injection molding was performed on the Micro-injection-molding machine DSM Xplore 12 mL. The barrel had a temperature of 250 °C and the melt got injected into the surface polished mold with a pressure of 6 bar for 10 s. The pressure was held for another 10 s before the round platelets with a diameter of 27 mm and a thickness of 1.1 mm could be obtained.

### 5.3.2.2 Saturation and foaming

#### Pre-Treatment

In order to eliminate the internal stress of the specimens resulting from the injection molding process, they are annealed in a closed iron mold at 135 °C for 4 h. The stress-free sample guarantee a uniform foaming.

#### CO<sub>2</sub>-uptake due to Saturation

For the saturation of the samples a Berghof HR 500 high-pressure autoclave was used. The saturation process took place at room temperature for 24 h at 50 bar CO<sub>2</sub>. To determine the CO<sub>2</sub>-uptake  $M_t$ , the sample was weighed before the saturation process ( $W_{ini}$ ) and at certain times ( $W_t$ ) after opening the autoclave. The resulting CO<sub>2</sub>-uptake can be calculated by using equation (3).

#### Foaming of the Polymer compounds

After saturation, the specimen were slowly depressurized and at air for 18 min to reach a CO<sub>2</sub>-saturation of ~6.5 %. Subsequently the samples were immersed in a hot silicon oil bath at 130 °C for 15 s to induce the foaming.

To stabilize the cells the emerging foams were first cooled in a cold oil bath and second in a cold-water bath for around 20 s each time. Finally, the resulting foams were washed with soap water and left drying at air for 24 h prior to further analysis.

It should be noted that a variety of foaming temperatures (125 – 140 °C; 5 °C-steps), with different foaming times (10 – 35 s; 5 s steps) and diverse CO<sub>2</sub>-saturations have been tested. Since the conditions mentioned above generated foams with very small cells and a low-density, they have been selected as the standard condition throughout the work.

### 5.3.3 Extrusion foaming

The foam extrusion were carried out on a tandem extrusion line from Dr. Collin GmbH (twin - screw extruder with 25 mm screw and L/D 42; single - screw extruder with 45 mm screw and L/D 30) equipped with a slit die with a 0.6 mm gap and 30 mm width. Neat extruded XPS foam and XPS foams with three selected concentrations of the additive, i.e. 0.1, 0.2 and 0.5 wt.% were produced. The various concentrations of additive in PS were obtained by dilution of a masterbatch with neat PS granulates by controlling their flow rates. A combination of 4 wt.% CO<sub>2</sub> and 3 wt.% EtOH was used as physical blowing agent. A calibrator was applied to prescribe the final dimensions of the extruded foam sample. To obtain a reference foam, neat PS granulates were extruded in the same manner.

The relevant processing parameters used for the foam extrusion are summarized in **Table 5.2**

**Table 5.2:** Processing parameters for foam extrusion of PS foams.

Inlet-melt temperature [°C]	Outlet-melt temperature [°C]	Die temperature [°C]	Screw speed [rpm]	Throughput [kg h <sup>-1</sup> ]	Blowing agent [wt.%]	
					CO <sub>2</sub>	EtOH
260	106 - 130	123 - 132	8	4.5	4	3

### O<sub>2</sub>-plasma treatment

For the O<sub>2</sub>-plasma etching a Plasma Cleaner Flecto 10 USB from Plasma Technology was used. The samples were placed on a glass slide in the plasma chamber and exposed for 60 min to a plasma power of 100 % at 0.15 mbar.

### 5.3.4 Foam injection molding

The foam injection molding was carried out on a Wittmann Battenfeld HM110/525 injection molding machine. The CellMould injection unit has a screw diameter of 35 mm and an L/D ratio of 25. In the polystyrene matrix 0.1 and 0.5 wt.% of the additives were incorporated by Lifocolor Farben GmbH & Co. KG in Lichtenfels in an extra compounding step. This step was carried out at a melt temperature of 240 °C and the resulting polymer was granulated afterwards. In order to take the thermal impact of this additional step into account, not only the additivated compounds but also those without additives were produced in this way. A total of four different materials were thus used in foam injection molding. Pure polystyrene as provided by the manufacturer, pure polystyrene which has undergone the additional compounding step just described, and the two with 0.1 and 0.5 wt.% of additive **6b**. Before each use, the material was pre-dried in a Wittmann Drymax E30 for 4 h at 80 °C. As physical blowing agent 0.7 % N<sub>2</sub> was added in the beginning of the extruder. The used breathing mold had a size of 445 x 318 mm and was initially adjusted to a thickness of 2 mm. For the actual foaming process, it was then moved up to 3.5 and 5.5 mm in a controlled manner. The relevant process parameters for the high-pressure process are listed in **Table 5.3**.

**Table 5.3:** Processing parameters for the foam injection using the high-pressure method with a breathing mold.

---

<b>Melt temperature [°C]</b>	<b>Mold temperature [°C]</b>	<b>Screw speed [m s<sup>-1</sup>]</b>	<b>Dynamic pressure [bar]</b>	<b>Injection pressure [bar]</b>	<b>Shot volume [ccm]</b>	<b>Cycle time [s]</b>	<b>Cooling time [s]</b>
240	40	0.2	130	1070	42	45.8	35

---

## 5.4 Synthesis of the additives

### 5.4.1 Synthesis of the benzene trisamides

#### 5.4.1.1 N,N',N''-Tris(3-methylbutyl)-1,3,5-benzenetricarboxamide - 2

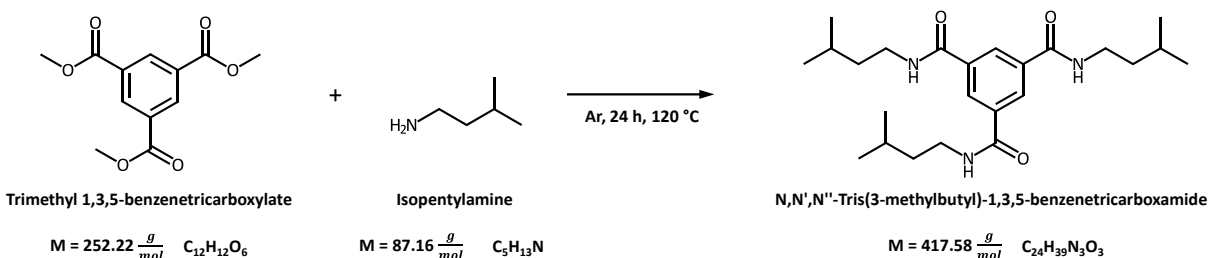


**Figure 5.1:** Reaction scheme of trimethyl 1,3,5-benzenetricarboxylate with isopentylamine to N,N',N''-Tris(3-methylbutyl)-1,3,5-benzenetricarboxamide – 2.

#### Synthesis:

181.6 g (0.72 mol)      Trimethyl 1,3,5-benzenetricarboxylate

313.5 g (3.6 mol)      Isopentylamine

Trimethyl 1,3,5-benzenetricarboxylate was placed in a Schlenk flask and dried under high vacuum. The isopentylamine was added under argon atmosphere and heated up to 120 °C. After 12 h under reflux the precipitated product was then crushed, washed with sufficient water, filtered and dried in high vacuum to receive 265 g (88 %) of the final product in form of a white powder.

#### Characterization:

$^1H$  NMR:      [DMSO- $d_6$ , 300 MHz,  $\delta$  in ppm]: 8.67-8.63 (3H, t,  $H_{Ar}$ ), 8,35 (3H, s, NH), 3.34-3.27 (6H, q, NH- $CH_2$ ), 1.62-1.56 (3H, sx,  $CH_2$ -CH-( $CH_3$ ) $_2$ ), 1.47-1.40 (6H, q,  $CH_2$ - $CH_2$ -CH), 0.92-0.90 (18H, d,  $CH_3$ )

MS:      (70 eV), m/z (%): 417 [ $M^+$ ]

TGA:       $T_{-5wt\%} = 360$  °C

DSC:       $T_m = 269$  °C

IR:      [ATR,  $\tilde{\nu}$   $cm^{-1}$ ]: 3262 (w), 2955 (w), 2929 (w), 2869 (w), 1649 (s), 1607 (w), 1513 (w), 1462 (w), 1452 (w)

## Experimental part

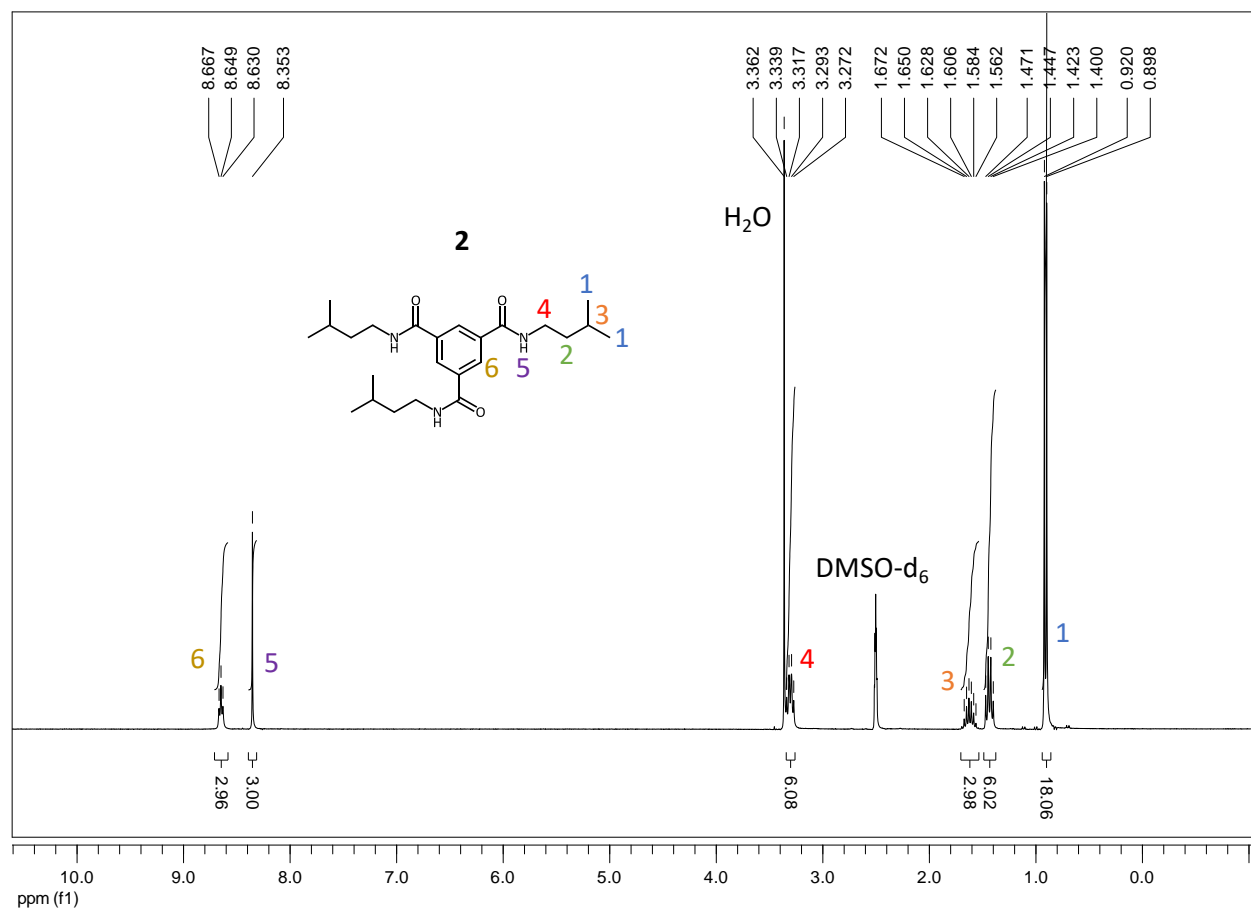


**Figure 5.2:**  $^1\text{H}$  NMR spectra of **2** in  $\text{DMSO-d}_6$ .

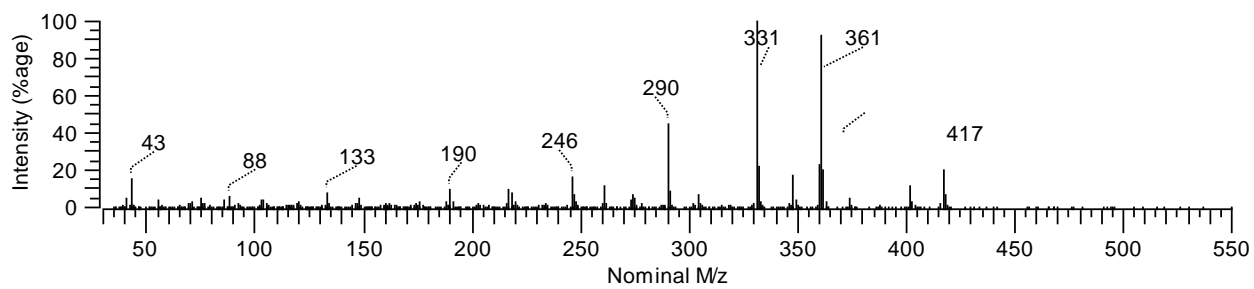


**Figure 5.3:** Mass spectra of **2**.

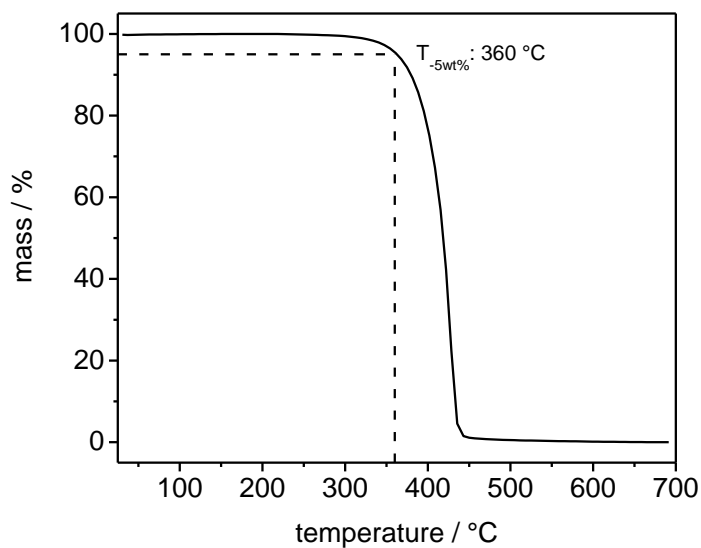


**Figure 5.4:** Thermogram of the thermogravimetric analysis of **2** with a heating rate of  $10 \text{ K}\cdot\text{min}^{-1}$  in the range 30 to 700 °C under nitrogen atmosphere. The temperature at which 5 % of the mass is lost is also stated ( $T_{-5\text{wt}\%}$ ).

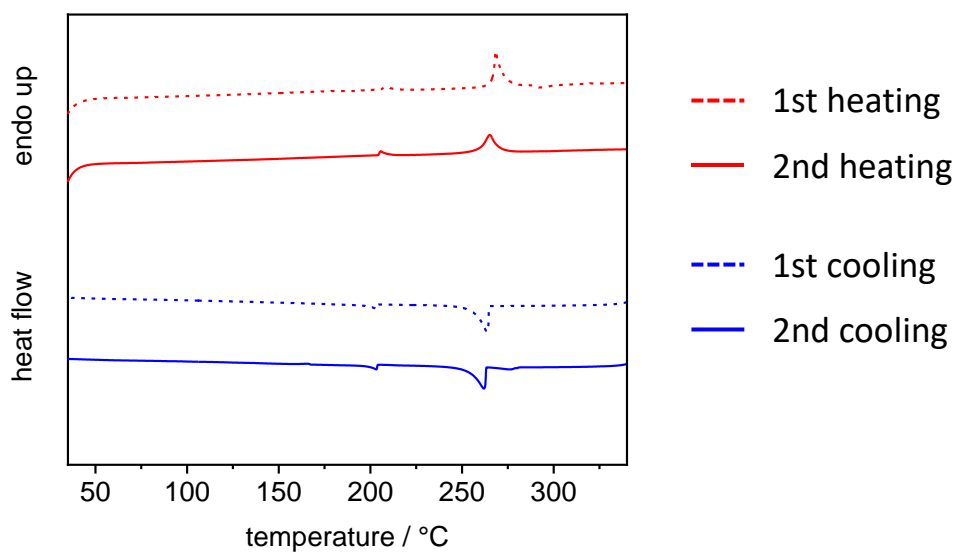


**Figure 5.5:** Differential scanning calorimetry thermograph of **2** including first and second heating and cooling respectively.

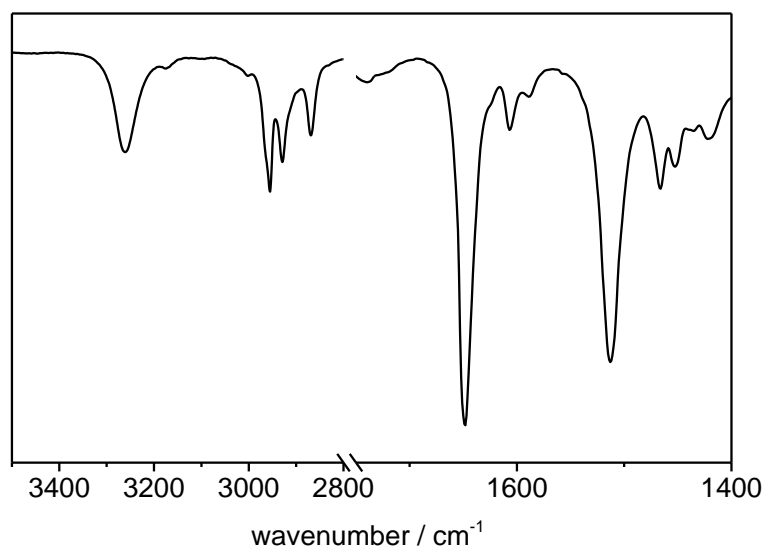


**Figure 5.6:** FT-IR spectra of **2** in the range of 3500 to 1400 cm<sup>-1</sup>.

## 5.4.2 Synthesis of the bisamides

## 5.4.2.1 N,N'-1,4-Phenylenebis[cyclohexanecarboxamide] - 3a

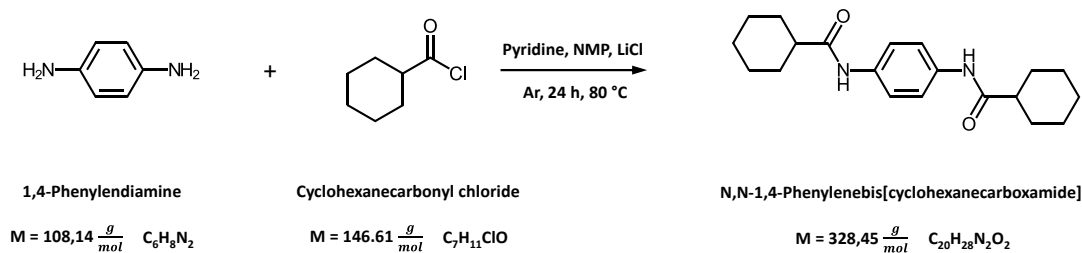


**Figure 5.7:** Reaction scheme of 1,4-Phenylenediamine with cyclohexanecarbonyl chloride to N,N'-1,4-Phenylenebis[cyclohexanecarboxamide] – **3a**.

**Synthesis:**

9 g (81 mmol)	1,4-Phenylenediamine
28.47 g (195 mmol)	Cyclohexanecarbonyl chloride
100 mL	Pyridine
300 mL	NMP
	LiCl

1,4-Phenylenediamine, pyridine, NMP and LiCl were mixed in a Schlenk flask and cooled down to 0 – 5 °C. Under argon atmosphere the cyclohexanecarbonyl chloride was added dropwise. The reaction was then heated to 80 °C for 12 h and afterwards precipitated in ice water. The solid was then filtered off and dried. For further purification the solid was recrystallized from DMF, filtered and dried in high vacuum to receive 25.1 g (92 %) of the final product in form of a white powder.

**Characterization:**

$^1H$ NMR:	[CDCl <sub>3</sub> /CF <sub>3</sub> COOD, 300 MHz, $\delta$ in ppm]: 7.47 (4H, s, H <sub>Ar</sub> ), 2.55-2.46 (2H, m, CH <sub>Cyc</sub> ), 2.10-1.28 (20, m, CH <sub>2Cyc</sub> )
MS:	(70 eV), m/z (%): 328 [M <sup>+</sup> ]
TGA:	T <sub>-5wt%</sub> = 339 °C
DSC:	T <sub>m1</sub> = 286 °C; T <sub>m2</sub> = 327 °C
IR:	[ATR, $\tilde{\nu}$ cm <sup>-1</sup> ]: 3302 (m), 2942 (s), 2851 (m), 1652 (m), 1540 (s), 1519 (s), 1447 (m), 1403 (s)

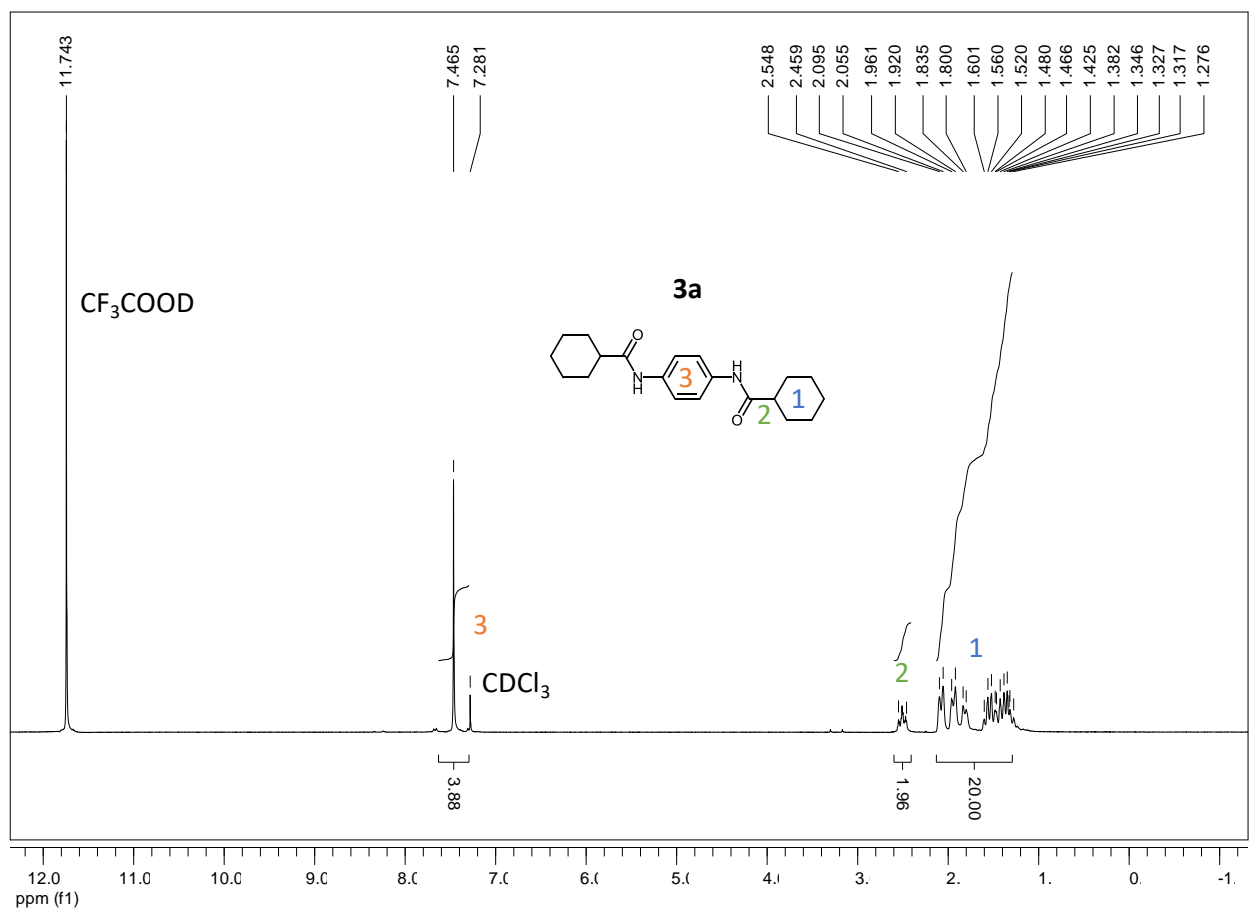


**Figure 5.8:**  $^1\text{H}$  NMR spectra of **3a** in  $\text{CDCl}_3/\text{CF}_3\text{COOD}$ .

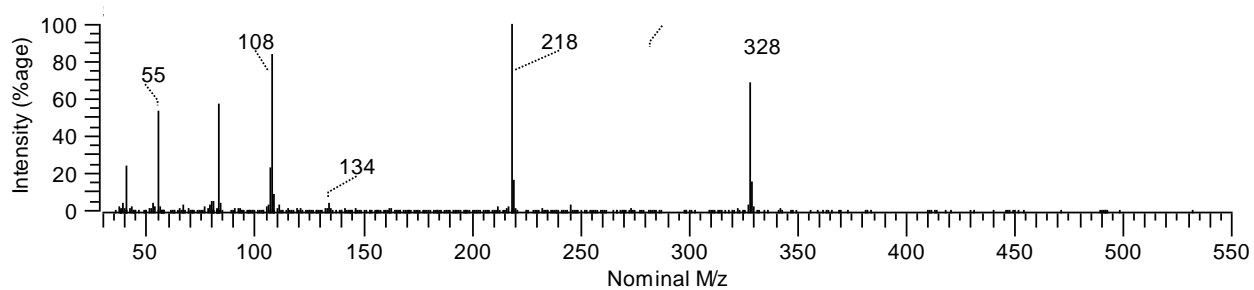


**Figure 5.9:** Mass spectra of **3a**.

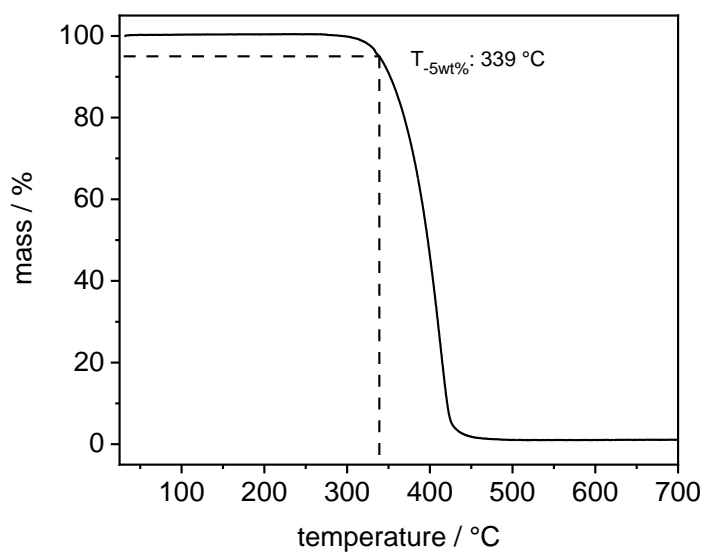


**Figure 5.10:** Thermogram of the thermogravimetric analysis of **3a** with a heating rate of  $10 \text{ K}\cdot\text{min}^{-1}$  in the range 30 to 700 °C under nitrogen atmosphere. The temperature at which 5 % of the mass is lost is also stated ( $T_{-5\text{wt}\%}$ ).

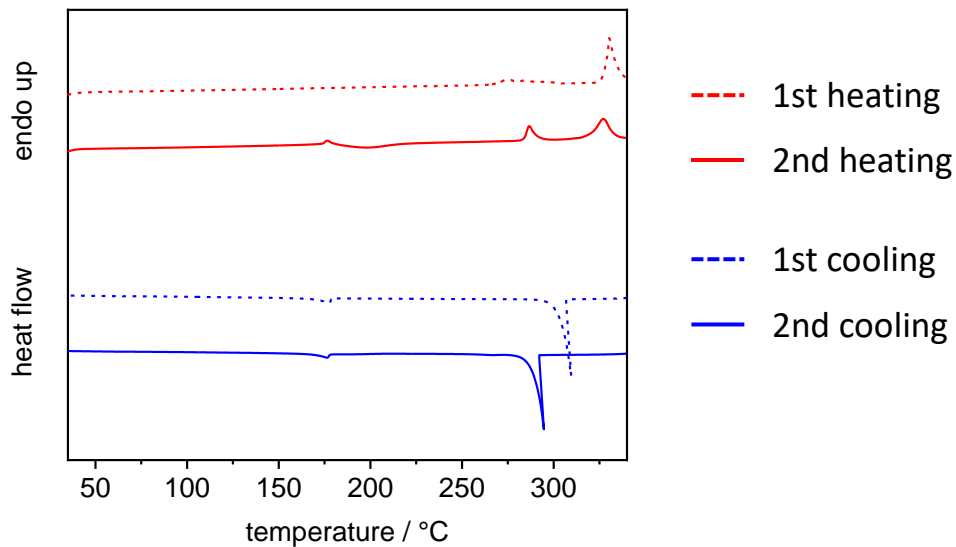


**Figure 5.11:** Differential scanning calorimetry thermograph of **3a** including first and second heating and cooling respectively.

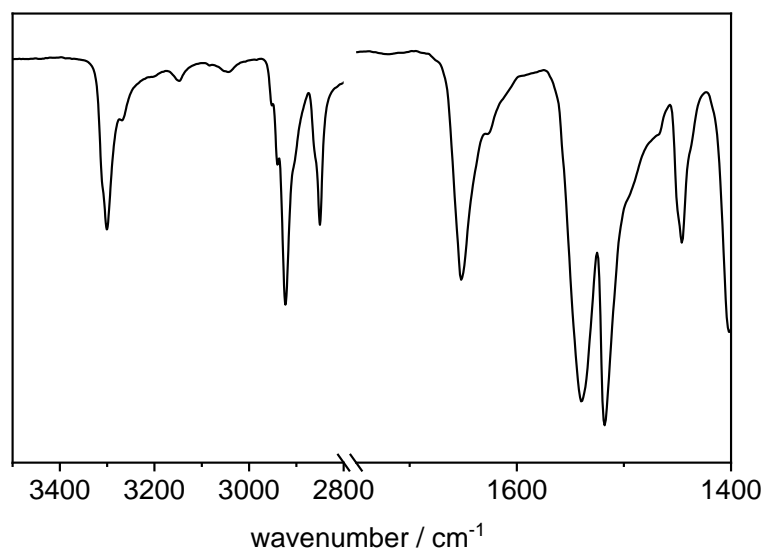


**Figure 5.12:** FT-IR spectra of **3a** xylene in the range of 3500 to 1400 cm<sup>-1</sup>.

## 5.4.2.2 N,N'-[Methylenebis(4,1-phenylene)]bis[benzamide] - 4a

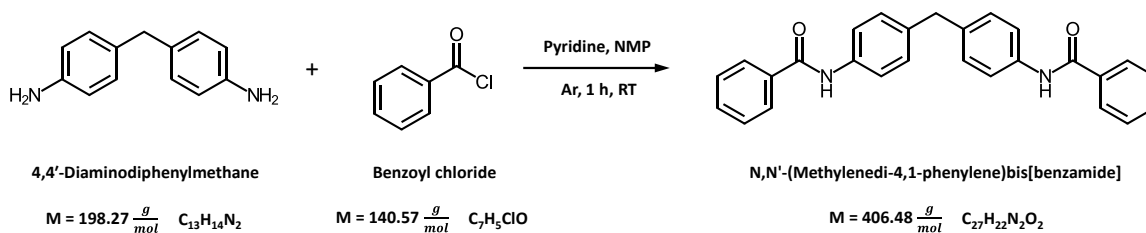


**Figure 5.13:** Reaction scheme of 4,4'-diaminodiphenylmethane with benzoyl chloride to N,N'-[Methylenebis(4,1-phenylene)]bis[benzamide] – 4a.

**Synthesis:**

5 g (25,2 mmol)	4,4'-Diaminodiphenylmethane
7.79 g (55,4 mmol)	Benzoyl chloride
4.5 mL	Pyridine
100 mL	NMP

4,4'-Diaminodiphenylmethane, pyridine and NMP were mixed in a Schlenk flask and cooled down to 0 – 5 °C. Under argon atmosphere and the benzoyl chloride was added dropwise and the mixture was heated to room temperature afterwards. After one hour the reaction mixture was precipitated in ice water and the solid was filtered off and dried. For further purification, the solid was refluxed in 500 mL MeOH, filtered and dried in high vacuum to receive 9.65 g (95 %) of the final product in form of a white powder.

**Characterization:**

$^1\text{H}$ NMR:	[DMSO, 300 MHz, $\delta$ in ppm]: 10.21 (2H, s, NH), 7.95-7.92 (4H, m, $\text{H}_{\text{Ar}}$ ), 7.71-7.68 (4H, d, $\text{H}_{\text{Ar}}$ ), 7.60-7.49 (6H, m, $\text{H}_{\text{Ar}}$ ), 7.22-7.19 (4H, d, $\text{H}_{\text{Ar}}$ ), 3,89 (2H, s, Ar- $\text{CH}_2$ -Ar)
MS:	(70 eV), m/z (%): 406 [ $\text{M}^+$ ]
TGA:	$T_{-5\text{wt}\%} = 408$ °C
DSC:	$T_m = 249$ °C
IR:	[ATR, $\tilde{\nu}$ $\text{cm}^{-1}$ ]: 3285 (w), 1743 (w), 1646 (s), 1604 (m), 1537 (s), 1513 (s), 1410 (m)

## Experimental part

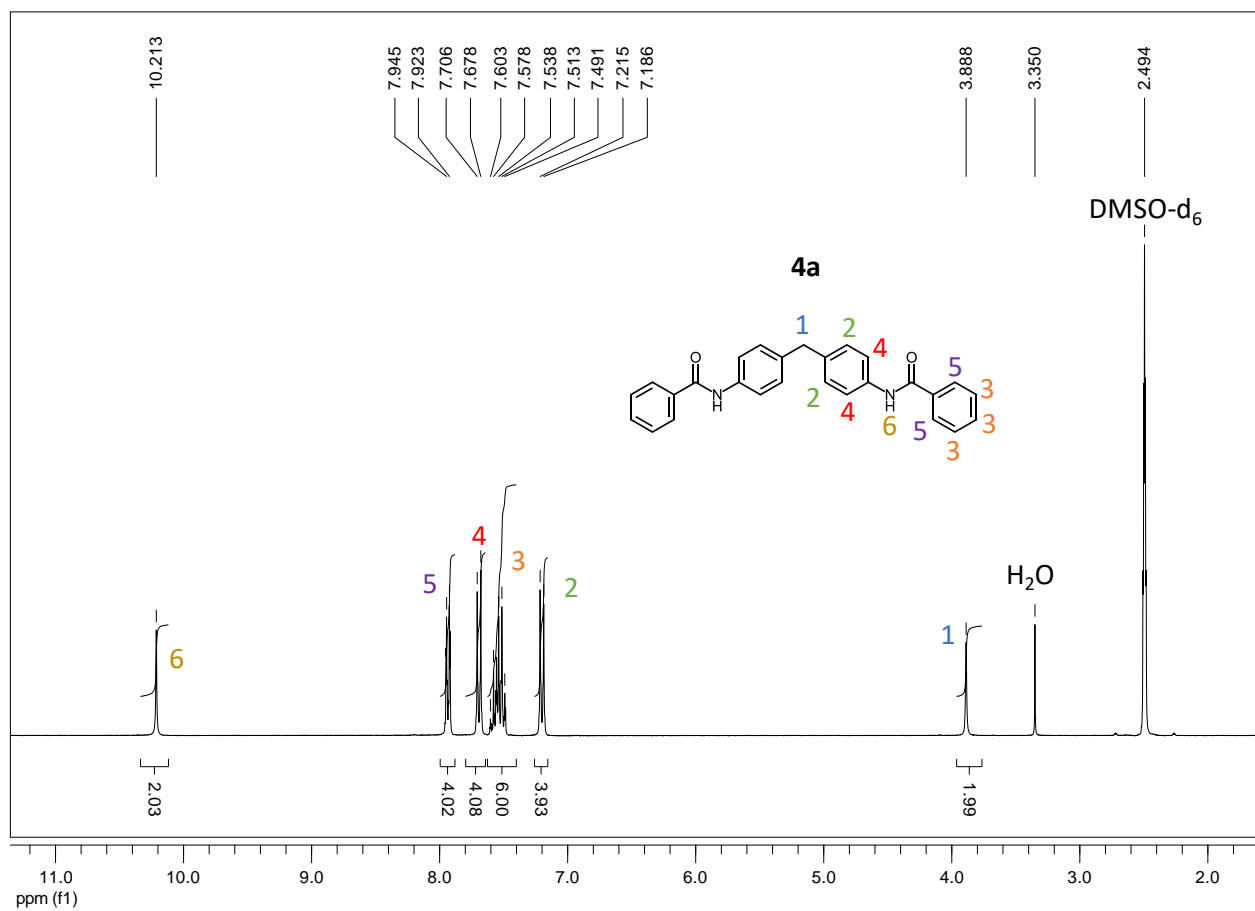


**Figure 5.14:**  $^1\text{H}$  NMR spectra of **4a** in  $\text{DMSO-d}_6$ .

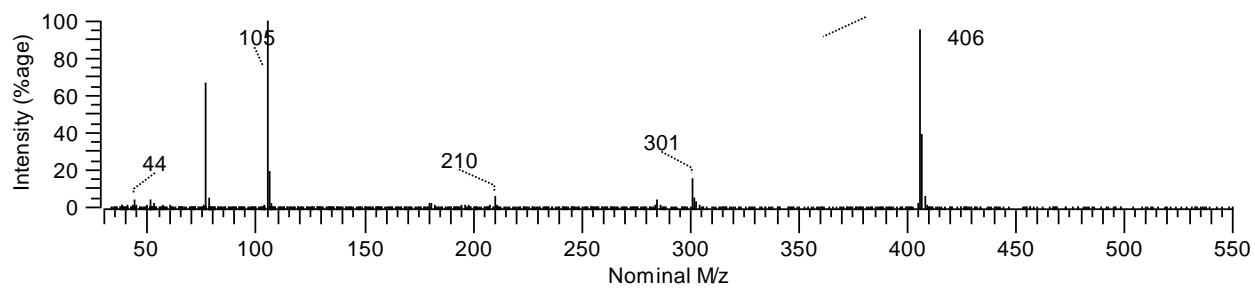


**Figure 5.15:** Mass spectra of **4a**.

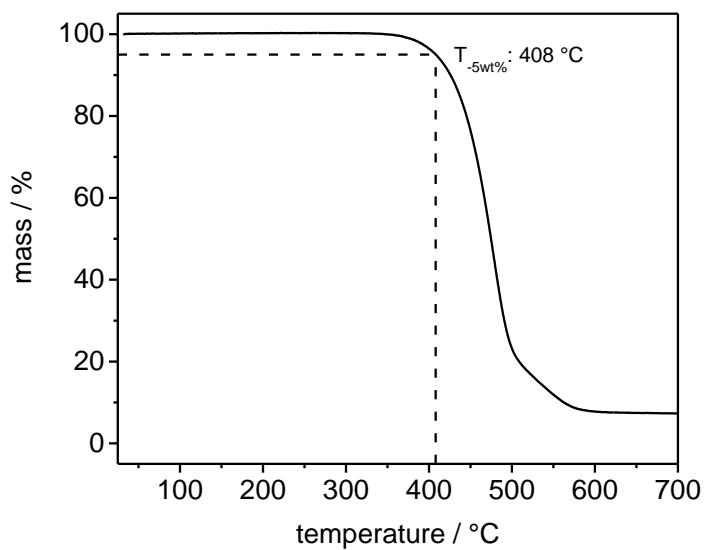


**Figure 5.16:** Thermogram of the thermogravimetric analysis of **4a** with a heating rate of  $10 \text{ K}\cdot\text{min}^{-1}$  in the range 30 to  $700 \text{ } ^\circ\text{C}$  under nitrogen atmosphere. The temperature at which 5 % of the mass is lost is also stated ( $T_{-5wt\%}$ ).

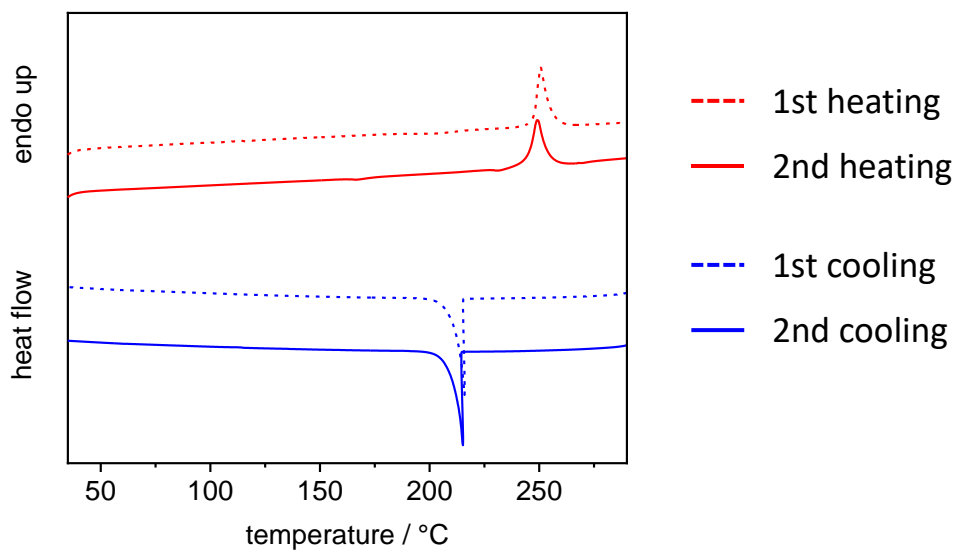


**Figure 5.17:** Differential scanning calorimetry thermographs of **4a** including first and second heating and cooling respectively.

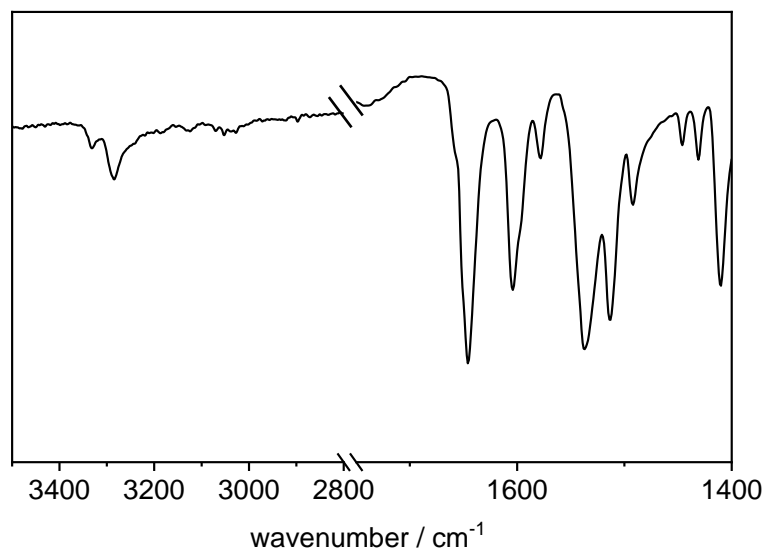


**Figure 5.18:** FT-IR spectra of **4a** in the range of 3500 to 1400  $\text{cm}^{-1}$ .

## 5.4.2.3 N,N'-[Methylenebis(4,1-phenylene)]bis[cyclohexanecarboxamide] - 4b

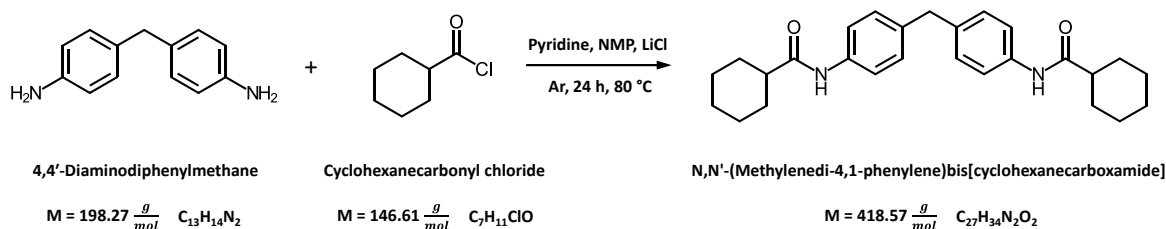


**Figure 5.19:** Reaction scheme of 4,4'-diaminodiphenylmethane with cyclohexanecarbonyl chloride to N,N'-[Methylenebis(4,1-phenylene)]bis[cyclohexanecarboxamide] – **4b**.

**Synthesis:**

3 g (15.0 mmol)	4,4'-Diaminodiphenylmethane
4.9 g (33 mmol)	Cyclohexanecarbonyl chloride
20 mL	Pyridine
100 mL	NMP
	LiCl

4,4'-Diaminodiphenylmethane, pyridine, NMP and LiCl were mixed in a Schlenk flask and cooled down to 0–5 °C. Under argon atmosphere and the cyclohexanecarbonyl chloride was added dropwise. The reaction was then heated to 80 °C for 12 h and afterwards precipitated in ice water. The solid was filtered off and dried. For further purification the solid was recrystallized from 500 mL MeOH, filtered and dried in high vacuum to receive 5.5 g (88 %) of the final product in form of a white powder.

**Characterization:**

<sup>1</sup> H NMR:	[DMSO, 300 MHz, $\delta$ in ppm]: 9.73 (2H, s, NH), 7.50-7.48 (4H, d, H <sub>Ar</sub> ), 7.10-7.07 (4H, d, H <sub>Ar</sub> ), 3.79 (2H, s, Ar-CH <sub>2</sub> -Ar), 2.32-2.25 (2H, m, CH <sub>Cyc</sub> ), 1.75-1.20 (20, m, CH <sub>2Cyc</sub> )
MS:	(70 eV), m/z (%): 418 [M <sup>+</sup> ]
TGA:	T <sub>-5wt.%</sub> = 380 °C
DSC:	T <sub>m</sub> = 222 °C
IR:	[ATR, $\tilde{\nu}$ cm <sup>-1</sup> ]: 3283 (w), 2929 (m), 2850 (m), 1657 (s), 1600 (s), 1512 (s), 1407 (s)

## Experimental part

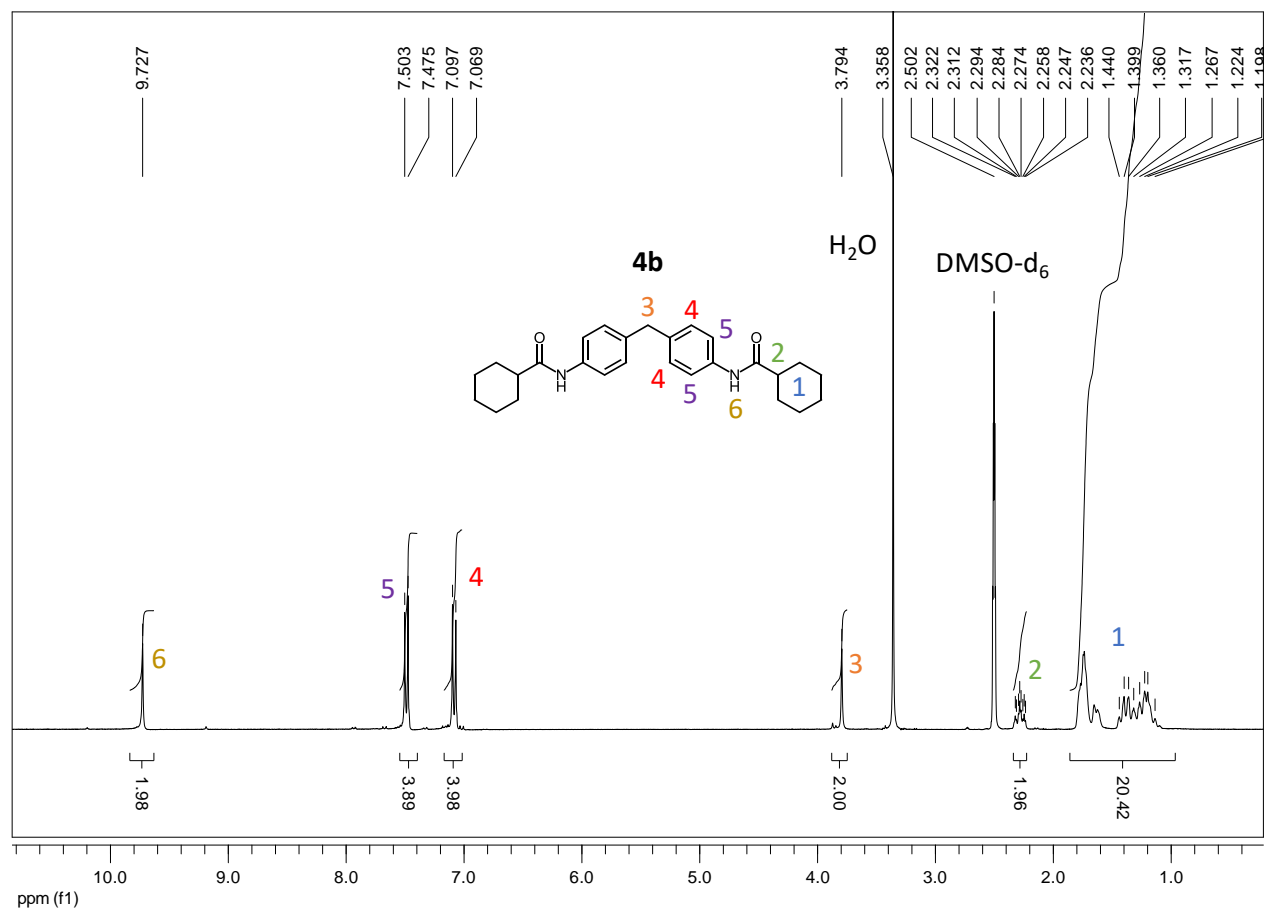


**Figure 5.20:**  $^1\text{H}$  NMR spectra of **4b** in DMSO- $d_6$ .

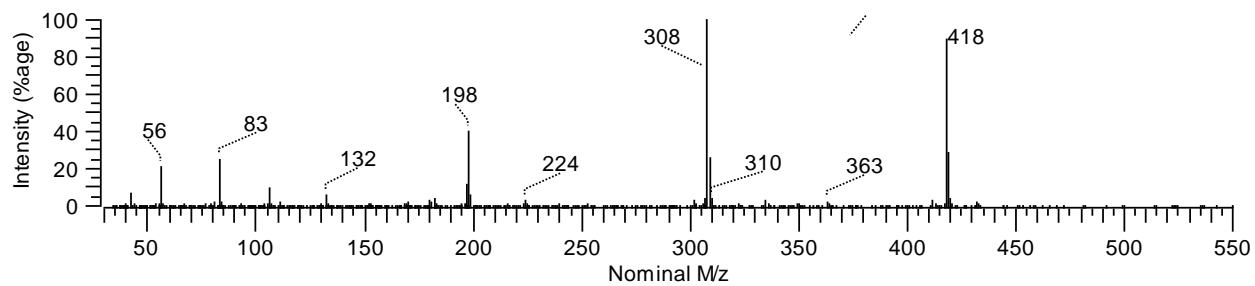


**Figure 5.21:** Mass spectra of **4b**.

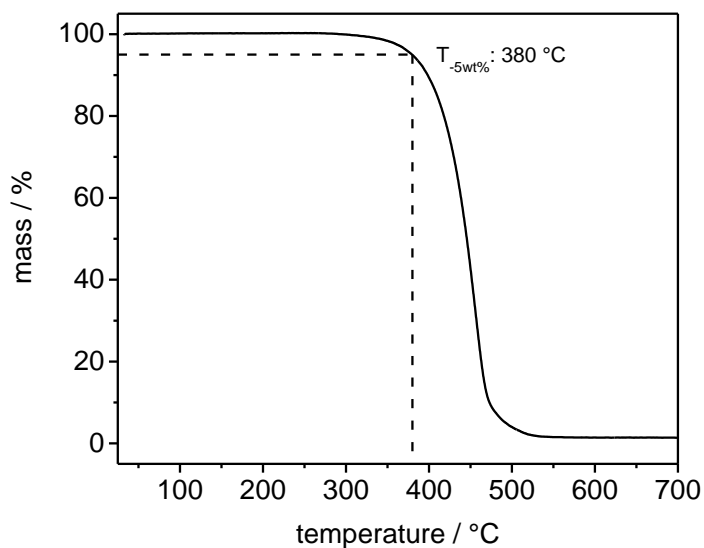


**Figure 5.22:** Thermogram of the thermogravimetric analysis of **4b** with a heating rate of  $10\text{ K}\cdot\text{min}^{-1}$  in the range 30 to 700 °C under nitrogen atmosphere. The temperature at which 5 % of the mass is lost is also stated ( $T_{-5wt\%}$ ).

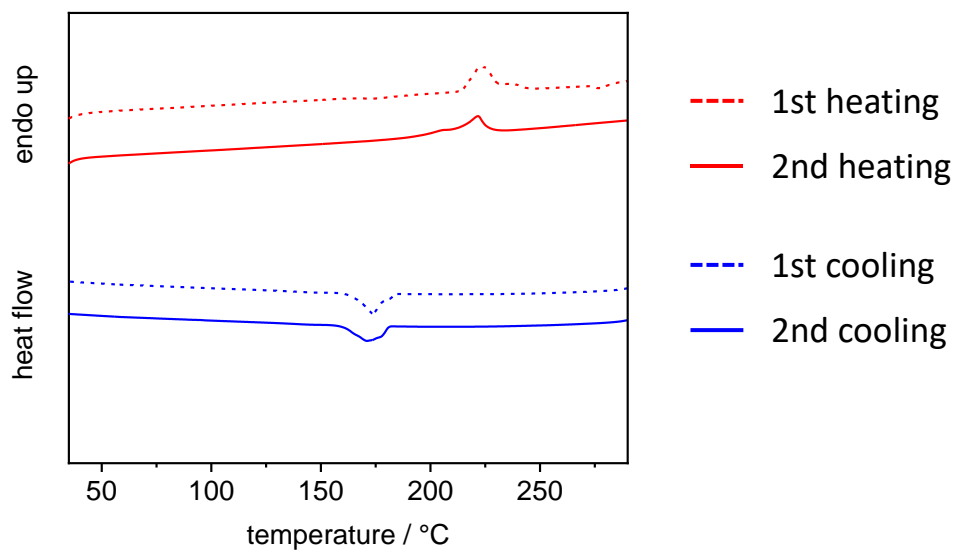


**Figure 5.23:** Differential scanning calorimetry thermographs of **4b** including first and second heating and cooling respectively.

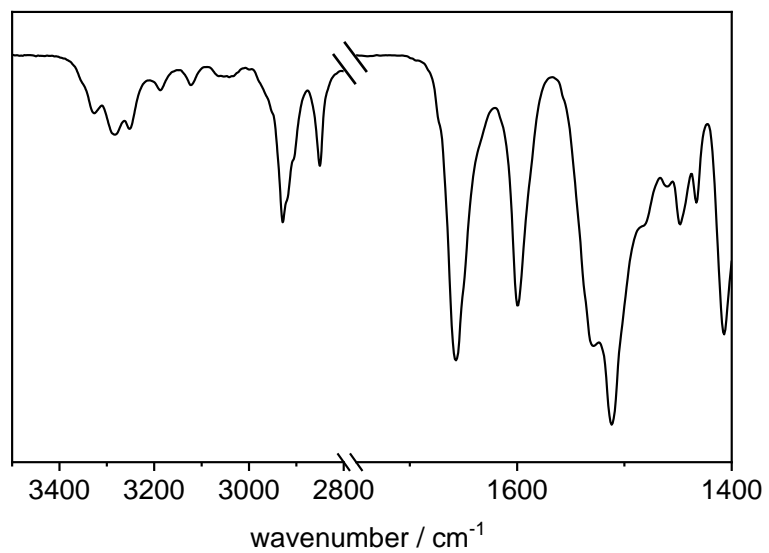


**Figure 5.24:** FT-IR spectra of **4b** in the range of 3500 to 1400  $\text{cm}^{-1}$ .

## 5.4.2.4 N,N'-[Methylenebis(4,1-phenylene)]bis[tertbutylcarboxamide] - 4c

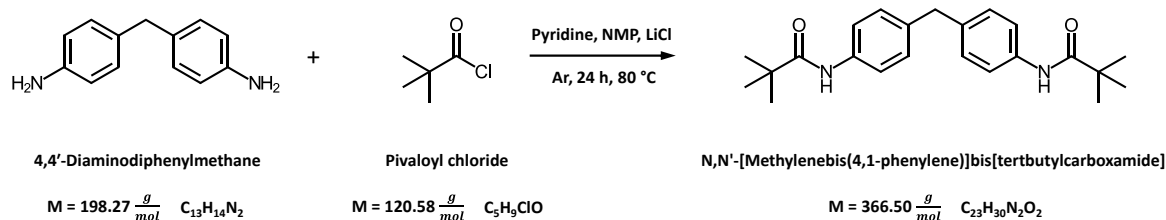


**Figure 5.25:** Reaction scheme of 4,4'-diaminodiphenylmethane with pivaloyl chloride to N,N'-[Methylenebis(4,1-phenylene)]bis[tertbutylcarboxamide] – 4c.

**Synthesis:**

3 g (15.0 mmol)	4,4'-Diaminodiphenylmethane
4 g (33 mmol)	Pivaloyl chloride
20 mL	Pyridine
100 mL	NMP
	LiCl

4,4'-Diaminodiphenylmethane, pyridine, NMP and LiCl were mixed in a Schlenk flask and cooled down to 0 – 5 °C. Under argon atmosphere the pivaloyl chloride was added dropwise. The reaction was stirred at 80 °C and afterwards precipitated in ice water. The solid was filtered off and dried. For further purification the solid was recrystallized from 500 mL ethyl acetate, filtered and dried in high vacuum to receive 4.1 g (75 %) of the final product in form of a white powder.

**Characterization:**

$^1\text{H}$ NMR:	[ $\text{CDCl}_3$ , 300 MHz, $\delta$ in ppm]: 7.46-7.44 (2H, d, $\text{H}_{\text{Ar}}$ ), 7.28 (2H, m, NH), 7.14-7.11 (2H, d, $\text{H}_{\text{Ar}}$ ), 3.92 (2H, s, Ar- $\text{CH}_2$ -Ar), 1.32 (18H, s, $\text{CH}_3$ )
MS:	(70 eV), m/z (%): 366 [ $\text{M}^+$ ]
TGA:	$T_{-5\text{wt.}\%} = 320$ °C
DSC:	$T_m = 239$ °C
IR:	[ATR, $\tilde{\nu}$ $\text{cm}^{-1}$ ]: 3327 (m), 2964 (m), 2906 (w), 2868 (w), 1654 (s), 1601 (m), 1513 (s), 1408 (s)

## Experimental part

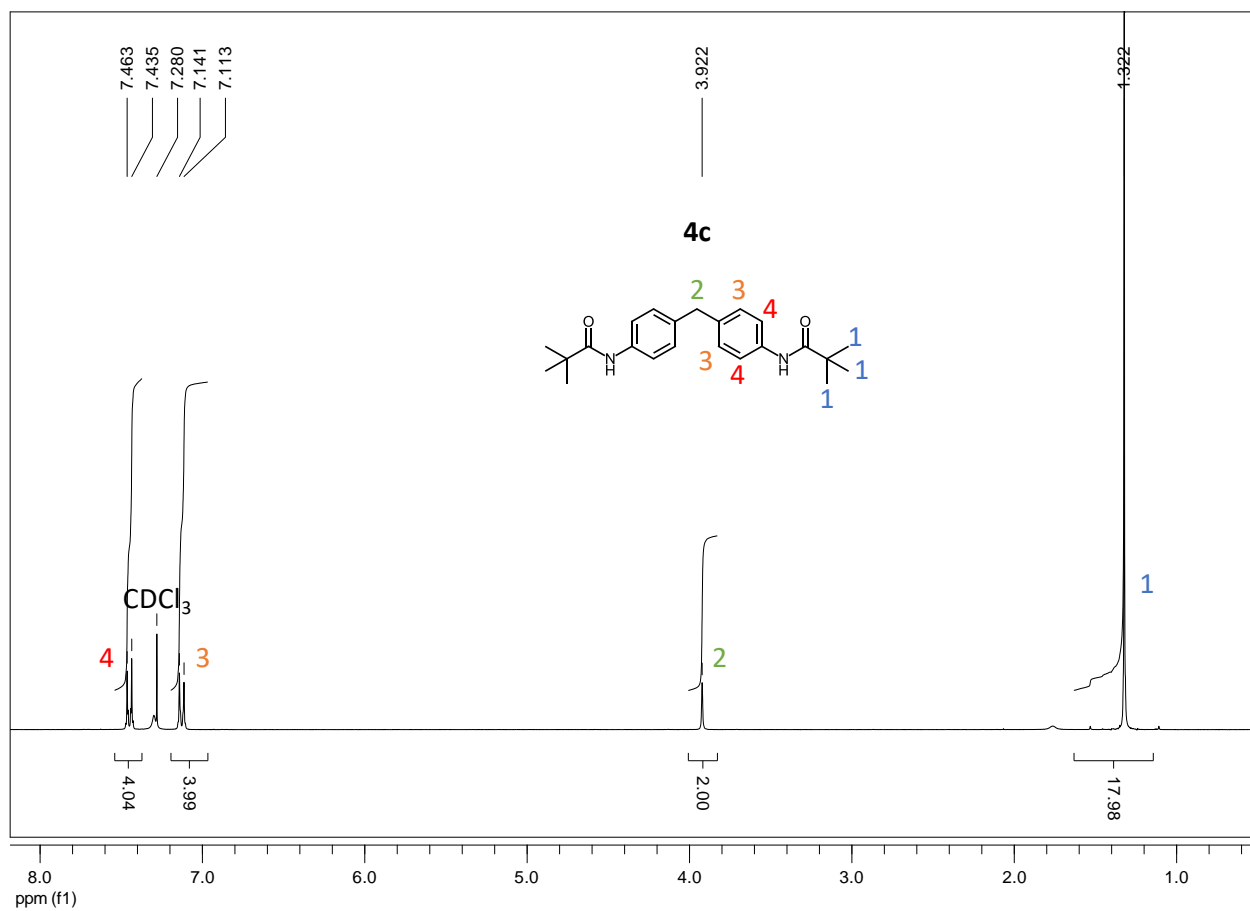


**Figure 5.26:** <sup>1</sup>H NMR spectra of **4c** in CDCl<sub>3</sub>.

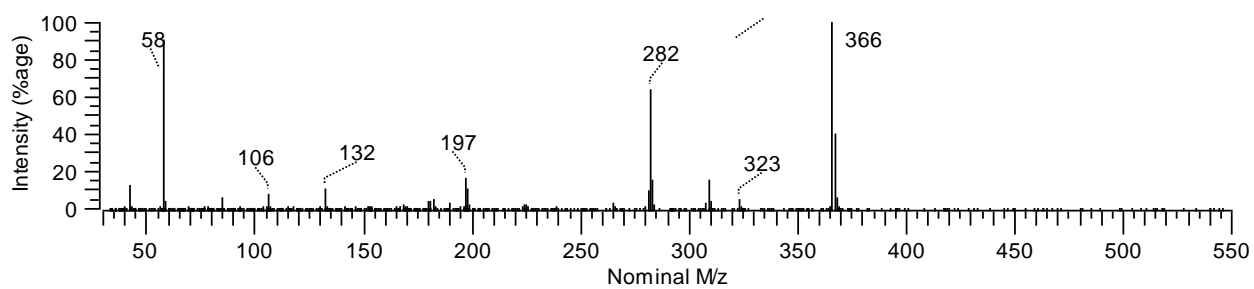


**Figure 5.27:** Mass spectra of **4c**.

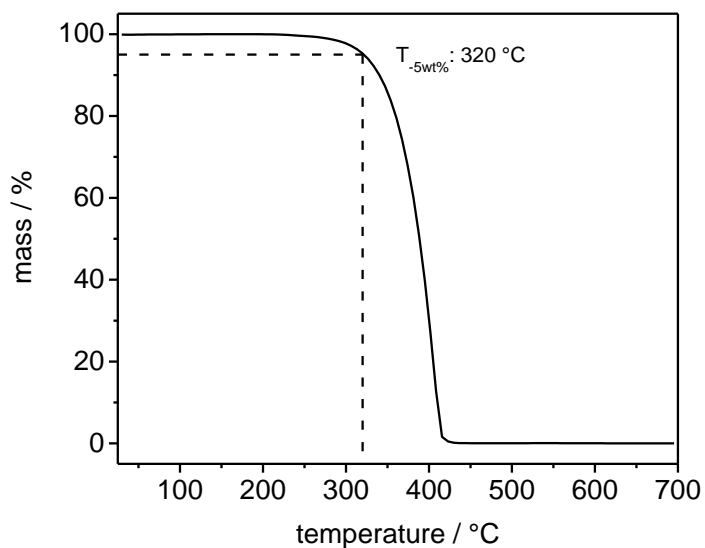


**Figure 5.28:** Thermogram of the thermogravimetric analysis of **4c** with a heating rate of  $10 \text{ K}\cdot\text{min}^{-1}$  in the range 30 to 700 °C under nitrogen atmosphere. The temperature at which 5 % of the mass is lost is also stated ( $T_{-5\text{wt}\%}$ ).

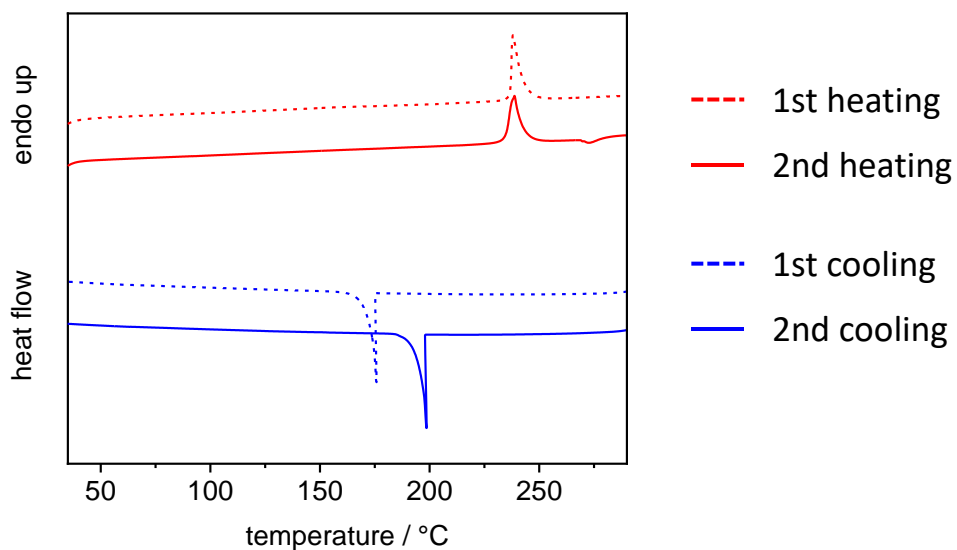


**Figure 5.29:** Differential scanning calorimetry thermographs of **4c** including first and second heating and cooling respectively.

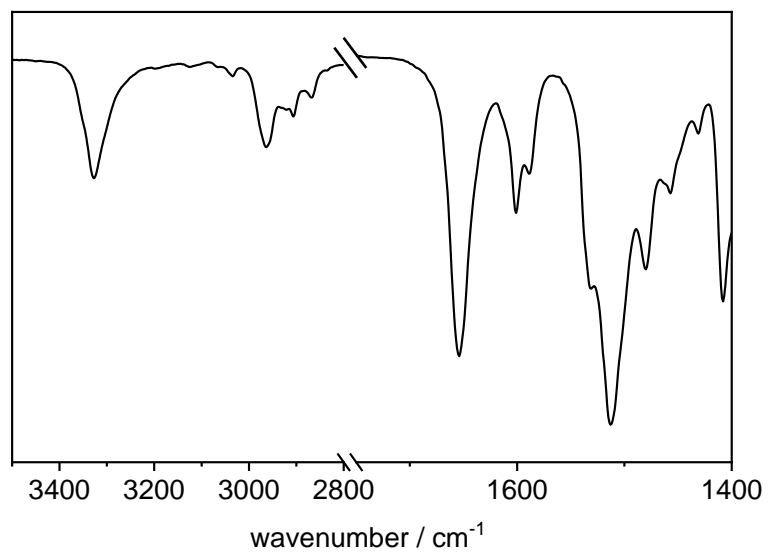


**Figure 5.30:** FT-IR spectra of **4c** in the range of 3500 to 1400 cm<sup>-1</sup>.

## 5.4.2.5 N,N'-[Methylenebis(4,1-phenylene)]bis[pentanamide] - 4d

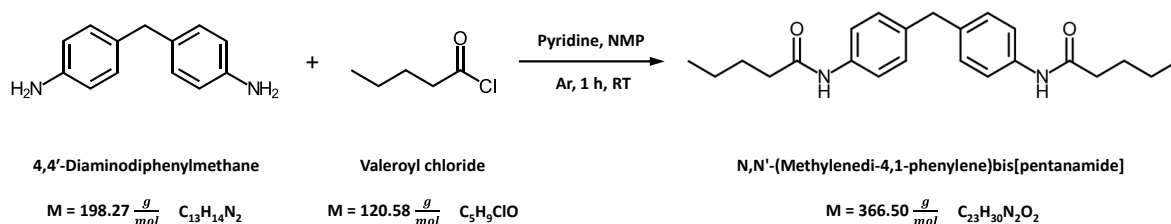


**Figure 5.31:** Reaction scheme of 4,4'-diaminodiphenylmethane valeroyl benzoyl chloride to N,N'-[Methylenebis(4,1-phenylene)]bis[pentanamide] – 4d.

**Synthesis:**

5 g (25.21 mmol)	4,4'-Diaminodiphenylmethane
6.02 g (55.47 mmol)	Valeroyl chloride
4.5 mL	Pyridine
100 mL	NMP

4,4'-Diaminodiphenylmethane, pyridine and NMP were mixed in a Schlenk flask and cooled down to 0 – 5 °C. Under argon atmosphere the valeroyl chloride was added dropwise and the mixture was heated to room temperature. After one hour at room temperature the reaction mixture was precipitated in ice water. The solid was then filtered off and dried. For further purification the solid was recrystallized from 300 mL MeOH, filtered and dried in high vacuum to receive 8.8 g (95 %) of the final product in form of a white powder.

**Characterization:**

$^1\text{H NMR}$ :	[DMSO, 300 MHz, $\delta$ in ppm]: 9.80 (2H, s, NH), 7.50-7.47 (4H, d, $\text{H}_{\text{Ar}}$ ), 7.11-7.09 (4H, d, $\text{H}_{\text{Ar}}$ ), 3.80 (2H, s, $\text{Ar-CH}_2\text{-Ar}$ ), 2.29-2.24 (4H, t, $\text{CO-CH}_2$ ), 1.58-1.53 (4H, qi, $\text{CH}_2\text{-CH}_2$ ), 1.34-1.29 (4H, sx, $\text{CH}_2\text{-CH}_3$ ), 0.91-0.86 (6H, t, $\text{CH}_2\text{-CH}_3$ )
MS:	(70 eV), $m/z$ (%): 366 [ $\text{M}^+$ ]
TGA:	$T_{-5\text{wt.}\%} = 351 \text{ }^\circ\text{C}$
DSC:	$T_m = 192 \text{ }^\circ\text{C}$
IR:	[ATR, $\tilde{\nu} \text{ cm}^{-1}$ ]: 3289 (m), 2958 (m), 2931 (m), 2873 (w), 1655 (s), 1594 (m), 1523 (s), 1407 (s)

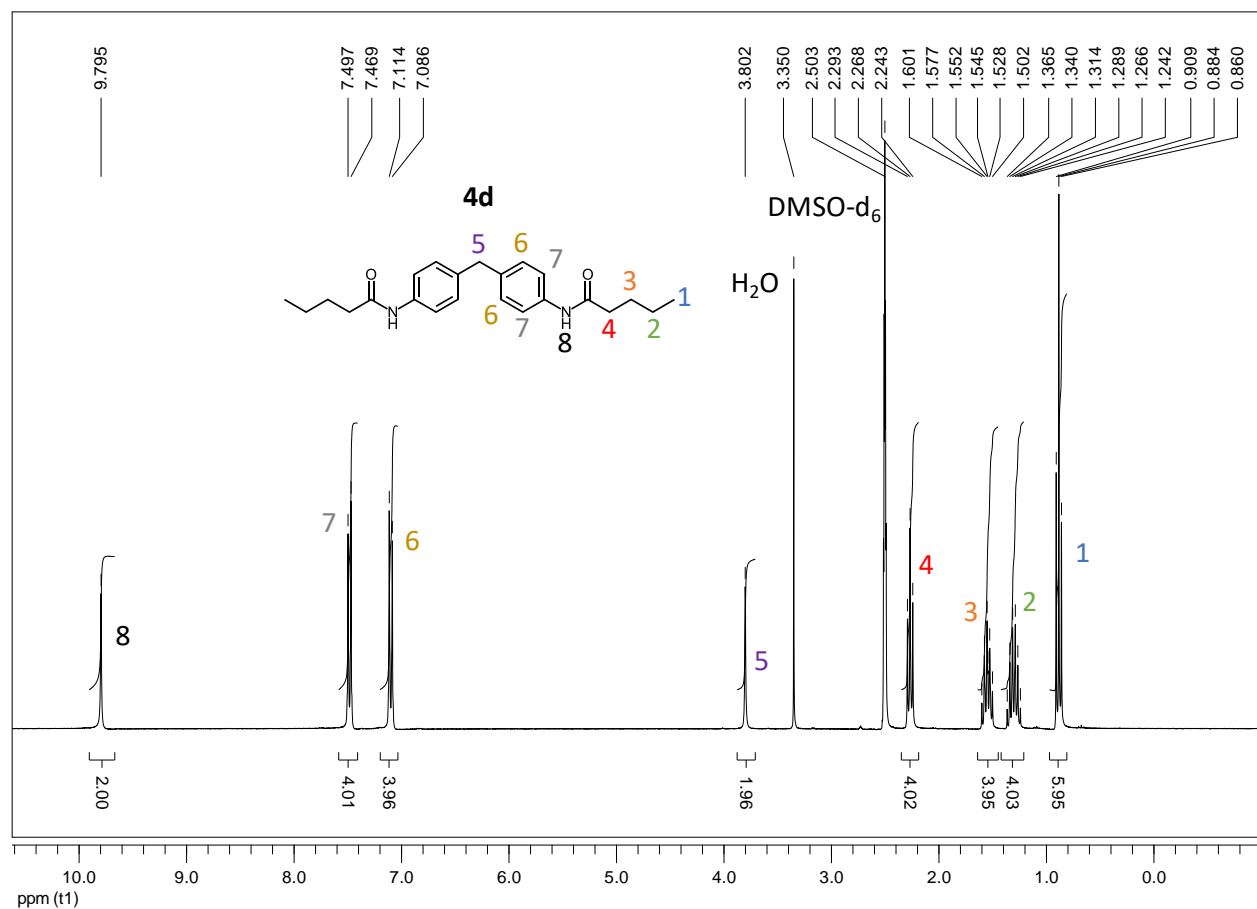


Figure 5.32: <sup>1</sup>H NMR spectra of **4d** in DMSO-d<sub>6</sub>.

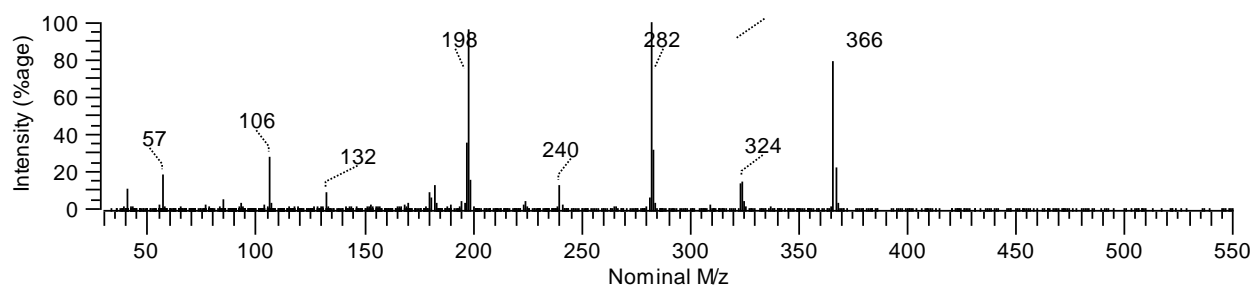
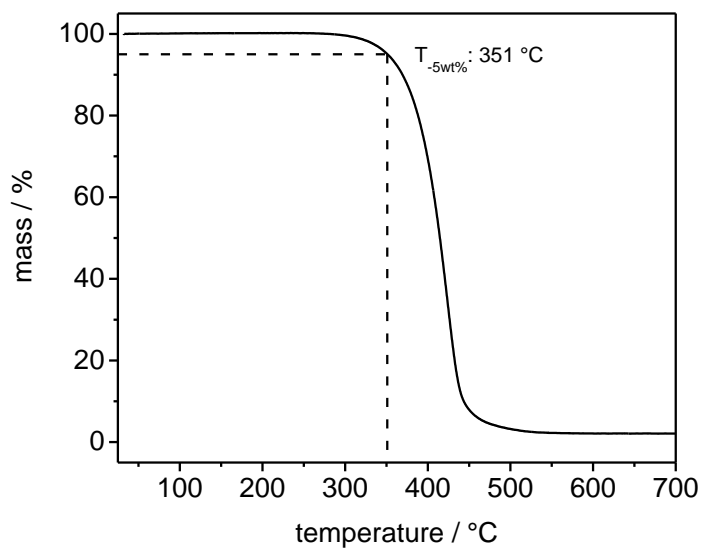
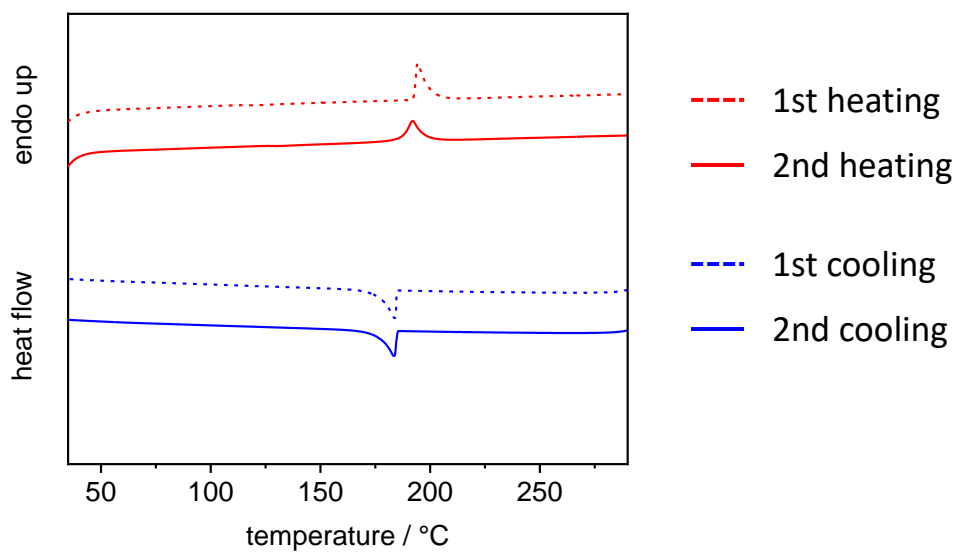


Figure 5.33: Mass spectra of **4d**.



**Figure 5.34:** Thermogram of the thermogravimetric analysis of **4d** with a heating rate of  $10 \text{ K}\cdot\text{min}^{-1}$  in the range 30 to 700 °C under nitrogen atmosphere. The temperature at which 5 % of the mass is lost is also stated ( $T_{-5\text{wt}\%}$ ).



**Figure 5.35:** Differential scanning calorimetry thermographs of **4d** including first and second heating and cooling respectively.

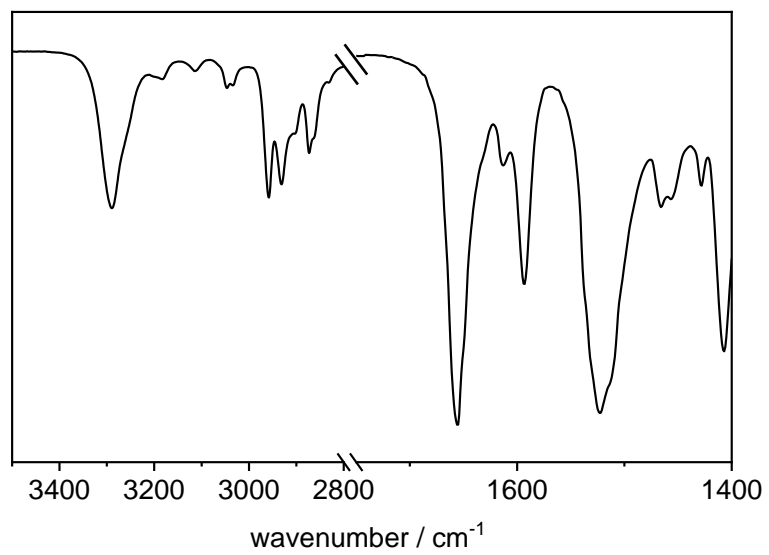


**Figure 5.36:** FT-IR spectra of **4d** in the range of 3500 to 1400  $\text{cm}^{-1}$ .

## 5.4.2.6 N,N'-[Methylenebis(2,6-dimethyl-4,1-phenylene)]bis[benzamide] - 5a

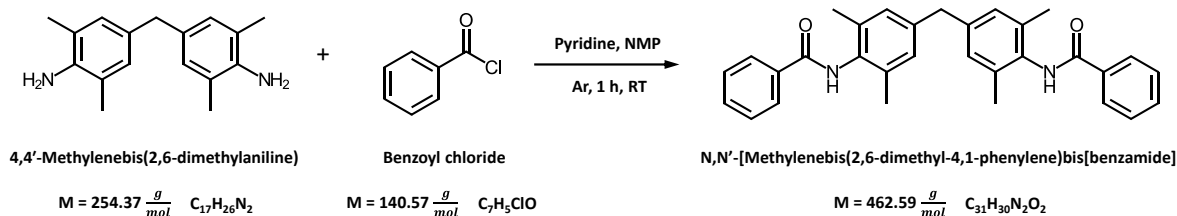


**Figure 5.37:** Reaction scheme of 4,4'-methylenebis(2,6-dimethylaniline) with benzoyl chloride to N,N'-[Methylenebis(2,6-dimethyl-4,1-phenylene)]bis[benzamide] – 5a.

**Synthesis:**

5 g (19.65 mmol)	4,4'-Methylenebis(2,6-dimethylaniline)
6.07 g (43.23 mmol)	Benzoyl chloride
3.5 mL	Pyridine
100 mL	NMP

4,4'-Methylenebis(2,6-dimethylaniline), pyridine and NMP were mixed in a Schlenk flask and cooled down to 0 – 5 °C. Under argon atmosphere the benzoyl chloride was added dropwise and the mixture was heated to room temperature. After one hour the reaction mixture was precipitated in ice water. The solid was then filtered off and dried. For purification the solid was boiled in 500 mL MeOH and dried in high vacuum to receive 7.5 g (82 %) of the final product in form of a white powder.

**Characterization:**

$^1\text{H}$ NMR:	[DMSO, 300 MHz, $\delta$ in ppm]: 9.70 (2H, s, NH), 7.99-7.97 (4H, m, $\text{H}_{\text{Ar}}$ ), 7.55-7.52 (6H, m, $\text{H}_{\text{Ar}}$ ), 6.99 (4H, s, $\text{H}_{\text{Ar}}$ ), 3.84 (2H, s, Ar- $\text{CH}_2$ -Ar), 2.15 (12H, s, $\text{CH}_3$ )
MS:	(70 eV), m/z (%): 462 [ $\text{M}^+$ ]
TGA:	$T_{-5\text{wt.}\%} = 401$ °C
DSC:	$T_m = 225$ °C
IR:	[ATR, $\tilde{\nu}$ $\text{cm}^{-1}$ ]: 3214 (m), 2917 (w), 1633 (s), 1604 (m), 1580 (m), 1509 (s), 1487 (s), 1437 (m), 1377 (w)

## Experimental part

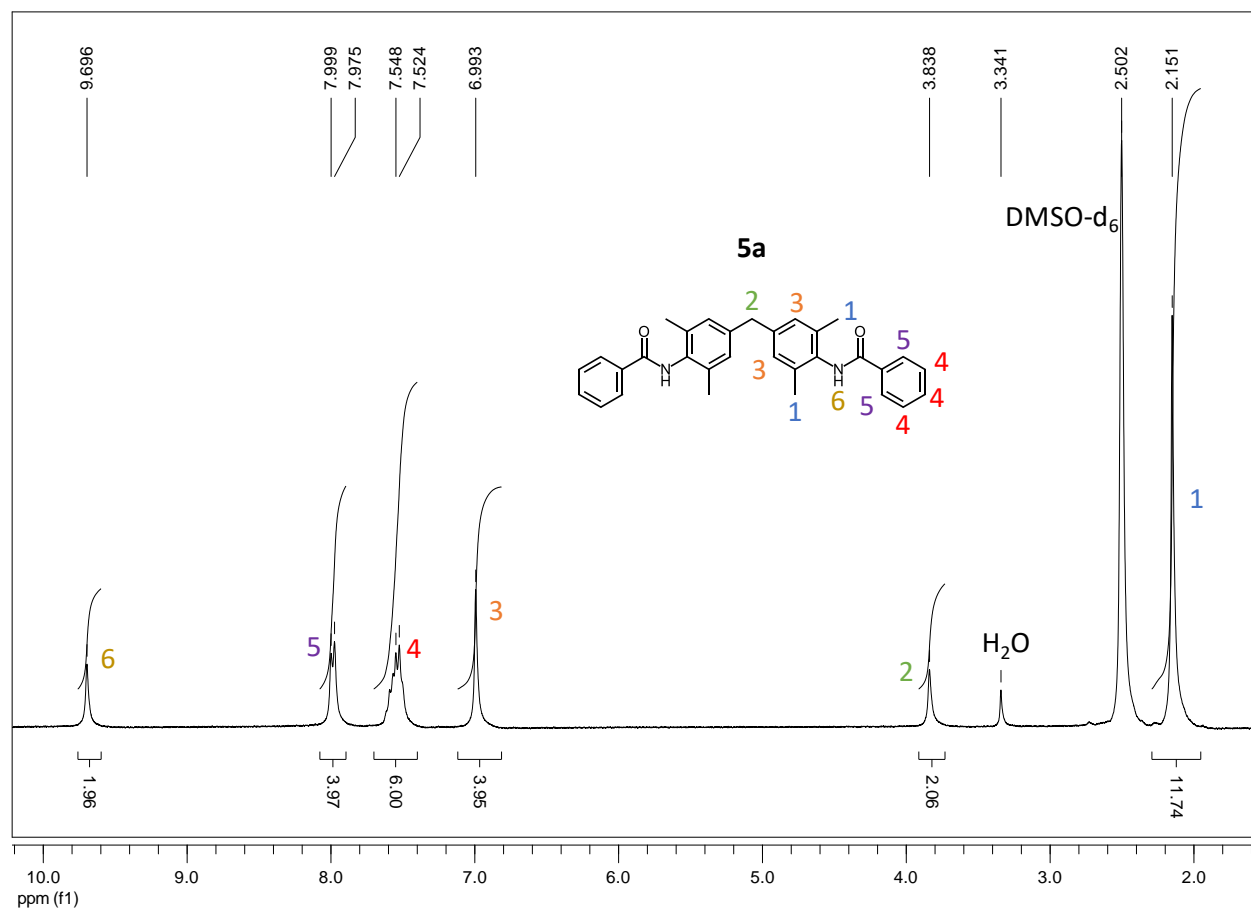


**Figure 5.38:**  $^1\text{H}$  NMR spectra of **5a** in  $\text{DMSO-d}_6$ .

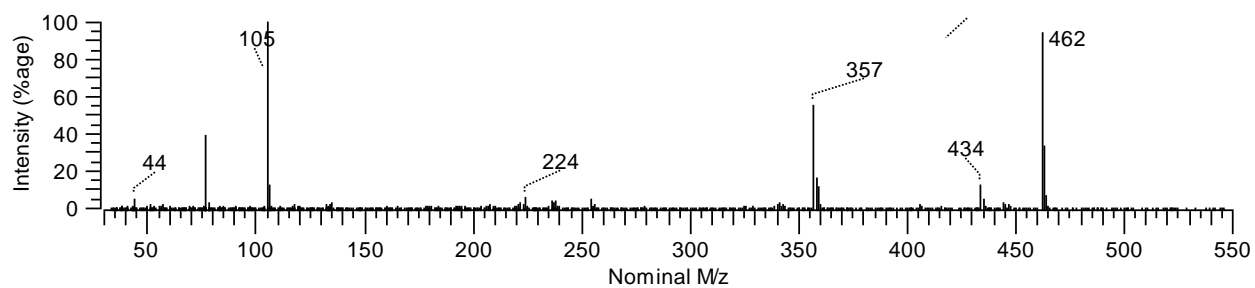


**Figure 5.39:** Mass spectra of **5a**.

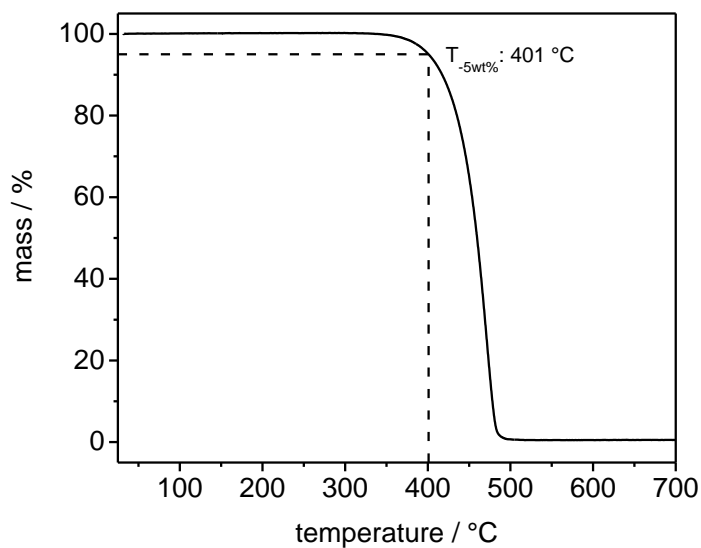


**Figure 5.40:** Thermogram of the thermogravimetric analysis of **5a** with a heating rate of  $10 \text{ K}\cdot\text{min}^{-1}$  in the range 30 to 700 °C under nitrogen atmosphere. The temperature at which 5 % of the mass is lost is also stated ( $T_{-5\text{wt}\%}$ ).

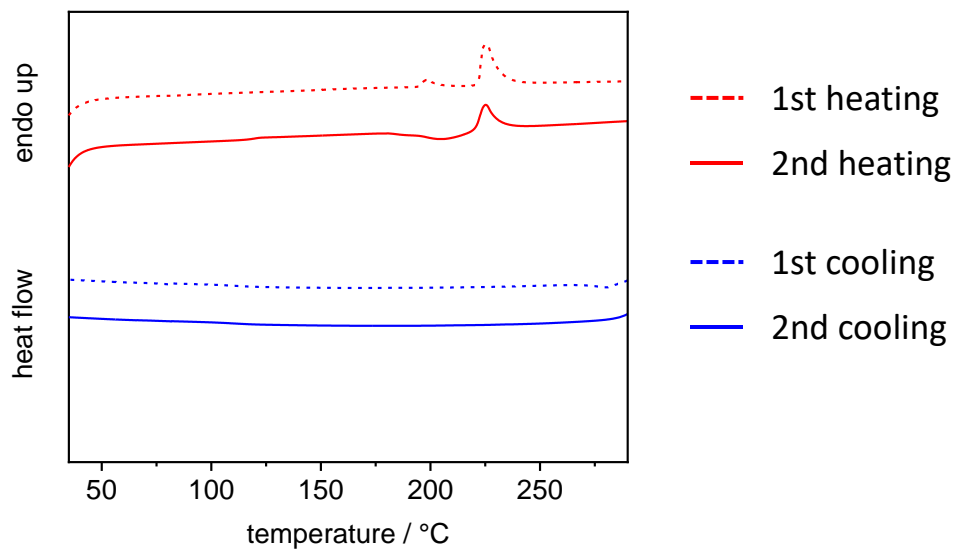


**Figure 5.41:** Differential scanning calorimetry thermographs of **5a** including first and second heating and cooling respectively.

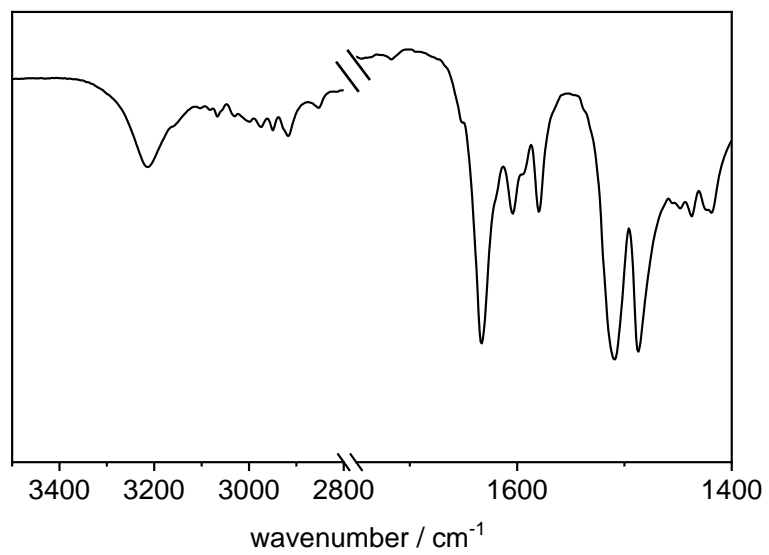


**Figure 5.42:** FT-IR spectra of **5a** in the range of 3500 to 1400 cm<sup>-1</sup>.

## 5.4.2.7 N,N'-[Methylenebis(2,6-dimethyl-4,1-phenylene)]bis[cyclohexanecarboxamide] - 5b

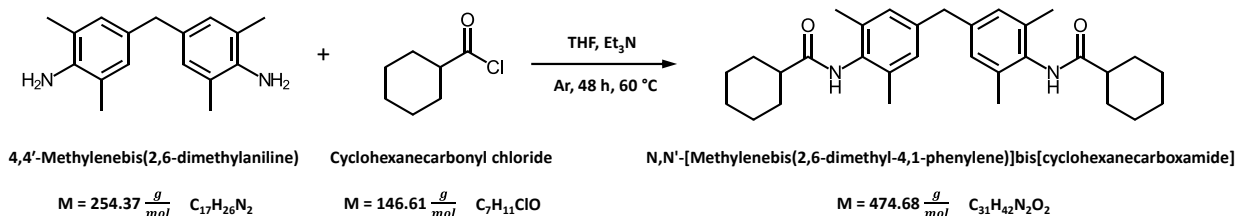


**Figure 5.43:** Reaction scheme of 4,4'-methylenebis(2,6-dimethylaniline) with cyclohexanecarbonyl chloride to N,N'-[Methylenebis(2,6-dimethyl-4,1-phenylene)]bis[cyclohexanecarboxamide] – 5b.

**Synthesis:**

3.56 g (14.00 mmol)	4,4'-Methylenebis(2,6-dimethylaniline)
4.51 g (30.76 mmol)	Cyclohexanecarbonyl chloride
4.28 mL	Et <sub>3</sub> N <sub>abs.</sub>
100 mL	THF <sub>abs.</sub>

4,4'-Methylenebis(2,6-dimethylaniline), Et<sub>3</sub>N and THF were mixed in a Schlenk flask and cooled down to 0 – 5 °C. Under argon atmosphere the cyclohexanecarbonyl chloride was added dropwise. After 48 h at 60 °C the reaction mixture was precipitated in ice water. The solid was then filtered off and washed with H<sub>2</sub>O. For further purification the solid was recrystallized from 250 mL DMF, filtered and dried in high vacuum to receive 5.6 g (84 %) of the final product in form of a white powder.

**Characterization:**

<sup>1</sup> H NMR:	[DMSO, 300 MHz, δ in ppm]: 8.99 (2H, s, NH), 6.88 (4H, s, H <sub>Ar</sub> ), 3.73 (2H, s, Ar-CH <sub>2</sub> -Ar), 2.38-2.26 (2H, m, CH <sub>Cyc</sub> ), 2.05 (12H, s, CH <sub>3</sub> ), 1.84-1.15 (20H, m, CH <sub>2Cyc</sub> )
MS:	(70 eV), m/z (%): 474 [M <sup>+</sup> ]
TGA:	T <sub>-5wt.%</sub> = 369 °C
DSC:	T <sub>m</sub> = 307 °C
IR:	[ATR, $\tilde{\nu}$ cm <sup>-1</sup> ]: 3268 (m), 2927 (s), 2853 (m), 1654 (s), 1607 (w), 1509 (s), 1445 (m), 1386 (w)

## Experimental part

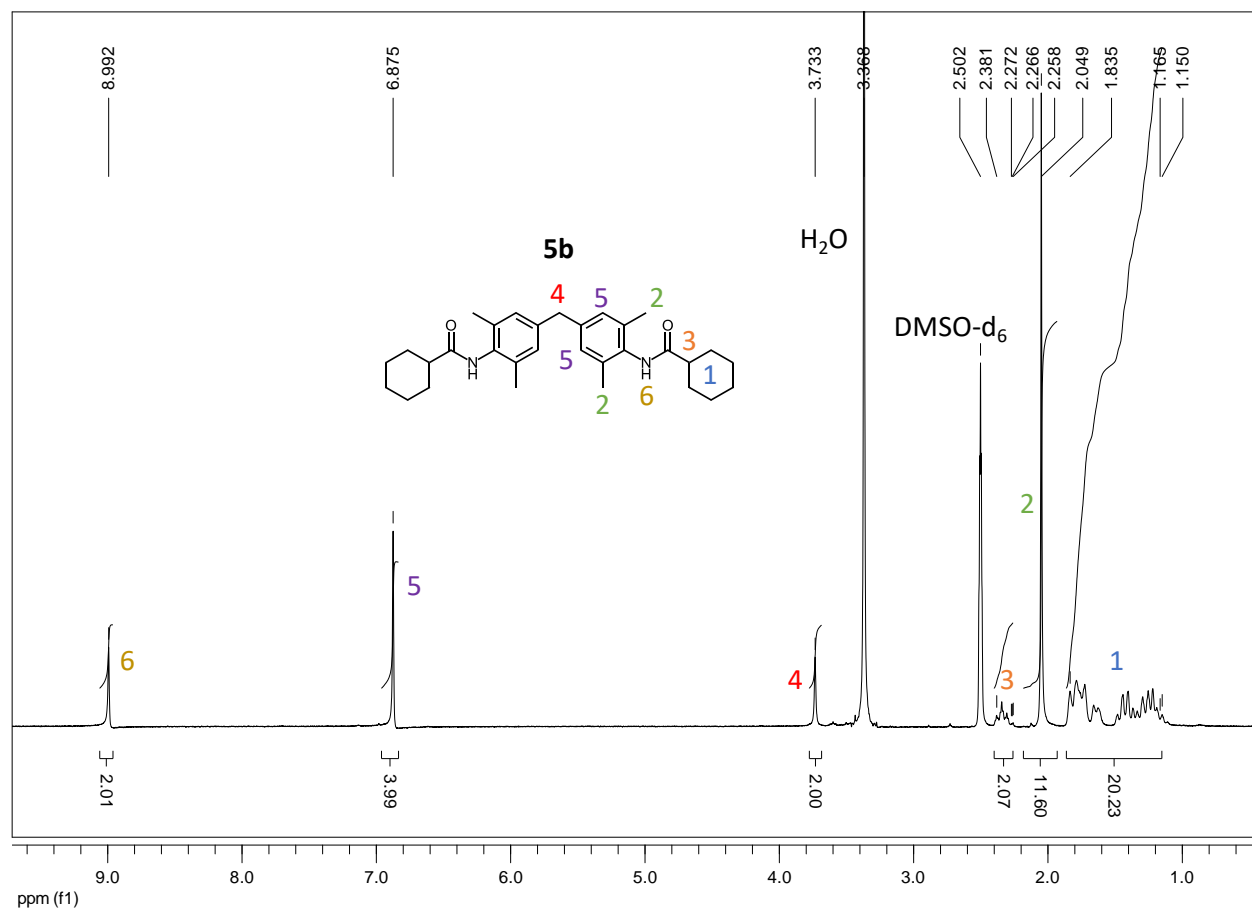


**Figure 5.44:**  $^1\text{H}$  NMR spectra of **5b** in  $\text{DMSO-d}_6$ .

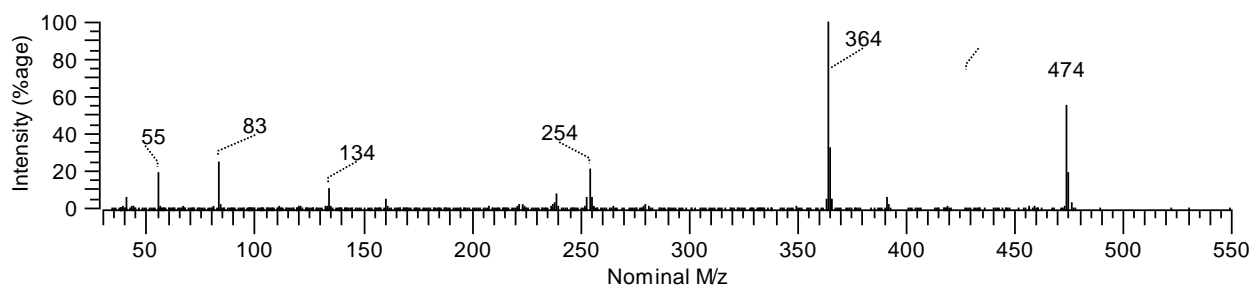


**Figure 5.45** Mass spectra of **5b**.

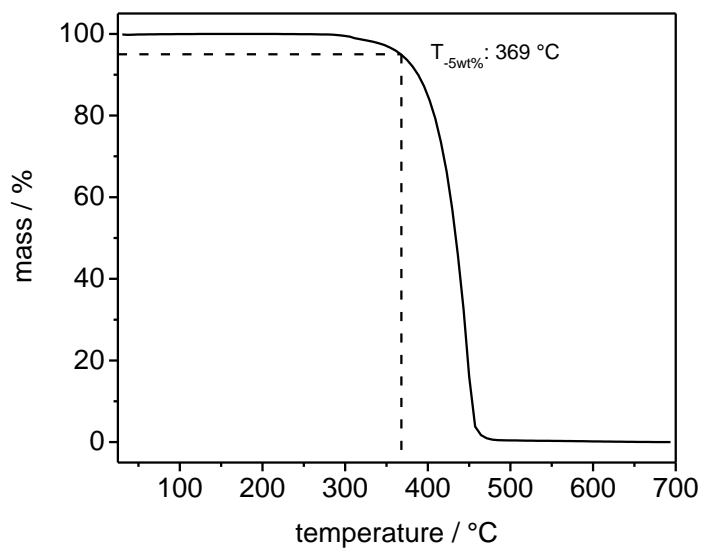


**Figure 5.46:** Thermogram of the thermogravimetric analysis of **5b** with a heating rate of  $10\text{ K}\cdot\text{min}^{-1}$  in the range 30 to 700 °C under nitrogen atmosphere. The temperature at which 5 % of the mass is lost is also stated ( $T_{-5wt\%}$ ).

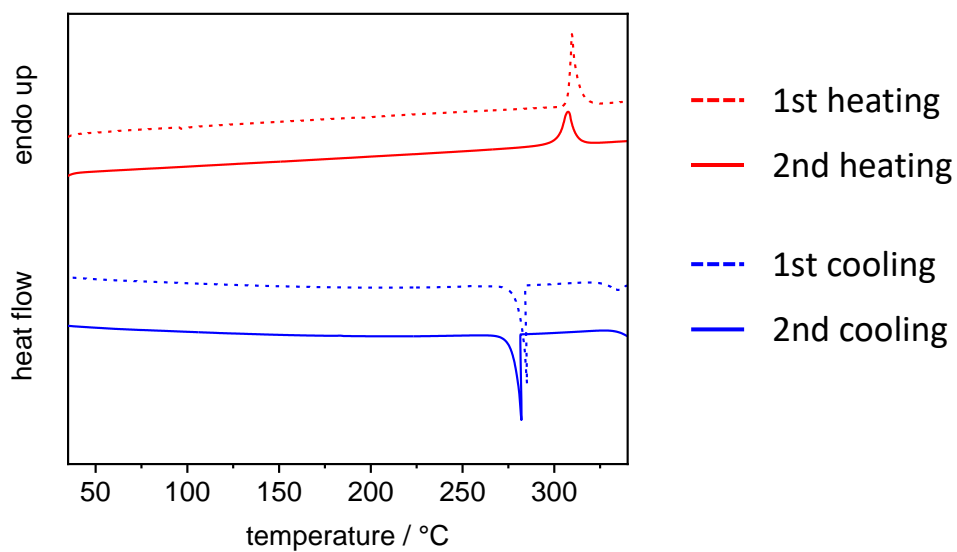


**Figure 5.47:** Differential scanning calorimetry thermographs of **5b** including first and second heating and cooling respectively.

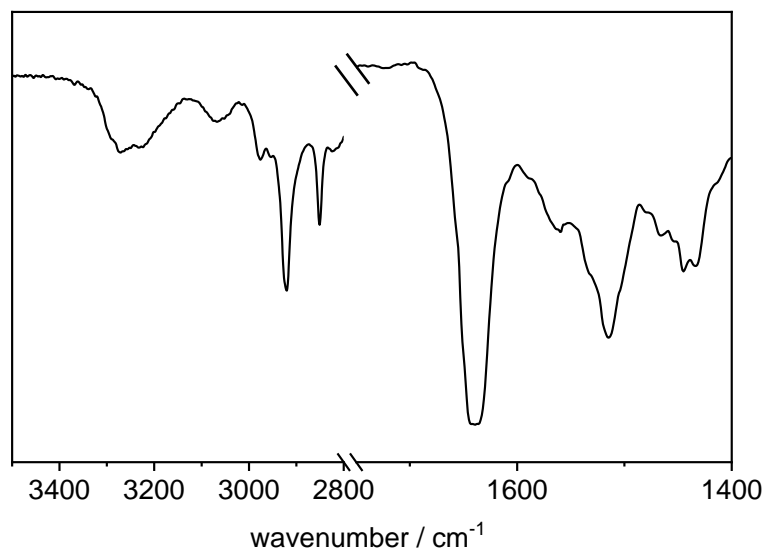


**Figure 5.48:** FT-IR spectra of **5b** in the range of 3500 to 1400  $\text{cm}^{-1}$ .

## 5.4.2.8 N,N'-[Methylenebis(2,6-dimethyl-4,1-phenylene)]bis[tertbutylcarboxamide] - 5c

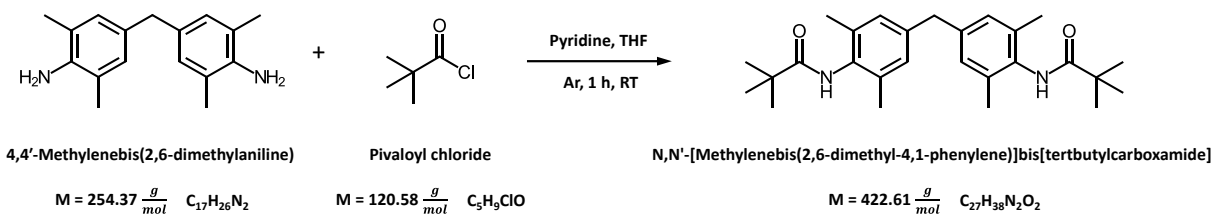


**Figure 5.49:** Reaction scheme of 4,4'-methylenebis(2,6-dimethylaniline) with pivaloyl chloride to N,N'-[Methylenebis(2,6-dimethyl-4,1-phenylene)]bis[tertbutylcarboxamide] – 5c.

**Synthesis:**

4 g (15.72 mmol)	4,4'-Methylenebis(2,6-dimethylaniline)
4.17 g (34.59 mmol)	Pivaloyl chloride
2.8 mL	Pyridine
100 mL	THF <sub>dried</sub>

4,4'-Methylenebis(2,6-dimethylaniline), pyridine and THF were mixed in a Schlenk flask and cooled down to 0 – 5 °C. Under argon atmosphere the pivaloyl chloride was added dropwise and the mixture was heated to room temperature. After one hour the reaction mixture was precipitated in ice water. The solid was then filtered off and dried. For further purification the solid was first recrystallized from 100 mL MeOH followed by a filtration over silica gel with DMF as solvent. The solvent was reduced, the solid was precipitated in water and dried at 80 °C to receive 4.9 g (74 %) of the final product in form of a white powder.

**Characterization:**

$^1\text{H}$ NMR:	[DMSO, 300 MHz, $\delta$ in ppm]: 8.74 (2H, s, NH), 6.89 (4H, s, H <sub>Ar</sub> ), 3.77 (2H, s, Ar-CH <sub>2</sub> -Ar), 2.05 (12H, s, Ar-CH <sub>3</sub> ), 1.22 (18H, s, CH <sub>3</sub> )
MS:	(70 eV), m/z (%): 422 [M <sup>+</sup> ]
TGA:	T <sub>-5wt.%</sub> = 323 °C
DSC	T <sub>m</sub> = 311 °C
IR:	[ATR, $\tilde{\nu}$ cm <sup>-1</sup> ]: 3281 (m), 2966 (w), 2917 (w), 1648 (s), 1516 (s), 1365 (w)

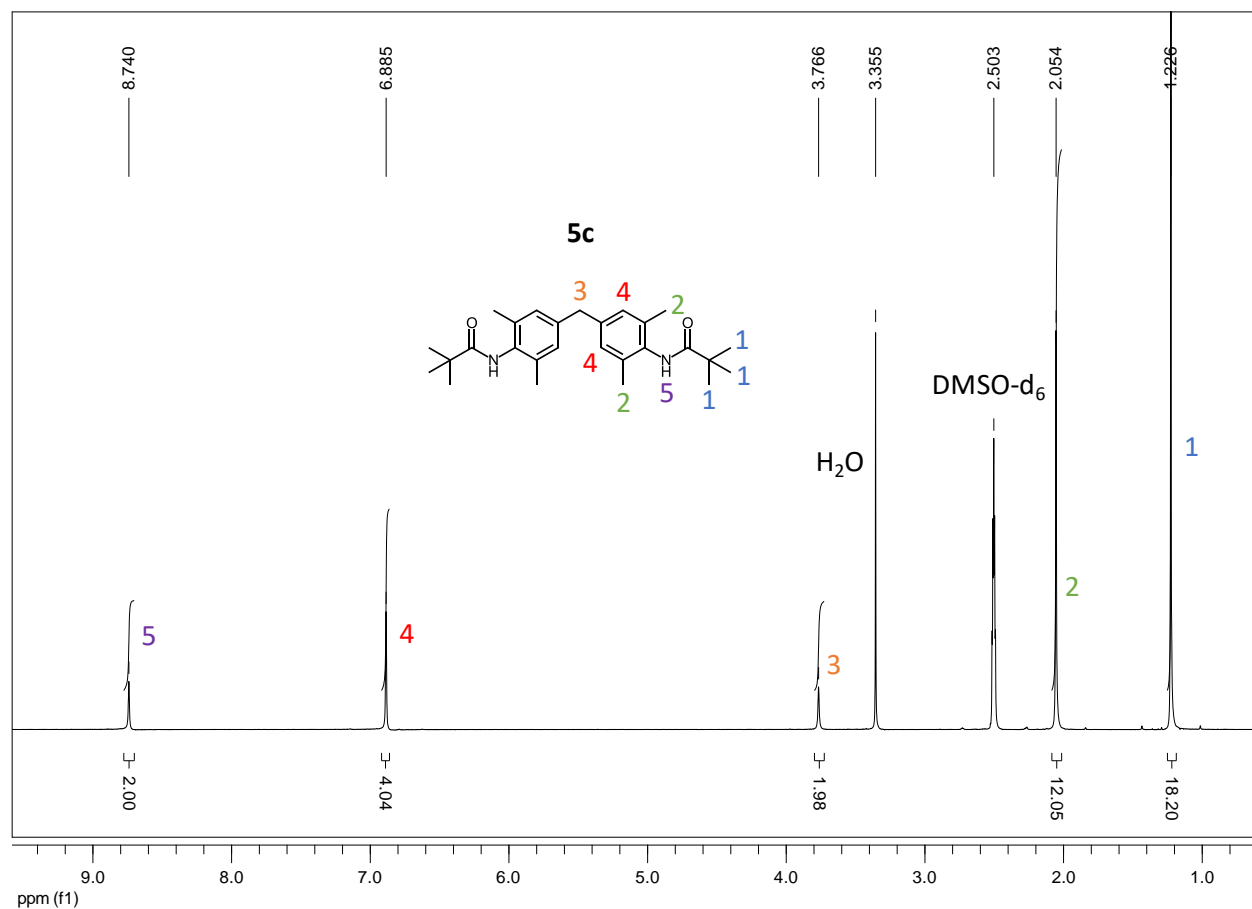


**Figure 5.50:** <sup>1</sup>H NMR spectra of **5c** in DMSO-d<sub>6</sub>.

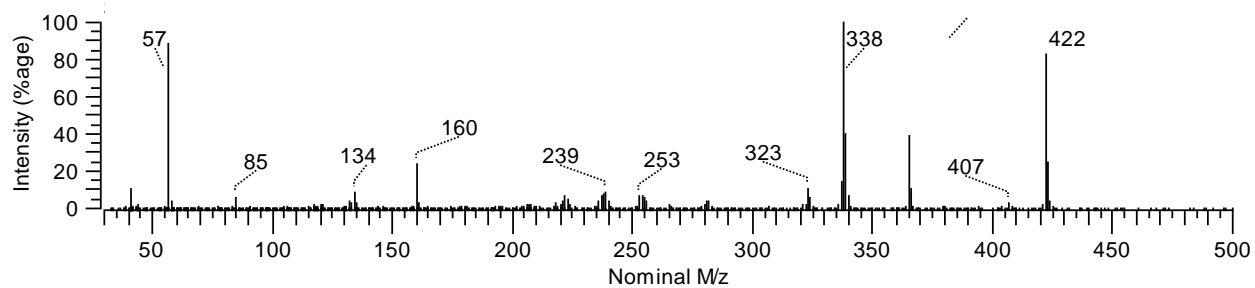


**Figure 5.51:** Mass spectra of **5c**.

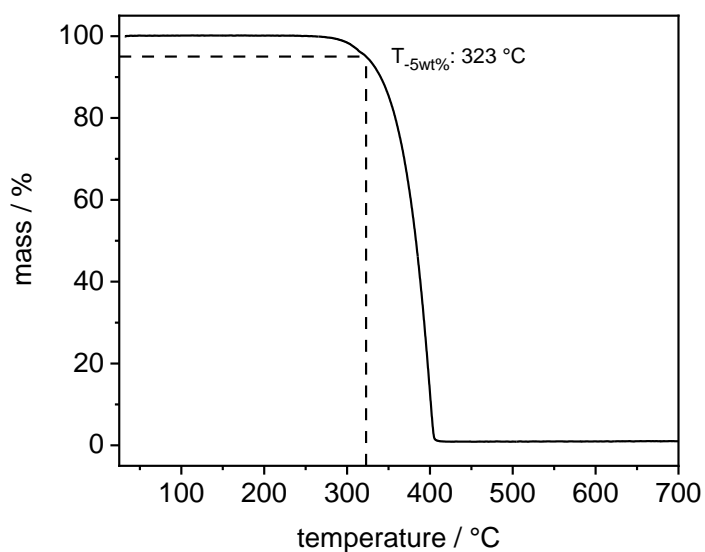


**Figure 5.52:** Thermogram of the thermogravimetric analysis of **5c** with a heating rate of  $10 \text{ K}\cdot\text{min}^{-1}$  in the range 30 to 700 °C under nitrogen atmosphere. The temperature at which 5 % of the mass is lost is also stated ( $T_{-5\text{wt}\%}$ ).

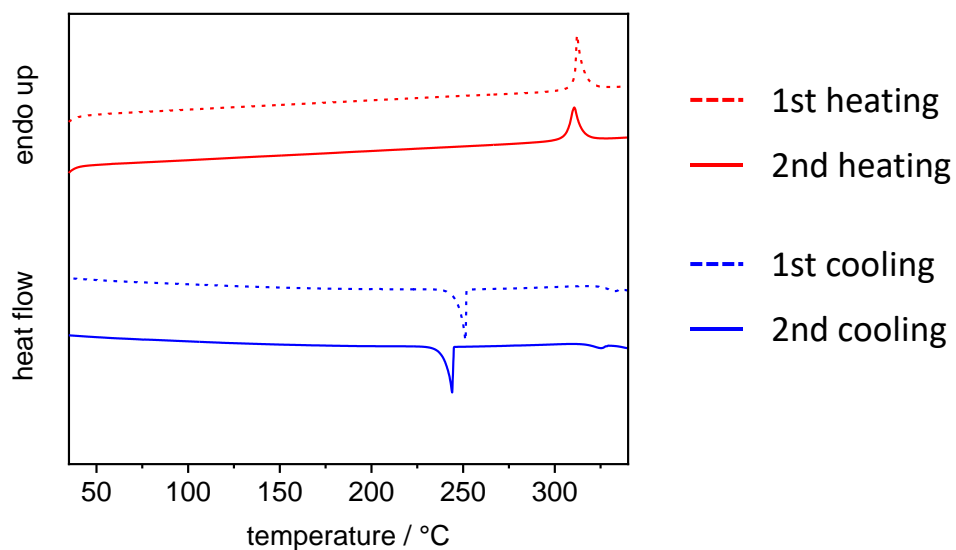


**Figure 5.53:** Differential scanning calorimetry thermographs of **5c** including first and second heating and cooling respectively.

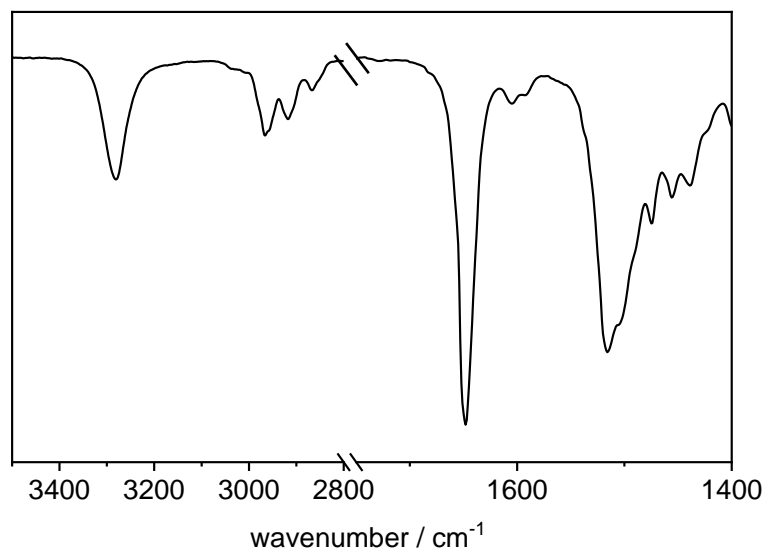


**Figure 5.54:** FT-IR spectra of **5c** in the range of 3500 to 1400  $\text{cm}^{-1}$ .

## 5.4.2.9 N,N'-[Methylenebis(2,6-dimethyl-4,1-phenylene)]bis[pentanamide] - 5d

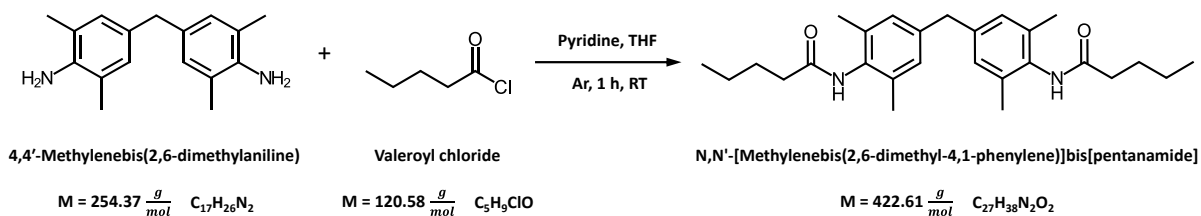


**Figure 5.55:** Reaction scheme of 4,4'-methylenebis(2,6-dimethylaniline) with valeroyl chloride to N,N'-[Methylenebis(2,6-dimethyl-4,1-phenylene)]bis[pentanamide] – 5d.

**Synthesis:**

3 g (11.79 mmol)	4,4'-Methylenebis(2,6-dimethylaniline)
2.81 g (25.94 mmol)	Valeroyl chloride
2.4 mL	Pyridine
200 mL	THF

4,4'-Methylenebis(2,6-dimethylaniline), pyridine and THF were mixed in a Schlenk flask and cooled down to 0 – 5 °C. Under argon atmosphere the valeroyl chloride was added dropwise and the mixture was heated to room temperature. After one hour the reaction mixture was precipitated in ice water. The solid was then filtered off and dried. For further purification the solid was recrystallized from 300 mL MeOH, filtered and dried in high vacuum to receive 3.6 g (72 %) of the final product in form of a white powder.

**Characterization:**

$^1\text{H NMR}$ :	[DMSO, 300 MHz, $\delta$ in ppm]: 9.09 (2H, s, NH), 6.89 (4H, s, $\text{H}_{\text{Ar}}$ ), 3.74 (2H, s, $\text{Ar-CH}_2\text{-Ar}$ ), 2.31-2.26 (4H, t, $\text{CO-CH}_2$ ), 2.07 (12H, s, $\text{Ar-CH}_3$ ), 1.63-1.54 (4H, q, $\text{CH}_2\text{-CH}_2$ ), 1.41-1.28 (4H, sx, $\text{CH}_2\text{-CH}_3$ ), 0.93-0.89 (6H, t, $\text{CH}_2\text{-CH}_3$ )
MS:	(70 eV), $m/z$ (%): 422 [ $\text{M}^+$ ]
TGA:	$T_{-5\text{w.t}\%} = 339 \text{ }^\circ\text{C}$
DSC:	$T_{\text{m}1} = 190 \text{ }^\circ\text{C}$ , $T_{\text{m}2} = 257 \text{ }^\circ\text{C}$
IR:	[ATR, $\tilde{\nu} \text{ cm}^{-1}$ ]: 3273 (m), 2952 (m); 2929 (m), 2869 (w), 1651 (s), 1603 (w), 1515 (s)

## Experimental part

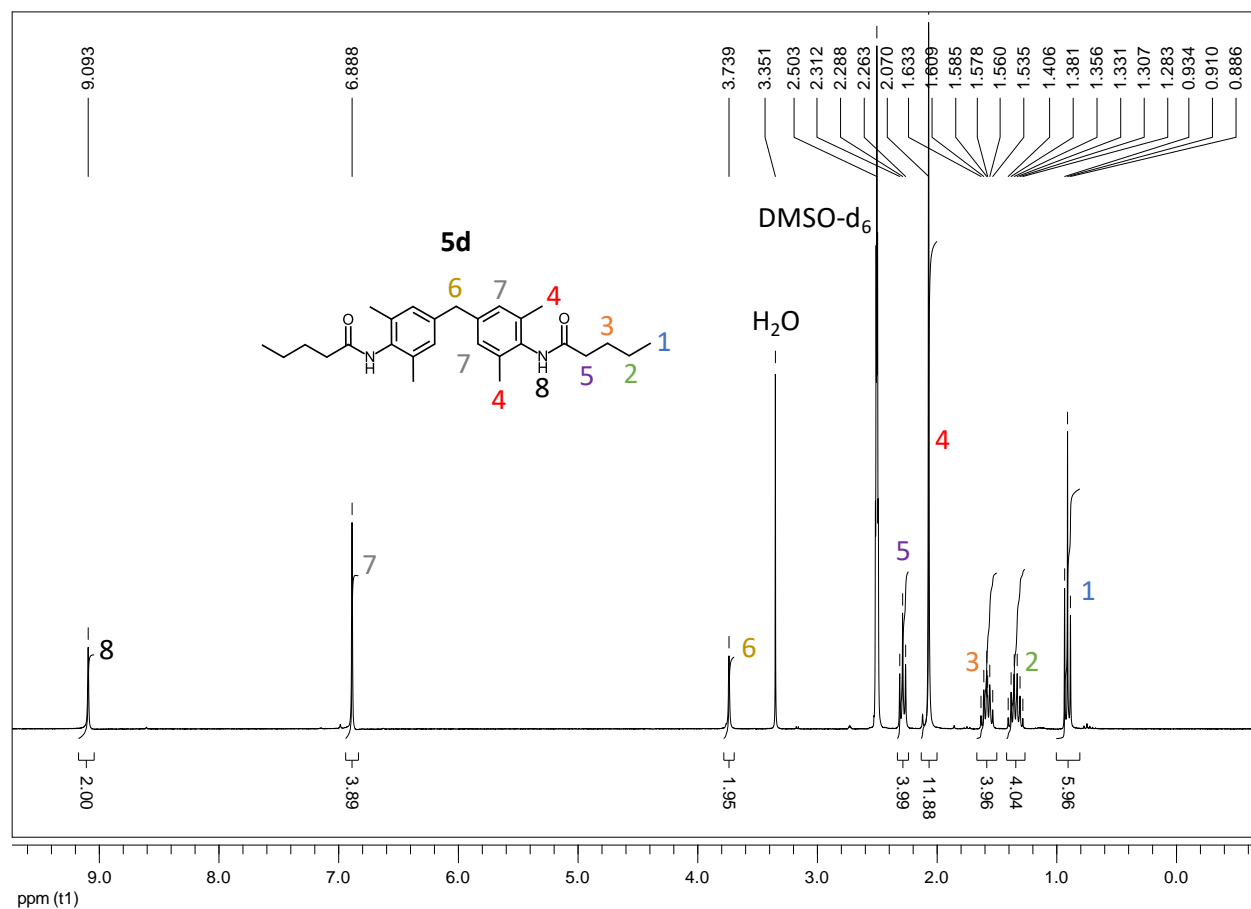


**Figure 5.56:**  $^1\text{H}$  NMR spectra of **5d** in  $\text{DMSO-d}_6$ .

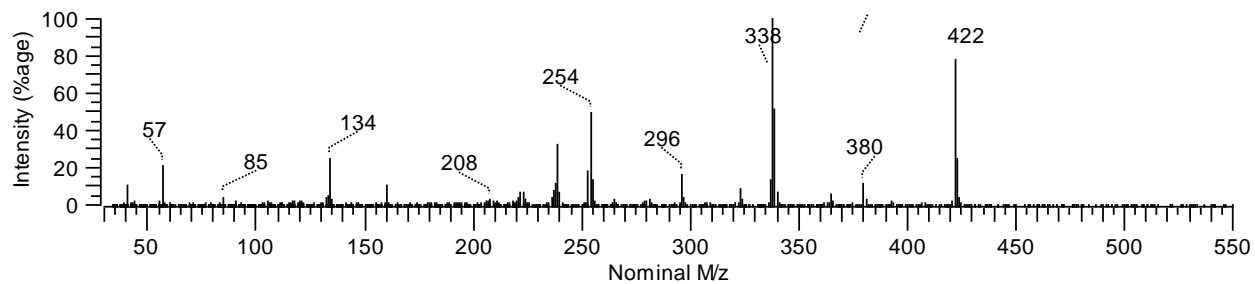


**Figure 5.57:** Mass spectra of **5d**.

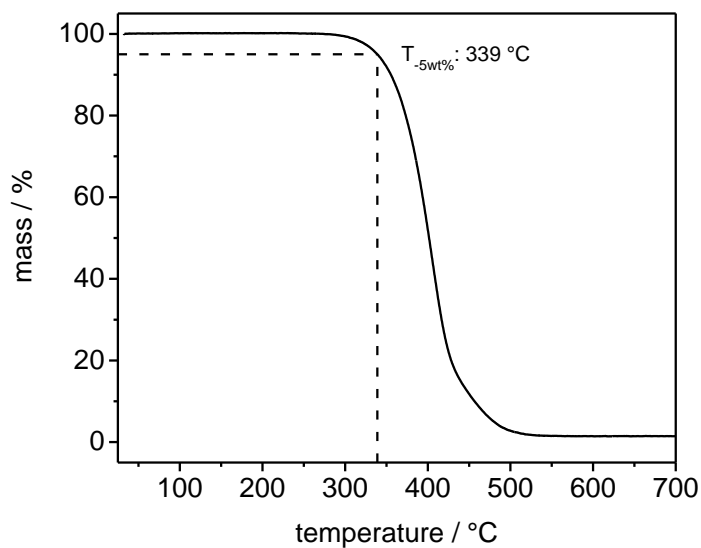


**Figure 5.58:** Thermogram of the thermogravimetric analysis of **5d** with a heating rate of  $10 \text{ K}\cdot\text{min}^{-1}$  in the range 30 to 700 °C under nitrogen atmosphere. The temperature at which 5 % of the mass is lost is also stated ( $T_{-5\text{wt}\%}$ ).

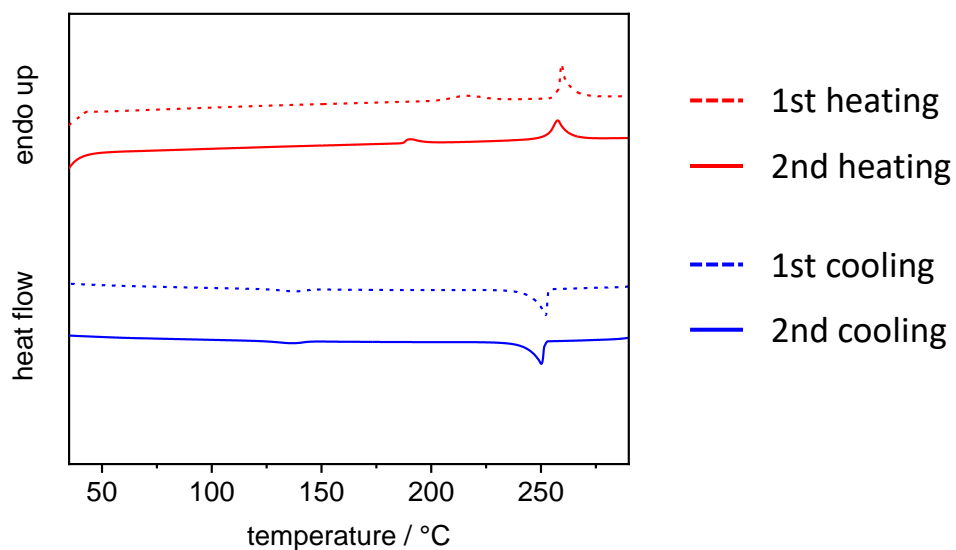


**Figure 5.59:** Differential scanning calorimetry thermographs of **5d** including first and second heating and cooling respectively.

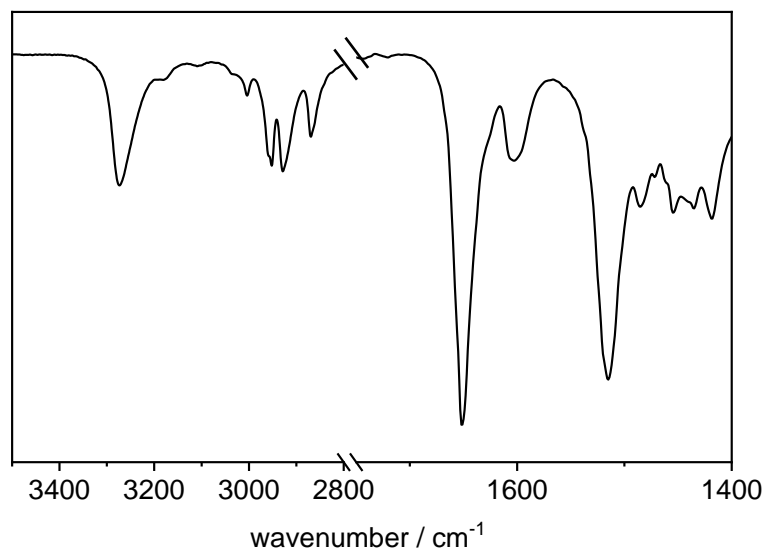


**Figure 5.60:** FT-IR spectra of **5d** in the range of 3500 to 1400 cm<sup>-1</sup>.

## 5.4.2.10 N,N'-[Methylenebis(2,6-diethyl-4,1-phenylene)]bis[benzamide] - 6a

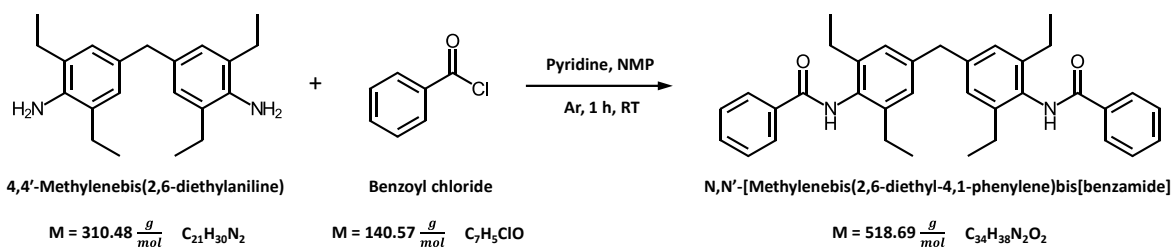


**Figure 5.61:** Reaction scheme of 4,4'-Methylenebis(2,6-diethylaniline) with benzoyl chloride to N,N'-[Methylenebis(2,6-diethyl-4,1-phenylene)]bis[benzamide] – 6a.

**Synthesis:**

5 g (16.10 mmol)	4,4'-Methylenebis(2,6-diethylaniline)
4.98 g (35.42 mmol)	Benzoyl chloride
2.8 mL	Pyridine
100 mL	NMP

4,4'-Methylenebis(2,6-diethylaniline), pyridine and NMP were mixed in a Schlenk flask and cooled down to 0 – 5 °C. Under argon atmosphere the benzoyl chloride was added dropwise and the mixture was heated to room temperature. After one hour the reaction mixture was precipitated in ice water. The solid was then filtered off and dried. For further purification the solid was boiled in 500 mL MeOH, filtered and dried in high vacuum to receive 7.0 g (83 %) of the final product in form of a white powder.

**Characterization:**

$^1H$ NMR:	[DMSO, 300 MHz, $\delta$ in ppm]: 9.69 (2H, s, NH), 7.99-7.96 (4H, m, $H_{Ar}$ ), 7.59-7.50 (6H, m, $H_{Ar}$ ), 7.04 (4H, s, $H_{Ar}$ ), 3.94 (2H, s, Ar- $CH_2$ -Ar), 2.52-2.49 (8H, s, $CH_2$ - $CH_3$ ), 1.12-1.07 (12H, t, $CH_3$ )
MS:	(70 eV), m/z (%): 518 [ $M^+$ ]
TGA:	$T_{-5wt. \%} = 389$ °C
DSC:	$T_m = 258$ °C
IR:	[ATR, $\tilde{\nu}$ $cm^{-1}$ ]: 3214 (w), 2963 (m), 2871 (w), 1644 (s), 1603 (w), 1512 (s), 1487 (s)

## Experimental part

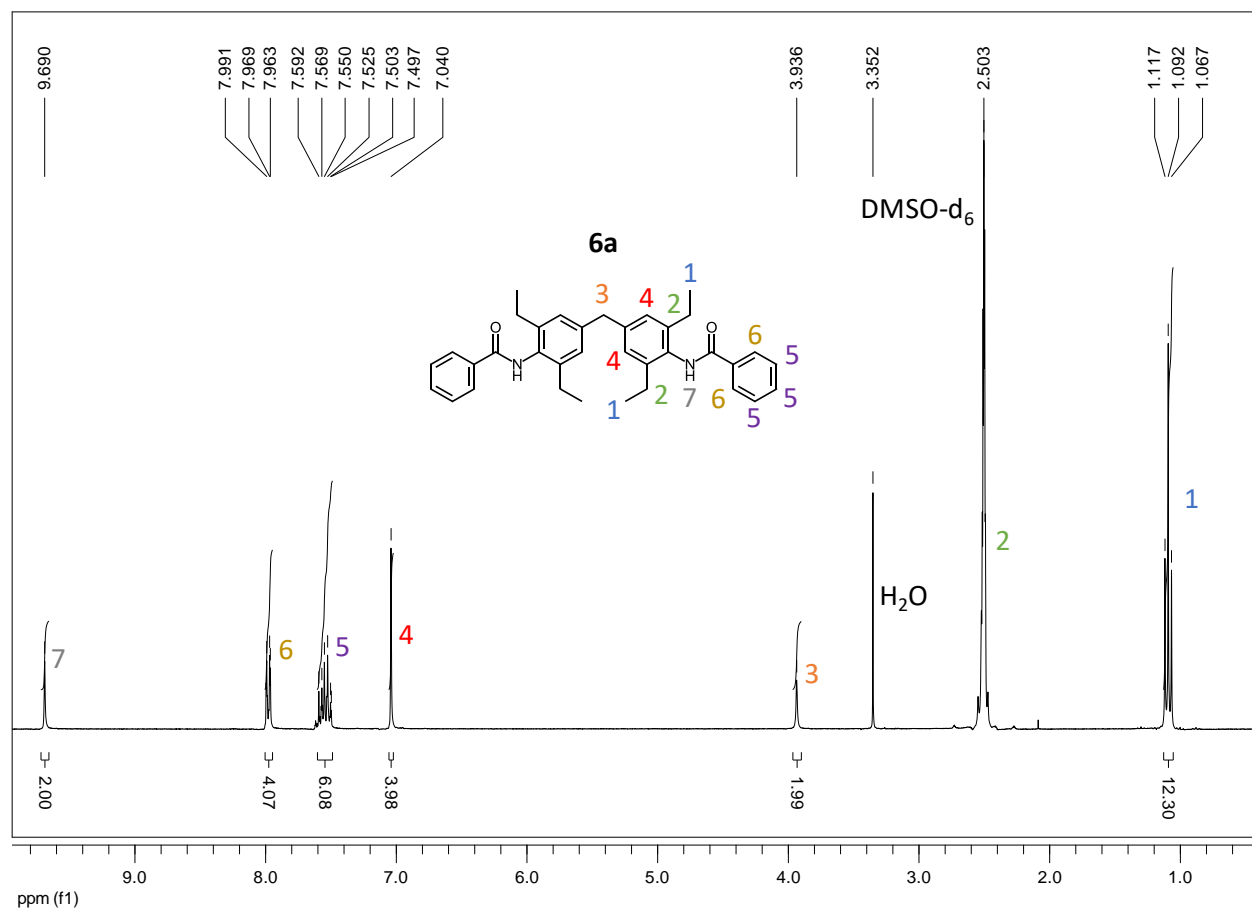


**Figure 5.62:** <sup>1</sup>H NMR spectra of **6a** in DMSO-d<sub>6</sub>.

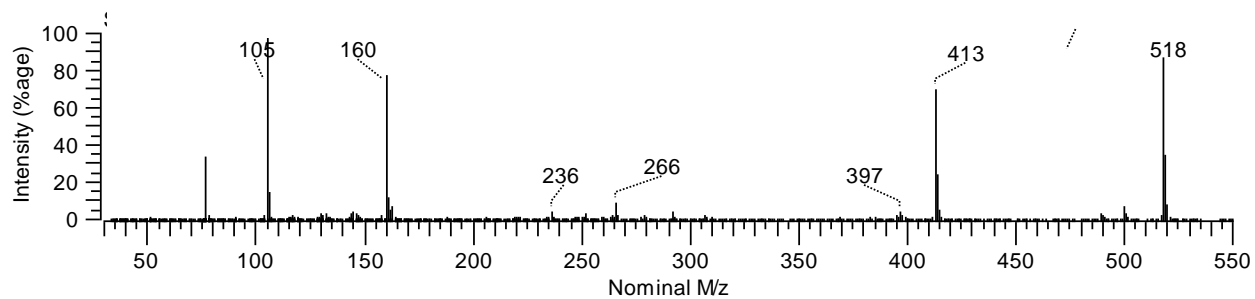


**Figure 5.63:** Mass spectra of **6a**.

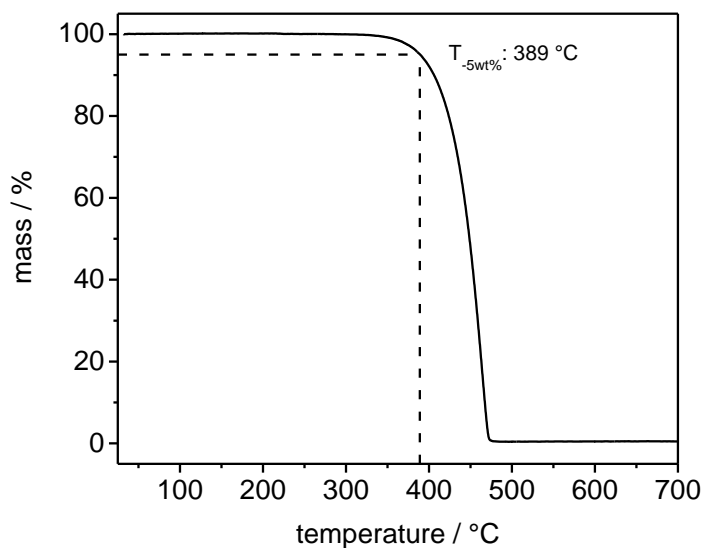


**Figure 5.64:** Thermogram of the thermogravimetric analysis of **6a** with a heating rate of  $10 \text{ K}\cdot\text{min}^{-1}$  in the range 30 to 700 °C under nitrogen atmosphere. The temperature at which 5 % of the mass is lost is also stated ( $T_{-5\text{wt}\%}$ ).

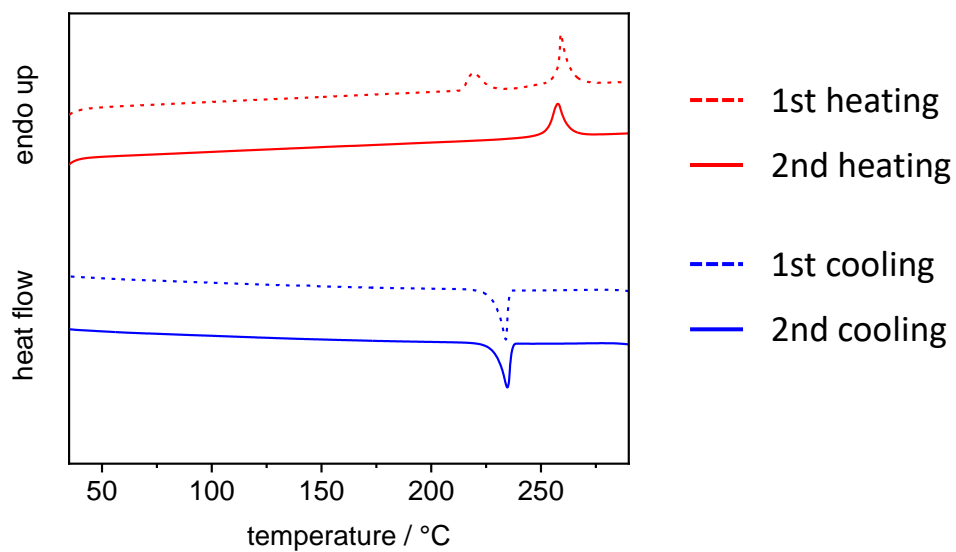


**Figure 5.65:** Differential scanning calorimetry thermographs of **6a** including first and second heating and cooling respectively.

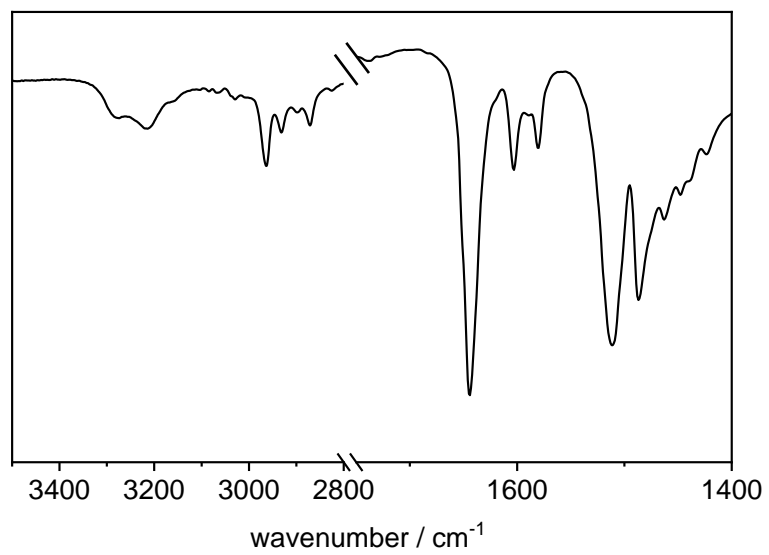


**Figure 5.66:** FT-IR spectra of **6a** in the range of 3500 to 1400 cm<sup>-1</sup>.

## 5.4.2.11 N,N'-[Methylenebis(2,6-diethyl-4,1-phenylene)]bis[cyclohexanecarboxamide] - 6b

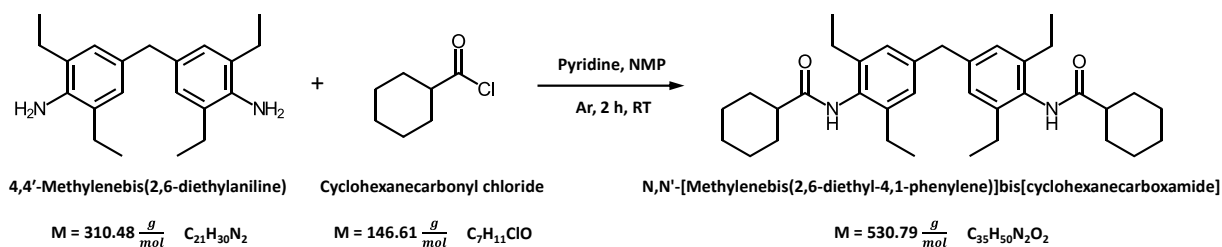


**Figure 5.67:** Reaction scheme of 4,4'-Methylenebis(2,6-diethylaniline) with cyclohexanecarbonyl chloride to N,N'-[Methylenebis(2,6-diethyl-4,1-phenylene)]bis[cyclohexanecarboxamide] – **6b**.

**Synthesis:**

9 g (28.00 mmol)	4,4'-Methylenebis(2,6-diethylaniline)
9.34 g (63.00 mmol)	Cyclohexanecarbonyl chloride
5.1 mL	Pyridine
120 mL	NMP

4,4'-Methylenebis(2,6-diethylaniline), pyridine and NMP were mixed in a Schlenk flask and cooled down to 0 – 5 °C. Under argon atmosphere the cyclohexanecarbonyl chloride was added dropwise. After a reaction time of two hours at room temperature 100 mL water has been added. Subsequently the mixture was stirred for another hour and afterwards filtered. For further purification the solid was refluxed in 200 mL acetone, filtered and dried in high vacuum to receive 14.2 g (92 %) of the final product in form of a white powder.

**Characterization:**

$^1\text{H}$ NMR:	[CDCl <sub>3</sub> /CF <sub>3</sub> COOD, 300 MHz, $\delta$ in ppm]: 6.95 (4H, m, H <sub>Ar</sub> ), 3.90 (2H, m, Ar-CH <sub>2</sub> -Ar), 2.61-2.53 (2H, m, CH <sub>Cyc</sub> ), 2.51-2.43 (8H, q, CH <sub>2</sub> -CH <sub>3</sub> ), 2.15–1.26 (20H, m, CH <sub>2Cyc</sub> ), 1.15-1.10 (12H, m, CH <sub>2</sub> -CH <sub>3</sub> )
MS:	(70 eV), m/z (%): 530 [M <sup>+</sup> ]
TGA:	T <sub>-5wt.%</sub> = 347 °C
DSC:	T <sub>m</sub> = 297 °C
IR:	[ATR, $\tilde{\nu}$ cm <sup>-1</sup> ]: 3258 (m), 2966 (w), 2925 (s), 2854 (m), 1644 (s), 1607 (m), 1512 (s), 1450 (m)

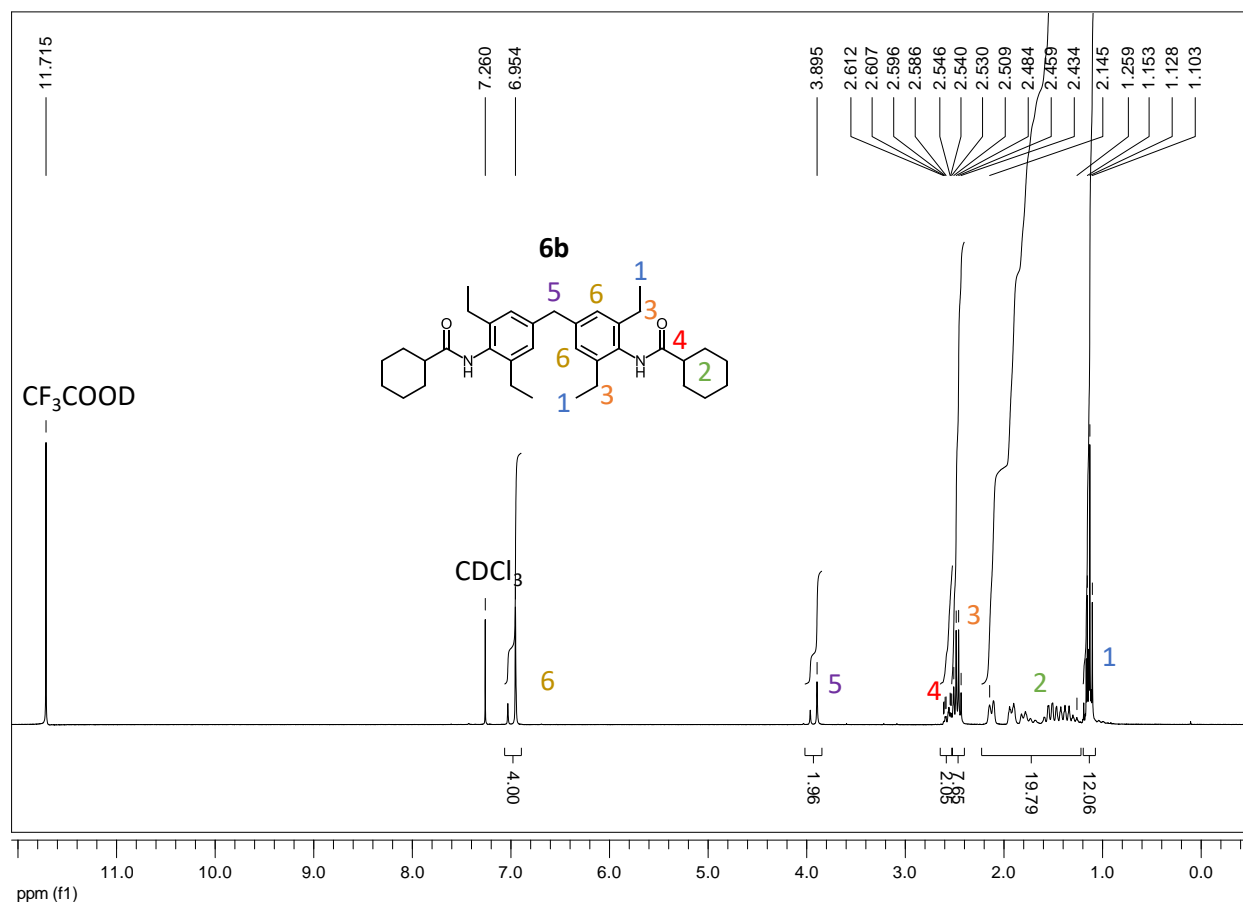


**Figure 5.68:** <sup>1</sup>H NMR spectra of **6b** in CDCl<sub>3</sub> and CF<sub>3</sub>COOD.

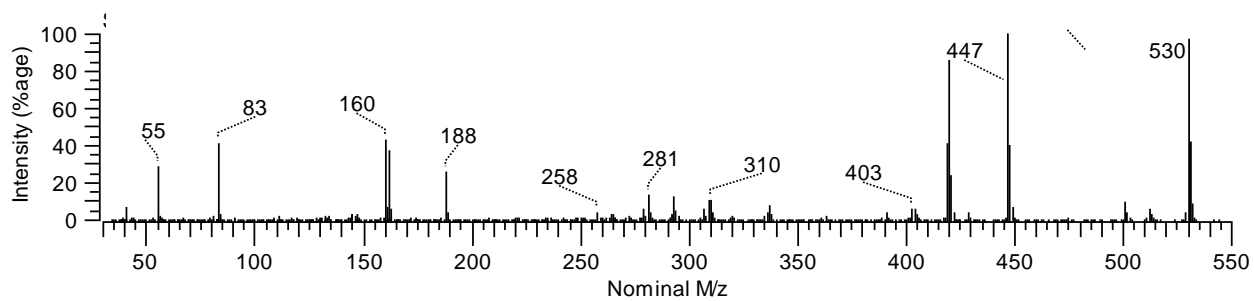


**Figure 5.69:** Mass spectra of **6b**.

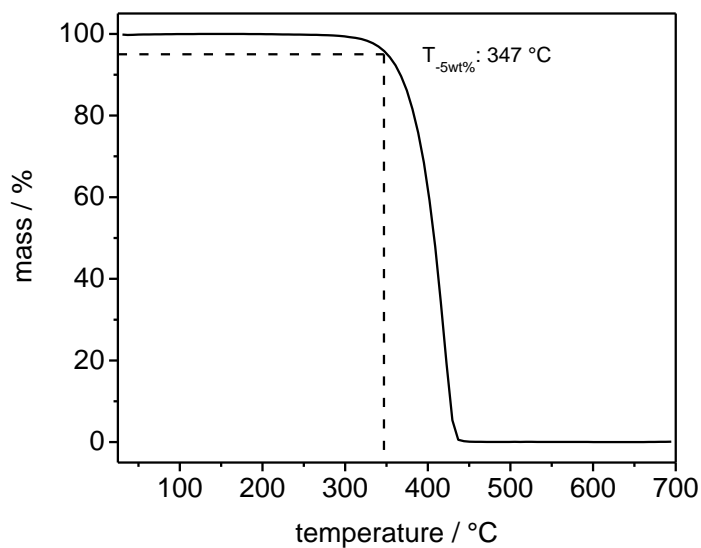


**Figure 5.70:** Thermogram of the thermogravimetric analysis of **6b** with a heating rate of  $10\text{ K}\cdot\text{min}^{-1}$  in the range 30 to 700 °C under nitrogen atmosphere. The temperature at which 5 % of the mass is lost is also stated ( $T_{-5wt\%}$ ).

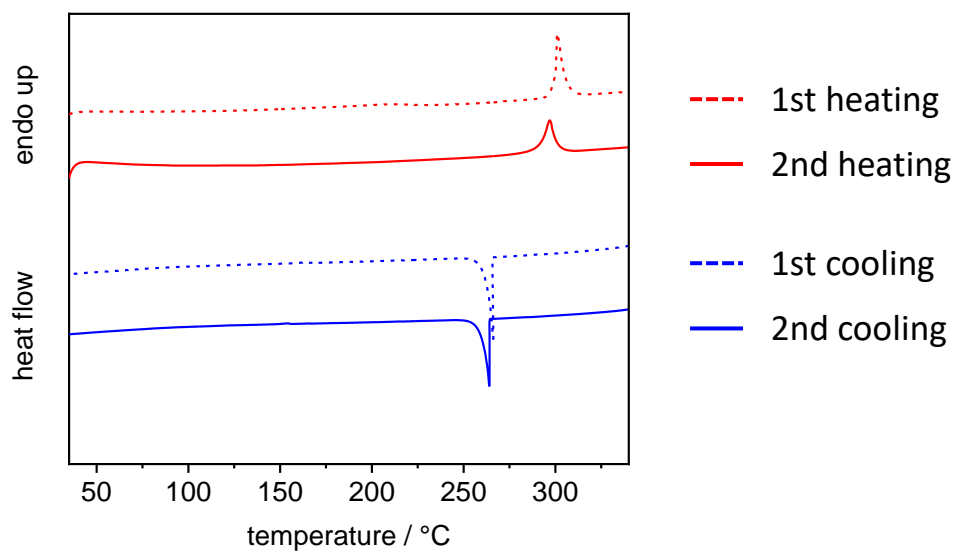


**Figure 5.71:** Differential scanning calorimetry thermographs of **6b** including first and second heating and cooling respectively.

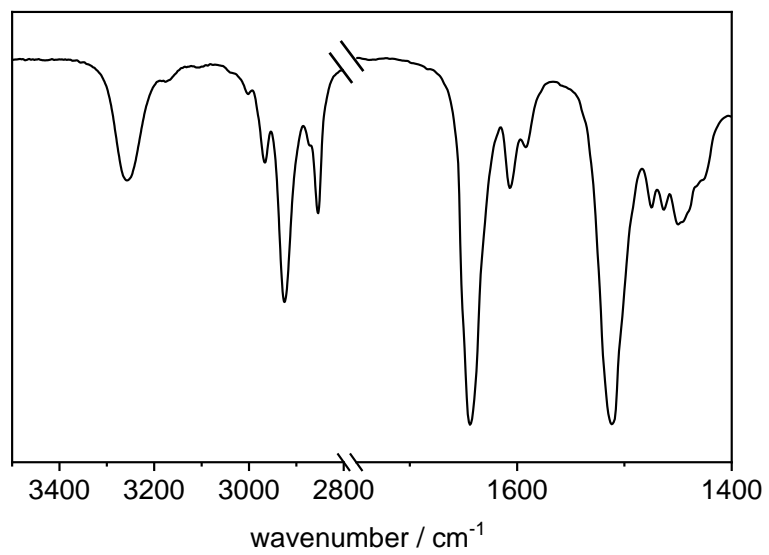


**Figure 5.72:** FT-IR spectra of **6b** in the range of 3500 to 1400  $\text{cm}^{-1}$ .

## 5.4.2.12 N,N'-[Methylenebis(2,6-diethyl-4,1-phenylene)]bis[tertbutylcarboxamide] - 6c

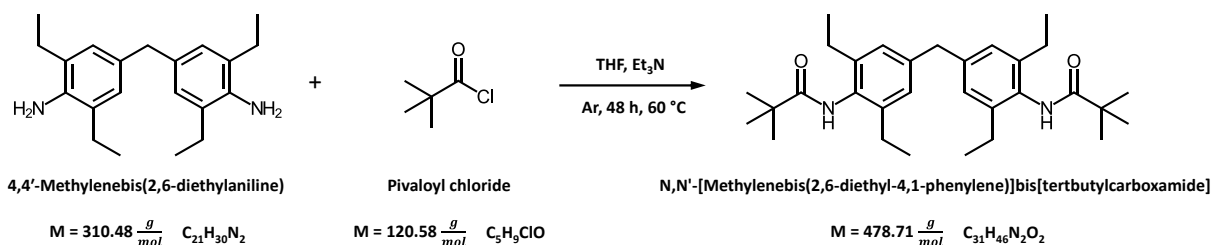


**Figure 5.73:** Reaction scheme of 4,4'-Methylenebis(2,6-diethylaniline) with pivaloyl chloride to N,N'-[Methylenebis(2,6-diethyl-4,1-phenylene)]bis[tertbutylcarboxamide] – 6c.

**Synthesis:**

4.34 g (14.00 mmol)	4,4'-Methylenebis(2,6-diethylaniline)
3.71 g (30.80 mmol)	Pivaloyl chloride
4.3 mL	Et <sub>3</sub> N.
50 mL	THF <sub>abs.</sub>

4,4'-Methylenebis(2,6-diethylaniline), Et<sub>3</sub>N and THF were mixed in a Schlenk flask and cooled down to 0 – 5 °C. Under argon atmosphere the pivaloyl chloride was added dropwise and the reaction was heated to 60 °C. After 48 h the reaction mixture was precipitated in ice water. The solid was then filtered off and recrystallized from 500 mL MeOH. For further purification the solid was recrystallized from 250 mL DMF, filtered and dried in high vacuum to receive 4.8 g (71 %) of the final product in form of a white powder.

**Characterization:**

<sup>1</sup> H NMR:	[DMSO, 300 MHz, δ in ppm]: 8.74 (2H, s, NH), 6.93 (4H, s, H <sub>Ar</sub> ), 3.86 (2H, s, Ar-CH <sub>2</sub> -Ar), 2.44-2.37 (8H, q, CH <sub>2</sub> -CH <sub>3</sub> ), 1.22 (18H, s, CH <sub>3</sub> ), 1.07-1.02 (12H, t, CH <sub>2</sub> -CH <sub>3</sub> )
MS:	(70 eV), m/z (%): 478 [M <sup>+</sup> ]
TGA:	T <sub>-5wt.%</sub> = 320 °C
DSC:	T <sub>m</sub> = 328 °C
IR:	[ATR, $\tilde{\nu}$ cm <sup>-1</sup> ]: 3258 (m), 2960 (m), 2932 (w), 2871 (w), 1643 (s), 1517 (s), 1474 (m)

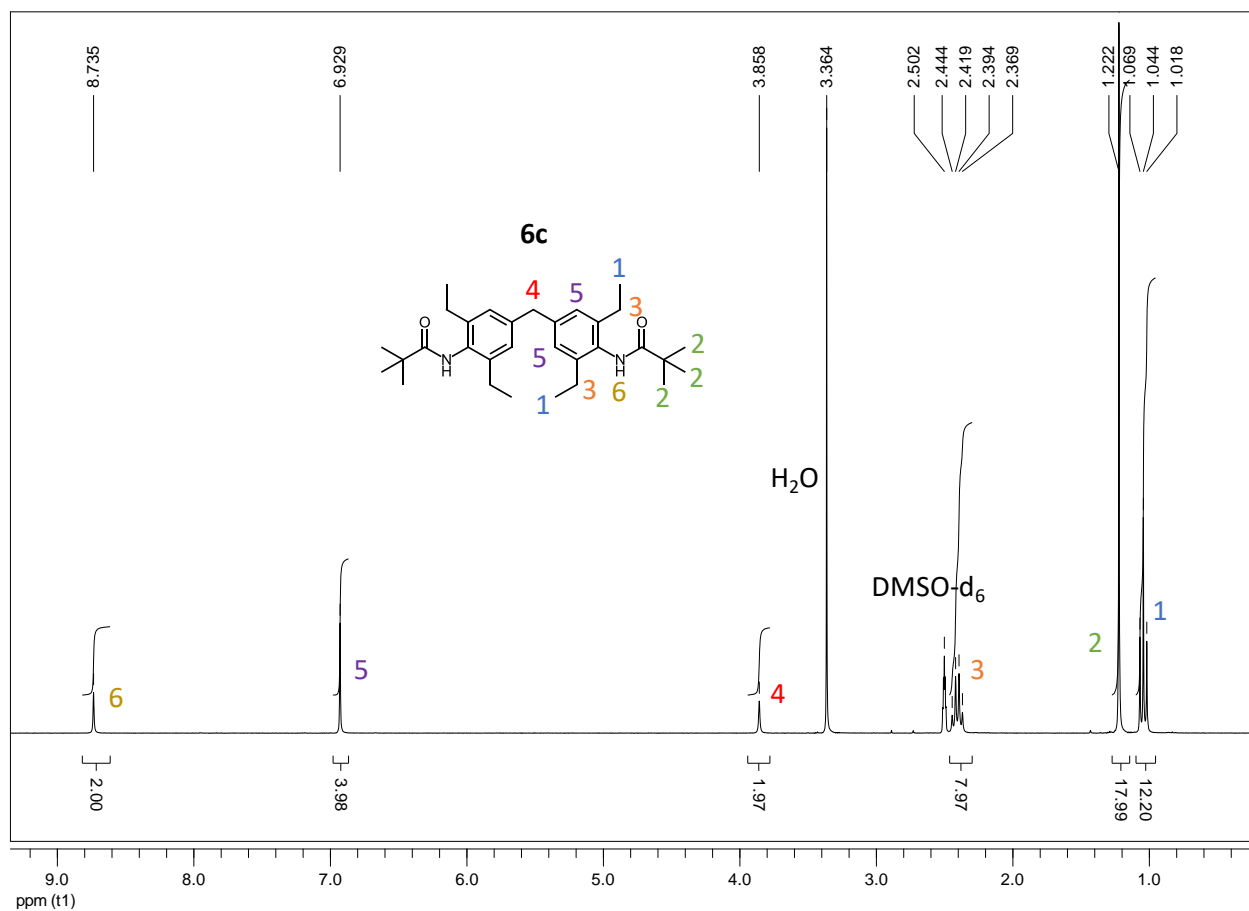


Figure 5.74:  $^1\text{H}$  NMR spectra of **6c** in  $\text{DMSO-d}_6$ .

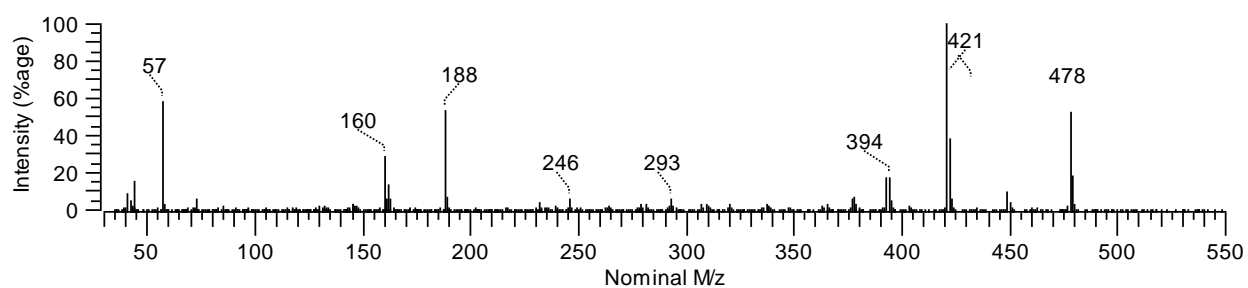
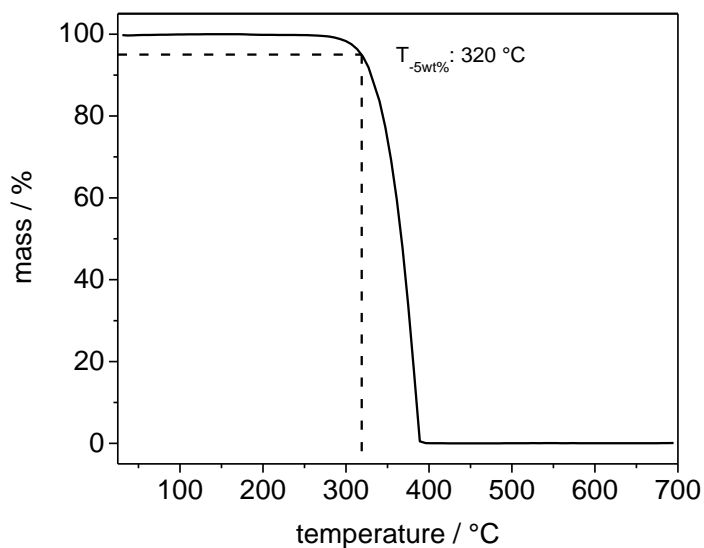
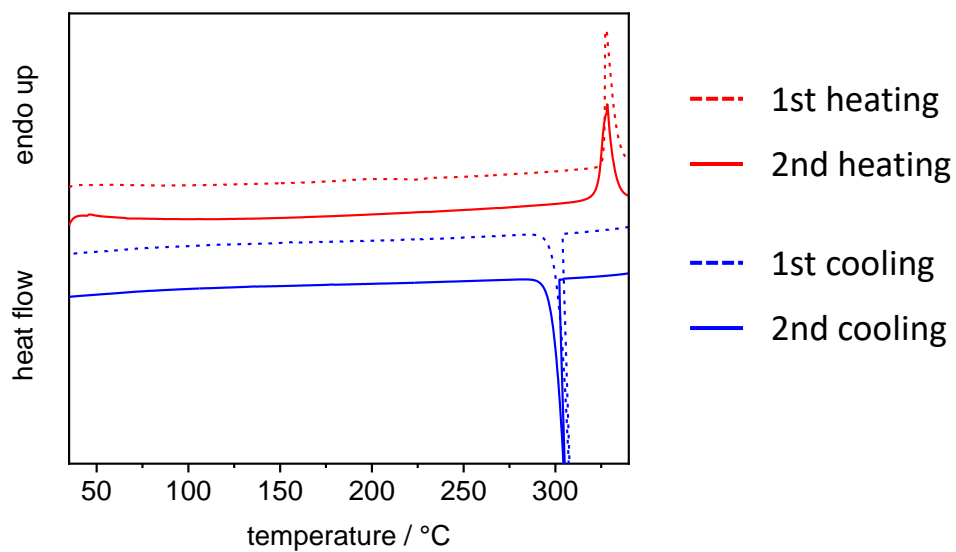


Figure 5.75: Mass spectra of **6c**.



**Figure 5.76:** Thermogram of the thermogravimetric analysis of **6c** with a heating rate of  $10 \text{ K}\cdot\text{min}^{-1}$  in the range 30 to 700 °C under nitrogen atmosphere. The temperature at which 5 % of the mass is lost is also stated ( $T_{-5\text{wt}\%}$ ).



**Figure 5.77:** Differential scanning calorimetry thermographs of **6c** including first and second heating and cooling respectively.

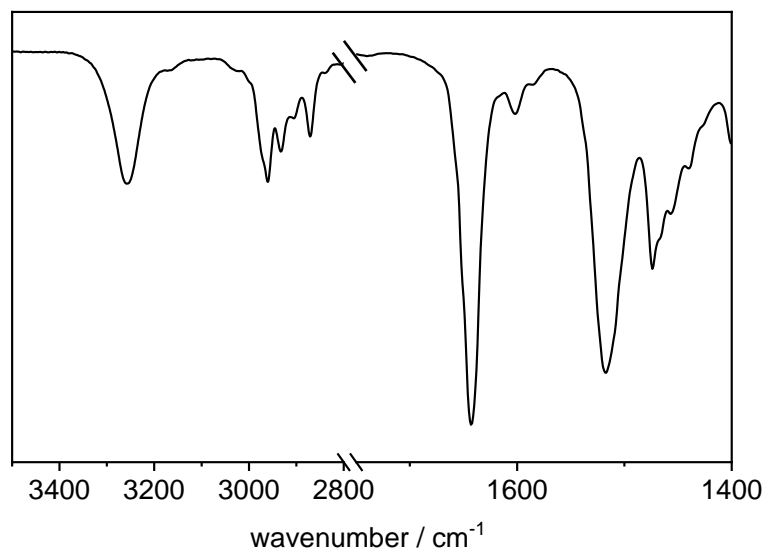


**Figure 5.78:** FT-IR spectra of **6c** in the range of 3500 to 1400  $\text{cm}^{-1}$ .

## 5.4.2.13 N,N'-[Methylenebis(2,6-diethyl-4,1-phenylene)]bis[pentanamide] - 6d

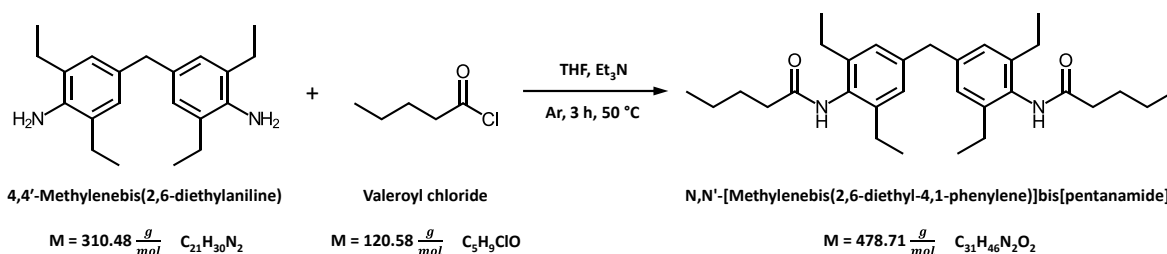


**Figure 5.79:** Reaction scheme of 4,4'-Methylenebis(2,6-diethylaniline) with valeroyl chloride to N,N'-[Methylenebis(2,6-diethyl-4,1-phenylene)]bis[pentanamide] – 6d.

**Synthesis:**

4.34 g (14.00 mmol)	4,4'-Methylenebis(2,6-diethylaniline)
3.71 g (30.8 mmol)	Valeroyl chloride
4.3 mL	Et <sub>3</sub> N
50 mL	THF

4,4'-Methylenebis(2,6-diethylaniline), Et<sub>3</sub>N and THF were mixed in a Schlenk flask and cooled down to 0 – 5 °C. Under argon atmosphere the valeroyl chloride was added dropwise and the mixture was heated to 50 °C. After 3 h the reaction mixture was precipitated in ice water. The solid was then filtered off and washed with H<sub>2</sub>O. For further purification the solid was recrystallized from 200 mL MeOH, filtered and dried in high vacuum to receive 3.7 g (56 %) of the final product in form of a white powder.

**Characterization:**

<sup>1</sup> H NMR:	[DMSO, 300 MHz, δ in ppm]: 9.08 (2H, s, NH), 6.93 (4H, s, H <sub>Ar</sub> ), 3.83 (2H, s, Ar-CH <sub>2</sub> -Ar), 2.46-2.39 (8H, q, CH <sub>2</sub> -CH <sub>3</sub> ), 2.31-2.26 (4H, t, CO-CH <sub>2</sub> ), 1.63-1.53 (4H, qi, CH <sub>2</sub> -CH <sub>2</sub> -CH <sub>2</sub> ), 1.41-1.29 (4H, sx, CH <sub>2</sub> -CH <sub>3</sub> ), 1.07-1.02 (12H, t, CH <sub>2</sub> -CH <sub>3</sub> ), 0.94-0.89 (6H, t, CH <sub>2</sub> -CH <sub>2</sub> -CH <sub>3</sub> )
MS:	(70 eV), m/z (%): 478 [M <sup>+</sup> ]
TGA:	T <sub>5wt.%</sub> = 293 °C
DSC:	T <sub>m1</sub> = 121 °C, T <sub>m2</sub> = 220 °C
IR:	[ATR, $\tilde{\nu}$ cm <sup>-1</sup> ]: 3259 (m), 2955 (s), 2928 (m), 2869 (m), 1649 (s), 1606 (w), 1509 (s), 1467 (m) 1451 (m)

## Experimental part

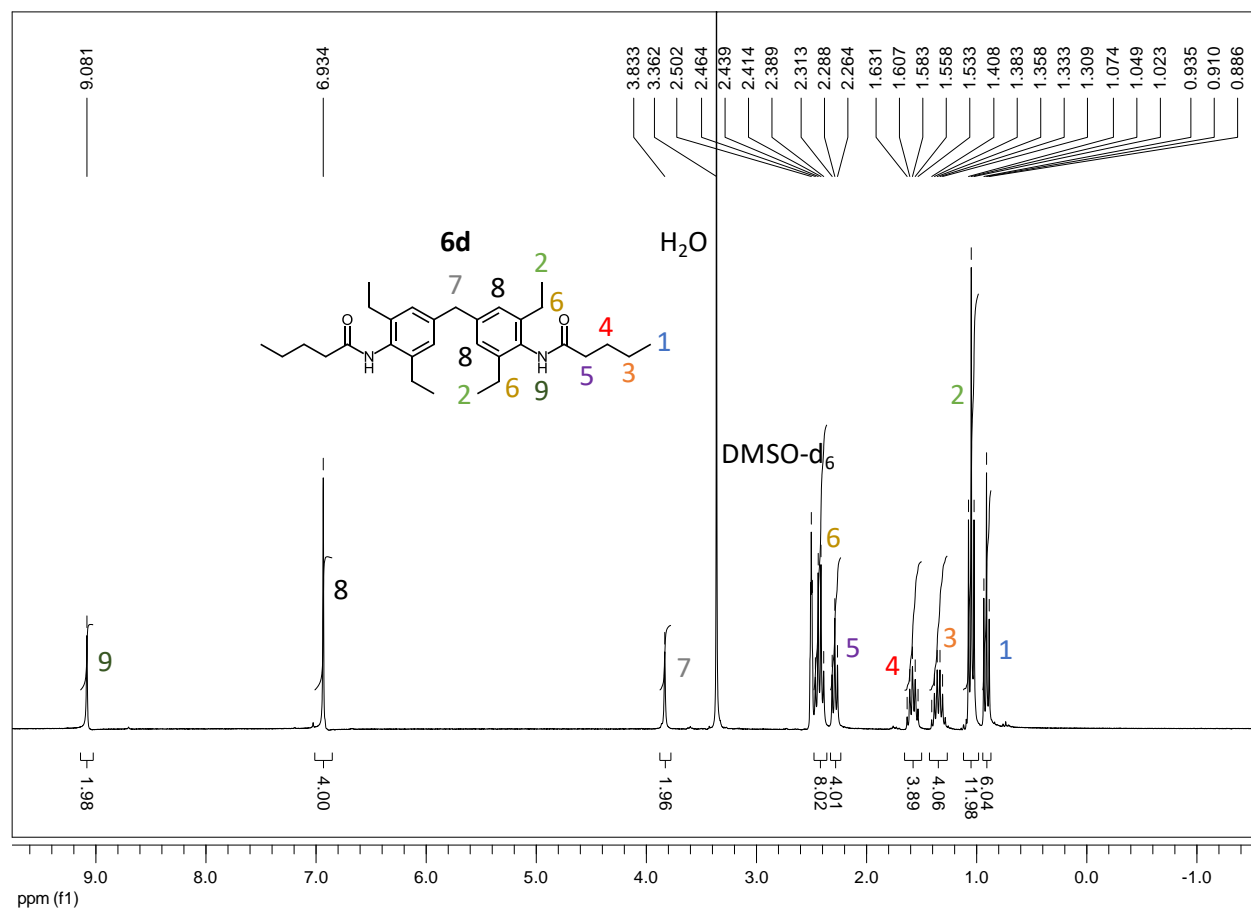


**Figure 5.80:**  $^1\text{H}$  NMR spectra of **6d** in  $\text{DMSO-d}_6$ .

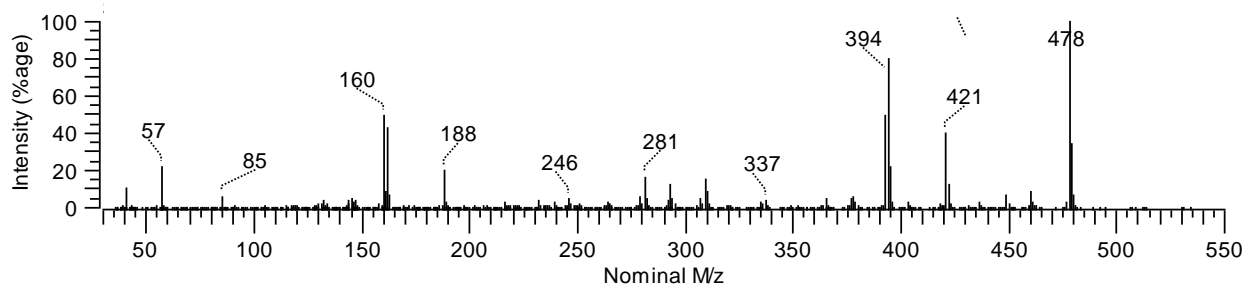


**Figure 5.81:** Mass spectra of **6d**.

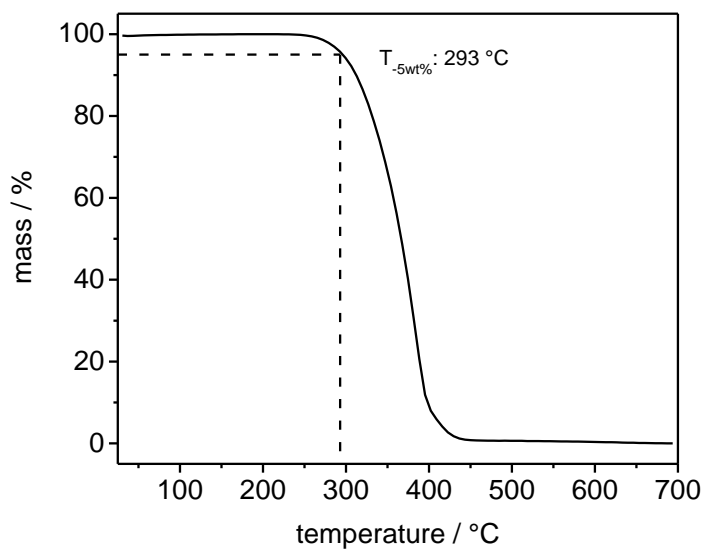


**Figure 5.82:** Thermogram of the thermogravimetric analysis of **6d** with a heating rate of  $10 \text{ K}\cdot\text{min}^{-1}$  in the range 30 to 700 °C under nitrogen atmosphere. The temperature at which 5 % of the mass is lost is also stated ( $T_{-5\text{wt}\%}$ ).

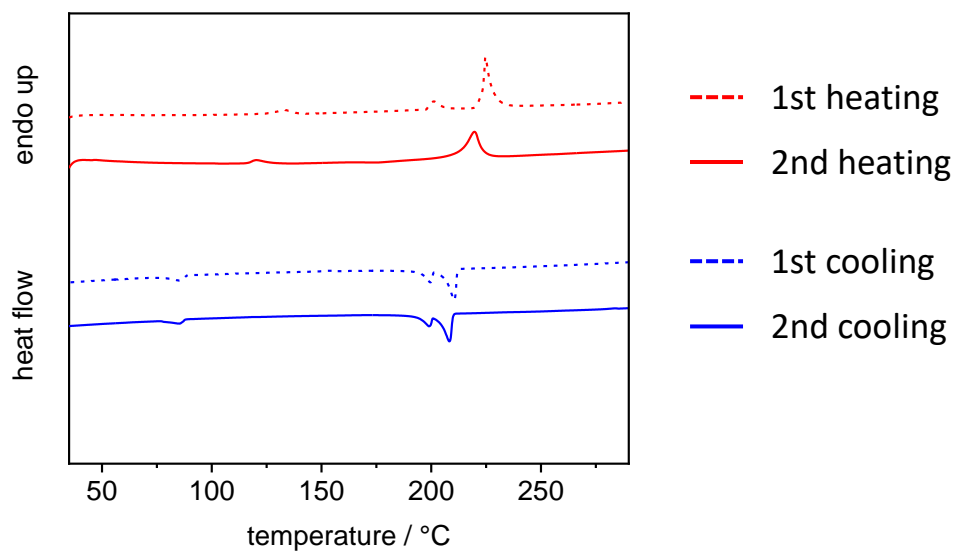


**Figure 5.83:** Differential scanning calorimetry thermographs of **6d** including first and second heating and cooling respectively.

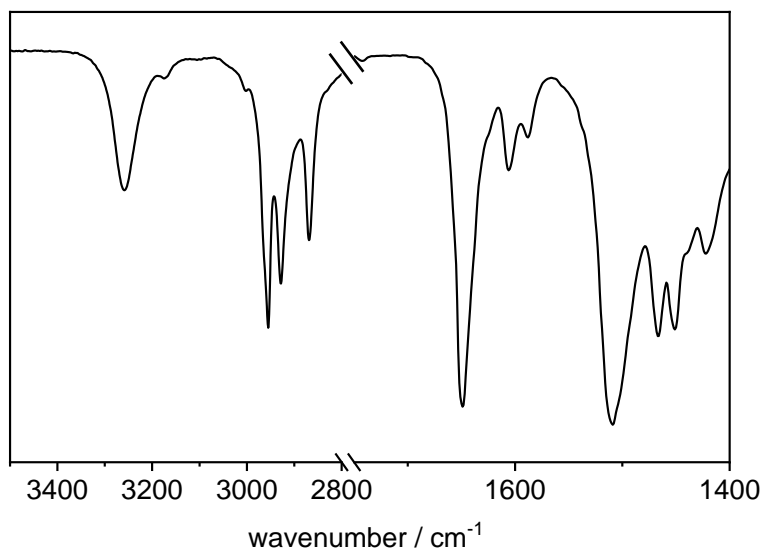


**Figure 5.84:** FT-IR spectra of **6d** of 3500 to 1400  $\text{cm}^{-1}$ .

## 6 Appendix

### 6.1 SEM micrographs of the polystyrene batch foams

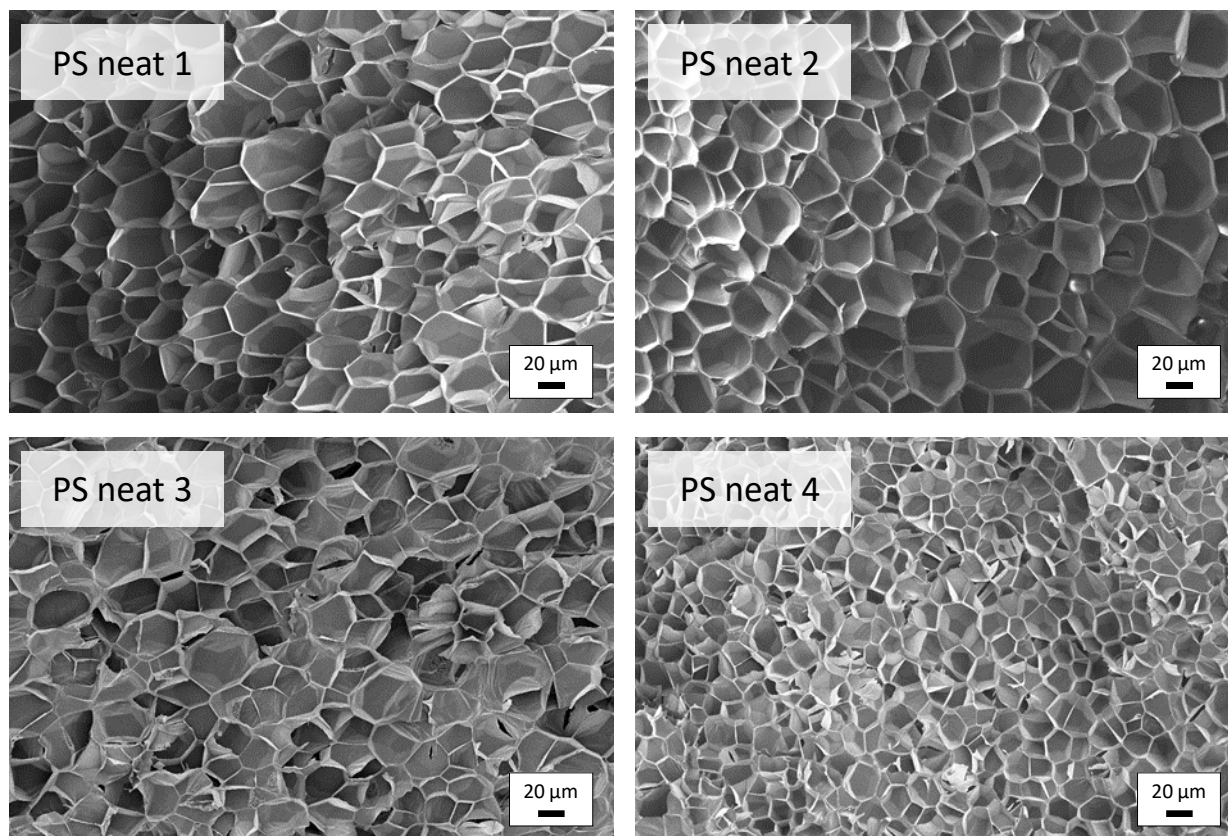


**Figure 6.1:** SEM micrographs of the neat PS batch foams.

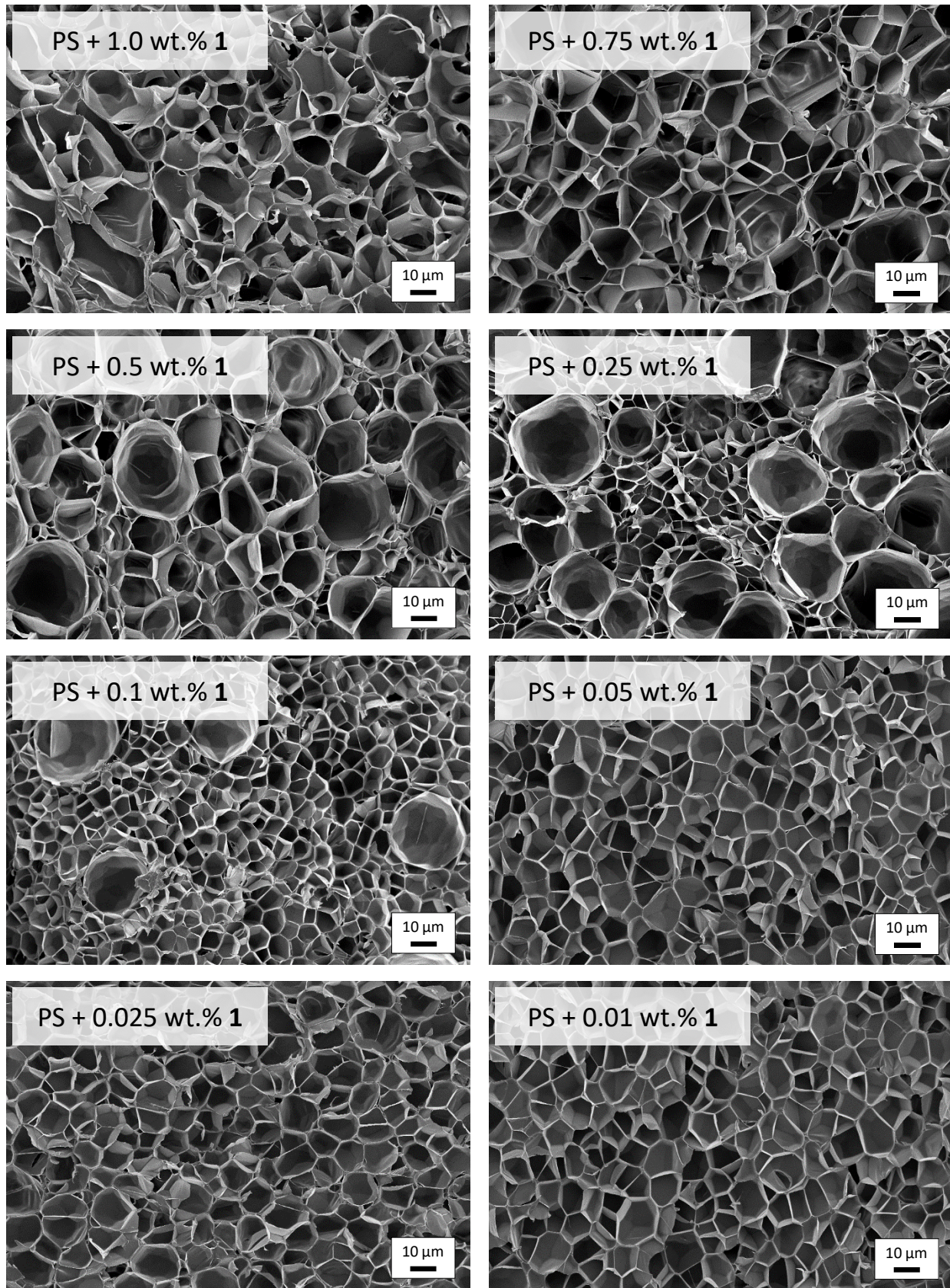


**Figure 6.2:** SEM micrographs of the PS batch foams containing additive 1 at various concentrations.

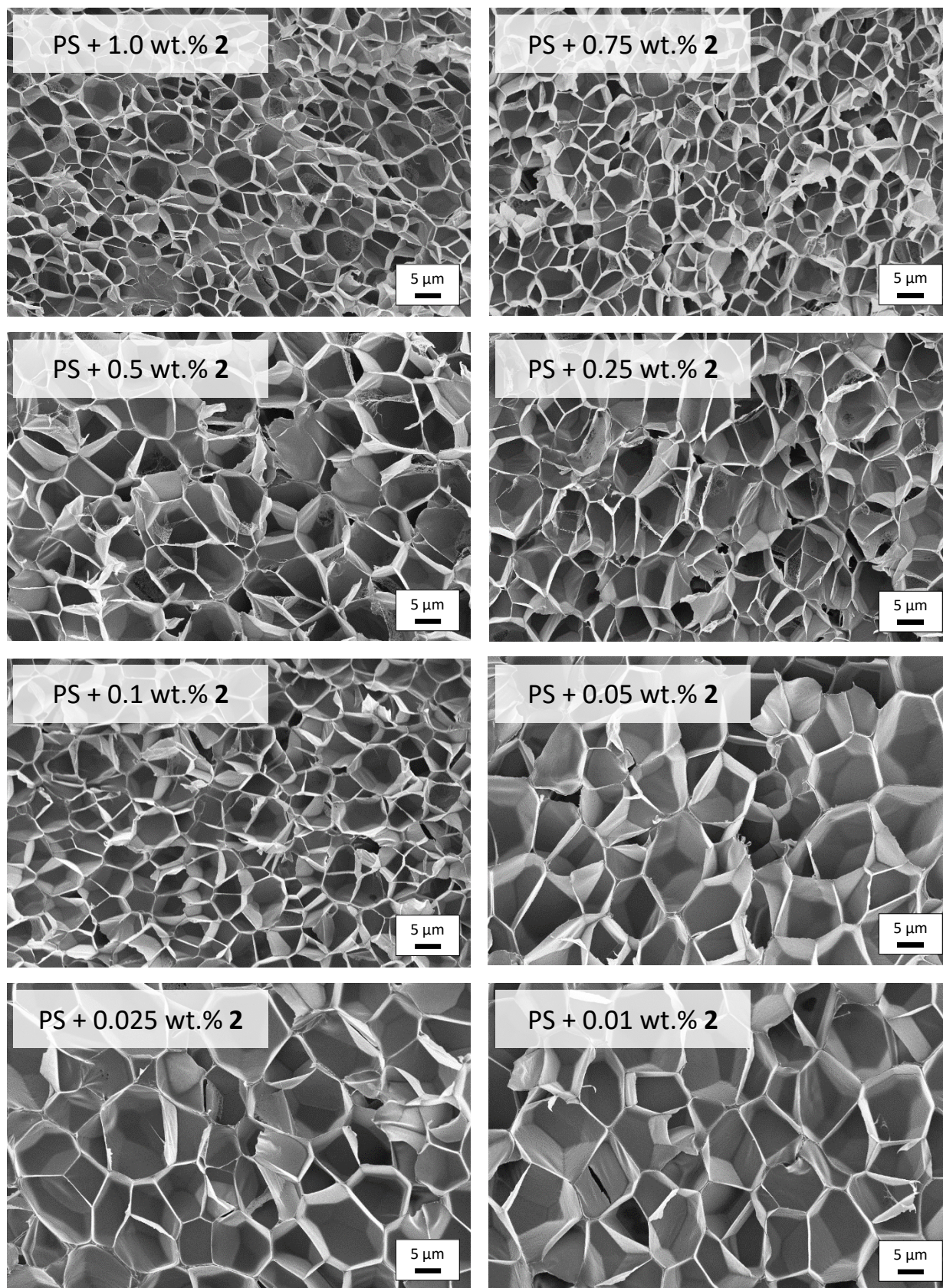


**Figure 6.3:** SEM micrographs of the PS batch foams containing additive 2 at various concentrations.

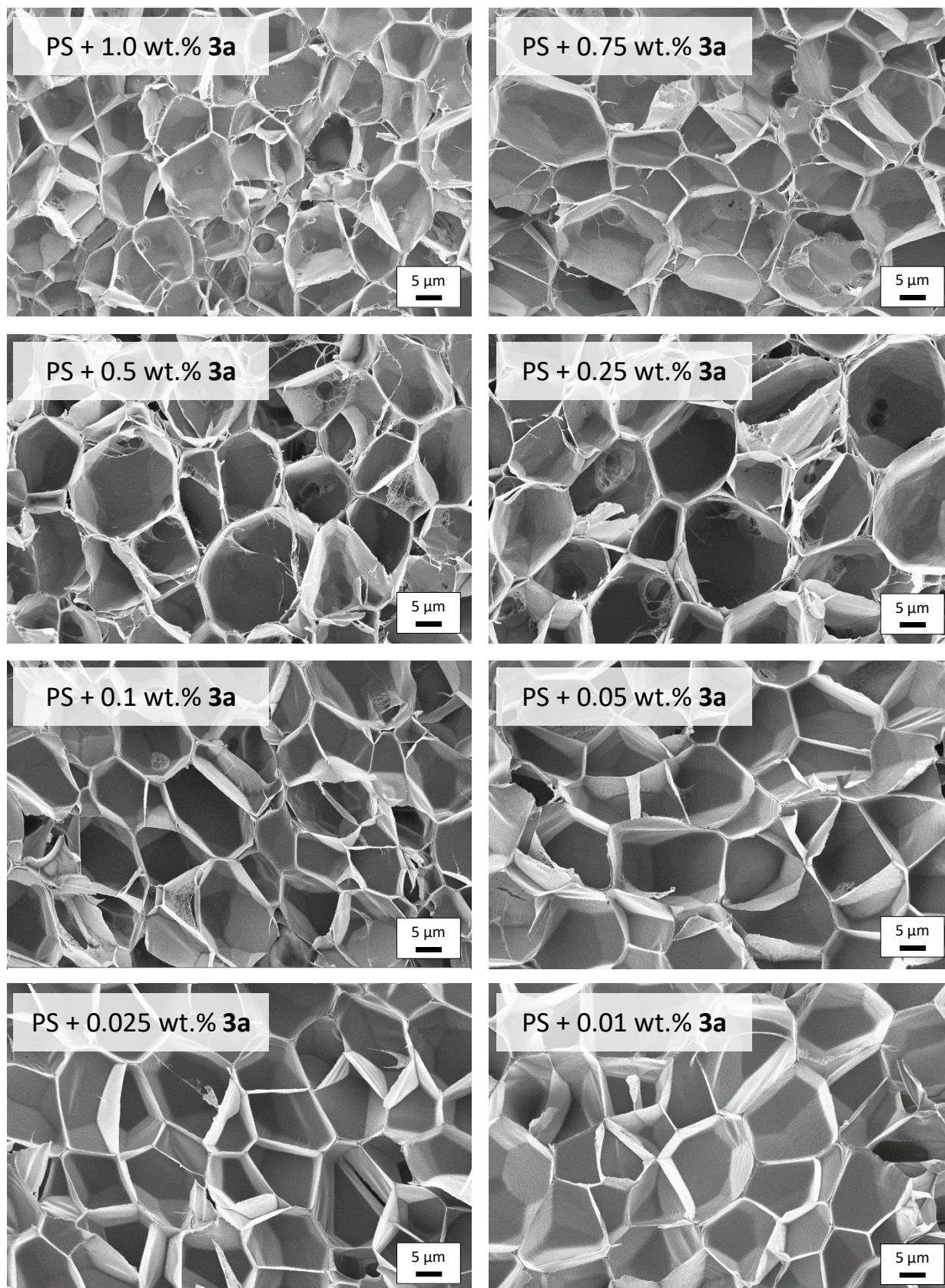


**Figure 6.4:** SEM micrographs of the PS batch foams containing additive **3a** at various concentrations.

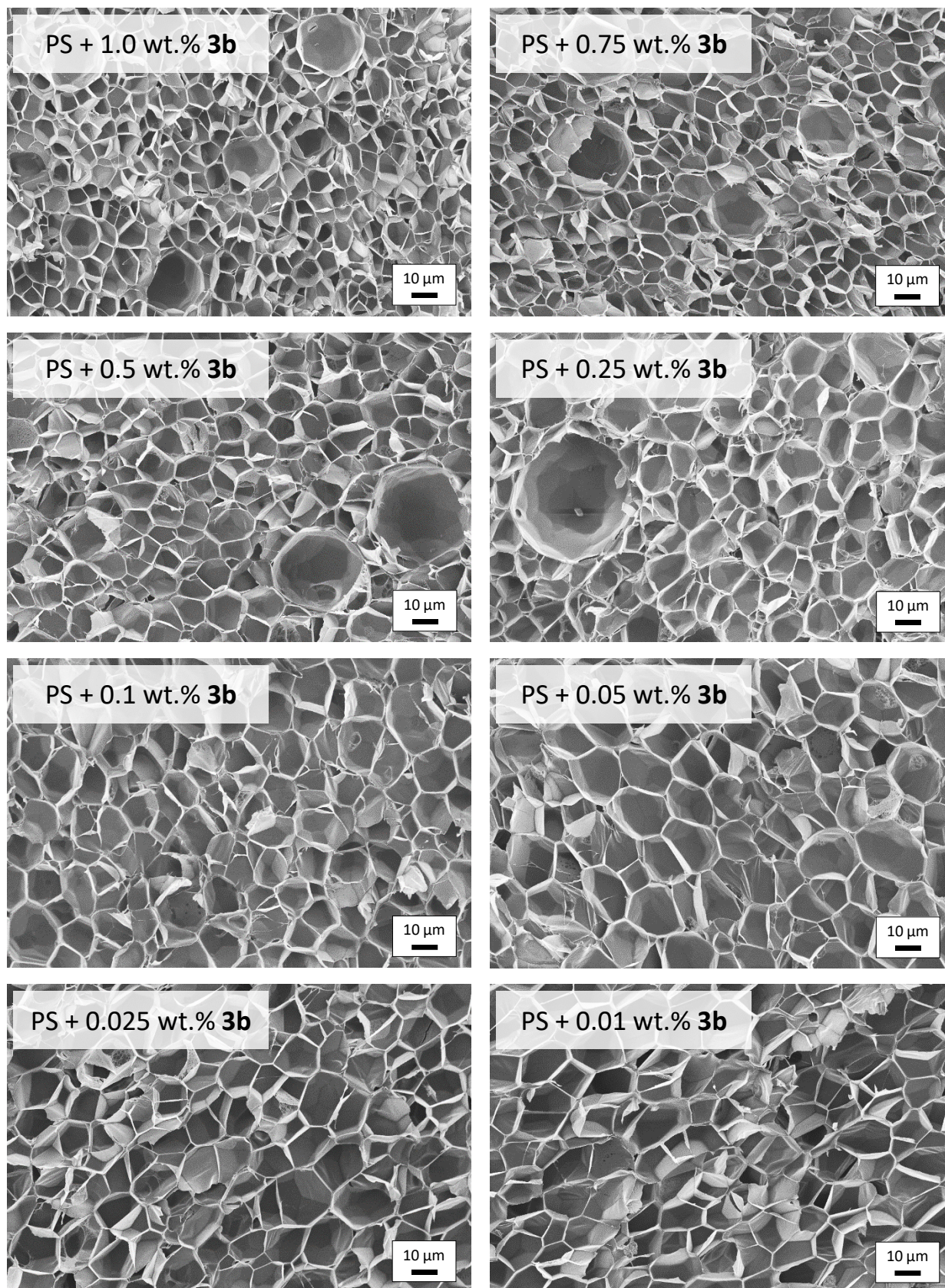


**Figure 6.5:** SEM micrographs of the PS batch foams containing additive **3b** at various concentrations.

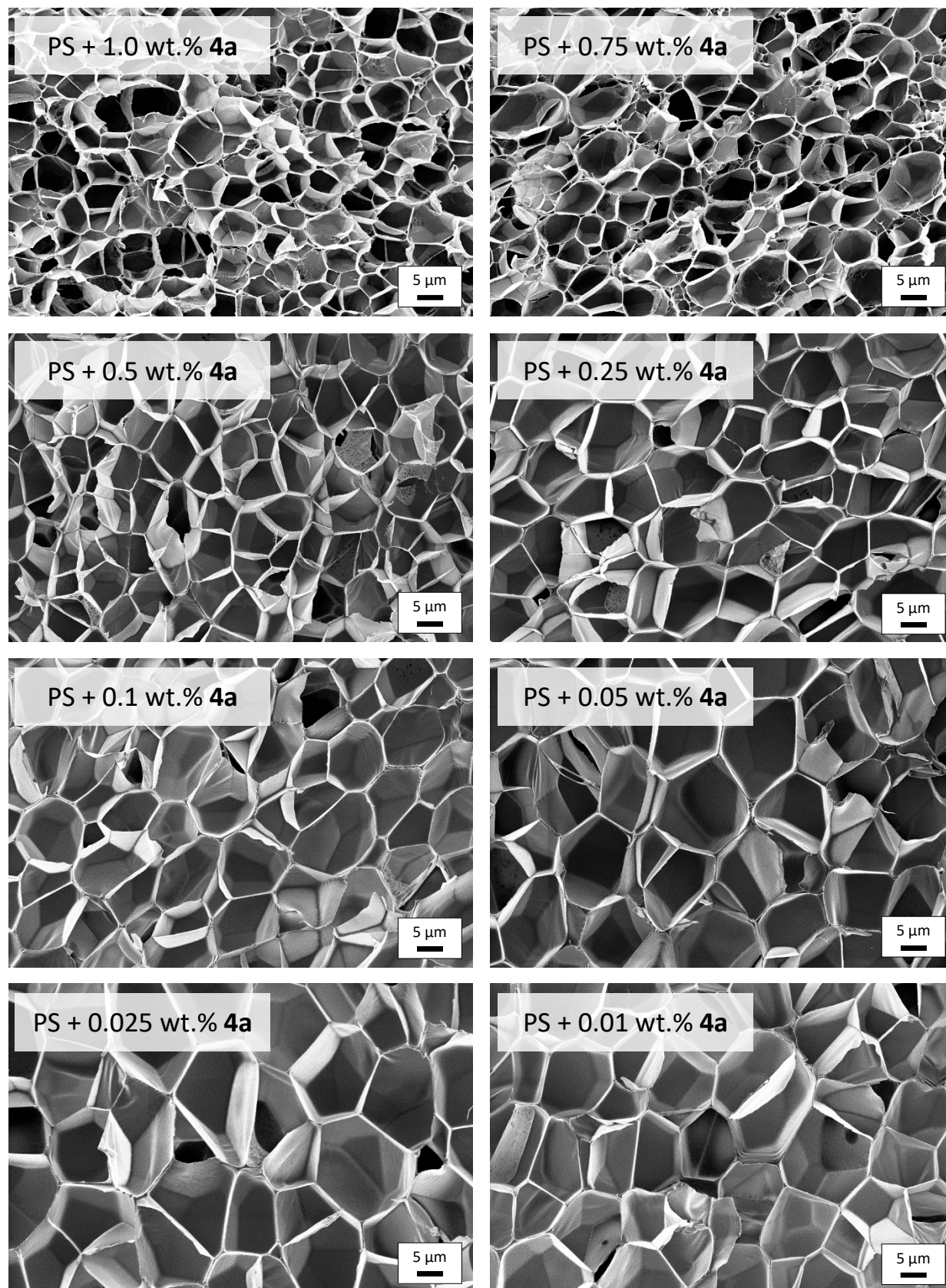


**Figure 6.6:** SEM micrographs of the PS batch foams containing additive **4a** at various concentrations.

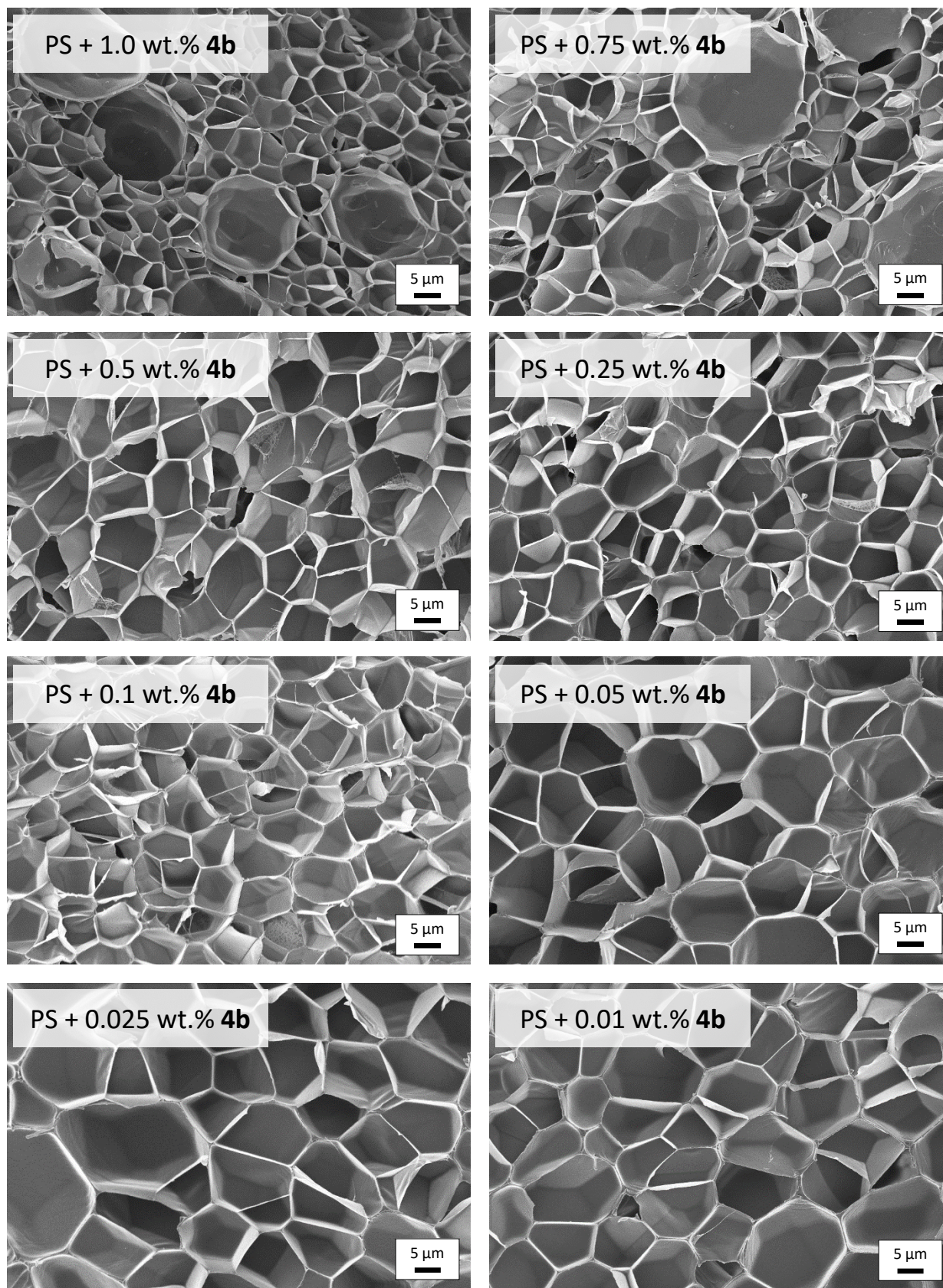


**Figure 6.7:** SEM micrographs of the PS batch foams containing additive **4b** at various concentrations.

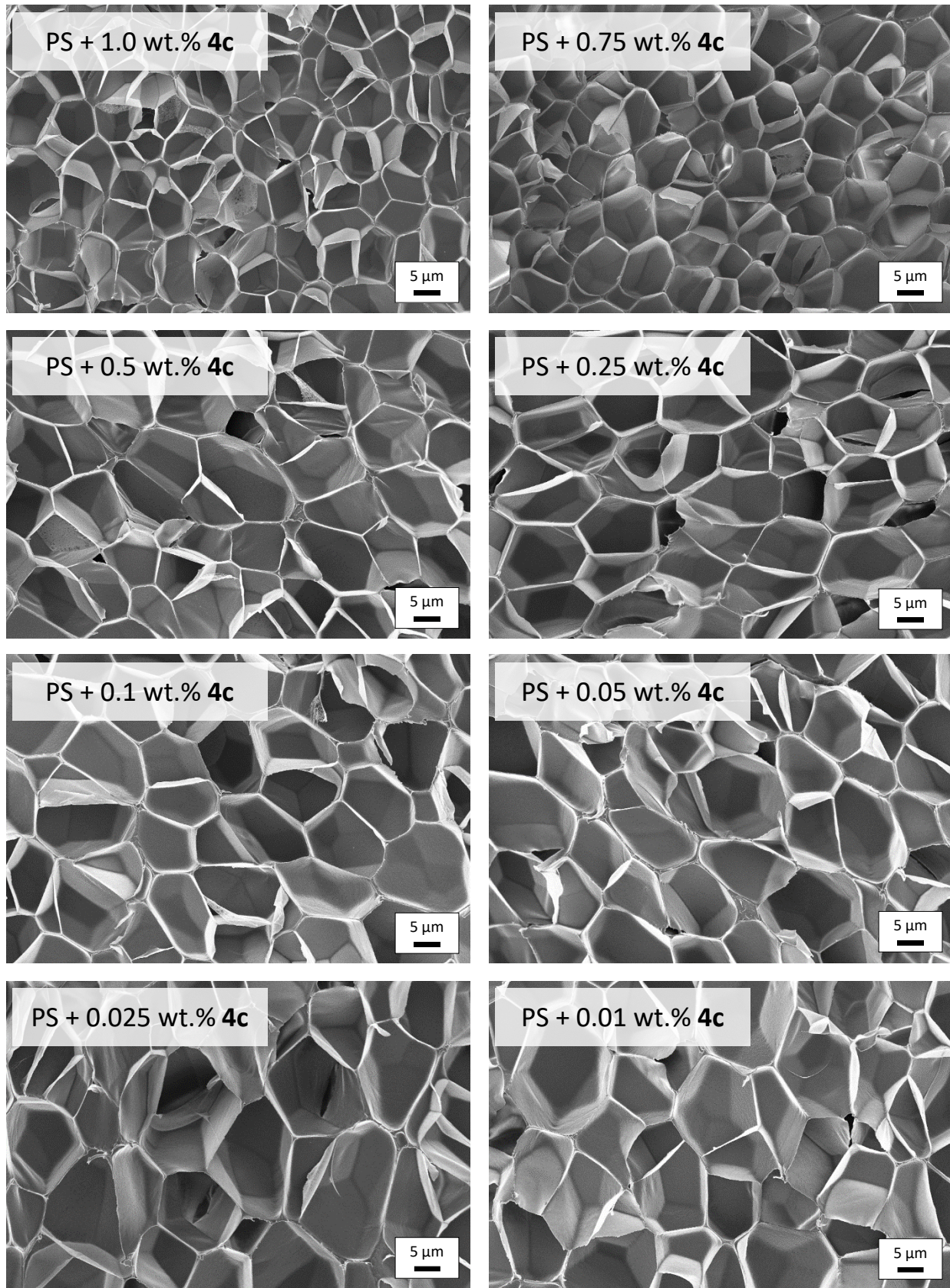


**Figure 6.8:** SEM micrographs of the PS batch foams containing additive **4c** at various concentrations.

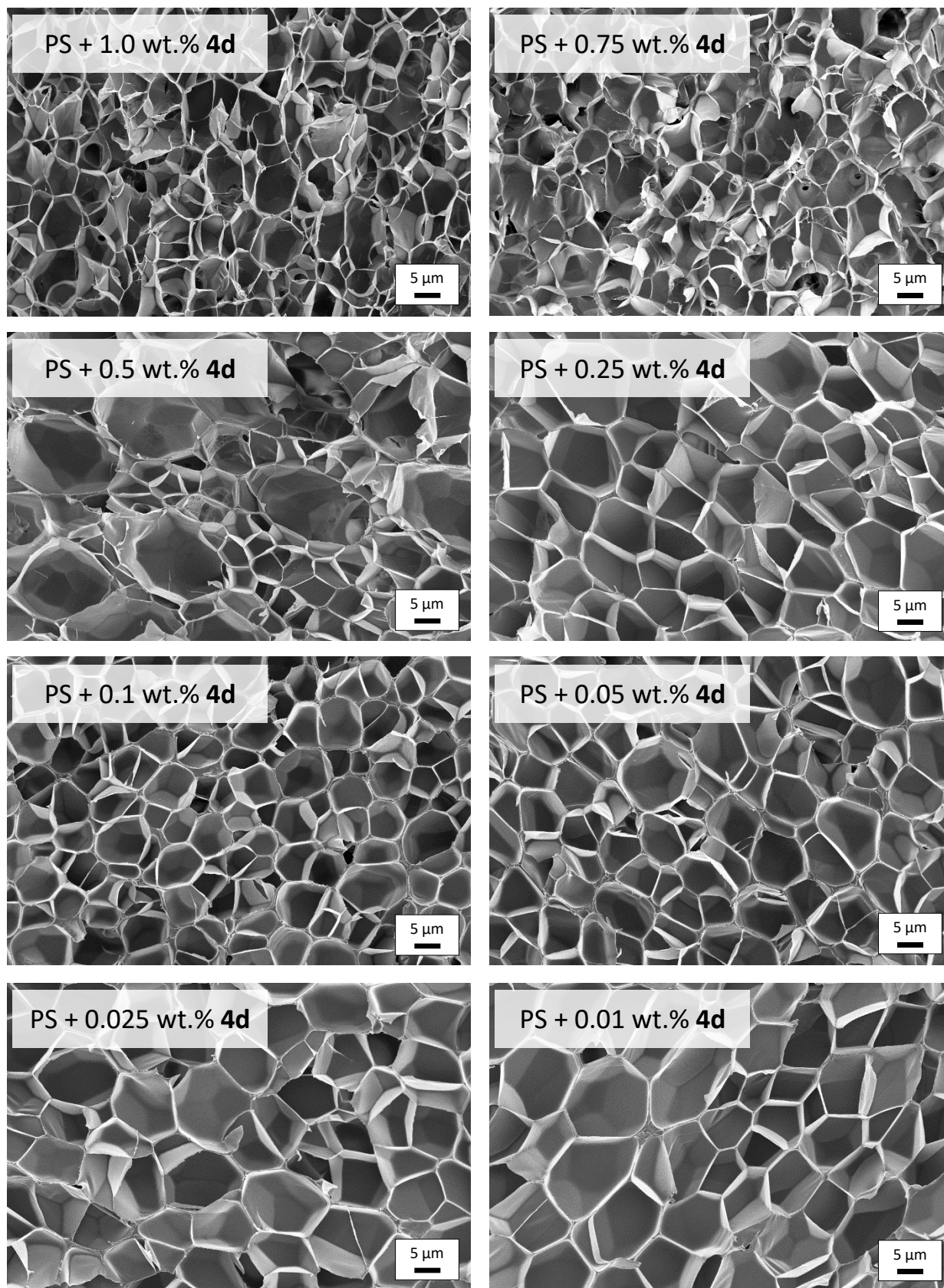


**Figure 6.9:** SEM micrographs of the PS batch foams containing additive **4d** at various concentrations.

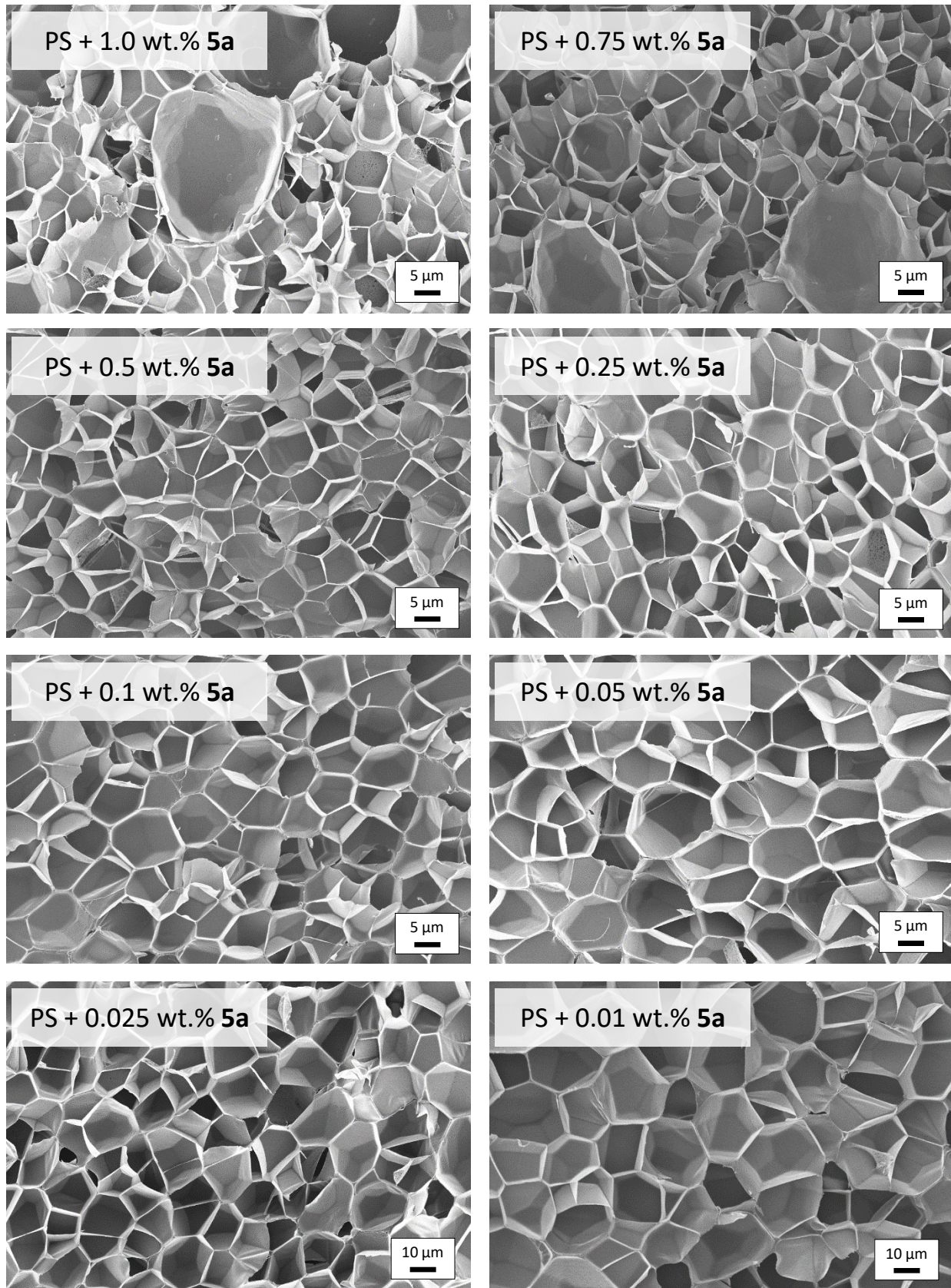


**Figure 6.10:** SEM micrographs of the PS batch foams containing additive 5a at various concentrations.

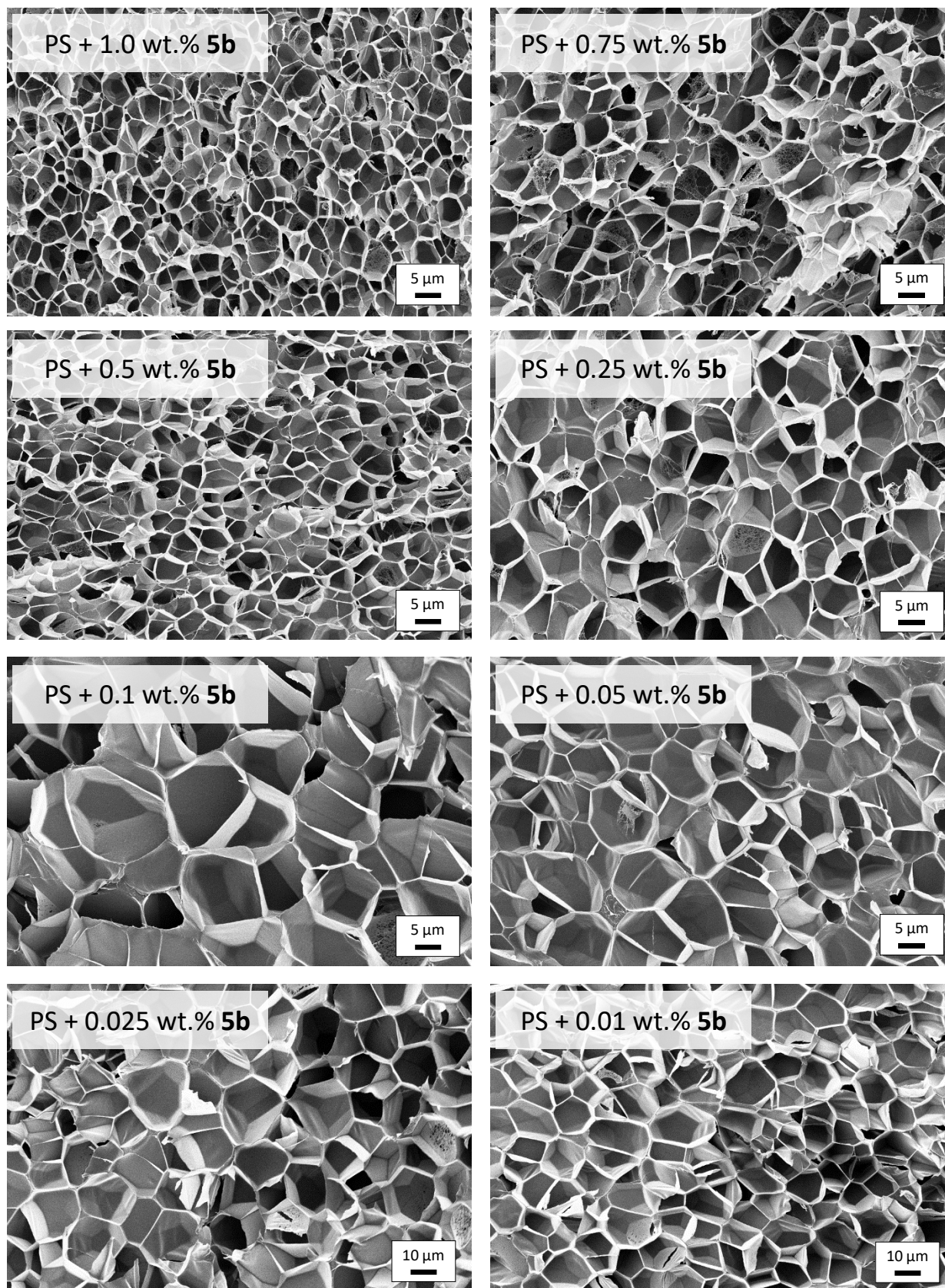


**Figure 6.11:** SEM micrographs of the PS batch foams containing additive **5b** at various concentrations.

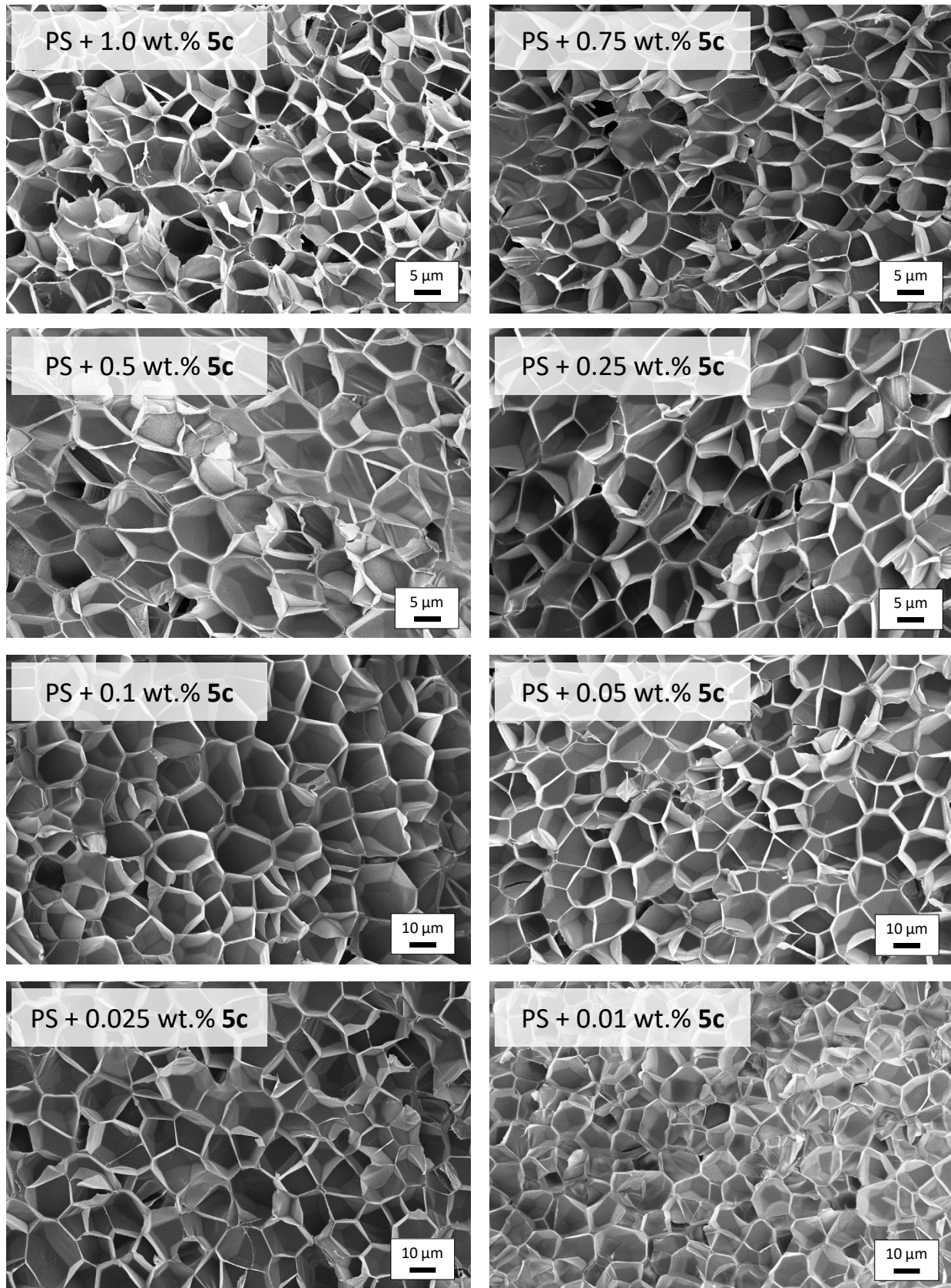


**Figure 6.12:** SEM micrographs of the PS batch foams containing additive 5c at various concentrations.

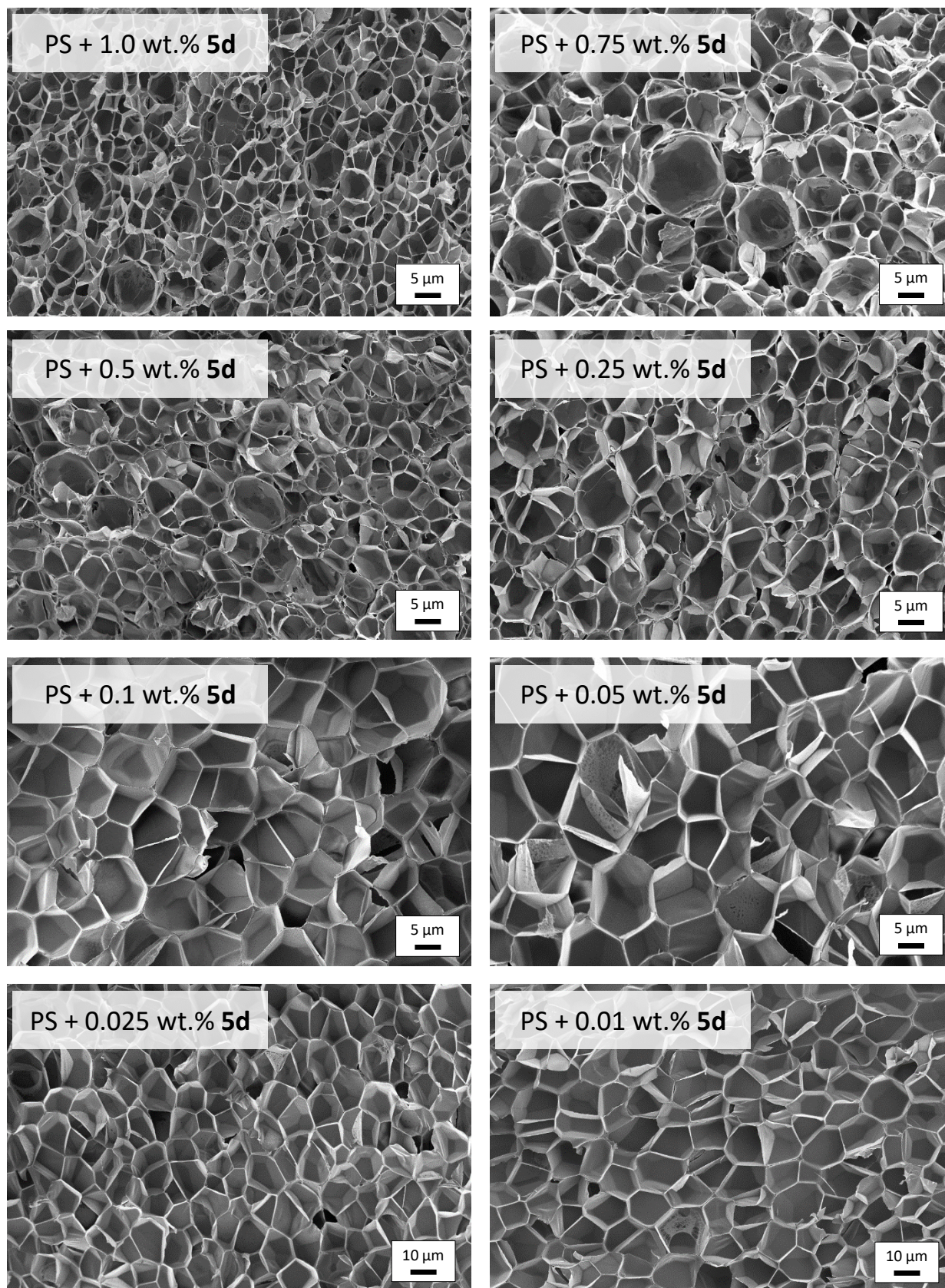


**Figure 6.13:** SEM micrographs of the PS batch foams containing additive 5d at various concentrations.

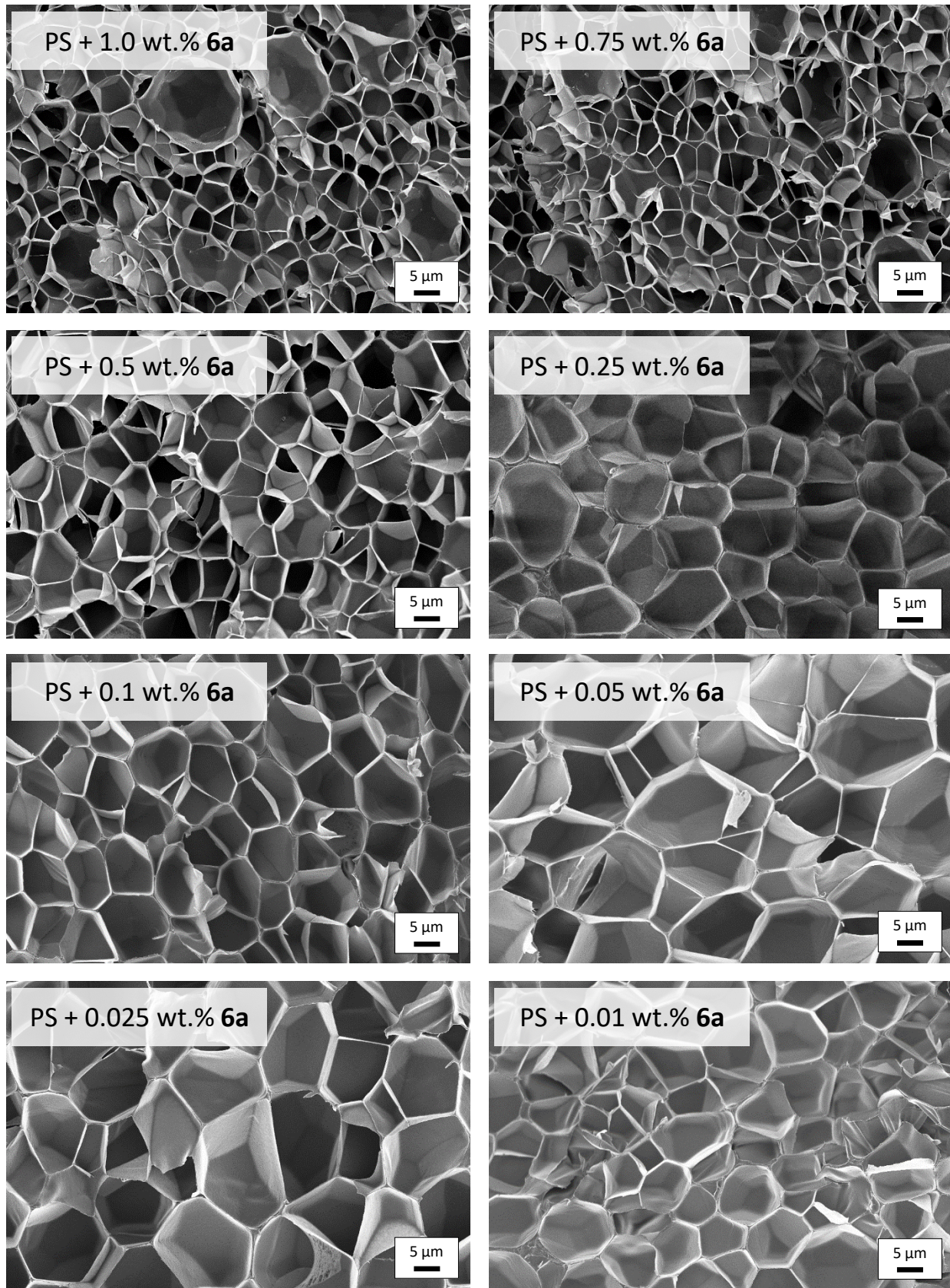


**Figure 6.14:** SEM micrographs of the PS batch foams containing additive **6a** at various concentrations.

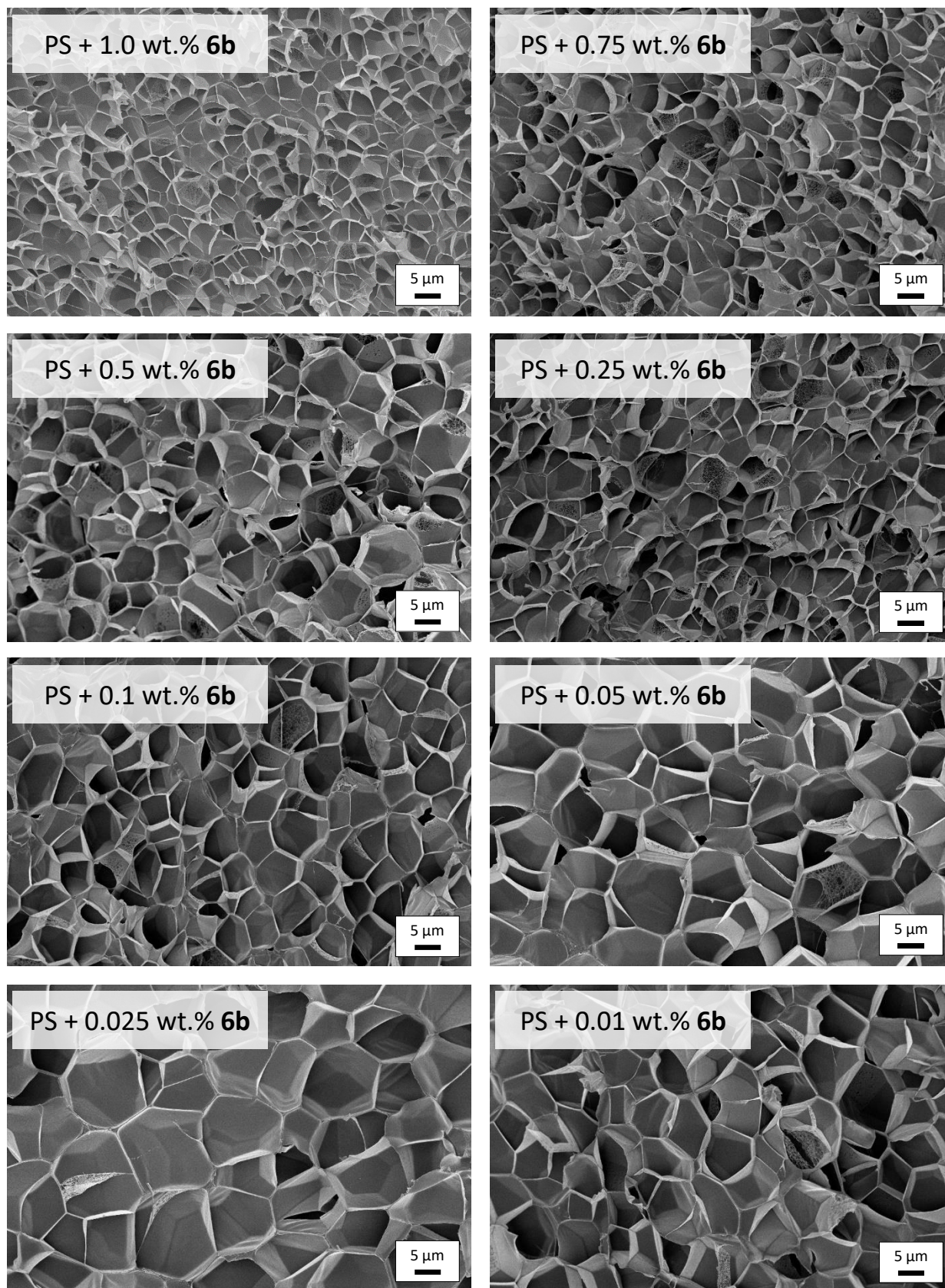


**Figure 6.15:** SEM micrographs of the PS batch foams containing additive **6b** at various concentrations.

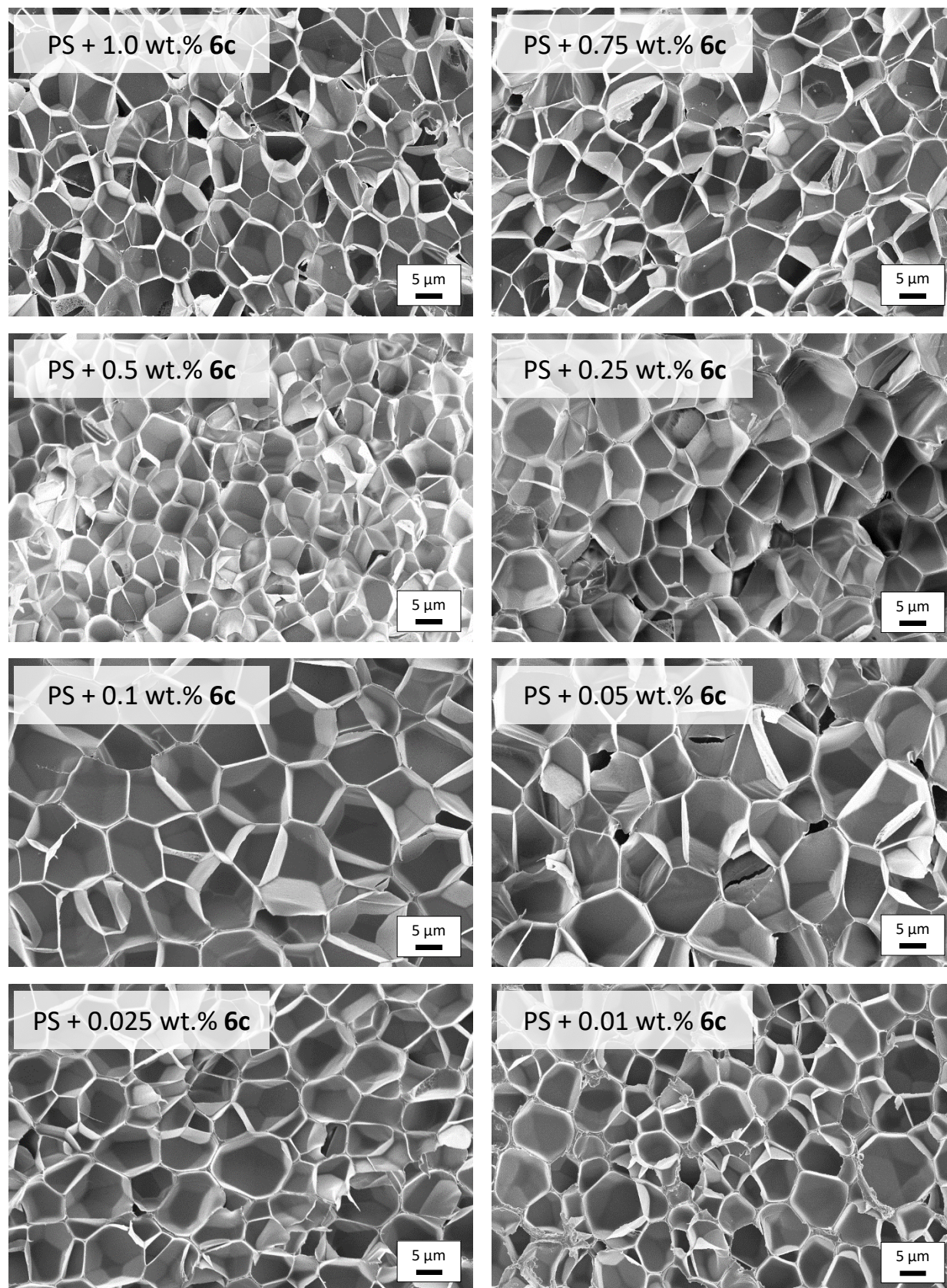


**Figure 6.16:** SEM micrographs of the PS batch foams containing additive 6c at various concentrations.

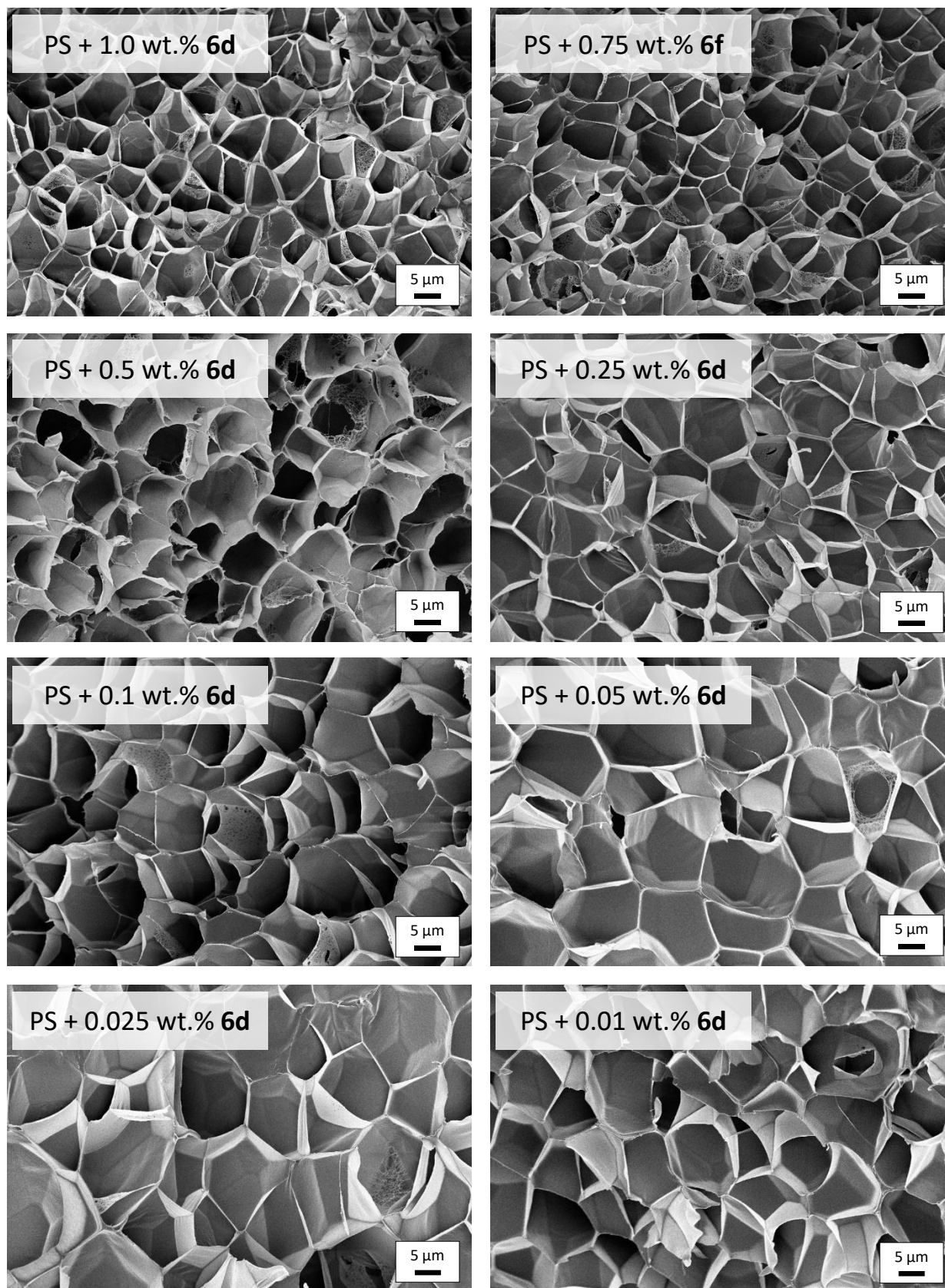


**Figure 6.17:** SEM micrographs of the PS batch foams containing additive **6d** at various concentrations.



## 7 References

- [1] P. L. Simona, P. Spiru, I. V. Ion, *Increasing the energy efficiency of buildings by thermal insulation*, *Energy Procedia* **2017**, 128, 393–399.
- [2] R. Garay, B. Arregi, P. Elguezabal, *Experimental Thermal Performance Assessment of a Prefabricated External Insulation System for Building Retrofitting*, *Procedia Environmental Sciences* **2017**, 38, 155–161.
- [3] F. Meggers, H. Leibundgut, S. Kennedy, M. Qin, M. Schlaich, W. Sobek, M. Shukuya, *Reduce CO<sub>2</sub> from buildings with technology to zero emissions*, *Sustainable Cities and Society* **2012**, 2, 29–36.
- [4] D. ürge-Vorsatz, L. D. Danny Harvey, S. Mirasgedis, M. D. Levine, *Mitigating CO<sub>2</sub> emissions from energy use in the world's buildings*, *Building Research & Information* **2007**, 35, 379–398.
- [5] C. Pavel, D. T. Blagoeva, *Competitive landscape of the EU's insulation materials industry for energy-efficient buildings*, *Publications Office of the European Union: Luxembourg*, 2018.
- [6] W. An, J. Sun, K. M. Liew, G. Zhu, *Flammability and safety design of thermal insulation materials comprising PS foams and fire barrier materials*, *Materials & Design* **2016**, 99, 500–508.
- [7] S.-T. Lee, *Foam Extrusion. Principles and Practice*, Technomic, Lancaster, **2000**.
- [8] Grand View Research (2019), *Polymer Foam Market Size, Share & Trends Analysis Report By Type, By Application, By Region, And Segment Forecasts, 2019 - 2025*, *Polymer Foam Market Size, Share & Trends Analysis Report By Type, By Application, By Region, And Segment Forecasts, 2019 - 2025*, Retrieved from <https://www.grandviewresearch.com/industry-analysis/polymer-foam-market>.
- [9] Demselben, *Ueber den flüssigen Storax (Styrax liquidus)*, *Annalen der Pharmacie* **1839**, 31, 265–277.
- [10] M. Berthelot, *Sur les caractères de la benzine et du styrolène, comparés avec ceux des autres carbures d'hydrogène*, *Bulletin de la Société Chimique de Paris* **1866**, 6, 289–298.
- [11] Deutsches Kunststoff Museum, "Zeittafel zur Geschichte der Kunststoffe", can be found under <http://www.deutsches-kunststoff-museum.de/rund-um-kunststoff/zeittafel-zur-geschichte/>.
- [12] Ceresana, *Marktstudie Polystyrol & Expandierbares Polystyrol (PS & EPS)*, *Marktstudie Polystyrol & Expandierbares Polystyrol (PS & EPS)* **2019**, Retrieved from <https://www.ceresana.com/de/marktstudien/kunststoffe/polystyrol-expandierbares-polystyrol/polystyrol-expandierbares-polystyrol-markt-anteil-kapazitaet-angebot-nachfrage-prognose-innovation-anwendung-wachstum-produktion-industrie.html>.
- [13] M. D. Lechner, K. Gehrke, E. H. Nordmeier, *Makromolekulare Chemie. Ein Lehrbuch für Chemiker, Physiker, Materialwissenschaftler und Verfahrenstechniker*, Springer Berlin Heidelberg, Berlin, **2014**.
- [14] G. Wypych in *Handbook of Polymers*, Elsevier, **2012**, pp. 541–547.

## References

---

- [15] S.-T. Lee, N. S. Ramesh, C. B. Park, *Polymeric foams. Science and technology*, CRC Press, Boca Raton, Fla., **2007**.
- [16] D. Eaves, *Handbook of polymer foams*, Rapra Technology, Shrewsbury, Shropshire, U.K., **2004**.
- [17] D. Klempner, *Handbook of polymeric foams and foam technology*, Hanser, Munich [etc.], **op. 1991**.
- [18] D. I. Collais, D. G. Baird, *Tesile toughness of microcellular foams of polystyrene, styrene-acrylonitrile copolymer, and polycarbonate, and the effect of dissolved gas on the tensile toughness of the same polymer matrices and microcellular foams*, *Polymer Engineering and Science* **1995**, *35*, 1167–1177.
- [19] J. S. Colton, N. P. Suh, *The nucleation of microcellular thermoplastic foam with additives: Part I: Theoretical considerations*, *Polymer Engineering and Science* **1987**, *27*, 485–492.
- [20] K. A. Seeler, V. Kumar, *Tension-Tension Fatigue of Microcellular Polycarbonate: Initial Results*, *Journal of Reinforced Plastics and Composites* **1993**, *12*, 359–376.
- [21] J. Schellenberg, M. Wallis, *Dependence of Thermal Properties of Expandable Polystyrene Particle Foam on Cell Size and Density*, *Journal of Cellular Plastics* **2010**, *46*, 209–222.
- [22] Y. Chen, R. Das, M. Battley, *Effects of cell size and cell wall thickness variations on the stiffness of closed-cell foams*, *International Journal of Solids and Structures* **2015**, *52*, 150–164.
- [23] M. F. Ashby, R. F. M. Medalist, *The mechanical properties of cellular solids*, *Metallurgical Transactions A* **1983**, *14*, 1755–1769.
- [24] R. Hasanzadeh, T. Azdast, A. Doniavi, M. Rostami, *A prediction model using response surface methodology based on cell size and foam density to predict thermal conductivity of polystyrene foams*, *Heat Mass Transfer* **2019**, *55*, 2845–2855.
- [25] C. Forest, P. Chaumont, P. Cassagnau, B. Swoboda, P. Sonntag, *Polymer nano-foams for insulating applications prepared from CO<sub>2</sub> foaming*, *Progress in Polymer Science* **2015**, *41*, 122–145.
- [26] S. S. Sundarram, W. Li, *On thermal conductivity of micro- and nanocellular polymer foams*, *Polymer Engineering and Science* **2013**, *53*, 1901–1909.
- [27] C. Okolieocha, *Dissertation*, Universität Bayreuth, **2019**.
- [28] R. Gendron, *Thermoplastic foam processing. Principles and development*, CRC Press, Boca Raton, **2004**.
- [29] I. Tsivintzelis, A. G. Angelopoulou, C. Panayiotou, *Foaming of polymers with supercritical CO<sub>2</sub>*, *Polymer* **2007**, *48*, 5928–5939.
- [30] M. Sauceau, C. Nikitine, E. Rodier, J. Fages, *Effect of supercritical carbon dioxide on polystyrene extrusion*, *The Journal of Supercritical Fluids* **2007**, *43*, 367–373.
- [31] E. Reverchon, S. Cardea, *Production of controlled polymeric foams by supercritical CO<sub>2</sub>*, *The Journal of Supercritical Fluids* **2007**, *40*, 144–152.

- [32] H. Janani, M.H.N. Famili, *Investigation of a strategy for well controlled inducement of microcellular and nanocellular morphologies in polymers*, *Polymer Engineering & Science* **2010**, *50*, 1558–1570.
- [33] C. Y. Gao, N. Q. Zhou, T. K. Shan, Z. X. Xin, *Key Parameters Influencing Microcellular Polystyrene Cell Morphology Blowing with Supercritical CO<sub>2</sub>*, *Key Engineering Materials* **2012**, *501*, 237–242.
- [34] J.-B. Bao, T. Liu, L. Zhao, G.-H. Hu, X. Miao, X. Li, *Oriented foaming of polystyrene with supercritical carbon dioxide for toughening*, *Polymer* **2012**, *53*, 5982–5993.
- [35] A. Nistor, A. Rygl, M. Bobak, M. Sajfirtova, J. Kosek, *Micro-Cellular Polystyrene Foam Preparation Using High Pressure CO<sub>2</sub>*, *Macromolecular Symposia* **2013**, *333*, 266–272.
- [36] L.-Q. Xu, H.-X. Huang, *Formation mechanism and tuning for bi-modal cell structure in polystyrene foams by synergistic effect of temperature rising and depressurization with supercritical CO<sub>2</sub>*, *The Journal of Supercritical Fluids* **2016**, *109*, 177–185.
- [37] M. M. M. Shirvan, M.H.N. Famili, M. S. Alkuh, A. Golbang, *The effect of pressurized and fast stabilization on one step batch foaming process for the investigation of cell structure formation*, *The Journal of Supercritical Fluids* **2016**, *112*, 143–152.
- [38] K. A. Arora, A. J. Lesser, T. J. McCarthy, *Preparation and Characterization of Microcellular Polystyrene Foams Processed in Supercritical Carbon Dioxide*, *Macromolecules* **1998**, *31*, 4614–4620.
- [39] X. Han, K. W. Koelling, D. L. Tomasko, L. J. Lee, *Continuous microcellular polystyrene foam extrusion with supercritical CO<sub>2</sub>*, *Polymer Engineering and Science* **2002**, *42*, 2094–2106.
- [40] C. B. Park, D. F. Baldwin, N. P. Suh, *Effect of the pressure drop rate on cell nucleation in continuous processing of microcellular polymers*, *Polymer Engineering and Science* **1995**, *35*, 432–440.
- [41] D. Tammaro, A. de Maio, M. G. P. Carbone, E. Di Maio, S. Iannace, *PS foams at high pressure drop rates*, *AIP Conference Proceedings* **2014**, 473–476.
- [42] X.-F. Peng, L.-Y. Liu, B.-Y. Chen, H.-Y. Mi, X. Jing, *A novel online visualization system for observing polymer extrusion foaming*, *Polymer Testing* **2016**, *52*, 225–233.
- [43] D. Liang, Z. Jixi, Y. Wenli, Z. Yaping, *Foaming Behaviour of Polystyrene with supercritical Carbon Dioxide*, *11th European Meeting on Supercritical Fluids* **2008**.
- [44] X. Xu, C. B. Park, D. Xu, R. Pop-Iliev, *Effects of die geometry on cell nucleation of PS foams blown with CO<sub>2</sub>*, *Polymer Engineering and Science* **2003**, *43*, 1378–1390.
- [45] H. Wu, Z. Du, H. Zhou, X. Wang, J. Mi, *Evaluation of solubility enhancement of carbon dioxide in polystyrene via introduction of water*, *Fluid Phase Equilibria* **2017**, *449*, 83–90.
- [46] A. Nistor, M. Topiar, H. Sovova, J. Kosek, *Effect of organic co-blowing agents on the morphology of CO<sub>2</sub> blown microcellular polystyrene foams*, *The Journal of Supercritical Fluids* **2017**, *130*, 30–39.

## References

---

- [47] C. V. Vo, A. N. Paquet, *An Evaluation of the Thermal Conductivity of Extruded Polystyrene Foam Blown with HFC-134a or HCFC-142b*, *Journal of Cellular Plastics* **2016**, *40*, 205–228.
- [48] R. Gendron, M. F. Champagne, Y. Delaviz, M. E. Polasky, *Foaming Polystyrene with a Mixture of CO<sub>2</sub> and Ethanol*, *Journal of Cellular Plastics* **2006**, *42*, 127–138.
- [49] C. Zhang, B. Zhu, D. Li, L. J. Lee, *Extruded polystyrene foams with bimodal cell morphology*, *Polymer* **2012**, *53*, 2435–2442.
- [50] M. Jiang, H. Chi, *Effect of Kaolin Clay Content on the Cell Morphology and Physical Properties of Injection Molded PS Foams*, *Advanced Materials Research* **2011**, *233-235*, 2451–2455.
- [51] X. Han, C. Zeng, L. J. Lee, K. W. Koelling, D. L. Tomasko, *Extrusion of polystyrene nanocomposite foams with supercritical CO<sub>2</sub>*, *Polymer Engineering & Science* **2003**, *43*, 1261–1275.
- [52] C. Gutiérrez, M. T. Garcia, R. Mencía, I. Garrido, J. F. Rodríguez, *Clean preparation of tailored microcellular foams of polystyrene using nucleating agents and supercritical CO<sub>2</sub>*, *Journal of Materials Science* **2016**, *51*, 4825–4838.
- [53] S. Liu, B. Zoetebier, L. Hulsman, Y. Zhang, J. Duvinneau, G. J. Vancso, *Nanocellular polymer foams nucleated by core-shell nanoparticles*, *Polymer* **2016**, *104*, 22–30.
- [54] P. Yu, G. Liu, K. Li, A. Huang, B. Chen, H. Mi, S. Zhang, X. Peng, *Fabrication of polystyrene/nano-CaCO<sub>3</sub> foams with unimodal or bimodal cell structure from extrusion foaming using supercritical carbon dioxide*, *Polymer Composites* **2016**, *37*, 1864–1873.
- [55] S. Costeux, L. Zhu, *Low density thermoplastic nanofoams nucleated by nanoparticles*, *Polymer* **2013**, *54*, 2785–2795.
- [56] J. Yang, L. Huang, Y. Zhang, F. Chen, M. Zhong, *Mesoporous silica particles grafted with polystyrene brushes as a nucleation agent for polystyrene supercritical carbon dioxide foaming*, *Journal of Applied Polymer Science* **2013**, *65*, 4308-4317.
- [57] S. Jiong, Z. Changchun, L. James, *Nucleation Effects of Nanoparticels on Microcellular Polystyrene Foams*.
- [58] P. Gong, G. Wang, M.-P. Tran, P. Buahom, S. Zhai, G. Li, C. B. Park, *Advanced bimodal polystyrene/multi-walled carbon nanotube nanocomposite foams for thermal insulation*, *Carbon* **2017**, *120*, 1–10.
- [59] Y.-C. Yen, T. Lee, D. Chiu, F.-C. Chang, L. J. Lee, *Polystyrene foams with inter-connected carbon particulate network*, *Journal of Cellular Plastics* **2014**, *50*, 437–448.
- [60] C. Li, G. Yang, H. Deng, K. Wang, Q. Zhang, F. Chen, Q. Fu, *The preparation and properties of polystyrene/functionalized graphene nanocomposite foams using supercritical carbon dioxide*, *Polymer International* **2012**, *62*, 1077-1084.

- [61] C. Zhang, B. Zhu, L. J. Lee, *Extrusion foaming of polystyrene/carbon particles using carbon dioxide and water as co-blowing agents*, *Polymer* **2011**, *52*, 1847–1855.
- [62] S.-K. Yeh, J. Yang, N.-R. Chiou, T. Daniel, L. J. Lee, *Introducing water as a coblowing agent in the carbon dioxide extrusion foaming process for polystyrene thermal insulation foams*, *Polymer Engineering & Science* **2010**, *50*, 1577–1584.
- [63] Z. Guo, J. Yang, M. J. Wingert, D. L. Tomasko, L. J. Lee, T. Daniel, *Comparison of Carbon Nanofibers and Activated Carbon on Carbon Dioxide Foaming of Polystyrene*, *Journal of Cellular Plastics* **2008**, *44*, 453–468.
- [64] J. Shen, C. Zeng, L. J. Lee, *Synthesis of polystyrene–carbon nanofibers nanocomposite foams*, *Polymer* **2005**, *46*, 5218–5224.
- [65] P. Gong, P. Buahom, M.-P. Tran, M. Saniei, C. B. Park, P. Pötschke, *Heat transfer in microcellular polystyrene/multi-walled carbon nanotube nanocomposite foams*, *Carbon* **2015**, *93*, 819–829.
- [66] C. Okolieocha, T. Köppl, S. Kerling, F. J. Tölle, A. Fathi, R. Mülhaupt, V. Altstädt, *Influence of graphene on the cell morphology and mechanical properties of extruded polystyrene foam*, *Journal of Cellular Plastics* **2015**, *51*, 413–426.
- [67] M. Aksit, B. Klose, C. Zhao, K. Kreger, H.-W. Schmidt, V. Altstädt, *Morphology control of extruded polystyrene foams with benzene-trisamide-based nucleating agents*, *Journal of Cellular Plastics* **2019**, *55*, 249–261.
- [68] M. Aksit, C. Zhao, B. Klose, K. Kreger, H.-W. Schmidt, V. Altstädt, *Extruded Polystyrene Foams with Enhanced Insulation and Mechanical Properties by a Benzene-Trisamide-Based Additive*, *Polymers* **2019**, *11*.
- [69] M. Stumpf, A. Spörrer, H.-W. Schmidt, V. Altstädt, *Influence of supramolecular additives on foam morphology of injection-molded i-PP*, *Journal of Cellular Plastics* **2011**, *47*, 519–534.
- [70] M. Mörl, C. Steinlein, K. Kreger, H.-W. Schmidt, V. Altstädt, *Improved compression properties of polypropylene extrusion foams by supramolecular additives*, *Journal of Cellular Plastics* **2017**, *54*, 483–498.
- [71] M. J. Molina, F. S. Rowland, *Stratospheric sink for chlorofluoromethanes: chlorine atom-catalysed destruction of ozone*, *Nature* **1974**, *249*, 810–812.
- [72] Ozone Secreteriat, *Handbook for the Montreal Protocol on Substances that Deplete the Ozone Layer*, **2019**.
- [73] S. Quinn, *Chemical blowing agents: providing production, economic and physical improvements to a wide range of polymers*, *Plastics, Additives and Compounding* **2001**, *3*, *5*, 16–21.

## References

---

- [74] H. Hurnik, *Proceedings Addcon world '98, Proceedings Addcon world '98, London, UK, 1998*, Paper No.16.
- [75] A. S. Prakash, W. A. Swam, A. N. Strachan, *The thermal decomposition of azodicarbonamide (1,1'-azobisformamide)*, *Journal of the Chemical Society, Perkin Transactions 2* **1975**, 46–50.
- [76] H. Domininghaus, *Die Kunststoffe und ihre Eigenschaften*, Springer, Berlin, **2004**.
- [77] M. Nianounakis (Ed.), *Biopolymers: Processing and Products. Chapter 9 - Foaming and Foamed Products*, Elsevier, **2015**.
- [78] G. Liu, C. B. Park, J. A. Lefas, *Production of low-density LLDPE foams in rotational molding*, *Polymer Engineering & Science* **1998**, 38, 1997–2009.
- [79] A. Wong, *Dissertation*, University of Toronto, Toronto, **2012**.
- [80] R. Gendron, C. Vachon, M. F. Champagne, Y. Delaviz, *Foam Extrusion of PS Blown with a Mixture of HFC-134a and Isopropanol*, *Cellular Polymers* **2004**, 23, 1–24.
- [81] R. Gendron, L. E. Daigneault, *Continuous extrusion of microcellular polycarbonate*, *Polymer Engineering & Science* **2003**, 43, 1361–1377.
- [82] S. Hilic, S. A. E. Boyer, A. A. H. Pádua, J.-P. E. Grolier, *Simultaneous measurement of the solubility of nitrogen and carbon dioxide in polystyrene and of the associated polymer swelling*, *Journal of Polymer Science Part B: Polymer Physics* **2001**, 39, 2063–2070.
- [83] P. Li, T. S. Chung, D. R. Paul, *Temperature dependence of gas sorption and permeation in PIM-1*, *Journal of Membrane Science* **2014**, 450, 380–388.
- [84] V. Siracusa, *Food Packaging Permeability Behaviour: A Report*, *International Journal of Polymer Science* **2012**, 2012, 1–11.
- [85] J. Brandrup, E. H. Immergut, E. A. Grulke (Eds.), *Polymer handbook*, Wiley, New York, **1999**.
- [86] O. Muth, T. Hirth, H. Vogel, *Investigation of sorption and diffusion of supercritical carbon dioxide into poly(vinyl chloride)*, *The Journal of Supercritical Fluids* **2001**, 19, 299–306.
- [87] J. Pinto, J. A. Reglero-Ruiz, M. Dumon, M. A. Rodriguez-Perez, *Temperature influence and CO<sub>2</sub> transport in foaming processes of poly(methyl methacrylate)-block copolymer nanocellular and microcellular foams*, *The Journal of Supercritical Fluids* **2014**, 94, 198–205.
- [88] D. H. Weinkauff, D. R. Paul in *ACS Symposium Series* (Ed.: W. J. Koros), American Chemical Society, Washington, DC, **1990**, pp. 60–91.
- [89] W. R. Vieth, *Diffusion in and through polymers. Principles and applications ; 17 tables*, Hanser, Muenchen, **1991**.

- [90] T. S. Chow, *Molecular Interpretation of the Glass Transition Temperature of Polymer-Diluent Systems*, *Macromolecules* **1980**, *13*, 362–364.
- [91] Y. P. Handa, Z. Zhang, *A new technique for measuring retrograde vitrification in polymer-gas systems and for making ultramicrocellular foams from the retrograde phase*, *Journal of Polymer Science Part B: Polymer Physics* **2000**, *38*, 716–725.
- [92] Z. Zhang, Y. P. Handa, *An in situ study of plasticization of polymers by high-pressure gases*, *Journal of Polymer Science Part B: Polymer Physics* **1998**, *36*, 977–982.
- [93] Z. Zhang, A. V. Nawaby, M. Day, *CO<sub>2</sub>-delayed crystallization of isotactic polypropylene: A kinetic study*, *Journal of Polymer Science Part B: Polymer Physics* **2003**, *41*, 1518–1525.
- [94] M. Takada, M. Tanigaki, M. Ohshima, *Effects of CO<sub>2</sub> on crystallization kinetics of polypropylene*, *Polymer Engineering & Science* **2001**, *41*, 1938–1946.
- [95] A. S. Tucker, C. A. Ward, *Critical state of bubbles in liquid-gas solutions*, *Journal of Applied Physics* **1975**, *46*, 4801–4808.
- [96] C. A. Ward, A. Balakrishnan, F. C. Hooper, *On the Thermodynamics of Nucleation in Weak Gas-Liquid Solutions*, *Journal of Basic Engineering* **1970**, *92*, 695–701.
- [97] R. Cole in *Advances in Heat Transfer*, Elsevier, **1974**, pp. 85–166.
- [98] J. C. Fisher, *The Fracture of Liquids*, *Journal of Applied Physics* **1948**, *19*, 1062–1067.
- [99] J. R. Street, A. L. Fricke, L. P. Reiss, *Dynamics of Phase Growth in Viscous, Non-Newtonian Liquids. Initial Stages of Growth*, *Industrial & Engineering Chemistry Fundamentals* **1971**, *10*, 54–64.
- [100] E. J. Barlow, W. E. Langlois, *Diffusion of Gas from a Liquid into an Expanding Bubble*, *IBM Journal of Research and Development* **1962**, *6*, 329–337.
- [101] T. R. Tuladhar, M. R. Mackley, *Experimental observations and modelling relating to foaming and bubble growth from pentane loaded polystyrene melts*, *Chemical Engineering Science* **2004**, *59*, 5997–6014.
- [102] N. S. Ramesh, D. H. Rasmussen, G. A. Campbell, *Numerical and experimental studies of bubble growth during the microcellular foaming process*, *Polymer Engineering & Science* **1991**, *31*, 1657–1664.
- [103] S. N. Leung, C. B. Park, D. Xu, H. Li, R. G. Fenton, *Computer Simulation of Bubble-Growth Phenomena in Foaming*, *Industrial & Engineering Chemistry Research* **2006**, *45*, 7823–7831.
- [104] I. M. Balashova, R. P. Danner, *Solubility and diffusivity of carbon dioxide in poly(styrene-co-acrylonitrile)*, *Fluid Phase Equilibria* **2016**, *428*, 92–94.
- [105] C. B. Park, L. K. Cheung, *A study of cell nucleation in the extrusion of polypropylene foams*, *Polymer Engineering & Science* **1997**, *37*, 1–10.

## References

---

- [106] H. E. Naguib, C. B. Park, U. Panzer, N. Reichelt, *Strategies for achieving ultra low-density polypropylene foams*, *Polymer Engineering & Science* **2002**, 42, 1481–1492.
- [107] M. Okamoto, P. H. Nam, P. Maiti, T. Kotaka, T. Nakayama, *Biaxial Flow-Induced Alignment of Silicate Layers in Polypropylene/Clay Nanocomposite Foam*, *Nano Letters* **2001**, 1, 503–505.
- [108] H. E. Naguib, C. B. Park, N. Reichelt, *Fundamental foaming mechanisms governing the volume expansion of extruded polypropylene foams*, *Journal of Applied Polymer Science* **2004**, 91, 2661–2668.
- [109] T. Standau, V. Altstädt in *Polypropylene Handbook* (Eds.: J. Karger-Kocsis, T. Bárány), Springer International Publishing, Cham, **2019**, pp. 579–641.
- [110] S. W. Cha, N. P. Suh, D. F. Baldwin, C. B. Park, U.S. Patent 5,158,986, **1991**.
- [111] J. E. Martini-Vyedensky, N. P. Suh, F. A. Waldman, U.S. Patent 4,473,665, **1982**.
- [112] V. Kumar, N. P. Suh, *A process for making microcellular thermoplastic parts*, *Polymer Engineering and Science* **1990**, 30, 1323–1329.
- [113] J. S. Colton, N. P. Suh, U.S. Patent 5,160,674, **1990**.
- [114] A. Braun, *Dissertation*, Montanuniversität Leoben, Leoben, **2011**.
- [115] S. H. Lee, Y. Zhang, M. Kontopoulou, C. B. Park, A. Wong, W. Zhai, *Optimization of Dispersion of Nanosilica Particles in a PP Matrix and Their Effect on Foaming*, *International Polymer Processing* **2011**, 26, 388–398.
- [116] J. G. Burt, *The Elements of Expansion of Thermoplastics Part II*, *Journal of Cellular Plastics* **1978**, 14, 341–345.
- [117] D. Y. Kim, J. H. Cha, K. H. Seo, *Effects of chain extender on properties and foaming behavior of polypropylene foam*, *RSC Advances* **2019**, 9, 25496–25507.
- [118] S. Li, M. Xiao, Y. Guan, D. Wei, H. Xiao, A. Zheng, *A novel strategy for the preparation of long chain branching polypropylene and the investigation on foamability and rheology*, *European Polymer Journal* **2012**, 48, 362–371.
- [119] J. Ludwiczak, M. Kozłowski, *Foaming of Polylactide in the Presence of Chain Extender*, *Journal of Polymers and the Environment* **2015**, 23, 137–142.
- [120] T. Standau, B. Hädelt, P. Schreier, V. Altstädt, *Development of a Bead Foam from an Engineering Polymer with Addition of Chain Extender: Expanded Polybutylene Terephthalate*, *Industrial & Engineering Chemistry Research* **2018**, 57, 17170–17176.
- [121] D. Raps, N. Hossieny, C. B. Park, V. Altstädt, *Past and present developments in polymer bead foams and bead foaming technology*, *Polymer* **2015**, 56, 5–19.
- [122] R. N. Britton, *Mouldable particle foam technology*, Smithers Rapra, London, **2009**.

- [123] J. Scheirs, D. B. Priddy, *Modern Styrenic Polymers: Polystyrenes and Styrenic Copolymers*, John Wiley & Sons, Ltd, Chichester, UK, **2003**.
- [124] J. Wagner, *Dissertation*, Heidelberg University, Heidelberg, **2012**.
- [125] T. Köppl, *Dissertation*, Universität Bayreuth, Bayreuth, **2014**.
- [126] P. Eyerer, *Polymer engineering. Technologien und Praxis*, Springer, Berlin, Heidelberg, **2008**.
- [127] J. Rossacci, S. Shivkumar, *Bead fusion in polystyrene foams*, *Journal of Materials Science* **2003**, *38*, 201–206.
- [128] T. Neumeyer, *Führen alle Wege zum gleichen Ziel? Technologien für das Schaumspritzgießen im Überblick. SKZ Polymerschäume*, Würzburg, **2018**.
- [129] M. Barzegari, *Dissertation*, Universität Laval, Quebec, **2009**.
- [130] L. Zhang, G. Zhao, G. Dong, S. Li, G. Wang, *Bubble morphological evolution and surface defect formation mechanism in the microcellular foam injection molding process*, *RSC Advances* **2015**, *5*, 70032–70050.
- [131] H. Guanghong, W. Yue in *Some Critical Issues for Injection Molding* (Ed.: J. Wang), InTech, **2012**.
- [132] R. M. Aseeva, D. Klempner, *Handbook of polymeric foams and foam technology*, Hanser, Munich, **2004**.
- [133] W.-Y. Jang, A. M. Kraynik, S. Kyriakides, *On the microstructure of open-cell foams and its effect on elastic properties*, *International Journal of Solids and Structures* **2008**, *45*, 1845–1875.
- [134] C. Okolieocha, D. Raps, K. Subramaniam, V. Altstädt, *Microcellular to nanocellular polymer foams*, *European Polymer Journal* **2015**, *73*, 500–519.
- [135] F.-L. Jin, M. Zhao, M. Park, S.-J. Park, *Recent Trends of Foaming in Polymer Processing: A Review*, *Polymers* **2019**, *11*.
- [136] S. A. Taghizadeh, A. Farrokhhabadi, G. Liaghat, E. Pedram, H. Malekinejad, S. F. Mohammadi, H. Ahmadi, *Characterization of compressive behavior of PVC foam infilled composite sandwich panels with different corrugated core shapes*, *Thin-Walled Structures* **2019**, *135*, 160–172.
- [137] Y. Wang, Y. Zheng, W. He, C. Wang, Y. Sun, K. Qiao, X. Wang, L. Gao, *Preparation of a novel sodium alginate/polyvinyl formal composite with a double crosslinking interpenetrating network for multifunctional biomedical application*, *Composites Part B: Engineering* **2017**, *121*, 9–22.
- [138] J. Zhao, Q. Zhao, C. Wang, B. Guo, C. B. Park, G. Wang, *High thermal insulation and compressive strength polypropylene foams fabricated by high-pressure foam injection molding and mold opening of nano-fibrillar composites*, *Materials & Design* **2017**, *131*, 1–11.

## References

---

- [139] A. Prociak, E. Malewska, M. Kurańska, S. Bąk, P. Budny, *Flexible polyurethane foams synthesized with palm oil-based bio-polyols obtained with the use of different oxirane ring opener*, *Industrial Crops and Products* **2018**, 115, 69–77.
- [140] E. Linul, C. Vălean, P.-A. Linul, *Compressive Behavior of Aluminum Microfibers Reinforced Semi-Rigid Polyurethane Foams*, *Polymers* **2018**, 10.
- [141] F. Carosio, M. Ghanadpour, J. Alongi, L. Wågberg, *Layer-by-layer-assembled chitosan/phosphorylated cellulose nanofibrils as a bio-based and flame protecting nano-exoskeleton on PU foams*, *Carbohydrate polymers* **2018**, 202, 479–487.
- [142] B. Sun, L. Kulinsky, *Fabrication of regular polystyrene foam structures with selective laser sintering*, *Materials Today Communications* **2017**, 13, 346–353.
- [143] B. Alander, A. J. Capezza, Q. Wu, E. Johansson, R. T. Olsson, M. S. Hedenqvist, *A facile way of making inexpensive rigid and soft protein biofoams with rapid liquid absorption*, *Industrial Crops and Products* **2018**, 119, 41–48.
- [144] S.-T. Lee, C. B. Park, *Foam Extrusion. Principles and Practice Second Edition*, Taylor & Francis Inc, Boca Roca, **2014**.
- [145] T. L. Heath, *The works of Archimedes*, University Press, Cambridge, **1897**.
- [146] F. A. L. Dullien, *Porous Media. Fluid Transport and Pore Structure*, Academic Press, San Diego, New York, Boston, London, Sydney, Tokyo, Toronto, **2015**.
- [147] P. Liu, D. Liu, H. Zou, P. Fan, W. Xu, *Structure and properties of closed-cell foam prepared from irradiation crosslinked silicone rubber*, *Journal of Applied Polymer Science* **2009**, 113, 3590–3595.
- [148] Q. Huang, R. Kloetzer, B. Seibig, D. Paul, *Extrusion of microcellular polysulfone using chemical blowing agents*, *Journal of Applied Polymer Science* **1998**, 69, 1753–1760.
- [149] J. Pinto, E. Solórzano, M. A. Rodríguez-Pérez, J. A. de Saja, *Characterization of the cellular structure based on user-interactive image analysis procedures*, *Journal of Cellular Plastics* **2013**, 49, 555–575.
- [150] D. Eaves, R. T. Limited, *Polymer Foams: Trends in Use and Technology (Rapra Industry Analysis Report Series)*, Smithers Rapra, **2001**.
- [151] T. Li, G. Zhao, G. Wang, L. Zhang, J. Hou, *Thermal-Insulation, Electrical, and Mechanical Properties of Highly-Expanded PMMA/MWCNT Nanocomposite Foams Fabricated by Supercritical CO<sub>2</sub> Foaming*, *Macromolecular Materials and Engineering* **2019**, 304, 1800789.
- [152] B. Notario, J. Pinto, E. Solorzano, J. A. de Saja, M. Dumon, M. A. Rodríguez-Pérez, *Experimental validation of the Knudsen effect in nanocellular polymeric foams*, *Polymer* **2015**, 56, 57–67.

- [153] S. Liu, J. Duvigneau, G. J. Vancso, *Nanocellular polymer foams as promising high performance thermal insulation materials*, *European Polymer Journal* **2015**, *65*, 33–45.
- [154] A. N. Abramenko, A. S. Kalinichenko, Y. Burtser, V. A. Kalinichenko, S. A. Tanaeva, I. P. Vasilenko, *Determination of the thermal conductivity of foam aluminum*, *Journal of Engineering Physics and Thermophysics* **1999**, *72*, 369–373.
- [155] M. A. Schuetz, L. R. Glicksman, *A Basic Study of Heat Transfer Through Foam Insulation*, *Journal of Cellular Plastics* **1984**, *20*, 114–121.
- [156] J. A. Valenzuela, L. R. Glicksman in *Thermal Insulation, Materials, and Systems for Energy Conservation in the '80s* (Eds.: F. A. Govan, D. M. Greason, J. D. McAllister), ASTM International, 100 Barr Harbor Drive, PO Box C700, West Conshohocken, PA 19428-2959, **1983**, 688-688-15.
- [157] M. Arduini-Schuster, J. Manara, C. Vo, *Experimental characterization and theoretical modeling of the infrared-optical properties and the thermal conductivity of foams*, *International Journal of Thermal Sciences* **2015**, *98*, 156–164.
- [158] R. A. Campo-Arnáiz, M. A. Rodríguez-Pérez, B. Calvo, J. A. de Saja, *Extinction coefficient of polyolefin foams*, *Journal of Polymer Science Part B: Polymer Physics* **2005**, *43*, 1608–1617.
- [159] A. Kaemmerlen, C. Vo, F. Asllanaj, G. Jeandel, D. Baillis, *Radiative properties of extruded polystyrene foams: Predictive model and experimental results*, *Journal of Quantitative Spectroscopy and Radiative Transfer* **2010**, *111*, 865–877.
- [160] J.-M. Lehn, *Supramolecular chemistry ? Scope and perspectives: Molecules ? Supermolecules ? Molecular devices*, *Journal of Inclusion Phenomena* **1988**, *6*, 351–396.
- [161] C. A. Schalley in *Analytical Methods in Supramolecular Chemistry* (Ed.: C. Schalley), Wiley-VCH Verlag GmbH & Co. KGaA, Weinheim, Germany, **2006**, pp. 1–16.
- [162] G. M. Whitesides, J. P. Mathias, C. T. Seto, *Molecular self-assembly and nanochemistry: a chemical strategy for the synthesis of nanostructures*, *Science (New York, N.Y.)* **1991**, *254*, 1312–1319.
- [163] E. Arunan, G. R. Desiraju, R. A. Klein, J. Sadlej, S. Scheiner, I. Alkorta, D. C. Clary, R. H. Crabtree, J. J. Dannenberg, P. Hobza et al., *Definition of the hydrogen bond (IUPAC Recommendations 2011)*, *Pure and Applied Chemistry* **2011**, *83*, 1637–1641.
- [164] J. W. Steed, J. L. Atwood, *Supramolecular chemistry*, John Wiley, Chichester, **op. 2009**.
- [165] A. Yonath, *Polar bears, antibiotics, and the evolving ribosome (Nobel Lecture)*, *Angewandte Chemie (International ed. in English)* **2010**, *49*, 4341–4354.

## References

---

- [166] N. Mohmeyer, N. Behrendt, X. Zhang, P. Smith, V. Altstädt, G. M. Sessler, H.-W. Schmidt, *Additives to improve the electret properties of isotactic polypropylene*, *Polymer* **2007**, *48*, 1612–1619.
- [167] F. Abraham, H.-W. Schmidt, *1,3,5-Benzenetrisamide based nucleating agents for poly(vinylidene fluoride)*, *Polymer* **2010**, *51*, 913–921.
- [168] F. Richter, H.-W. Schmidt, *Supramolecular Nucleating Agents for Poly(butylene terephthalate) Based on 1,3,5-Benzenetrisamides*, *Macromolecular Materials and Engineering* **2013**, *298*, 190–200.
- [169] M. Blomenhofer, S. Ganzleben, D. Hanft, H.-W. Schmidt, M. Kristiansen, P. Smith, K. Stoll, D. Mäder, K. Hoffmann, *“Designer” Nucleating Agents for Polypropylene*, *Macromolecules* **2005**, *38*, 3688–3695.
- [170] M. Kersch, L. Pischke, H.-W. Schmidt, V. Altstädt, *Influence of trisamide-based additives on the morphological and mechanical properties of isotactic polypropylene*, *Polymer* **2014**, *55*, 3227–3233.
- [171] M. Kersch, H.-W. Schmidt, V. Altstädt, *Influence of different beta-nucleating agents on the morphology of isotactic polypropylene and their toughening effectiveness*, *Polymer* **2016**, *98*, 320–326.
- [172] T. A. Shepard, C. R. Delsorbo, R. M. Louth, J. L. Walborn, D. A. Norman, N. G. Harvey, R. J. Spontak, *Self-organization and polyolefin nucleation efficacy of 1,3:2,4-di-p-methylbenzylidene sorbitol*, *Journal of Polymer Science Part B: Polymer Physics* **1997**, *35*, 2617–2628.
- [173] M. Kristiansen, M. Werner, T. Tervoort, P. Smith, M. Blomenhofer, H.-W. Schmidt, *The Binary System Isotactic Polypropylene/Bis(3,4-dimethylbenzylidene)sorbitol: Phase Behavior, Nucleation, and Optical Properties*, *Macromolecules* **2003**, *36*, 5150–5156.
- [174] D. Libster, A. Aserin, N. Garti, *Advanced nucleating agents for polypropylene*, *Polymers for Advanced Technologies* **2007**, *18*, 685–695.
- [175] R. Mahaffey, US 4,371,645, **1981**.
- [176] K. Hamada, H. Uchiyama, US 4,016,118, **1975**.
- [177] C. Mathieu, A. Thierry, J. C. Wittmann, B. Lotz, *Specificity and versatility of nucleating agents toward isotactic polypropylene crystal phases*, *Journal of Polymer Science Part B: Polymer Physics* **2002**, *40*, 2504–2515.
- [178] W. Stocker, M. Schumacher, S. Graff, A. Thierry, J.-C. Wittmann, B. Lotz, *Epitaxial Crystallization and AFM Investigation of a Frustrated Polymer Structure: Isotactic Poly(propylene),  $\beta$  Phase*, *Macromolecules* **1998**, *31*, 807–814.

- [179] N. Mohmeyer, H.-W. Schmidt, P. M. Kristiansen, V. Altstädt, *Influence of Chemical Structure and Solubility of Bisamide Additives on the Nucleation of Isotactic Polypropylene and the Improvement of Its Charge Storage Properties* †, *Macromolecules* **2006**, *39*, 5760–5767.
- [180] Q. Lu, Q. Dou, *Effect of a Novel Family of N,N'-Diphenyl Bisamides on the Formation of  $\beta$  Crystalline Form in Isotactic Polypropylene*, *Journal of Polymer Science Part B: Polymer Physics* **2009**, *41*, 254–259.
- [181] F. Abraham, S. Ganzleben, D. Hanft, P. Smith, H.-W. Schmidt, *Synthesis and Structure-Efficiency Relations of 1,3,5-Benzenetrisamides as Nucleating Agents and Clarifiers for Isotactic Poly(propylene)*, *Macromolecular Chemistry and Physics* **2010**, *211*, 171–181.
- [182] F. Abraham, R. Kress, P. Smith, H.-W. Schmidt, *A New Class of Ultra-Efficient Supramolecular Nucleating Agents for Isotactic Polypropylene*, *Macromolecular Chemistry and Physics* **2013**, *214*, 17–24.
- [183] M. Kristiansen, P. Smith, H. Chanzy, C. Baerlocher, V. Gramlich, L. McCusker, T. Weber, P. Pattison, M. Blomenhofer, H.-W. Schmidt, *Structural Aspects of 1,3,5-Benzenetrisamides—A New Family of Nucleating Agents*, *Crystal Growth & Design* **2009**, *9*, 2556–2558.
- [184] C. S. Zehe, J. A. Hill, N. P. Funnell, K. Kreger, K. P. van der Zwan, A. L. Goodwin, H.-W. Schmidt, J. Senker, *Mesoscale Polarization by Geometric Frustration in Columnar Supramolecular Crystals*, *Angewandte Chemie (International ed. in English)* **2017**, *56*, 4432–4437.
- [185] Y. Matsunaga, N. Miyajima, Y. Nakayasu, S. Sakai, M. Yonenaga, *Design of Novel Mesomorphic Compounds: N, N', N''-Trialkyl-1,3,5-benzenetricarboxamides*, *Bulletin of the Chemical Society of Japan* **1988**, *61*, 207–210.
- [186] D. Ogata, T. Shikata, K. Hanabusa, *Chiral Amplification of the Structure and Viscoelasticity of a Supramolecular Polymeric System Consisting of N, N', N''-Tris(3,7-Dimethyloctyl)Benzene-1,3,5-Tricarboxamide and n-Decane*, *The Journal of Physical Chemistry B* **2004**, *108*, 15503–15510.
- [187] S. Lee, J.-S. Lee, C. H. Lee, Y.-S. Jung, J.-M. Kim, *Nonpolymeric thermosensitive benzenetricarboxamides*, *Langmuir : the ACS journal of surfaces and colloids* **2011**, *27*, 1560–1564.
- [188] A. Bernet, R. Q. Albuquerque, M. Behr, S. T. Hoffmann, H.-W. Schmidt, *Formation of a supramolecular chromophore: a spectroscopic and theoretical study*, *Soft Matter* **2012**, *8*, 66–69.
- [189] B. A. Rodeheaver, J. S. Colton, *Open-celled microcellular thermoplastic foam*, *Polym. Eng. Sci.* **2001**, *41*, 380–400.

## References

---

- [190] Ineos Styrolution, "Styrolution PS 168N/L. Technical Datasheet", can be found under [https://www.ineos-styrolution.com/INTERSHOP/web/WFS/Styrolution-Portal-Site/en\\_US/-/USD/ViewPDF-Print.pdf?SKU=200300060596&RenderPageType=ProductDetail](https://www.ineos-styrolution.com/INTERSHOP/web/WFS/Styrolution-Portal-Site/en_US/-/USD/ViewPDF-Print.pdf?SKU=200300060596&RenderPageType=ProductDetail), **2016**.
- [191] B. Klose, D. Kremer, M. Aksit, K. P. van der Zwan, K. Kreger, J. Senker, V. Altstädt, H.-W. Schmidt, *Kinked Bisamides as Efficient Supramolecular Foam Cell Nucleating Agents for Low-Density Polystyrene Foams with Homogeneous Microcellular Morphology*, *Polymers* **2021**, *13*(7), 1094.
- [192] T. Urushihara, N. Ueda, N. Kawamoto, US 8,420,721 B2, **2013**.
- [193] Y. Kitagawa, S. Miki, H. Kitagawa, N. Ikeda, JP 06279378, **1993**.

## 8 Acknowledgement

First of all, I would like to thank Prof. Dr. Hans-Werner Schmidt for the opportunity to write my dissertation at the Chair of Macromolecular Chemistry I at the University of Bayreuth. Due to the excellent supervision, the constant readiness for technical discussions and the inspiration with new ideas, it was possible to work on this very exciting topic in an excellent way.

I would also like to thank the German Research Foundation DFG for financially supporting my work within the framework of the Collaborative Research Center SFB 840 in subproject B4.

Furthermore, I would like to thank my cooperation partner, the Chair of Polymer Materials at the University of Bayreuth. First and foremost, Prof. Dr. Volker Altstädt for the very informative discussion sessions and the opportunity to conduct all relevant foam experiments at his chair. Furthermore, I would like to thank my direct cooperation partner Merve Aksit for the good cooperation and the guidance of the foam extrusions. I would also like to thank Sebastian Gröschel for his help with these experiments.

Further thanks are owed to Neue Materialien Bayreuth GmbH, with their help I was able to carry out the foam injection molding tests together with Katharina Krause and Sven Bauer. This also required the help of Lifocolor Farben GmbH & Co. KG, who performed the necessary compounding work under the direction of Markus Blomenhofer. A heartfelt thank you for this.

Special gratitude goes to Dr. Klaus Kreger for his very helpful technical discussions and advice which contributed significantly to the success of this work. Also for his assistance with the written work.

I would like to thank the technical staff Doris Hanft, Sandra Ganzleben and Jutta Failner for the synthesis of the used additives. I would also like to thank Martina Heider for her instruction and support in the use of scanning electron microscopy. Thanks are also owed to Alexander Kern and Jonas Mayer for their support in all IT matters as well as for their assistance with various technical tasks.

Petra Weiss and Christina Wunderlich deserve a special thank you for their excellent handling of all organizational matters.

I would also like to thank all current and former inmates of the model laboratory 597 for the great working atmosphere and the fruitful discussions. Furthermore, I would like to thank the whole working group of MC I for the great time and the friendships that were formed outside of work. A Merci also goes to the Kicker community who always provided me with ice cream and sweets thanks to the "Giro list".

## Acknowledgement

---

I would also like to thank Timon, Alexander, Sebastian, Paula, and Florian who worked on my projects as master students in the course of internships. Furthermore, I would like to thank Teresa and Michael, who also worked on a part of my projects in the course of their bachelor thesis.

For my parents:

Der größte Dank gilt meinen Eltern, Ingrid und Peter sowie der gesamten Familie. Ihr habt mir ein sorgenfreies Chemiestudium ermöglicht woraus diese Arbeit erst entstehen konnte. Danke für die Unterstützung und das Vertrauen zu jeder Zeit! Diese Arbeit ist nicht nur für mich, sondern auch für euch. Ihr Seid der HAMMER!

Schließlich möchte ich mich auch bei dir, Marion bedanken für deine stetige Unterstützung nicht nur beim Anfertigen dieser Arbeit, sondern auch außerhalb des Universitätslebens. Ohne dich wäre die Zeit in Bayreuth nur halb so schön gewesen und ich freue mich umso mehr, dass du mit mir zusammen den nächsten Abschnitt gemeinsam bestreitest.

## (Eidesstattliche) Versicherungen und Erklärungen

### **(§ 9 Satz 2 Nr. 3 PromO BayNAT)**

Hiermit versichere ich eidesstattlich, dass ich die Arbeit selbstständig verfasst und keine anderen als die von mir angegebenen Quellen und Hilfsmittel benutzt habe (vgl. Art. 64 Abs. 1 Satz 6 BayHSchG).

### **(§ 9 Satz 2 Nr. 3 PromO BayNAT)**

Hiermit erkläre ich, dass ich die Dissertation nicht bereits zur Erlangung eines akademischen Grades eingereicht habe und dass ich nicht bereits diese oder eine gleichartige Doktorprüfung endgültig nicht bestanden habe.

### **(§ 9 Satz 2 Nr. 4 PromO BayNAT)**

Hiermit erkläre ich, dass ich Hilfe von gewerblichen Promotionsberatern bzw. -vermittlern oder ähnlichen Dienstleistern weder bisher in Anspruch genommen habe noch künftig in Anspruch nehmen werde.

### **(§ 9 Satz 2 Nr. 7 PromO BayNAT)**

Hiermit erkläre ich mein Einverständnis, dass die elektronische Fassung meiner Dissertation unter Wahrung meiner Urheberrechte und des Datenschutzes einer gesonderten Überprüfung unterzogen werden kann.

### **(§ 9 Satz 2 Nr. 8 PromO BayNAT)**

Hiermit erkläre ich mein Einverständnis, dass bei Verdacht wissenschaftlichen Fehlverhaltens Ermittlungen durch universitätsinterne Organe der wissenschaftlichen Selbstkontrolle stattfinden können.

---

*Ort, Datum*

*Unterschrift*